# A STUDY OF DOWN-CONVERSION AND UP-CONVERSION IN LANTHANIDE DOPED IN SILICA GLASS CO-DOPED IN METAL NANO-PARTICLE TOWARDS PHOTONICS APPLICATIONS

**A THESIS SUBMITTED IN PARTIAL FULFILLMENT OF THE REQUIREMENTS FOR THE DEGREE OF DOCTOR OF PHILOSOPHY IN PHYSICS**

**MRIGANKADEEP BHARADWAJ**

**MZU REGISTRATION NO. 1906296**

**Ph.D. REGISTRATION NO. AND DATE: MZU/Ph.D./1458 of 26.07.2019**


**DEPARTMENT OF PHYSICS, SCHOOL OF PHYSICAL SCIENCE**

**MIZORAM UNIVERSITY, AIZAWL**

**MIZORAM, INDIA**

**FEBRUARY, 2024**

# A STUDY OF DOWN-CONVERSION AND UP-CONVERSION IN LANTHANIDE DOPED IN SILICA GLASS CO-DOPED IN METAL NANO-PARTICLE TOWARDS PHOTONICS APPLICATIONS

**BY**

**Mrigankadeep Bharadwaj**

**Department of Physics, Mizoram University**

**Under the Supervision of**

**Prof. Suman Rai**

**Submitted**

**In partial fulfillment of the requirement of the Degree of Doctor of Philosophy in Physics of Mizoram University, Aizawl**

DEPARTMENT OF PHYSICS

SCHOOL OF PHYSICAL SCIENCE

MIZORAM UNIVERSITY, AIZAWL,

MIZORAM

Prof. Suman Rai

*Senior Professor*

*E-mail: srai.rai677@gmail.com*

Mobile: +91-8732853277

+91-9936067009

**No.** **Date: 16.02.2025**

***Certificate***

*This is to certify that the thesis entitled "**A Study of Downconversion and Upconversion in Lanthanide doped in Silica Glass co-doped in metal nano-particle towards Photonics applications**" submitted by **Mrigankadeep Bharadwaj** for the degree of **Doctor of Philosophy** under Mizoram University, Aizawl, Mizoram, India embodies the record of original investigations carried out by him under my supervision. He has been duly registered and the thesis presented is worthy of being considered for the award of the Ph.D degree. This work has not been submitted for any degree of any other university.*

**(Prof. Suman Rai)**

**Supervisor**

***Declaration of the Candidate***

***Mizoram University***

***February, 2025***

*I, **Mrigankadeep Bharadwaj**, hereby declare that the subject matter of this thesis is the record of the work done by me, that the contents of this thesis did not form basis of the award of any previous degree to me or to do the best of my knowledge to anybody else, and that the thesis has not been submitted by me for any research degree in any other University/Institute.*

*This thesis is being submitted to Mizoram University for the degree of Doctor of Philosophy in Physics and experimental works are performed in Department of Physics, Mizoram University.*

**Mrigankadeep Bharadwaj**

**(Candidate)**

**Prof. Zaithanzauva Pachuau** **(Prof. Suman Rai)**

**(Head)** **(Supervisor)**

## ***ACKNOWLEDGEMENTS***

*The formal culmination of my PhD journey marks a significant milestone in my professional life. As I on this auspicious juncture, I extend my heartfelt thanks to individual from diverse spheres whoever played crucial role in guiding me through this odyssey of wisdom. I begin by invoking the goddess of knowledge and intellect, Maa Saraswati, with a prayer:*

***"Oh Devi Saraswati, You have been imparting knowledge to us from your vast ocean.***

***Please adorn this universe with your immense intellect."***

*Foremost, I express my deepest gratitude to my supervisor,* ***Prof. Suman Rai*** *whose unwavering guidance, support, and commitment have been instrumental throughout my research. I firmly believe that his decision to mentor me was pivotal turning point in my life. Prof. Rai provided essential resources and through guidance, shaping my entire PhD journey.*

***I would like to express my heartfelt grattitutr to, Dr Ankita Gaur, School of Energy Sciences and Technology*** *of IIT Guwahati* ***for her*** *unwavering support, guidance, mentorship throughout my PhD journey. As my external supervisioer and corresponding author, she provided invaluable expertise, acess to research materials and laboratory including characterization facility in CIF, IIT Guwahati. I am deeply grateful for the opportunity to work with to work with her as a Research Inter in her lab at IITG, which was an enriching experience.*

*I am grateful to CSIR- NPL for providing PL confocal mapping and Upconversion luminescence spectra of sample which is a crucial part of my research work. I am also grateful to CSIR-NIIST for providing some of important data of our samples. I am grateful to the Department of Physics, Mizoram University, as the institute provides me different characterization facilities for my PhD work. I am also grateful to CIF, IIT Guwahati.*

*I would like to thank the Head of the Department of Physics for allowing me to work as a registered scholar in the Department of Physics, Mizoram University. I*

*would also like to thank all the faculty members in the Department of Physics for their valuable suggestions and directions regarding my research work. I also thank the non-teaching staff of the department for always being very helpful whenever I have needed it. I am also grateful to my fellow Research Scholar Firdoos da, Avik da, Pu Ruatpuai, Pu KMS and all other for unconditional support in this journey.*

*My thanks extend to well-wishers, friends, family members and fellow villagers, especially Ajay Nath, Bhargav Borthakur, Pankaj Gogoi, Nayan Boruah, Sabranika Boruah, Hemanta Kotoky, Sarat Kotoky, Dipali Boruah, Rupali Bordoloi, Rupjyouti Boruah and Prof. Dipak Jyoti Boruah. I cherish the memory of my best well-wishers and friends Ashok Boruah, Late Birendra Nath Borpuzari, Late Tarun Kr Boruah, Late Pabitra Kr. Boruah, who supported me in various ways.*

*Lastly, I am grateful to my two sisters (Ms Juri Borpuzari and Ms Jumi Boruah), for their patience over three and half decades and unwavering faith in me. I extend appreciation to my two brothers-in-law (Mr Abhijit Borpuzari and Mr Kuntal Kaushik) for standing by me whenever needed. I am grateful to my parents in law (Mr. Sitaram Dutta and Ms. Nijara Dutta) for keeping faith on me. My future wife, Ms Panchalika Dutta, has been the architect of my success, providing constant personal and financial support while emotionally grounding me. Special thanks to Mr Bipul Boruah and Ms. Dipty Boruah for their continuous support and blessings.*

*In conclusion, I extend my prayers for the personal and professional upliftment of all those who directly or indirectly contribute to my journey.*

Dated- 16th February, 2025 (Mrigankadeep Bharadwaj)

Mizoram University

# CONTENTS


| | | Page No. |
|---|---|---|
| Certificate | | i |
| Declaration of the Candidate | | ii |
| Acknowledgments | | iii |
| Contents | | v |
| List of Figures | | xiv |
| List of Tables | | xviii |
| List of Abbreviations | | xx |
| Chapter 1: | Background of the thesis | 1-55 |
| | 1.1 Introduction | 1 |
| | 1.2 Rare Earth elements | 3 |
| | 1.3 Photoluminescence spectra | 5 |
| | 1.3.1. Downconversion luminescence | 5 |
| | 1.3.2. Upconversion luminescence | 6 |
| | 1.3.3. Quantum efficiency | 7 |
| | 1.4 Theoretical brackground | 8 |
| | 1.4.1. Crystal field interaction | 9 |
| | 1.4.1.1. The relativistic approach | 10 |
| | 1.4.1.2. Non-relativistic approach | 10 |
| | 1.4.1.3. Intermediate coupling approximation | 11 |
| | 1.4.1.4. Electrostatic interaction: The central-field approximation | 11 |

1.4.1.5. The spin-orbit interaction 13
1.4.1.6. Wigner symbols 14
1.4.1.7. Wigner-Eckart theorem 14
1.4.1.8. The Reduced Matrix Element
1.4.2. J-O intensity parameters 16
1.4.2.1. The transition probability of a transition 16
1.4.2.2. Laporte selection rule: Symmetry of host
1.4.2.3. The virtual-cavity model 17
1.4.2.3.1. The Calculated Oscillator Strength ($f_{cal}$) 18
1.4.2.3.2. The Experimental Oscillator Strength ($f_{exp}$) 18
1.4.2.3.3. Root-Mean-Square (RMS) deviation 18
1.4.3. Significance of J-O parameters 18
1.5 Factors of UCL and DCL 19
1.5.1. Dopants: Activator-Sensitizer pair 19
1.5.2. Concentration quenching 20
1.5.3. Phonon energy of host 20
1.5.4. Doping impurity elements 22
1.5.4.1. Transition metal impurity 23
1.5.4.2. Semiconductor impurity 23
1.5.5. Dielectric superlensing effect : Mie resonance 24
1.5.6. Excitation irradiance 24

1.5.7. Core-Shell 24
1.5.8. Plasmonic material 25
1.6 Potential applications 25
1.6.1. Photovoltaic Solar Cell 25
1.6.2. Multicolor tuning for Bio-label 26
1.6.3. Optical thermometry: nanoheater 26
1.6.4. Bio-application 28
1.6.5. Other applications 28
1.7 Review of literature : in the context of present work 29
1.7.1. $Pr^{3+}$ -$Yb^{3+}$ pair 29
1.7.2. $Nd^{3+}$ -$Yb^{3+}$ pair 31
1.7.3. $Er^{3+}$ -$Yb^{3+}$ pair 34
1.7.4. Zinc silicate host 34
1.7.5. Titania Silicate host 39
1.8 Scope of study 43
1.8.1. $Pr^{3+}$-$Yb^{3+}$ ion pair co-doping in $TiO_2$-$SiO_2$ binary composite 43
1.8.2. $Nd^{3+}$-$Yb^{3+}$ ion pair co-doped in ZnO-$SiO_2$ composite 44
1.9 Conclusion 44
References 46
Chapter 2: Experimental Techniques 58-87
2.1 Introduction 58

2.2 Synthesis 58

2.2.1 Precursors and starting material 59

2.2.2 Synthesis method 60

2.2.2.1 Sol-Gel process 60

2.2.2.2 Host modifier 65

2.2.2.2.1. $SiO_2$-$TiO_2$ binary host for $RE^{3+}$ ion doping 65

2.2.2.2.2. ZnO-$SiO_2$ binary host for $RE^{3+}$ ion doping 66

2.2.2.2.3 Thin film preparation 67

2.3 Physical characterisation 68

2.3.1. Density and porosity 66

2.3.2 Measurement of Refractive index 69

2.3.3. Effective mass approximation (EMA) 70

2.4 Structural and microstructural strudies 71

2.4.1. ATR-FTIR spectroscopy 71

2.4.1.1. Instrument 71

2.4.2. XRD Technique 72

2.4.2.1. Instrument 74

2.4.3. The Morphological characterization 75

2.4.3.1. FETEM analysis 75

2.4.3.1.1. Instrument 77

2.4.3.2. FESEM analysis 77

2.4.3.2.1. Instrument 78

2.5 Thermal Analysis 79

2.5.1 Thermo gravimetric – Derivative Thermo gravimetric analysis 79

2.5.1.1. Instrument 80

2.6. Optical Characterization 81

2.6.1. Ultraviolet-Visible & Near Infrared (UV-VIS & NIR) absorption spectroscopy spectra 81

2.6.2. Photoluminescence spectra 81

2.6.3. Photoluminescence excitation spectra 83

2.6.4 Instrumentation 83

2.6.4.1. Spectrometer (iHR320) 83

2.6.4.2. Horiba Fluromax 4 84

2.7. Conclusion 84

References 86

Chapter 3: Structural, Morphological and Thermal characterization of $Pr^{3+}$-$Yb^{3+}$ ion co-doped in Titania-Silicate dense glass and thin film 88-110

3.1 Introduction 88

3.2 SYNTHESIS: $RE^{3+}$ ion co-doped $TiO_2$-$SiO_2$ binary composite 89

3.3. Structural characterization 91

3.3.1 XRD analysis 91

3.3.2. ATR-FTIR Spectra 92

3.4. Morphological Characterization 94

3.4.1. FETEM analysis 94

3.4.2. FESEM analysis 95

3.5. Thermal Characterization 97

3.6. Optical Characterization 98

3.6.1. Absorption spectra 98

3.6.2. Upconversion luminescence spectra 99

3.6.3. Downconversion luminescence spectra 100

3.6.4. Results and discussion 101

3.6.4.1. J-O parameters 101

3.6.4.2. Energy transfer upconversion 103

3.6.4.3. CIE-chromaticity diagram 104

3.6.4.4. Confocal PL microscopy 105

3.7. Conclusions 105

References 107

Chapter 4: Structural, Morphological and Thermal characterization of $Nd^{3+}$-$Yb^{3+}$ ion co-doped in Zinc-Silicate dense glass and thin film 111-134

4.1 Introduction 111

4.2. SYNTHESIS: $RE^{3+}$ ion co-doped $ZnO$-$SiO_2$ binary composite 112

4.3. Structural Characterization 113

4.3.1. XRD analysis 115

4.3.2. ATR-FTIR spectra 115

4.4. Morphological Characterization 117

4.4.1. FETEM analysis 117

4.4.2. FESEM analysis 118

4.5. Thermal characterization 120

4.6. Optical characterization 121

4.6.1. Absorption spectra 121

4.6.2. Upconversion luminescence spectra 122

4.6.3. Downconversion luminescence spectra 124

4.6.4. Results and discussion 125

4.6.4.1. J-O parameters 125

4.6.4.2. Cooperative sensitization upconversion 127

4.6.4.2. CIE-chromaticity diagram 128

4.6.4.3. Confocal PL microscopy 128

4.4 Conclusions 129

References 131

Chapter 5: $Pr^{3+}/Er^{3+}$ and $Nd^{3+}/Er^{3+}$ pair co-doped Titania-Silicate and Zinc-Silicate dense glass ceramic for IR luminescent application 135-159

5.1. Introduction 135

5.2. Synthesis: $Pr^{3+}/Er^{3+}$ ion pair in Titania-Silicate dense glass ceramic material 137

5.2.1. Structural characterization 137

5.2.1.1. XRD analysis 137

5.2.1.2. ATR-FTIR spectra 138

5.2.2. Morphological Characterization 139

5.2.2.1. FETEM analysis 139

5.2.3. Optical characterization 140

5.2.3.1. UV-Vis-NIR Absorption spectra 140

5.2.3.2. Downconversion luminescence spectra 141

5.2.3.3. Luminescence mechanism of $Pr^{3+}/Er^{3+}$ ion pair 142

5.2.3.4. CIE diagram 144

5.3. Synthesis of $Nd^{3+}/Er^{3+}$ ions pair in Zinc-Silicate dense glass ceramic material 144

5.3.1. Structural characterization 144

5.3.1.1. XRD analysis 145

5.3.1.2. ATR-FTIR spectra 146

5.3.2. Morphological Characterization 147

5.3.2.1. FETEM analysis 147

5.3.3. Optical characterization 148

5.3.3.1. UV-VIS-NIR Absorption spectra 148

5.3.3.2. Downconversion luminescence spectra 149

5.3.3.3. Luminescence mechanism of $Nd^{3+}/Er^{3+}$ ion pair 151

5.3.3.4. CIE diagram 154

| | | |
|---|---|---|
| | 5.4. Conclusion | 154 |
| | References | 156 |
| Chapter 6: | Conclusion cum summary | 155-157 |
| | Future prospects | 156 |
| | Particulars of the candidate | |
| | Bio-data | |
| | List of publications | |
| | Paper presented in conference/seminars/workshop attended | |

## List of Figures


| Sl. No. | Fig. No. | Title | Page No. |
|---|---|---|---|
| 1 | 1.1 | Schematic diagram of various probable DCL mechanisms of $RE^{3+}$ ion (i) single ion, (ii-iv) sensitizer-acceptor pair, (v) sensitizer-acceptor pair with no intermediate energy state in sensitizer as adopted by Huang et al., | 05 |
| 2 | 1.2 | Schematic diagram of upconversion luminescence mechanisms (i) ESA; (ii) ETU; (iii) CSU (iv) PA. The full arrows, dashed/dotted, dotted arrows represent emission, photon excitation, and energy transfer process correspondingly. | 07 |
| 3 | 1.3 | Schematic diagram of $4f^N$ energy level splitting of $RE^{3+}$ due to various perturbations as Zhou et al., envision | 10 |
| 4 | 2.1 | Schematic sol-gel process | 65 |
| 5 | 2.2 | Experimental arrangement for refractive index estimation | 69 |
| 6 | 2.3 | (a) Schematic diagrams and (b) Image of FTIR spectrophotometer | 72 |
| 7 | 2.4 | (a) Schematic incident and diffracted radiation from crystal planes (b) Image of X-Ray diffractometer | 74 |
| 8 | 2.5 | (a) Schematic diagram and (b) Image of FETEM (IITG) | 77 |
| 9 | 2.6 | (a) Schematic diagram and (b) Image of FESEM (IITG) | 79 |
| 10 | 2.7 | (a) Schematic diagram of TG/DTA thermal analyzer (b) Image of TGA-4000 from PerkinElmer (IITG) | 80 |
| 11 | 2.8 | Schematic diagram of the recording (a) Absorption and (b) Photoluminescence spectra. (c) Image of iHR320 imaging spectrometer (MZU). | 84 |

| | | | |
|---|---|---|---|
| 12 | 3.1 | Schematic diagram of (a) ex-situ sol-gel preparation (b) image of the STPYX-DGC materials | 90 |
| 13 | 3.2 | XRD spectra of the STPY07-DGC samples at different annealing temperature. | 91 |
| 14 | 3.3 | XRD spectra of the STPY07-TF thin film at different annealing temperature | 92 |
| 15 | 3.4 | ATR-FTIR spectra of the STPY07-DGC sample at different annealing temperature. | 93 |
| 16 | 3.5 | FETEM image at magnification bar at (a) 20 nm (b) 200 nm, (c) SAED pattern, (d) EDS spectra of the annealed STPY07-DGC material. | 95 |
| 17 | 3.6 | FESEM image of the STPY07- thin film annealed at 900 °C | 96 |
| 18 | 3.7 | FESEM-EDS image of the STPY07-TF annealed at 900 °C | 96 |
| 19 | 3.8 | (a)TG-DTA and (b) TG-DSC curve of the STPY07-xerogel | 97 |
| 20 | 3.9 | Absorption spectra of the STPY07-DGC material | 98 |
| 21 | 3.10 | Upconversion luminescence spectra of STPYX-DGC samples under 980nm excitation | 99 |
| 22 | 3.11 | DCL spectra of the STPYX-DGC materials for 450nm excitation | 100 |
| 23 | 3.12 | Schematic energy transfer upconversion mechanisms of $Pr^{3+}$- $Yb^{3+}$ ion pair | 100 |
| 24 | 3.13 | CIE chromaticity diagram | 103 |
| 25 | 3.14 | PL confocal mapping of the STPY15-DGC material | 104 |
| 26 | 4.1 | Schematic diagram of preparation of the SZNYX binary host | 105 |
| 27 | 4.2 | XRD pattern of the SZNY07-DGC sample annealed at different temperature | 113 |
| 28 | 4.3 | XRD pattern of the SZNY07-TF samples annealed at (a) | 114 |

| | | | |
|---|---|---|---|
| | | 235 $^{o}$C (b) 700 & 900$^{o}$C | |
| 29 | 4.4 | ATR-FTIR spectra of the SZNY07-DGC sample annealed at different temperatures | 115 |
| 30 | 4.5 | TEM image of the SZNY07-DGC sample annealed at 900 °C | 116 |
| 31 | 4.6 | SEM image of SZNY07-TF annealed at 900 °C | 118 |
| 32 | 4.7 | SEM-EDS image of SZNY07-TF annealed at 900 °C | 119 |
| 33 | 4.8 | TG –DSC curve of the SZNY07 xerogel. Inset TG-DTA curve | 121 |
| 34 | 4.9 | Absorption spectra of the SZNY07-DGC materials | 122 |
| 35 | 4.10 | UCL spectra of the SZNYX-DGC materials under 980nm excitation | 123 |
| 36 | 4.11 | DCL spectra of the SZNYX-DGC sample under 450nm excitation | 124 |
| 37 | 4.12 | Schematic diagram of the CSU mechanism in $Yb^{3+}$-$Nd^{3+}$ ion pair | 127 |
| 38 | 4.13 | CIE 1931 chromaticity diagram of the SZNYX-DGC sample | 128 |
| 39 | 4.14 | PL confocal mapping of the SZNY15-DGC sample | 129 |
| 40 | 5.1 | XRD spectra of the $Er^{3+}/Pr^{3+}$:$TiO_2$-$SiO_2$ dense glass material annealing at 900 ºC. | 138 |
| 41 | 5.2 | ATR-FTIR spectra of the $Er^{3+}/Pr^{3+}$:$TiO_2$-$SiO_2$ dense glass material at different annealing temperature. | 139 |
| 42 | 5.3 | FETEM image with magnification bar at 200 nm (b) SAED pattern of the annealed $Er^{3+}/Pr^{3+}$:$TiO_2$-$SiO_2$ dense glass ceramic material annealed at 900 ºC. | 140 |
| 43 | 5.4 | Absorption spectra of the $Er^{3+}/Pr^{3+}$:$TiO_2$-$SiO_2$ dense glass material | 141 |
| 44 | 5.5 | DCL spectra of the $Er^{3+}/Pr^{3+}$:$TiO_2$-$SiO_2$ dense glass material under 450 nm excitation | 142 |
| 45 | 5.6 | Schematic absorption and DCL mechanisms of the | 141 |

| | | | |
|---|---|---|---|
| | | $Er^{3+}/Pr^{3+}$:$TiO_2$-$SiO_2$ dense glass material | |
| 46 | 5.7 | CIE 1931 chromaticity diagram of DCL emission of the $Er^{3+}/Pr^{3+}$:$TiO_2$-$SiO_2$ dense glass material | 144 |
| 47 | 5.8 | XRD pattern of the $Er^{3+}/Nd^{3+}$:ZnO-$SiO_2$ dense glass material annealed at 900 ºC | 145 |
| 48 | 5.9 | ATR-FTIR spectra of the $Er^{3+}/Nd^{3+}$:ZnO-$SiO_2$ dense glass material annealed at 900 ºC. | 146 |
| 49 | 5.10 | (a) FETEM image (b) HRTEM image of the $Er^{3+}/Nd^{3+}$:ZnO-$SiO_2$ dense glass material annealed at 900 °C | 147 |
| 50 | 5.11 | SAED pattern of the $Er^{3+}/Nd^{3+}$:ZnO-$SiO_2$ dense glass material annealed at 900 °C | 148 |
| 51 | 5.12 | Absorption spectra of the $Er^{3+}/Nd^{3+}$:ZnO-$SiO_2$ dense glass material | 149 |
| 52 | 5.13 | DCL spectra of the $Er^{3+}/Nd^{3+}$:ZnO-$SiO_2$ dense glass material under 450 nm excitation | 150 |
| 53 | 5.14 | DCL spectra of the $Er^{3+}/Nd^{3+}$:ZnO-$SiO_2$ dense glass material under 808 nm excitation | 151 |
| 54 | 5.15 | Schematic diagram of the absorption and DCL mechanism in the $Er^{3+}/Nd^{3+}$:ZnO-$SiO_2$ dense glass material | 152 |
| 55 | 5.16 | CIE 1931 chromaticity diagram of the $Er^{3+}/Nd^{3+}$:ZnO-$SiO_2$ dense glass material | 153 |

## List of Tables


| Sl. No. | Table No. | Title | Page No. |
|---|---|---|---|
| 1 | 1.1 | Comparison between QD, OD, and UCNPs material based on bio-applications | 02 |
| 2 | 1.2 | Electronic structure of Rare-Earth ions | 04 |
| 3 | 1.3 | Different hosts for the $Pr^{3+}$-$Yb^{3+}$ / $Nd^{3+}$-$Yb^{3+}$ ion pair co-doping with phonon energy | 21 |
| 4 | 1.4 | List of literature available in $Pr^{3+}$-$Yb^{3+}$ ion co-doped in different host | 30 |
| 5 | 1.5 | List of literature available in $Nd^{3+}$-$Yb^{3+}$ ion co-doped in different host | 33 |
| 6 | 1.6 | List of literature available in $Er^{3+}$-$Yb^{3+}$ ion co-doped in different host | 35 |
| 7 | 1.7 | Progress in $RE^{3+}$ ion doping in ZnO-$SiO_2$ host through different sol-gel synthesis route | 36 |
| 8 | 1.8 | Progress in $RE^{3+}$ ion doping in$TiO_2$-$SiO_2$ host through sol-gel route | 39 |
| 9 | 2.1 | List of physical and chemical synthesis process | 60 |
| 10 | 3.1 | FTIR peak positions and its different assignments for STPY07-DGC samples | 94 |
| 11 | 3.2 | Judd-Ofelt intensity parameters and oscillator strengths of $Pr^{3+}$ ion | 101 |
| 12 | 3.3 | Comparison of calculated Judd-Ofelt intensity parameters | 102 |
| 13 | 3.4 | Radiative parameters of the STPY07-DGC sample | 102 |
| 14 | 4.1 | FTIR peak positions and its different assignments for SZNY07-DGC samples | 117 |
| 15 | 4.2 | Judd-Ofelt intensity parameters and oscillator strengths of $Nd^{3+}$ ion | 125 |
| 16 | 4.3 | Comparison of calculated Judd-Ofelt intensity parameters | 126 |
| 17 | 4.4 | Radiative parameters of the SZNY07-DGC sample | 126 |

| | | | |
|---|---|---|---|
| 18 | 5.1 | Selective transition in DCL spectra of the $Er^{3+}/Pr^{3+}$:$TiO_2$-$SiO_2$ dense glass material for excitation wavelength 450 nm | 143 |
| 19 | 5.2 | Selective transitions of UCL spectra of the $Er^{3+}/Nd^{3+}$:ZnO-$SiO_2$ dense glass material | 153 |

## List of Abbreviations

| | | |
|---|---|---|
| A | = | Acceptor |
| Al | = | Aluminium |
| ATR | = | Attenuated Total Reflection |
| BBE | = | band to band emission |
| CCD | = | Charge- Coupled Device |
| CdSe | = | Cadmium Selenide |
| Ce = | = | Cerium |
| Conc.$HNO_3$ | = | Concentrated nitric acid |
| CR | = | Cross-relaxation |
| CSU | = | Cooperative sensitization upconversion |
| D | = | Donor |
| DC | = | Downconversion |
| DCL | = | Downconversion luminescence |
| DCNPs | = | Downconversion nanoparticles |
| DLE | = | deep-level emission |
| DS | = | Downshifting |
| DTA | = | Derivative thermo-gravimetry analysis |
| Dy | = | Dysprosium |
| E | = | Energy |
| ED | = | Electric Dipole |
| EDS | = | Energy dispersive X-ray spectrometer |
| EM | = | Electromagnetic |
| EMA | = | Effective mass approximation |
| EQ | = | Electric Quadrupole |
| Er | = | Erbium |
| ES | = | Excited State |
| ESA | = | Excited state absorption |
| ET | = | Energy Transfer |
| ETU | = | Energy transfer upconversion |

| | | |
|---|---|---|
| EtOH | = | Ethanol |
| Eu | = | Europium |
| FTIR | = | Fourier transform infrared spectroscopy |
| FWHM | = | Full-Width Half-Maximum |
| GS | = | Ground State |
| $H_2O$ | = | Water |
| HNO3 | = | Nitric Acid |
| Ho | = | Holmium |
| HRTEM | = | High-Resolution Transmission Electron Microscopy |
| IR | = | Infra-red |
| J-O | = | Judd-Ofelt |
| La | = | Lanthanum |
| LED | = | Light –emitting diode |
| LEDs | = | Light –emitting diodes |
| Lu | = | Lutetium |
| MD | = | Magnetic Dipole |
| MZU | = | Mizoram University |
| NBO | = | Non-Bridging Oxygen |
| NCs | = | Nanocrystals |
| Nd | = | Neodymium |
| NIR | = | Near-infrared |
| NPs | = | Nanoparticles |
| NR | = | Non radiative |
| O | = | Oxygen |
| OH | = | Hydroxyl group |
| OR | = | Alkoxide group |
| OD | = | Organic dyes |
| PAU | = | Photon Avalanche Upconversion |
| PL | = | Photoluminescence |
| Pm | = | Promethium |

| | | |
|---|---|---|
| Pr | = | Praseodymium |
| QC | = | Quantum cutting |
| QDs | = | Quantum Dots |
| QE | = | Quantum Efficiency |
| QY | = | Quantum yields |
| RE | = | Rare-Earth |
| REEs | = | Rare-Earth elements |
| REM | = | Reduced Matrix Elements |
| REO | = | Rare-Earth Oxide |
| RMS | = | Root Mean Square |
| S | = | Singlet |
| Sc | = | Scandium |
| SEM | = | Scanning Electron Microscopy |
| Si | = | Silicon |
| SiO2 | = | Silicon Dioxide |
| Sm | = | Samarium |
| $Sm(NO_3)_3.6H_2O$ | = | Samarium Nitrate Hexahydrate |
| SPR | = | Surface plasmon resonance |
| SO | = | Spin Orbit |
| SQF | = | Spectroscopic Quality Factor |
| T | = | Triplet |
| Tb | = | Terbium |
| $Tb(NO_3)_3.5H_2O$ | = | Terbium Nitrate Pentahydrate |
| TEM | = | Transmission Electron Microscopy |
| TEOS | = | Tetraethylorthosilicate |
| TG | = | Thermo-gravimetry |
| $TiO_2$ | = | Titanium Oxide |
| Tm | = | Thulium |
| UC | = | Upconversion |
| UCL | = | Upconversion luminescence |
| UCNPs | = | Upconversion nanoparticles |

| | | |
|---|---|---|
| UV | = | Ultraviolet |
| UV-VIS | = | Ultraviolet-Visible |
| XRD | = | X-Ray Diffraction |
| Y | = | Yttrium |
| $Y_2O_3$ | = | Yttrium Oxide |
| Yb | = | Ytterbium |
| ZnO | = | Zinc-Oxide |
| ZnS | = | Zinc Sulfide |

# *CHAPTER- 1*

## *INTRODUCTION AND REVIEW OF LITERATURE*

***This chapter represents the Introduction and Literature Review of the Present Thesis Work done.***

*Chapter - 1*

---

# *INTRODUCTION AND REVIEW OF LITERATURE*

---

## 1.1. INTRODUCTION

Luminescent materials, including glass, thin-film, fiber, nano- or micro-composite, are highly interesting due to their absorption and emission of light in the ultraviolet–visible and infrared regions. These materials find lucrative applications in various fields, such as anti-reflection coatings and spectral converters in photovoltaic solar cells (Richards 2006), bio-sensing (Wen et al. 2018), bio-imaging (Escudero et al. 2017), thermometry and nano-heater (Anna M. Kaczmarek, Kaczmarek, and Deuna 2018), luminescent Ink (Loo et al. 2019), confocal microscopy (Liang et al. 2019), optical memory (Kunkel and Goldner 2018), and more. In recent decade, Quantum dots (QD), Organic dyes (OD), and Upconversion nanoparticles (UCNPs) have emerged as three important luminescent materials adhering to Strokes' Law. UCNPs, on the other hand, conform to both Stokes' and anti-Stokes' Laws. These materials exibit various merits and demerits, particularly concerning their bio-applications as presented in Table 1. Quantum dots offer advantages such as broadband excitation multiplexing, size-tunable luminescence, and a high photo-blenching threshold. However, their notable disadvantage includes toxicity and blinking effect. Organic dye molecules feature narrow absorption spectra and wide asymmetric emission spectra with high quantum yield. The major advantage of UCNPs lies in their variable absorption and emission centers with narrow emission lines, setting them aside from quantum dots and organic dye (Wen et al. 2018). Upconversion luminescent (UCL) materials have been synthesized by doping $RE^{3+}$ ions (e.g., $Pr^{3+}$, $Nd^{3+}$, $Er^{3+}$, $Yb^{3+}$, etc. ) into various solid hosts (Reisfeld and Kalisky 1981), (Liégard et al. 2005), (Dihingia and Rai 2012), (Battisha 2007), (Meijer et al. 2010), (Pudovkin, Ginkel, and Lukinova 2021), (Sun et al. 2013), (Faria,

Gonçalves, and Camargo 2021). They exhibit privileged anti-Stoke luminescence, multiplexing, and dopant tunable luminescence (Escudero et al. 2017). One of the major drawbacks of the UCL materials is their low quantum yields (QY), which have been a primary focus to develop brighter luminescent materials. The luminescence of $RE^{3+}$ ions in solid host materials can be categorized into three main types: (a) quantum cutting (QC) by downconversion (DC), (b) upconversion (UC), and (c) downshifting (DS) luminescence which will be discussed in detail in section 1.3.

Table 1.1: Comparison between QD, OD, and UCNPs material based on bio-applications

| Properties | QD | OD | UCNP |
|---|---|---|---|
| **Penetration depth** | ○ | ○ | ■ |
| **No auto-fluorescence** | ○ | ○ | ■ |
| **Photo-stability** | ■ | ○ | ■ |
| **Non-toxic** | ○ | ■ | ■ |
| **Chemical stability** | ■ | ■ | ■ |
| **Narrow emission line** | ○ | ○ | ■ |
| **Functionalization** | ○ | ■ | ■ |
| **Quantum Yield** | ■ | ■ | ○ |
| | | | |
| | ○(No) | ■ (Yes) | |

In the past decade, UCL and DCL materials have been prepared in various shape and size, made possible by the availability of various physical and chemical synthesis routes such as sol-gel, hydrothermal, vapor deposition etc. The sol-gel and hydrothermal route are particularly intriguing, as they can be utilized to obtain the final product with desired shapes and sizes in nano- and micro-range, in spherical and cylindrical form. Consequently, UCNPs and DCNPs emerge as highly attractive luminescent materials, thanks to properties like volume-to-surface aspect ratio, among others. These materials have garnered considerable recognition in both the photovoltaic and bio-photonics applications.

In photovoltaic applications, the UCNPs and DCNPs layer have been employed as spectral converters to address the spectral mismatch of the AM1.5G solar spectrum in solar cell, a significant ongoing research interest. Solar photons incident upon the solar cell are not

absorbed by the bandgap if their energy falls below or exceeds the bandgap (Van Der Ende, Aarts, and Meijerink 2009), (Kumar et al. 2018). This limitation is mitigated by adjusting the solar spectrum using either UCNPs (Fischer et al. 2010) or DCNPs layer (Huang et al. 2013), enhancing photon absorption within the energy gap of the solar cell (Wen and Tanner 2011). UCL proves especially advantageous for solar cell with a large bandgap, where "transmission losses" dominate. The QC by DC mechanism is favorable for solar cells with a smaller bandgap, where "thermalization losses" are the primary factor in losses (Wen and Tanner 2011). The bio-application of the $RE^{3+}$ ion pair significantly reduces overheating effects and enhances the penetration depth of the laser within tissues in the second biological window (Liang et al. 2021), (Dibaba et al. 2019).

Here, we specifically discuss UCL and DCL of three particular $RE^{3+}$ ion pairs ($Pr^{3+}$-$Yb^{3+}$ / $Er^{3+}$ -$Yb^{3+}$/ $Nd^{3+}$ -$Yb^{3+}$) from the perspective of important photonic applications. The discussion includes crucial parameters of the UCL mechanism to optimize UCL materials. Additionally, this introduction highlights some of the essential applications of luminescent materials. Finally, we conclude by presenting the scope of the study, including the chapterization of the research work.

## 1.2. RARE EARTH ELEMENT

Rare-Earth elements encompass lanthanum (Z=57) through lutetium (Z=71), as well as Scandium and Yttrium. A distinct fluorescence transition in the Ultra-violet (UV)-visible (VIS) and near-infrared (NIR) regions of the electromagnetic (EM) spectrum is observed in paramagnetic $RE^{3+}$ ions with an electronic configuration of [Xe] $4f^N\ 6s^2$. In this configuration, the $4f^N$ electrons are partially shielded by the outer electron in the $5s^2$, $5p^6$, and $6s^2$ shells, while the ligands in the first and second coordination sphere exert diminishing perturbations on the electronic configurations of the $RE^{3+}$ ions, This shielding imparts a unique spectroscopic property of $RE^{3+}$ ions, rendering them relatively independent of their environment and distinguishing them from transition metals. The *4f-4f* transitions within $RE^{3+}$ ions are initiated within this shielding, resulting in extended lifetimes (metastable state) of the excited states and narrow-band emissions (Binnemans 2009). The gradual reduction in the ionic radius of $RE^{3+}$ ions from Lanthanum to Lutetium is known as the "lanthanide contraction". The Dieke diagram (Carnall et al. 1989) displays numerous energy levels of various $RE^{3+}$ ions, which have been

extensively utilized in identifying the electronic states. W.T. Carnall, H. Crosswhite, and H.M. Crosswhite conducted a substantial amount of calculations, assuming the environment independence of $RE^{3+}$ ions, to determine Reduced Matrix Elements (RME) of the tensor operator $[U^{(k)}]$ for Electric-Dipole interaction (Hehlen, Brik, and Kramer 2013). The Judd-Ofelt (J-O) theory is a powerful mathematical tool with three parameters derived from various approximation-based solutions of the time-independent Schrödinger equation. It enables to estimate various radiative properties of $RE^{3+}$ ions in various host materials.

Table 1.2: Electronic structure of $RE^{3+}$ ions (Carnall, W. T.; Crosswhite, H.; Crosswhite 1977)

| Element (Symbol) | Atomic Number | Electronic configuration | Color of oxides | Ground State (GS) | Selective Excited State (ES) |
|---|---|---|---|---|---|
| **Cerium (Ce)** | 58 | $[Xe]4f^{1}5d^{1}6s^{2}$ | Pale yellow | $^{2}F_{5/2}$ | $^{2}F_{7/2}$ |
| **Praseodymium (Pr)** | 59 | $[Xe]4f^{3}6s^{2}$ | Black | $^{3}H_{4}$ | $^{3}H_{5,6}$; $^{3}F_{2,3,4}$; $^{1}G_{4}$; $^{1}D_{2}$; $^{3}P_{0,1,2}$ |
| **Neodymium (Nd)** | 60 | $[Xe]4f^{4}6s^{2}$ | Grayish blue | $^{4}I_{9/2}$ | $^{4}I_{11/2,13/2}$; $^{4}F_{3/2,7/2,9/2}$; $^{4}H_{11/2}$; $^{4}G_{7/2}$ |
| **Promethium (Pm)** | 61 | $[Xe]4f^{5}6s^{2}$ | n.a | $^{5}I_{4}$ | $^{5}I_{5,6,7,8}$ ; $^{5}F_{1,2,3}$ |
| **Samarium (Sm)** | 62 | $[Xe]4f^{6}6s^{2}$ | Cream | $^{6}H_{5/2}$ | $^{6}H_{7/2,9/2,11/2,13/2}$; $^{6}F_{1/2,3/2,5/2,7/2,9/2,11/2}$ |
| **Europium (Eu)** | 63 | $[Xe]4f^{7}6s^{2}$ | White | $^{7}F_{0}$ | $^{7}F_{2,4,6}$; $^{5}D_{0,1,2}$ |
| **Gadolinium (Gd)** | 64 | $[Xe]4f^{7}5d^{1}6s^{2}$ | White | $^{8}S_{7/2}$ | $^{6}P_{7/2}$ |
| **Terbium (Tb)** | 65 | $[Xe]4f^{9}6s^{2}$ | Brown | $^{7}F_{6}$ | $^{7}F_{4,2}$, $^{5}D_{4}$ |
| **Dysprosium (Dy)** | 66 | $[Xe]4f^{10}6s^{2}$ | Yellowish | $^{6}H_{15/2}$ | $^{6}H_{13/2,\ 11/2,9/2,7/2,5/2}$; $^{6}F_{11/2,9/2,7/2,5/2,3/2,1/2}$ |
| **Holmium (Ho)** | 67 | $[Xe]4f^{11}6s^{2}$ | Yellowish | $^{5}I_{8}$ | $^{5}I_{7,6,5,4}$; $^{5}F_{5}$ |
| **Erbium (Er)** | 68 | $[Xe]4f^{12}6s^{2}$ | Pink | $^{4}I_{15/2}$ | $^{4}I_{13/2,11/2,9/2}$; $^{4}F_{9/2}$ |
| **Thulium (Tm)** | 69 | $[Xe]4f^{13}6s^{2}$ | Greenish | $^{3}H_{6}$ | $^{3}F_{4,3}$; $^{3}H_{5,4}$ |
| **Ytterbium (Yb)** | 70 | $[Xe]4f^{14}6s^{2}$ | Greenish | $^{2}F_{7/2}$ | $^{2}F_{5/2}$ |

## 1.3. PHOTOLUMINESCENCE SPECTRA

Photoluminescence (PL) spectra of $RE^{3+}$ ions collectively represent the emission of a photon , rather than “fluorescence” or “phosphorescence”. These terms are used to distinguish between a spin-allowed transition (singlet → singlet emission) and a spin-forbidden transition (triplet → singlet emission), respectively. The PL spectra from $RE^{3+}$ ions are classified into upconversion and downconversion luminescence depending upon Stokes’ and anti-Stokes’ Law.

### 1.3.1. Downconversion luminescence (DCL):

DCL is a linear process where the wavelength of the emitted photon is always longer than that of the incident photon, as shown in Figure 2(i-v). It follows Strokes' law as high energy incident photons are converted into one or more low-energy photons. If two or more photons of lower energy are emitted, it is termed downconversion by quantum cutting (QC) and if only one low energy photon emerge, it is called downshifting (DS). DCL exhibits high conversion efficiencies (approximately 100%) where the energy of one high-energy photon splits into multiple photons of lower-energy (Meijer et al. 2010). DS is a subcategory of the DCL process with subunity quantum efficiencies and is involved in transforming high-energy photon into a lower-energy photon (Kumar et al. 2020).UCL is a non-linear process that arises in $RE^{3+}$ ions whenever the absorption of two or more lower energy photons get converted into single photon of higher energy.

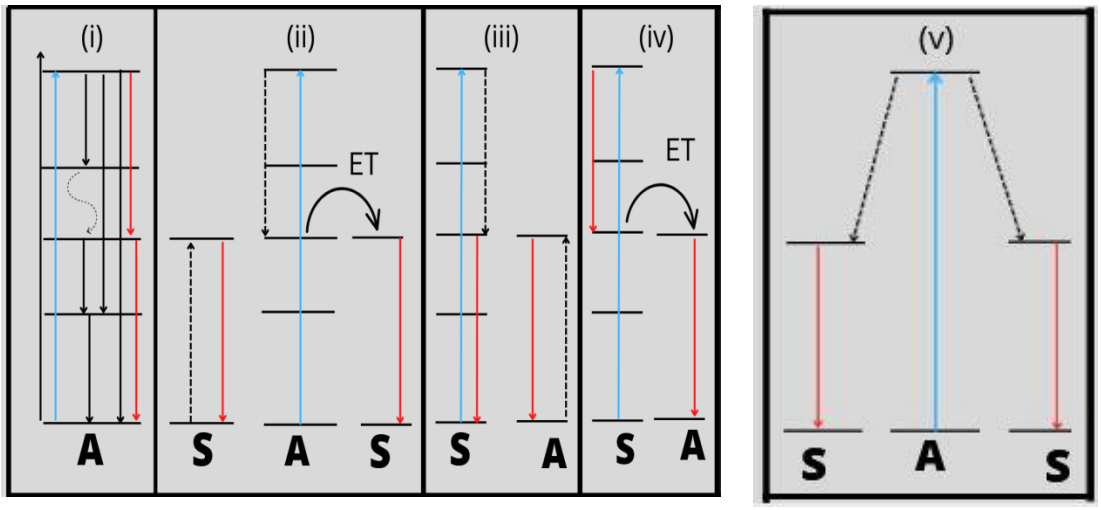


Figure 1.1: Schematic diagram of various probable DCL mechanisms of $RE^{3+}$ ion (i) single ion, (ii-iv) sensitizer-acceptor pair, (v) sensitizer-acceptor pair with no intermediate energy

state in sensitizer as adopted by Huang et al., (Huang et al. 2013).

### 1.3.2. **Upconversion luminescence (UCL):**

UCL is an anti-stroke process where successive absorption of NIR excitation promotes nonlinear emission in the UV- VIS region (Wang and Liu 2009). It was first envisioned as a theoretical possibility by Nicolaas Bloembergen in 1959, and Francois Auzel was the first to report it a decade later (Auzel 1990). UCL of $RE^{3+}$ ions is classified into four distinct types (Zhou et al. 2015): (a) excited-state absorption; (b) energy transfer upconversion; (c) cooperative sensitization upconversion (d) photon avalanche .

**Excited-state absorption (ESA)** occurs via multi-phonon relaxation among the energy levels of a single $RE^{3+}$ ion through transfer of energy (ET) to the electrons and host crystal before relaxing to the ground state with the help of a long-lived metastable state, as in Figure 1.2(i). The maximum efficiency (η) reported for $RE^{3+}$ ion-doped $NaYF_4$ host to date is around $10^{-5}$ $cm^2$ $W^{-1}$ (Zhou et al. 2015).

**Energy Transfer Upconversion (ETU)** requires an activator-acceptor pair, where both the $RE^{3+}$ ions in the excited state (ES) cooperatively exchange energy from the donor (activator) ion to the nearby acceptor (sensitizer) ion. This absorption of energy promotes the sensitizer ion to a higher ES (ESA), and relaxation from this excited state initiates the emission of a photon with higher energy than the excited photon, as in Figure 1.2 (ii) (Zhou et al. 2015). This process depends on factors such as the absorption capacity of the acceptor; the presence of donor-acceptor pair in close vicinity; energy transfer efficiency among the sensitizer-activator pair; and various other luminescence quenching effects etc. $RE^{3+}$ ions co-doped $NaYF_4$ host was reported with maximum efficiency around $\eta = 10^{-3}$ $cm^2$ $W^{-1}$ (Zhou et al. 2015).

**Cooperative Sensitization Upconversion (CSU)** is similar to the ESU process, but the acceptor (e.g, $Tb^{3+}$) with physically non-existent intermediate states, as shown in Figure 1.2 (iii). The maximum efficiency reported for $RE^{3+}$ ions co-doped $NaYF_4$ host is around $10^{-6}$ $cm^2$ $W^{-1}$ was reported (Zhou et al. 2015).

**Photon Avalanche Upconversion (PAU)**occurs in bulk materials with two different ions in GS and ES, analogous to quenching, where both the ions populate an intermediate energy level, as in Fig. 1.2 (iv) (Zhou et al. 2015). PA is rarely observed in UCNPs due to the challenging conditions for establishing avalanches.

**Bandgap tuning** is also a luminescence process in which two low-energy photons emerge from the host after absorbing a high-energy photon, without the involvement of two different $RE^{3+}$ ions (Mir et al. 2020).

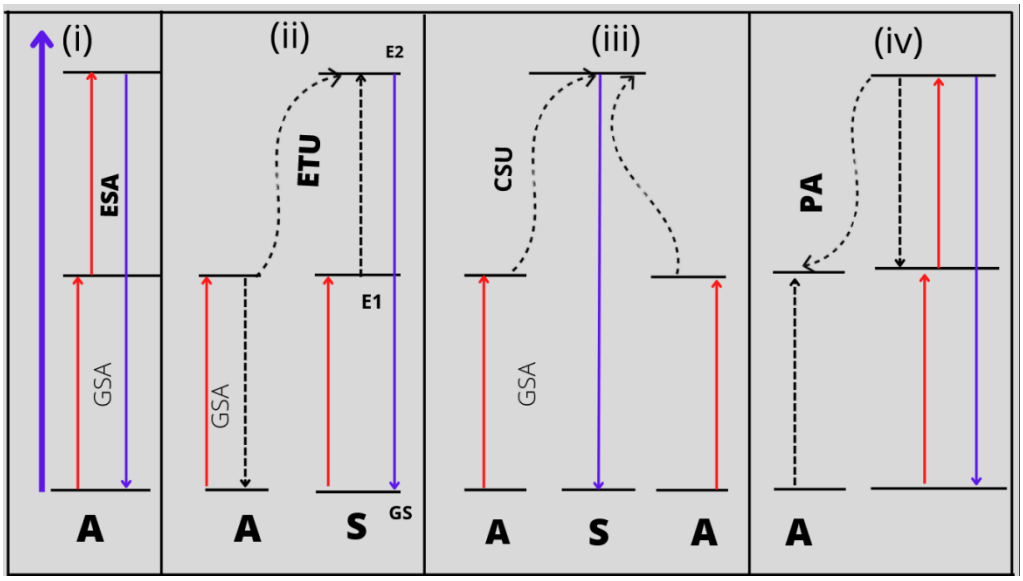


Figure 1.2: Schematic diagram of upconversion luminescence mechanisms (i) ESA; (ii) ETU; (iii) CSU (iv) PA. The full arrows, dashed/dotted, dotted arrows represent emission, photon excitation, and energy transfer process correspondingly (Wang and Liu 2009)

### 1.3.3. Quantum Efficiency (QE)

The QE of UCNPs is expressed as the ratio between the total lifetimes of an excited state and the radiative lifetime of the same state. Consider the population density (N) of donor electrons in the excited state that may decay through radiative ($k_r$) or nonradiative ($k_{nr}$) pathways from the excited state (ES). The evolution of the ES with respect to time can be described by:

$$\frac{dN}{dt} = -(k_r + k_{nr})N \qquad (1.\ \mathbf{1})$$

The exponential decay of luminescence with a time constant τ is

$$\boldsymbol{\tau = \frac{1}{k_r + k_{nr}}} \qquad (1.\ \mathbf{2})$$

Thus, the quantum efficiency can be calculated using the following formula (Vasconcelos and Pinto 2017):

$$\boldsymbol{\eta_{PL} = \frac{k_r}{k_r + k_{nr}} = \frac{\tau}{\tau_R}} \qquad (1.\ \mathbf{3})$$

The lifetime of the ES in the absence of nonradiative decay processes is termed a radiative lifetime ($\tau_R = 1/k_r$), which is typically estimated using J–O theory. The lifetime ($\tau$) can be computed from intensity decay curves (Huang et al. 2013).

## 1.4. THEORETICAL BACKGROUND

Professor Brian G. Wybourne once suggested that the discovery of J-O was an indication of the right time for solving the $RE^{3+}$ ion through understanding the fascinating luminescence of $RE^{3+}$ ion. This can be considered as the initial step in the journey to comprehend $RE^{3+}$ ions and the actinides, with no foreseeable end in close vicinity (Walsh 2006). The Hamiltonian of $RE^{3+}$ ion-doped solids have a major contribution (80–90%) from the combined magnitude of the electrostatic and spin-orbital parts as shown in Fig 1.3. The remaining part is a contribution of crystal field and higher-order atomic interactions (Hehlen et al. 2013). The total Hamiltonian of the $RE^{3+}$ ion in a host is represented as,

$$\boldsymbol{H = H_o + H_e + H_{SO} + \quad + \quad + \cdots + H_{CF}} \qquad \mathbf{(1.\ 4)}$$

The free-ion Hamiltonian can be expressed as (Carnall et al. 1989),

$$\boldsymbol{H = H_o + \sum_{k=0,2,4,6} F^k(nf,nf) f_k + \zeta_f A_{so} + \alpha L(L+1) + \beta G(G_2) + \gamma G(R_7)} \qquad \mathbf{(1.\ 5)}$$
$$\boldsymbol{+ \sum_{i=2,3,4,6,7,8} t_i T^i + \sum_{h=0,2,4} m_h M^h}$$
$$\boldsymbol{+ \sum_{f=2,4,6} p_f P^f \ldots\ldots\ldots \sum_{k,q,i} B_q^{(k)} C_q^{(k)}(i)}$$

The spherically symmetric one-electron Hamiltonian (*Ho*) symbolizes the kinetic energy of an electron and its interaction with the nucleus. It includes the electrostatic (Columbic repulsive interaction between pairs of *4f* electrons; $F_k$) and spin-orbital integrals (the coupling of spin and orbital angular momenta; $\zeta_f$) with respective angular components of the electrostatic interaction ($f_k$ ) and spin-orbit interactions ($f_k$ and $A_{so}$) (Binnemans 2015). These parameters associated with the two body correction terms are denoted as α, β, and γ with G ($G_2$) and G($R_7$) representing Casimir's operators for the groups $G_2$ and $R_7$. Here, *L* stands for orbital angular momentum (Binnemans 2015). Judd's three-particle configuration interaction terms, $t_iT^i$ (*i*=2, 3, 4, 6, 7, 8), arise from the effect of perturbation offered by specific configurations that differ from the $4f^N$ configuration in the quantum numbers of a single electron. At this point, $t_i$ and $T^i$ represent three particle operators and parameters, correspondingly. Magnetic interrelated corrections ($m_h$ and $p_f$) also contribute. The spin-to-spin and spin-to-other-orbit relativistic corrections are symbolized with the Marvin integral $M_h$ (h = 0, 2, 4) (Binnemans 2015). The electrostatically co-related spin-orbit perturbation $P^f$ (f = 2, 4, 6) is participated in the excitation of a 4*f* electron into a higher-lying 4 *f* shell (Binnemans 2015).

### 1.4.1. Crystal Field Interaction

The crystal field interaction of the Hamiltonian with a single-particle crystal field parameter for different site symmetries is represented as (Binnemans 2015),

$$\boldsymbol{H_{CF} = \sum_{k,q,i} B_q^{(k)} C_q^{(k)}\,(i)} \qquad \textbf{(1. 6)}$$

Here, the spherical tensor [$C_q^{(k)}(i)$] of rank *k* relies on the coordinates of the $i^{th}$ electron, and this summation, encompassing *i*, run over all 4*f* electrons of the ion of importance. The values of *k* and *q* determine the non-zero value of the $B_q(k)$ parameter, depending on the site symmetry (Carnall et al. 1989). The crystal-field perturbation transforms the spherical symmetry of the Hamiltonian of $RE^{3+}$ ion, splitting $^{2S+1}L_J$ term into the number of crystal field (Stark level) level (Binnemans 2015).

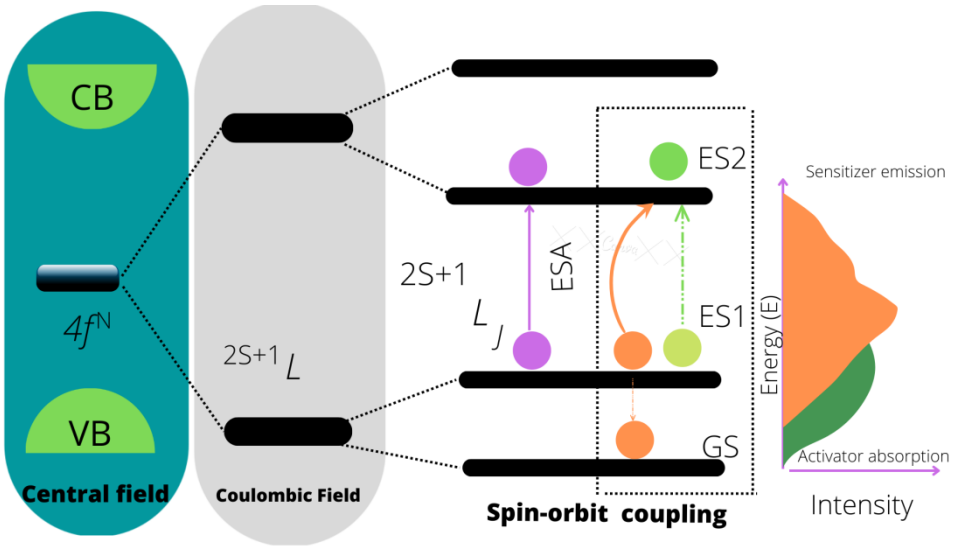


**Figure 1.3:** Schematic diagram of $4f^N$ energy level splitting of $RE^{3+}$ due to various perturbations as Zhou et al., envision (Zhou et al. 2015)

1.4.1.1. **The Relativistic Approach:**

The Dirac equation is employed in the *j-j* ($J=\sum j_i$ with $j_i=s_i + l_i$) basis. It explicitly depends on the radial integral components arising from the solutions of the Dirac equation, as well as the total angular momentum quantum number (*j*) along with a one-electron orbital quantum number (*l*) (Smentek and Wybourne 2000).

Two distinct problems emerge from the above assessment, as reported elsewhere (Smentek 1988):

i) Determining the form of the relativistic effective operators that can be expressed in an appropriate perturbative structure as relativistic radial integrals with tensor operators.

ii) Quantitatively evaluating system-specific matrix elements for the radial integrals and tensor operator (Smentek and Wybourne 2000).

This work is still in progress and falls outside of the scope of this specific review

**1.4.1.2. Non-Relativistic Approach:**

In the time-independent Schrodinger equation, the Hamiltonian operator of the $RE^{3+}$ ion operates on the wavefunction of $^{2S+1}L_J$ multiplets of the $RE^{3+}$ ion to estimate different energies, where

various radial integrals are invariant to the total angular momentum quantum number *j* of an electron. Unfortunately, there is no exact solution available for this multi-electron Schrödinger equation.

#### 1.4.1.3. Intermediate coupling approximation

Under the intermediate coupling approximation, three assumptions are made to solve the time-independent Schrödinger equation (Hehlen et al. 2013),

(a) The repulsive electrostatic ($H_e$) and spin-orbit coupling ($H_{so}$) account for the energy-level structure of the $4f^N$ state in the $RE^{3+}$ ion.

(b) Spin-Orbit coupling ($H_{so}$) is comparable to the electrostatic interaction ($H_e$) among the *4f* electrons for the $RE^{3+}$ ion, and the magnitude of $H_{so}$ increases with the fourth power of nuclear charge (*Z*).

(c) The $H_{so}$ coupling perturbs the $^{2S+1}L$ terms of a $[Xe]4f^N$ configuration of the $RE^{3+}$ ion, causing it to split into several $^{2S+1}L_J$ multiplets and following the L–S (Russel–Saunders) coupling scheme.

The explicit matrix form of the time-independent Schrödinger equation with square and symmetrical $H_{ij}$ is as follows:

$$\begin{bmatrix} \boldsymbol{H_{11}} & \boldsymbol{H_{12}} & \cdots & \boldsymbol{H_{1Z}} \\ \boldsymbol{H_{21}} & \boldsymbol{H_{22}} & \cdots & \boldsymbol{H_{2z}} \\ \vdots & \vdots & \ddots & \vdots \\ \boldsymbol{H_{z1}} & \boldsymbol{H_{z2}} & \cdots & \boldsymbol{H_{zz}} \end{bmatrix} \begin{bmatrix} \boldsymbol{\Psi_1} \\ \boldsymbol{\Psi_2} \\ \vdots \\ \boldsymbol{\Psi_z} \end{bmatrix} = \begin{bmatrix} \boldsymbol{E_1} \\ \boldsymbol{E_2} \\ \vdots \\ \boldsymbol{E_z} \end{bmatrix} \begin{bmatrix} \boldsymbol{\Psi_1} \\ \boldsymbol{\Psi_2} \\ \vdots \\ \boldsymbol{\Psi_z} \end{bmatrix} \qquad \textbf{(1. 7)}$$

#### 1.4.1.4. Electrostatic interaction: The central-field approximation

The central field approximation for the electrostatic potential operator is based on the assumption of independent motion of each electron in the field [$-U(r_i)/e$] which arises from the contribution of the nucleus and other electrons as an averaged spherical central field (Hehlen et al. 2013). Thus wavefunctions ($\Psi$) are expressible in terms of the spherical harmonics $Y_{l, ml}(\theta, \varphi)$ and radial function $R_{nl}(r)$. Hamiltonian operator for the electrostatic potential operator (Hehlen et al. 2013),

$$\boldsymbol{He = \frac{e^2}{r_{ij}} \propto \sum_{k=0,2,4,6} C_i^{(k)} C_j^{(k)}} \qquad \textbf{(1. 8)}$$

Here $C_q^{(k)} = \sqrt{\frac{4\pi}{(2k+1)Y_{kq}}}$ and $Y_{kq}$ are spherical harmonics.

The electrostatic matrix element of $H_e$ with $l$=3 is,

$$\left\langle 4f^N SL \middle| C_i^{(k)} C_j^{(k)} \middle| 4f^N \acute{S}\acute{L} \right\rangle \qquad (1.\ 9)$$
$$= \delta_{S\acute{S}} \delta_{L\acute{L}} (-1)^L (7)^2$$
$$\times \sum_{k=0,2,4,6} \begin{pmatrix} 3 & k & 3 \\ 0 & 0 & 0 \end{pmatrix}^2 \begin{Bmatrix} 3 & 3 & k \\ 3 & 3 & L \end{Bmatrix} F_{(k)}$$

The separation of the variable for $H_e$ is possible through its expression in terms of Legendre polynomials (Carnall, Fields, and Rajnak 1968),

$$\boldsymbol{E_o = \sum_{k=0}^{6} f^k F_{(k)}} \qquad \textbf{(1. 10)}$$

Here

$$f^k = \delta_{S\acute{S}} \delta_{L\acute{L}} (-1)^L (7)^2 \times \begin{pmatrix} 3 & k & 3 \\ 0 & 0 & 0 \end{pmatrix}^2 \begin{Bmatrix} 3 & 3 & k \\ 3 & 3 & L \end{Bmatrix} \qquad \textbf{(1. 11)}$$

The electrostatic energy ($E_O$) as in Eq. (1.10), is articulated in terms of products of Slater radial integrals [$F_{(k)}$], and angular coefficients (*p)* where this sum is constrained to *k=0, 2, 4 & 6* due to null value of *3j* and/or *6j* symbols for all other *k* terms. The electrostatic operator is not acting on the spin, hence the *Kronecker delta* destroys the matrix element with $S \neq S'$ and $L \neq L'$. The $^{2S+1}$L terms of $RE^{3+}$ ion with the identical L and S are differentiated with an extra sequential index τ which is later solved using two notations $F_{(k)}$ and $F^{(k)}$ by Nielsen and Koster for the Slater integrals, based on the Racah' idea of respective classification of states to get all matrix elements of electrostatic operator for the configurations of all the $4f^N$ electrons with parameters [$E^{(k)}$] related to Slater integral reported elsewhere (Hehlen et al. 2013),

$$\boldsymbol{\left\langle 4f^N SL \middle| He \middle| 4f^N \acute{S}\acute{L} \right\rangle = \sum_{k=0}^{3} e_k E^k} \qquad (1.\ \textbf{12})$$

### 1.4.1.5. The spin-orbit interaction

The Hamiltonian operator for spin-orbit interaction is (Hehlen et al. 2013):

$$\boldsymbol{Hso} = \sum_{\boldsymbol{i=1}}^{\boldsymbol{N}} \boldsymbol{\xi(r_i)(s_i.l_i)} \qquad (1.\ \mathbf{13})$$

Here $r_i$ stands for the radial coordinate of the $i^{th}$ electron with the orbital ($l_i$), and spin ($s_i$) angular momentum, and the central field potential [$U(r_i)$] (Hehlen et al. 2013),

$$\xi(r_i) = \frac{\hbar^2}{m^2c^2r_i}\left\{\frac{(dU(r_i))}{dr_i}\right\} \qquad (1.\ 14)$$

The matrix elements of $H_{so}$,

$$\left\langle \boldsymbol{4f^N SLJ}\middle|\boldsymbol{Hso}\middle|\boldsymbol{4f^N \acute{S}\acute{L}\acute{J}}\right\rangle \qquad (1.\ 15)$$

$$= \boldsymbol{\xi(-1)^{J+L+\acute{S}}\sqrt{l(l+1)(2l+1)}}$$

$$\times \begin{Bmatrix} \boldsymbol{S} & \boldsymbol{\acute{S}} & \boldsymbol{1} \\ \boldsymbol{\acute{L}} & \boldsymbol{L} & \boldsymbol{J} \end{Bmatrix} \left\langle \boldsymbol{l^N SL}\middle|\boldsymbol{V^{(11)}}\middle|\boldsymbol{l^N \acute{S}\acute{L}}\right\rangle$$

The energy arising from spin-orbit interaction ($E_{SO}$) may be expressed as for *4f* configuration with *l=3* and the constant parameter of spin-orbit coupling ($\xi$) for a host-specific each state of *4f* configuration with the angular part of the spin-orbit interaction ($A_{SO}$) and radial integral ($\zeta_{4f}$) as follows (Hehlen et al. 2013).

$$\boldsymbol{E_{SO} = A_{SO}\zeta_{4f}} \qquad (1.\ \mathbf{16})$$

The approximation-based total energy is the sum of the energy eigenvalue of spin-orbit interaction ($E_{SO}$) and electrostatic interaction ($E_o$) (Carnall et al. 1968).

### 1.4.1.6. Wigner symbols

The Wigner 3-j symbol provides a mathematical treatment for two coupled angular momenta, with a similar relation as the Clebsch–Gordan (Hehlen et al. 2013),

$$\begin{pmatrix} \boldsymbol{a} & \boldsymbol{b} & \boldsymbol{c} \\ \boldsymbol{\alpha} & \boldsymbol{\beta} & \boldsymbol{\gamma} \end{pmatrix} \quad (1.\ 17)$$

$$= (-\mathbf{1})^{a-b-\gamma}\sqrt{\Delta(\boldsymbol{a},\boldsymbol{b},\boldsymbol{c})}\sqrt{[(\boldsymbol{a}+\boldsymbol{\alpha})!\,(\boldsymbol{a}-\boldsymbol{\alpha})!\,(\boldsymbol{b}+\boldsymbol{\beta})!\,(\boldsymbol{b}-\boldsymbol{\beta})!\,(\boldsymbol{c}+\boldsymbol{\gamma})!\,(\boldsymbol{c}-}$$

$$\times \sum_{\boldsymbol{t}} \frac{(-\mathbf{1})^{\boldsymbol{t}}}{\boldsymbol{x}(\boldsymbol{t})}$$

Where

$$x(t) = t!\,(c-b+t+\alpha)!\,(c-a+t-\beta)!\,(a+b-c-t)!\,(a-t \quad (1.18)$$
$$-\alpha)!\ \times (b-t+\beta)!$$

And

$$\Delta(a,b,c) = \frac{(a+b-c)!\,(a-b+c)!\,(-a+b+c)!}{(a+b+c+1)!} \quad (1.\ 19)$$

Three angular momenta ($j_1$, $j_2$, $j_3$) are coupled to stimulate the Wigner 6-j symbol as a sum of products of 3-j symbols as reported elsewhere (Hehlen et al. 2013),

$$\begin{Bmatrix} \boldsymbol{j_1} & \boldsymbol{j_2} & \boldsymbol{j_3} \\ \boldsymbol{J_1} & \boldsymbol{J_2} & \boldsymbol{J_3} \end{Bmatrix} = \sqrt{\Delta(\boldsymbol{j_1 j_2 j_3}) \times \Delta(\boldsymbol{j_1 J_2 J_3}) \times \Delta(\boldsymbol{J_1 j_2 J_3}) \times \Delta(\boldsymbol{J_1 J_2 j_3})} \quad (1.\ 20)$$

$$\times \sum_{\boldsymbol{t}} \frac{-\mathbf{1}^{\boldsymbol{t}}(\boldsymbol{t}+\mathbf{1})}{\boldsymbol{f}(\boldsymbol{t})}$$

Here summation is running over all *t* such that all factorials in *f(t)* are greater than equal to zero.

$$f(t) = (t-j_1-j_2-j_3)!\,(t-j_1-J_2-J_3)!\,(t-J_1-j_2-J_3)! \quad (1.\ 21)$$
$$\times (t-J_1-J_2-j_3)!\,(j_1+j_2+J_1+J_2-t)!$$
$$\times (j_2+j_3+J_2+J_3-t)!\,(j_3+j_1+J_3+J_1-t)!$$

### 1.4.1.7.Wigner-Eckart theorem

Wigner-Eckart theorem states that each element of the matrix related to a specific tensor operator is considered simply as a product of the Wigner *3j*-symbol with the subsequent RME of the tensor operator, calculating only once for a specific combination of $T_q^{(k)}$ , *j*, and *j´* (Hehlen et al. 2013). Mathematically

$$\left\langle j'm'\alpha'\left|T_q^{(k)}\right|jm\alpha\right\rangle = (-1)^{j'-m'}\begin{pmatrix} j' & k & j \\ -m' & q & m\end{pmatrix}\left\langle j'\alpha'\left|T^{(k)}\right|j\alpha\right\rangle \qquad (1.\ 22)$$

The multi-electron system with various interactions is expressed with tensor operators [$T_q^{(k)}$] transforming as spherical harmonics $Y_{k,q}(\theta,\varphi)$.

### 1.4.1.8. The Reduced Matrix Elements (RME)

The RME of the Electric Dipole (ED) transition operator for the transition from Ψ→Ψ′, operating on the states [$|l^N SLJ\rangle$] of a $4f^N$ electron configuration which is a linear combination of the angular momentum of the states of the preceding $4f^{N-1}$ electron configuration [$|l^N L'J'\rangle$] and one another *4f* electron. Here, *S* and *L* quantum number are coupled to yield *J* (Hehlen et al. 2013):

$$\left\langle j'm'\alpha'\left|T_q^{(k)}\right|jm\alpha\right\rangle = (-1)^{j'-m'}\begin{pmatrix} j' & k & j \\ -m' & q & m\end{pmatrix}\left\langle j'\alpha'\left|T^{(k)}\right|j\alpha\right\rangle \qquad \mathbf{(1.\ 23)}$$

The RME for Spin-Orbit interaction operator [$V^{(1x)}$], operating on state [$|l^N SLJ\rangle$] of $4f^N$ electron configuration:

$$\left\langle l^N SL\left|V^{(1x)}\right|l^N S\acute{L}\right\rangle \qquad (1.\ 24)$$
$$= N\sqrt{s(s+1)(2s+1)(2S+1)(2L+1)(2\acute{S}+1)(2L'+1)}$$
$$\times \sum_{\Psi(l^{N-1})}\left\langle l^{N-1}\overline{SL}\middle|l^N SL\right\rangle\begin{Bmatrix} S & \acute{S} & 1 \\ s & s & \bar{S}\end{Bmatrix}\begin{Bmatrix} L & \acute{L} & x \\ l & l & \bar{L}\end{Bmatrix}(-1)^{\bar{S}+\bar{L}+S+L+s+l+x+1}$$

When *s* =1/2 and *l* =3 for *4f* electron,

$$\left\langle l^{14-N}SL\left|V^{(1x)}\right|l^{14-N}\acute{S}\acute{L}\right\rangle = (-1)^x\left\langle l^N SL\left|V^{(1x)}\right|l^N\acute{S}\acute{L}\right\rangle \qquad (1.\ 25)$$

The RME of Magnetic Dipole (MD) transition operator [$L+gS$], operating on state [$|l^N SLJ\rangle$] of $4f^N$ electron configuration (Hehlen et al. 2013):

For $J'=J$ with g-factor of electron $g= 2.002319304362$

$$\left\langle l^N SLJ\left|L+gS\right|l^N SL\acute{J}\right\rangle = g\sqrt{J(J+1)(2J+1)} \qquad (1.\ 26)$$

For $J'=J-1$,

$$\langle l^N SLJ|L + gS|l^N SL(J-1)\rangle \qquad (1.\ 27)$$
$$= (g-1)\sqrt{\frac{(S+L+J+1)(S+L-J+1)(J+L-S)(J+S-L)}{4J}}$$

### 1.4.2. J–O Intensity Parameters

The J-O theory was primarily manifested with keeping in mind $^{2S+1}L_J$ multiplate $RE^{3+}$ ion, although the parity-forbidden *4f* → *4f* transitions are partially allowed in presence of crystal field interaction.

#### 1.4.2.1. **The transitions probability of a transition**

The transition probability from [$\Psi_1 \rightarrow \Psi_2$] state is proportional to the transition moment,

$$\overrightarrow{M_{12}} = \int \Psi_2 \vec{\mu} \Psi_1 d\tau \qquad (1.\ 28)$$

Here μ is dipole moment operator.

#### 1.4.2.2. Laporte selection rule: Symmetry of host

Laporte selection rule guarantees non-zero values integral in [Eq. (26)] for the symmetric (gerade) direct product of $[\Psi_2 \otimes \vec{\mu} \otimes \Psi_1]$ with respect to the center of symmetry where mixing of odd-parity crystal-field or vibrations to *4f* wavefunctions with ungerade (u) inversion symmetry is possibly allowing these transitions (Hehlen et al. 2013). A new wavefunction (*X*) is admixed with an even-parity state ($\Phi_{nl}$) into the pure $4f^N$ wavefunction ($f^N JM_J$) via an odd-parity crystal field (*V*) with $[E(f^N JM_J) - E(\Phi_{nl})]$ energy difference as reported elsewhere (Hehlen et al. 2013),

$$|X\rangle = \frac{|f^N JM_J\rangle + \sum_{\Phi_{nl}}(\langle f^N JM_J|V|\Phi_{nl}\rangle)\,|X\rangle}{E(f^N JM_J) - E(\Phi_{nl})} \qquad (1.29)$$

The elements of matrix with ED moment for a transition between two admixed wavefunctions of $RE^{3+}$ ion are represented in,

$$\left\langle X\left|D_q^{(k)}\right|\acute{X}\right\rangle = \sum_{\varphi_{nl}}\left\{\frac{\langle f^N JM_J|V|\Phi_{nl}\rangle\left\langle f^N \acute{J}\acute{M}_J\left|D_q^{(k)}\right|\Phi_{nl}\right\rangle}{E(f^N JM_J)-E(\Phi_{nl})} + \frac{\langle f^N \acute{J}\acute{M}_J|V|\Phi_{nl}\rangle\left\langle f^N JM_J\left|D_q^{(k)}\right|\Phi_{nl}\right\rangle}{E\left(f^N JM_J\right)-E(\Phi_{nl})}\right\} \quad (1.\ 30)$$

Two assumptions were considered to solve the Eq. (1.30) as follows (Hehlen et al. 2013):

1) The even-parity state [ $\varphi_{nl}$] has entirely degenerate sub-levels.
2) $E\left(f^N JM_J\right)-E(\varphi_{nl}) = E\left(f^N JM_J\right)-E(\varphi_{nl})$

With these assumptions, the ED-induced absorption $\left|f^N JM_J\right\rangle \rightarrow \left|f^N J'M'_J\right\rangle$ can be used to derive the calculated oscillator strength from three J-O parameters [$\Omega_{(\lambda)}$] (Hehlen et al. 2013). Here $\chi_{ED}^{abs}$ is the local-field correction.

$$f_{ED}^{abs} = \frac{8\pi^2 m_e}{3h}\frac{\nu}{(2J+1)}\frac{\chi_{ED}^{abs}}{n}\sum_{\lambda=2,4,6}\Omega_\lambda\left|\langle f^N JM_J|U^{(\lambda)}|f^N \acute{J}\acute{M}_J\rangle\right|^2 \quad (1.\ \mathbf{31})$$

The magnetic-dipole (MD) induced absorption $\left|f^N JM_J\right\rangle \rightarrow \left|f^N J'M'_J\right\rangle$ with the oscillator strength (Hehlen et al. 2013),

$$f_{MD}^{abs} = \frac{h\nu}{6m_e c^2}\frac{n}{(2J+1)}\lambda\left|\langle f^N JM_J|L+gS|f^N \acute{J}\acute{M}_J\rangle\right|^2 \quad (1.\ \mathbf{32})$$

For material without any magnetic properties have zero local field correction for the magnetic field. Thus total oscillator strength is:

$$f^{abs} = f_{ED}^{abs} + f_{MD}^{abs} \quad (1.\ 33)$$

### 1.4.2.3. The virtual-cavity model

The ED-induced absorption is accompanied by the local field correction from the virtual cavity model (Hehlen et al. 2013),

$$\chi_{ED}^{abs} = \left[\frac{E_{loc}}{E}\right]^2 = \left[\frac{(n^2+2)}{3}\right]^2 \quad (1.34)$$

#### 1.4.2.3.1. The Calculated Oscillator Strength ($f_{cal}$)

Thus theoretical oscillator strength ($f_{cal}$) with local field correction of Eq. (**32**) is articulated as a sum of the transition matrix element comprising the J-O parameters ($\Omega_t$) which relies on the host (Hehlen et al. 2013),

$$f_{ED}^{abs} = \frac{8\pi^2 m_e}{3h}\frac{\nu}{(2J+1)n}\frac{(n^2+2)^2}{9n}\sum_{\lambda=2,4,6}\Omega_\lambda \left|\langle f^N J M_J \left| U^{(\lambda)} \right| f^N \acute{J} \acute{M}_J \rangle\right|^2 \qquad (1.\ 35)$$

Here $\nu=c/\lambda$, $\lambda$ stand for the mean wavelength of the transition, c represents the velocity of light in vacuum, $m_e$ is electron mass, $h$ is the Planck's constant, $n$ is the index of refraction, and $\| U^{(\lambda)} \|$ is the RME between initial and terminal level.

#### 1.4.2.3.2. The Experimental Oscillator Strength ($f_{exp}$)

The $f_{exp}$ are estimated from absorption spectra as follows,

$$f_{exp} = \frac{4\varepsilon_\circ m_e c^2}{e^2}\frac{10\log(10)}{N_A}\int \in(\bar{\nu})d\bar{\nu} \qquad (1.\ 36)$$

$$= 4.319\times10^{-9}\frac{mol.cm^2}{l}\int \in(\bar{\nu})d\bar{\nu}$$

The integration over the respective peak is estimated from the area of absorption peaks in the energy (ν) domain to avoid distortion in spectral distribution,

#### 1.4.2.3.3. Root-Mean-Square (RMS) deviation

The relative RMS deviation is estimated from the calculated and experimental oscillator strength with the number of parameters ($p=3$) as reported elsewhere (Hehlen et al. 2013) ,

$$RMS_{rel} = \sqrt{\frac{1}{n-p}\sum_{i=1}^{n}\left(\frac{f_i^{exp}-f_i^{calc}}{f_i^{exp}}\right)^2} \qquad (1.\ 37)$$

The non-radiative relaxation process involves $RE^{3+}$ ions dissipating excitation energy through thermal mechanisms, such as collision quenching and vibrational relaxation, rather than emitting a photon. Additionally, $RE^{3+}$ ions in the excited state can depopulate the excited state

through processes like multi-phonon relaxation, cross-relaxation (CR), Upconversion (UC), energy migration, etc (Hehlen et al. 2013).

### 1.4.3. Significance of JO parameters

Thus J-O parameters ($\Omega_t$) are evaluated from the absorption spectra for a particular $RE^{3+}$ ion-doped host. The dependence of $\Omega_2$ parameter's dependence is observed based on the local environment around the $RE^{3+}$ ion and the covalence between $RE^{3+}$ and ligand anions. The RE-O bonding indicates the asymmetry of the local environment around $RE^{3+}$ ions. Therefore, $\Omega_2$ has a small value for ionic host materials (such as fluoride glasses) and lage value for covalent host materials (like silicate glasses) (Brik et al. 2015). The $\Omega_4$ parameter is related to the viscosity and rigidity of the host material.

## 1.5. FACTORS OF UCL AND DCL

UCL and DCL mechanisms in luminescent materials face a bottleneck of insufficient emission intensity, which must be improved to optimize photonic performance. The discussion includes key concepts that can be tuned for optimization.

### 1.5.1. Dopants: Activator- Sensitizer pair

UCNPs and DCNPs with sensitizer-activator ion pairs have been extensively reported in various host materials to achieve efficient ETU luminescence. This concept benefits from closely matched intermediate excited states, resulting in a high quantum yield (QY) by reducing nonradiative decay (Wen et al. 2018) . The high absorption cross-section of $Yb^{3+}$ ions in a single excited state plays a crucial role as an efficient activator ion for the most efficient ETU process, and vice-versa (Villanueva-Delgado, Krämer, and Valiente 2015), (Meijer et al. 2010). In the ETU process, various $RE^{3+}$ ions ($Pr^{3+}$, $Nd^{3+}$, $Er^{3+}$ etc.) with different intermediate energy levels can serve as sensitizer ions. A schematic diagram (Fig. 5) of the $Yb^{3+}$-$Pr^{3+}$ ions pair illustrates the absorption of two NIR photons through GSA [$Pr^{3+}(^3H_4 \rightarrow {}^1G_4$ ); $Yb^{3+}(^2F_{7/2} \rightarrow {}^2F_{5/2})$]. The energy transfer from $Yb^{3+}$ ions to nearby $Pr^{3+}$ ions [$^2F_{5/2} \rightarrow {}^1G_4$] promotes the electron to a higher excited state through ESA [$Pr^{3+}(^3P_0 \rightarrow {}^1G_4)$] process.

### 1.5.2. Concentration quenching

Dexter and Schulman reported luminescence quenching in bulk materials occurring at activator concentrations between 0.001-0.01 M, limiting the use of highly $RE^{3+}$ ion-doped materials for brighter luminescence (Liu et al. 2017). Therefore, $RE^{3+}$ ion doping concentration of low value is a significant obstacle to producing brighter luminescent nanomaterials with small size. Various strategies are available to overcome concentration quenching (Zhou et al. 2015), such as (a) blocking the path of energy migration to the surface, (b) increasing the sensitizer-acceptor distance within the host crystal with large unit cell, (c) minimizing ion segregation by uniformly doping the host, (d) introducing surface plasmon resonance (SPR) with gold and silver particle co-doping to modulate the electromagnetic field around $RE^{3+}$ ions, (e) modulating the local crystal field for local distortion in the crystal lattice, and (f) introducing a host with low site symmetry to reduce nonradiative decay . The Förster critical distance naturally falls in 2−6 nm range, so the doping concentration of RE3+ ion should maintain below $10^{-3}$ M for organic dye-doped $SiO_2$ and $10^{-2}$ M for UCNPs (Wen et al. 2018).

### 1.5.3. Phonon energy of host

The $RE^{3+}$ ion host must be an optically transparent material with low phonon energy (as shown in Table 3). Incorporation $RE^{3+}$ ions into inorganic lattice host matrices initiates the mixing of certain odd-parity configurations, enabling otherwise forbidden electric dipole transitions of these ions (Kumar et al. 2017). A phonon represents a quantized vibration mode occurring in a crystal lattice (Ahrens 2009). The high phonon or vibrational energies of $RE^{3+}$ ion hosts escalate the probability of NR relaxations. Consequently, quenching of PL spectra is inevitable and is proportional to the number of vibrational quanta (hυ) of the matrix required to bridge the gap between the highest non-emitting level and the lowest emitting level of the $RE^{3+}$ ion. This quenching drops promptly as the number of vibrational quanta escalate (Ahrens 2009), (Escudero et al. 2017).

Oxide hosts exhibit high chemical stability, although their phonon energies are relatively high, often exceeding 500 $cm^{-1}$ due to the stretching vibration of the host lattice (Wang and Liu 2009). However, oxide glasses are more advantageous hosts than crystals, as nearly every element in the periodic table can be incorporated into glasses, allowing for easier control of quantity and shape control (Qiu et al. 2000). $RE^{3+}$ ions are preferred in hosts with a coordination number (CN) ≥ 6 (Mir et al. 2020) . Oxide and fluoride lattices, which possess higher

coordination numbers (CN=8 or 9), are well-suited hosts. The wide band gap of these hosts contributes to poor absorption of visible light and poor charge transport. For optoelectronic applications, such as solar light harvesting and LEDs, efforts have been made to dope $RE^{3+}$ ions into the lattice of semiconductors. However, $RE^{3+}$ ion doping in semiconductors remains challenging as most semiconductors offer a tetrahedral coordination environment (CN= 4) for $RE^{3+}$ dopant (Mir et al. 2020).

**Table 1.3: Different hosts for the $Pr^{3+}$-$Yb^{3+}$/$Nd^{3+}$-$Yb^{3+}$ ion pair co-doping with phonon energy**

| Host | Specific composition | State | Phonon energy ($cm^{-1}$) | Advantage | Ref. |
|---|---|---|---|---|---|
| **Borate** | **$GdAl_3(BO_3)_4$** | Phosphor | 1400 | NA | (Zhang and Yang 2007) |
| | **Tellurite** | Glass | 780 | High refractive index; Low reflection loss | (Dwivedi, Rai, and Rai 2008) |
| **Fluoride** | **$NaYF_4$** | Phosphor | 200-450 | NA | (Chen, Huang, and Zhang 2009) |
| **Fluoride** | **$LaF_3$-$ZrF_4$** | Glass-ceramic | 350 | Transparent, low phonon energy, crystal-like PL and high solubility of $RE^{3+}$ ion | (Dieudonné et al. 2013) |
| **Fluoride** | **$KY_3F_{10}$** | Powder | 420 | Low phonon energy; high solubility of $RE^{3+}$ ion | (Serrano et al. 2011) |
| **Fluoride** | **$LaF_3$** | Powder | 350 | NA | (Anna M. Kaczmarek et al. 2018) |
| **Borate** | **Lead borate** | Glass | 1321 | Higher doping levels of $RE^{3+}$ ions, flexible geometry and ease of fabrication | (Wen and Tanner 2011) |

| | | | | | |
|---|---|---|---|---|---|
| **Oxide** | **$CaYAlO_4$** | Powder | 756 | High solubility of $RE^{3+}$ ion | (Guille et al. 2012) |
| **Fluoride** | **$GdF_3$** | Powder | 400 | NA | (Nizamutdinov et al. 2019) |
| **Silicate** | **Lanthanum-aluminum-silicate** | Glass | 1100 | High solubility of rare earth ions; transparency of a wide spectral range | (Liang et al. 2021) |
| | **YOF** | Phosphor | NA | NA | (Saeed, Coetsee, and Swart 2020) |
| | **Germinate** | Glass | 840 | High refractive index; Low reflection loss | (Reisfeld and Kalisky 1981) |
| **phosphate** | **Lead meta-phosphate** | Glass | 1200 | NA | (Liégard et al. 2005) |
| **Silicate** | **Titania-silicate** | Thin film | 1100 | NA | (Battisha 2007) |
| **Fluoride** | **Yttrium-fluoride** | Powder | 500 | High concentration of doping ions | (Meijer et al. 2010), (Pudovkin et al. 2021) |
| | **$LiNbO_3$** | Crystals | NA | NA | (Sun et al. 2013) |
| **phosphate** | **Fluoro-phosphate** | Glass | 1100 | melt quench | (Faria et al. 2021) |
| **Silicate** | **Sodium-calcium-silicate** | Glass | 1100 | Low phonon energy; high energy gap | (Muniz et al. 2023) |
| AVL: Available | | | NA: Not available | | |

### 1.5.4. Doping impurity elements

Semiconductor and transition elements have been employed as hosts or modifiers for $RE^{3+}$ ions, as discussed in reference (Prathibha et al. 2021), (Hien et al. 2019), (Raevskaya et al. 2014), (Chang et al. 2017), (Dihingia and Rai 2012). The addition of semiconductor and transition element impurities enhances luminescence performance, as detailed below.

#### 1.5.4.1. Transition metal impurity

Transition metal ions (e.g., $Ti^{4+}$) are commonly used in inorganic host materials due to their similar ionic size to $RE^{3+}$ ions and their ability to create crystal defects. Titanium oxide ($TiO_2$) is a naturally occurring material derived from titanium ore (approximately 95% pure) and exists in the orthorhombic brookite structure (space group Pcab, density = 4.12 g/ $cm^2$), tetrahedral anatase (space group $I4_1/amd$, density = 3.894 g/$cm^2$), and rutile (space group P42/ mnm, density = 4.25 g/$cm^2$) structures. Titanium oxide is valuable in environmental and energy research (Sta et al. 2014). The rutile phase is the most stable, while anatase and brookite transform into the rutile upon heating. Anatase has applications in lithium-ion batteries (Amin et al. 2018), dye-sensitized solar cells (Liang et al. 2013), self-cleaning coatings (Li and He 2013), and as a catalyst (Kumar et al. 2020).

#### 1.5.4.2. Semiconductor impurity

Semiconductor nanocrystals, like $Zn^{2+}$ , with larger ionic dimensions, are used as host materials to push $RE^{3+}$ ions to the remotest layer of these nanocrystals (Wang and Liu 2009). ZnO is an N-type semiconductor with a wide band gap ($E_g$ ~ 3.3 eV or 376 nm at 300 K) (Kumar et al. 2017) and a large excitation binding energy (60 meV) (Hien et al. 2019). Semiconductor nanocrystals also exhibit the benefits of quantum confinement, where the semiconductor bandgap widens due to smaller particle size, leading to electron-hole pair localization in a restricted environment, resulting in quantized energy levels for electrons and holes (Bang, Yang, and Holloway 2005). The hexagonal wurtzite phase of ZnO is preferred due to its stability at room temperature and normal atmospheric pressure, which differs from the zinc blende and rock salt structures (Kumar et al. 2020) while the wurtzite structure has a tetrahedral coordination of four zinc ions ($Zn^{2+}$) at the corners and one oxygen ion ($O^{2-}$) at the center or vice versa. The size of crystallites and doping concentration are crucial factors in modulating the energy band gap of ZnO. DCL processes are accompanied by emission from defects in the ZnO host for $RE^{3+}$ ion doping (Kumar et al. 2017). Two emissions are observed from ZnO: (a) band-to-band emission (BBE; UV region) resulting from recombination of a bonded (Columbic force) electrons-hole pairs within the valance and conduction bands, and (b) deep-level emission (DLE; VIS region) initiated by extrinsic impurities or intrinsic defects in ZnO (Kumar et al. 2017).

### 1.5.5. Dielectric superlensing effect: Mie resonance

A convergent low-power incident light beam serves as a photonic hotspot with high field intensity. Dielectric microbeads act as a superlens, allowing for collimation of highly divergent emission for far-field accumulation through Mie resonance (Liang et al. 2019). Liang et al., manipulated the wavefront of both excitation and emission fields through dielectric superlensing to achieve amplified PL intensity.

### 1.5.6. Excitation Irradiance

The efficiency of heavily $RE^{3+}$ ion-doped luminescent materials is significantly impacted by concentration quenching, where an excess of nearby $RE^{3+}$ ions in the ground state absorb excitation energy. Therefore, an adequate excitation photon flux ensures that the majority of $RE^{3+}$ ions are promoted to the excited (intermediate) states (Wen et al. 2018). High-energy flux excitation activates otherwise dark activators and enhances luminescence intensity (Zhao et al. 2013). High irradiance increases the path length from excited states to ground states, which, in turn, enhances luminescence intensity (Zhao et al. 2013). This effect has been observed in various studies, such as the intensity enhancement of UCL spectra of $Tm^{3+}$ ion-doped $NaYF_4$ phosphor at high excitation irradiance (Zhao et al. 2013), quadratic excitation power dependence and excitation power dependence and corresponding color tunability for $Pr^{3+}$ -$Yb^{3+}$ codoped tellurite glass reported by Dwivedi et al. (Dwivedi et al. 2008), the intensity enhancement of UCL for $Yb^{3+}$-$Er^{3+}$:$BiNbO_4$ powder at different pump power, as reported by Sales et al. (Sales et al. 2016).

### 1.5.7. Core-Shell

The arrangement of core-shell structures in luminescent materials is achieved by combining the Stober sol-gel and hydrothermal methods. Luminescent $RE^{3+}$ ions in the core are protected by an inert shell to prevent the non-radiative (NR) decay triggered by surface defects and other vibrational deactivation from surface-bound ligands or solvents (Li et al. 2014). **For instance,** Lee et al. prepared $SiO_2$@$TiO_2$ core-shell particles with controlled shell thickness using a modified Stöber method (Lee et al. 2007). Song et al., prepared $NaGdF_4$:$Nd^{3+}$-$Yb^{3+}$ luminescent nanoparticles with both core and shell made of $NaGdF_4$ through a coprecipitation method, followed by hydrothermal treatment and annealing in a vacuum, to record temperature-dependent UCL spectra when excited at 980 nm and DS emission spectra with 808 nm excitation (Song et al. 2021). Zhu *et el*., prepared $Pr^{3+}$-$Yb^{3+}$ codoped monodisperse luminescent nanoparticles in in

$NaGdF_4$ with and without active shell (eg $Yb^{3+}$:$NaYF_4$) to achieve intense NIR emission. The efficient ET from $Pr^{3+}$ to $Yb^{3+}$ ions was observed in materials with active coating, along with a longer lifetime of the $^3P_0$ level of $Pr^{3+}$ ions under 445 nm excitation (Zhu et al. 2014). Core-shell luminescent structures with rod, plate, and dumbbells shapes also warrant investigation for possible applications.

### 1.5.8. Plasmonic material

Plasmonic materials, such as gold and silver, are doped into nanocrystals to confer plasmonic properties. These plasmonic electric fields can tune the localized electric field related to dipole moment by modifying the surrounding crystal field of acceptor-sensitizer ions (Escudero et al. 2017). Plasmonic structures confine light below the diffraction limit, facilitating the generation of large local energy densities. However, it should be noted that the quenching of UCL spectra can occur due to the heat generation by transfer of energy from the UCL material to the metal ion (Eriksen et al. 2019)**.**

## 1.6. POTENTIAL APPLICATIONS

$RE^{3+}$ ion-doped materials have empowered a wide range of utilities, for example solar-energy harvesting, bio-applications, and super-resolution microscopy (Wen et al. 2018). The diverse and lucrative potential applications are driving further research in this area, as evidenced by the increasing number of publications over the last 20 years. A clear overview can be obtained from the pie chart of the survey conducted on the Web of Science (WoS) (version 5.32), showing the percentage of published research in nanomedicine, biophotonics, and additional allied areas (Loo et al. 2019).

### 1.6.1. Photovoltaic Solar Cell

A photovoltaic solar cell converts a photon into an electron-hole pair only if its energy is close to the semiconductor's bandgap energy. Photons with energy lower than the bandgap energy pass through the cell without being absorbed (sub-bandgap transparency), while supra-bandgap photons are absorbed, and the excess energy of the excited electrons is converted into thermal energy (Serrano et al. 2011). UCL and DCL mechanisms are employed to create passive luminescence conservation layers, overcoming lattice thermalization loss and sub-band gap

losses by maximizing sunlight utilization from the AM1.5G spectrum (Richards 2006). For a detailed discussion of the use of DCL and UCL mechanism in photovoltaics, refer to Huang et al., (Huang et al. 2013).

### 1.6.2. Multicolor tuning for Bio-label

Bio-labels exhibit strong absorption at specific excitation wavelength and well-resolved emission spectra, alongside chemical stability. The emission spectrum of $RE^{3+}$ ions varies significantly in different hosts due to the presence of the dopant ions in different site symmetries. Different contributions of dopant ions at the surface and in the interior of the particles lead to variations in the emission spectra, and these surface dopant concentrations increase with smaller nanocrystalline dimensions. Color tunability of $RE^{3+}$ ion-doped nanocrystals is achieved by modulating the dimensions and concentrations of surface dopant ions, resulting a redshift in emission as particle dimensions decrease (Wang and Liu 2009). Wang and Liu prepared $Yb^{3+}/Er^{3+}/Tm^{3+}$: $NaYF_4$ phosphors to demonstrate UCL multicolor tuning with a dual emission process.

### 1.6.3. Optical thermometry: nanoheater

$RE^{3+}$ ion-doped solid host materials have been used as optical sensors and nano-heaters due to their higher temperature sensitivity, outstanding photo-stability, extended luminescent lifetimes, sharp emission bands, high brightness, high melting point, chemical stability, and low toxicity (Pudovkin et al. 2021). Optical nanoheaters, novel materials at nano- or micro-scale, can generate heat when excited by NIR lasers (Soni, Dey, and Rai 2015). Optical sensors (thermometer) rely on the luminescence response of active ions embedded into solid hosts. They offer an alternative to overcoming environment and size-related limitation of contact sensor. The advantages include high spatial resolution, sensitivity, fast signal acquisition, and absence of electromagnetic interference (Faria et al. 2021). The working range of a thermometer depends on the energy gap of $RE^{3+}$ ion (Faria et al. 2021). For example, $Eu^{3+}$ ions have a high energy gap (~1500 $cm^{-1}$), making them suitable for high-temperature measurements. $Er^{3+}$ ions emit in the visible region ($E_g$ < 800 $cm^{-1}$), making them suitable for room temperature measurements. The closely spaced energy levels of $Nd^{3+}$ ions enable emission in the near-infrared region spanning the first (700 – 950 nm) and second (1000 – 1350 nm) biological windows (Faria et al. 2021). The working range of $Nd^{3+}$ ions extends to much higher temperatures, as $Nd^{3+}$ ions have three thermally-coupled levels, and the simultaneous usage of twofold intensity ratios enhances

temperature sensing accuracy. The co-doping of $Yb^{3+}$ ions with the aforementioned $RE^{3+}$ ions promotes an additional emission band with the possibility of FIR.

***Fluorescence intensity ratio (FIR) and fluorescence lifetime (FL)***

FIR and FL techniques have been used for temperature sensing with the assistance of a population of thermally coupled exciting levels of the $RE^{3+}$ ion (ES I & ES II). An induced small change in fluorescence is correlated with the population of a specific $RE^{3+}$ ion level participating in a transition, along with the rate of spontaneous emission transition, at room temperature (Faria et al. 2021).

The electrons in the lower energy level (ES I) move to the upper energy level (ES II) as the temperature of the system rises, directly influencing the emission spectrum. Here, the emission intensity of ES I decreases, while the emission intensity of ES II increases (Faria et al. 2021). FIR thermometry is possible with thermally coupled energy states of $RE^{3+}$ ions (e.g. $Pr^{3+}$, $Tm^{3+}$ and $Dy^{3+}$ etc).

The Boltzmann distribution law states that temperature influences populations (N) of each energy level, such that the thermalization of the two emissive levels is much quicker than the associated radiative rates with time-independent emission rates ($k_i^{rad}$). The FIR is represented as (Faria et al. 2021),

$$R(T) = \frac{I_2(T)}{I_1(T)} = \frac{k_2^{rad} N_2(T)}{k_1^{rad} N_1(T)} = Ae^{-\frac{\Delta E}{k_B T}} \tag{1.38}$$

Measuring the thermometric parameter [R(T)] specifies the temperature and its variation. The term "A" depends on the levels of energies, degeneracies, and spontaneous emission rates. Thus, the exponential of temperature and the difference in energy gap of thermally coupled levels ($\Delta E = E_2 - E_1$) determine the thermometric parameters.

Finally, the absolute sensitivity ($S_{abs}$) is determined by the observed change in the thermometric parameter R(T) with respect to temperature.

$$S_{abs} = \frac{dR}{dT} \tag{1.39}$$

Temperature sensing is achievable with luminescent materials containing pairs of $RE^{3+}$ ions ($Ho^{3+}/Yb^{3+}$, $Tm^{3+}/Yb^{3+}$, $Er^{3+}/Yb^{3+}$), which have thermally coupled levels or stark sublevels that are usually split when incorporated into a ligand field/crystal field (Soni et al. 2015). Soni et al. prepared $Tm^{3+}$–$Yb^{3+}$: $Na_2Y_2B_2O_7$ phosphor based on the $^1G_4$ stark sub-level of $Tm^{3+}$ ions for optical sensing and frequency upconversion. Song et al. reported temperature-dependent UCL

emission in the 323-575 K range for $NaGdF_4$:$Nd^{3+}$-$Yb^{3+}$ luminescent core@shell nanoparticle (Song et al. 2021). Kaczmarek et al., prepared $LaF_3$: $Pr^{3+}$/$Yb^{3+}$ nanoparticles to explore potential temperature-sensing applications with the help of DCL spectra (Anna M. Kaczmarek et al. 2018). Meijer et al., reported emission peak broadening in $Nd^{3+}$ -$Yb^{3+}$ codoped Yttrium Fluoride phosphors for temperature sensing applications in the 3-300 K range (Meijer et al. 2010).

### *1.6.4.* Bio-application

In flow cytometry, a laser beam is focused on fluorophore attached to cells with a property that forces them to flow through a detector. UCNPs and DCNPs are extensively used as fluorophore in *in-vitro* and *in-vivo* bio-applications due to the strong absorption of $Yb^{3+}$ (980 nm) and $Nd^{3+}$ (808 nm) ion in the transparent biological window (650–1350 nm), where deeper tissue penetration and higher photobiocompatibility can be achieved, as living cells can endure an intense beam of NIR photons (Wen et al. 2018). The heat generation in living cell is further reduced with the DCL of the sensitized 808 nm by $Nd^{3+}$ ions to nearby $Yb^{3+}$ ions, reducing radiation absorption by water by a factor of 20 (Y. Wang et al. 2013). The high tissue penetration depth and low autofluorescence background are two additional advantages of this application (Y. Wang et al. 2013), (Zhou et al. 2015).

### 1.6.5. Other applications

Quantum computing (Kunkel and Goldner 2018) and Confocal microscopy (Tavernaro et al. 2017) are two noteworthy domains of ongoing research where UCNPs and DCNPs have potential applications.

## 1.7. REVIEW OF LITERATURE: In the context of present work

The pair of $RE^{3+}$ ($Pr^{3+}$-$Yb^{3+}$/$Nd^{3+}$-$Yb^{3+}$/ $Er^{3+}$-$Yb^{3+}$) ions have been co-doped in different host materials, whereas the available data on their synthesis, structure, and luminescence properties are tabulated in Table [5-7]. The power and temperature dependence of UCL or DCL spectra are also monitored. ETU and CSU processes are two of the most efficient UCL processes, which require a pair of sensitizer-activator ions; hence, the above-mentioned pairs are of uttermost significance, respectively.

### 1.7.1. $Pr^{3+}$ -$Yb^{3+}$ pair

The diverse emission bands, broadband and ultra-broadband emission of the low toxic $Pr^{3+}$ ion (Wen and Tanner 2011), have privileged in switchless scintillation and photo-bleaching, deep excitation penetration, and cell-free auto-fluorescence coverage applications (Liang et al. 2021). It has very low absorption in the NIR region (Villanueva-Delgado et al. 2015). The $Pr^{3+}$ ion has two important metastable states, $^3P_0$ (20,000 $cm^{-1}$) and $^1G_4$ (10,000 $cm^{-1}$) (Serrano et al. 2011), which can be resonate with the solo energy band of the $Yb^{3+}$ ion at 10,000 $cm^{-1}$. Here, the $Pr^{3+}$ -$Yb^{3+}$ ion pair has been co-doped in different host material to obtain UCL and DCL spectra as shown in Table 5.

Zhang and Yang reported the synthesis of the $Pr^{3+}$-$Yb^{3+}$ ion pair co-doped [$GdAl_3(BO_3)_4$] phosphor through the combustion synthesis route to report DCL spectra at varying $Yb^{3+}$ ion concentrations. The gradual quenching of $^3P_0 \rightarrow {}^3H_6$ transition of the $Pr^{3+}$ ion was perceived at high $Yb^{3+}$ ion concentrations, along with a reduction in the decay lifetime of the excited state of the $Pr^{3+}$ ion (Zhang and Yang 2007). Dwivedi et al., prepared $Pr^{3+}$ -$Yb^{3+}$ co-doped tellurite glass with the melt and quenched method to report white light from the sensitization of NIR photons. The absorption spectra indicated the presence of $Yb^{3+}$ ion. The intense blue and red anti-Stoke bands in UCL spectra were reported, along with some weak green bands (Dwivedi et al. 2008).

Chen et al., prepared $Pr^{3+}$ -$Yb^{3+}$ ions co-doped hexagonal $NaYF_4$ phosphor with the facile hydrothermal route method to report intense DCL spectra in the VIS-NIR region upon blue photon sensitization ($\lambda_{ex}$ =443nm). The PL excitation spectra indicated the presence of $Yb^{3+}$ ion (Chen et al. 2009). Dieudonne et al., prepared $Pr^{3+}$-$Yb^{3+}$ codoped $ZrF_4$ planar waveguide glass-ceramic by the physical vapor deposition method to present absorption spectra and luminescence spectra for excitation wavelength ($\lambda_{ex}$) of 980 and 443 nm at different $Yb^{3+}$ ion concentrations (Dieudonné et al. 2013). Braud et al., prepared $Pr^{3+}$-$Yb^{3+}$ codoped $KY_3F_{10}$ glass with the melt and quenched method to present DCL spectra at optimum $Yb^{3+}$ ion concentrations, whereas the reduction in the lifetime of $^3P_0$ state is correlated with the rise in ET efficiency at higher $Yb^{3+}$ ion concentration (Serrano et al. 2011).

Wen and Tanner, prepared $Pr^{3+}$-$Yb^{3+}$ ion pair codoped lead borate ($PbO–B_2O_3$) glass with the melt-quench method to report the DCL spectra ($\lambda_{exc}$ =454.5nm) at different concentration of

$Yb^{3+}$ ion and temperature. The intensity enrichment was observed in the NIR region with the rise in $Yb^{3+}$ ion concentrations in comparison to the intensity in the VIS region. The decay time of the $Pr^{3+}$ ion decreases swiftly with an increase in $Yb^{3+}$ ion concentration, thus demonstrating a fast CR from $Pr^{3+}$ ion to $Yb^{3+}$ ion due to the short-distance interaction between the two different $RE^{3+}$ ion species (Wen and Tanner 2011). Guille et al., prepared $Pr^{3+}$-$Yb^{3+}$ ions codoped $CaYAlO_4$ (CYA) host by the solid-state reaction to report the optimized DCL spectrum for $\lambda_{ex}$ = 450 nm excitation wavelength with an intense peak for the $^3H_4 \rightarrow {}^3P_2$ transition (Guille et al. 2012). Nizamutdinov et al., prepared $Yb^{3+}$-$Pr^{3+}$ ions pair codoped in $GdF_3$ and $YF_3$ host with the melt-quenched method to study DCL spectra under 445nm excitation wavelength. The enhancement in the lifetime of the $^3P_0$ state of the $Pr^{3+}$ ion was reported for ET from the $Yb^{3+}$ ion (Nizamutdinov et al. 2019). Liang et al., prepared $Yb^{3+}$-$Pr^{3+}$ ions pair codoped lanthanum aluminum silicate (SAL) glasses with a high-temperature melting process to report DCL spectra under 442 and 980 nm excitation sources at different doping concentrations (Liang et al. 2021). The presence of $Yb^{3+}$ ion co-doping benefited the absorption intensity of the $Pr^{3+}$ ion (Liang et al. 2021).

Saeed et al., prepared $Yb^{3+}$/$Pr^{3+}$ codoped yttrium oxyfluoride (YOF) phosphor with the pyrolysis method, which turns rhombohedral (R3m(166) space group) YOF structure after annealing at 900 ◦C to record visible DCL spectra. The optimum UCL spectra were reported for 2 mol % $Yb^{3+}$ ion concentrations. Luminescence quenching for a high concentration of $Pr^{3+}$ ion through cross-relaxation processes was also confirmed with the variation of decay time (in μs) of $Pr^{3+}$ and $Yb^{3+}$ ions (Saeed et al. 2020).

Table 1.4: List of literature available in $Pr^{3+}$-$Yb^{3+}$ ion co-doped in different host

| **Host** | **Type (Structure )** | **Absorption Spectra** | **DCL spectra $\lambda_{ex}$ (nm)** | **UCL spectra $\lambda_{ex}$ (nm)** | **Power (mW)** | **Temp-erature (K)** | **Ref** |
|---|---|---|---|---|---|---|---|
| **$GdAl_3(BO_3)_4$** | Phosphor (NA) | AVL | 489 | NA | NA | NA | (Zhang and Yang 2007) |
| **Tellurite** | Glass | AVL | NA | 980 | 100-500 | NA | (Dwivedi |

| | | | | | | | |
|---|---|---|---|---|---|---|---|
| | (NA) | | | | | | et al. 2008) |
| **$NaYF_4$** | Phosphor (Hexagonal) | AVL | 443 | NA | NA | NA | (Chen et al. 2009) |
| **$LaF_3$-$ZrF_4$** | Glass-ceramic | AVL | 476 | 980 | NA | NA | (Dieudonné et al. 2013) |
| **$KY_3F_{10}$** | Powder (Single crystal) | NA | 440 | NA | NA | NA | (Serrano et al. 2011) |
| **$LaF_3$** | Powder (NA) | | 375 | NA | NA | 15-105 | (Anna M. Kaczmarek et al. 2018) |
| **Lead borate** | Glass (NA) | AVL | 454.5 | NA | NA | 10-100 | (Wen and Tanner 2011) |
| **$CaYAlO_4$** | Powder | AVL | 450 | NA | NA | NA | (Guille et al. 2012) |
| **$GdF_3$/ $YF_3$** | Powder | | 450 | | | | (Nizamutdinov et al. 2019) |
| **Lanthanum-aluminum-silicate** | (SAL) glasses | AVL | 455 | 980 | NA | NA | (Liang et al. 2021) |
| **YOF** | Phosphor (Rhombohedral) | AVL | 225; 250 | NA | NA | NA | (Saeed et al. 2020) |
| | NA: Not Available | | | AVL: Available | | | |

### 1.7.2. $Nd^{3+}$-$Yb^{3+}$ pair

$Nd^{3+}$ ions have the highest absorption cross-section ($\sigma_{abs}$= $1.2\times10^{-19}$ $cm^2$ ) among $RE^{3+}$ ions at 808 nm, and twenty-time lower water absorption than that of 980 nm (Villanueva-Delgado et al. 2015), (Song et al. 2021), whereas it has emission in the biological windows I (650–1000 nm) and II (1000–1350 nm). Efficient energy transfer to sensitizer ions ($Pr^{3+}$, $Er^{3+}$, $Ho^{3+}$ etc) is promising through the $Yb^{3+}$ ion using the $Nd^{3+}$ ($^4F_{3/2}$)→$Yb^{3+}$ ($^2F_{5/2}$) transition as a bridge (Song et al. 2021). Thus, the $Yb^{3+}$-$Nd^{3+}$ ion pair benefits from the isolation of $Nd^{3+}$ ions from direct ionic interactions and energy cycling through energy capture (Song et al. 2021). The bio-application of the $Nd^{3+}$/$Yb^{3+}$ pair drastically reduces overheating effects and significantly boosts

the penetration depth of the laser inside the tissue in the second biological window (Liang et al. 2021), (Dibaba et al. 2019). The $Nd^{3+}$ ion has photoemission with different metastable intermediate states with long lifetimes in the IR ($^4F_{3/2}\rightarrow {}^4I_{11/2}$), NIR ($^4F_{3/2}\rightarrow {}^4I_{9/2}$) & ($^4F_{5/2}+ {}^2H_{9/2}\rightarrow {}^4I_{9/2}$), and red region ($^4F_{7/2}+{}^4S_{3/2}\rightarrow {}^4I_{9/2}$). Here, $Nd^{3+}$ -$Yb^{3+}$ ion pair has been co-doped in different host materials to obtain UCL and DCL spectra, as shown in Table 6.

Reisfeld and Kalisky prepared $Yb^{3+}$-$Nd^{3+}$ co-doped tellurite and germinate glass fabricated by the melt quenched method to report absorption and DCL spectra ($\lambda_{exc}$ =575 nm). The decay curve with the reduced lifetime of the $^4F_{3/2}$ level of the $Nd^{3+}$ ion was observed due to the energy transfer to the $Yb^{3+}$ ion (Reisfeld and Kalisky 1981). Liegard et al., prepared $Yb^{3+}$-$Nd^{3+}$ co-doped Lead metaphosphate [$Pb(PO_3)_2$] glass fabricated with the melt-quenched process to report enhanced lasing of the 980 nm laser through radiative and nonradiative (partly resonant –partly phonon-assisted) processes using an 808 nm diode laser excitation source. The lifetime of $Nd^{3+}$ ions was observed to be decreased with the presence of $Yb^{3+}$ ions (Liégard et al. 2005).

Battisha I. K. 2006 prepared $Yb^{3+}$-$Nd^{3+}$ ions pair co-doped $SiO_2$–$TiO_2$ thin film nano-composite fabricated by a spin-coating sol-gel process to report UCL spectra, where distinct peaks were observed in the visible region for samples annealed at temperature greater than 350°C (Battisha 2007). Meijer et al., prepared $Yb^{3+}$-$Nd^{3+}$ co-doped yttrium fluoride ($YF_3$) crystalline powder phosphor by co-precipitation method to report DCL spectra with the CR through $^4G_{9/2} \rightarrow {}^4F_{3/2}$ transition which further transfer to $Yb^{3+}$ ion. The decay lifetime reduction of the $Nd^{3+}$ ion is evidence of ET from $Yb^{3+}$ ion with increasing $Yb^{3+}$ ion concentration (Meijer et al. 2010). Sun et al., prepared $Nd^{3+}$-$Yb^{3+}$ ion pair co-doped $LiNbO_3$ crystals with the Czochralski method to report DCL spectra for an 808 nm excitation wavelength in the 850-1500nm range with three emission bands. The emission intensity for the $Nd^{3+}$ ion dimmed with the presence of $Yb^{3+}$ ion, parallel with the reduction of the decay time of $Nd^{3+}$ ion, evidencing ET from $Nd^{3+}$ ion to $Yb^{3+}$ ion (Sun et al. 2013).

Pudovkin et al., prepared the $Nd^{3+}$-$Yb^{3+}$ ions co-doped orthorhombic $YF_3$ (Pnma space group) phosphor annealed above 500°C in a vacuum with co-precipitation method and hydrothermal treatment. The temperature dependence of the DCL spectra in the temperature range (80–320 K) was reported with an excitation wavelength 355 nm corresponding to the $^4I_{9/2} \rightarrow {}^4D_{3/2}$ transition of the $Nd^{3+}$ ion. The rise in emission intensity of $Yb^{3+}$ ion was evidence of ET from $Nd^{3+} \rightarrow Yb^{3+}$ ion (Pudovkin et al. 2021). Faria et al., prepared $Nd^{3+}$-$Yb^{3+}$ co-doped

fluorophosphate [$BaF_2$-$SrF_2$- $Al(PO_3)_3$ -$AlF_3$ - $YF_3$] glass by melt-quench method to investigate temperature sensing through FIR technique, where emission spectra under 520 nm excitation peaked around 800 nm ($Nd^{3+}$), 870 nm ($Nd^{3+}$), and 975 nm ($Yb^{3+}$) at temperature ranging from 25-240 °C. The absorption spectrum was observed to be enhanced with the increase in $Yb^{3+}$ ion concentration in the 400-1100 nm range (Faria et al. 2021).

Muniz et al., prepared $Nd^{3+}$-$Yb^{3+}$ co-doped sodium calcium silicate glass by the melt quench method to report absorption spectra and UCL spectra under 808 and 975 nm excitation wavelengths. The power-dependent DCL spectra were also reported for the as-synthesized sample for a 590 nm excitation source in the 20-80 mW range (Muniz et al. 2023).

Table 1.5: List of literature available in $Nd^{3+}$-$Yb^{3+}$ ion co-doped in different host

| Host | Host (Structure) | Absorption spectra | DCL spectra $\lambda_{ex}$ (nm) | UCL spectra $\lambda_{ex}$ (nm) | Power (mW) | Temp-erature (K) | Ref |
|---|---|---|---|---|---|---|---|
| **Tellurite and germinate** | Glass | AVL | 575 | NA | NA | NA | (Reisfeld and Kalisky 1981) |
| **Lead meta-phosphate** | Glass (NA) | AVL | 808 | NA | NA | NA | (Liégard et al. 2005) |
| **Titania-silicate** | Thin film | NA | NA | 808 | NA | NA | (Battisha 2007) |
| **Yttrium-fluoride** | Powder | AVL | 354, 520 | NA | NA | NA | (Meijer et al. 2010) |
| **$LiNbO_3$** | Crystals | AVL | 808 | NA | NA | NA | (Sun et al. 2013) |
| **Yttrium-fluoride** | Phosphor (Orthorhombic) | NA | 355 | NA | NA | 80-300 | (Pudovkin et al. 2021) |
| **Fluoro-phosphate** | Glass | AVL | 520 | NA | NA | 298-513 | (Faria et al. 2021) |
| **Sodium-calcium-silicate** | Glass | AVL | 590 | 808, 975 | 20-80 | | (Muniz et al. 2023) |
| | | NA: Not Available | | AVL: Available | | | |

### 1.7.3. $Er^{3+}$ -$Yb^{3+}$ pair

The $Er^{3+}$ ion also has ladder-like energy levels that can absorb and emit light in the VIS-NIR region with metastable states [$^4F_{3/2}$ (ca. 20,500 $cm^{-1}$) and $^4I_{11/2}$ (~ 10,500 $cm^{-1}$)], which is approximately double and equal to the energy of the $Yb^{3+}$ ion respectively (Lluscà et al. 2014). The $Er^{3+}$ ion has photoemission with different metastable intermediate states with long lifetimes in the IR region ($^4I_{13/2} \rightarrow {}^4I_{15/2}$), the Red region ($^4F_{9/2} \rightarrow {}^4I_{15/2}$), and the Green region ($^2H_{11/2}$; $^4S_{3/2} \rightarrow {}^4I_{15/2}$). Here $Er^{3+}$ -$Yb^{3+}$ ion pair has been co-doped in different host material to obtain UCL and DCL spectra, as shown in Table 7.

Auzel was the first to demonstrate UCL spectra in the $Er^{3+}$ -$Yb^{3+}$ ion pair co-doped in a glass host (Auzel 1990). Battisha I. K., prepared $Yb^{3+}$-$Er^{3+}$ co-doped $SiO_2$–$TiO_2$ thin film nano-composite fabricated with a spin-coating sol-gel process to report UCL spectra, where distinct peaks were observed in the VIS region for the sample annealed at temperature higher than 350°C (Battisha 2007). Dwivedi et al., prepared $Er^{3+}$-$Yb^{3+}$ co-doped tellurite glass with the melt and quenched method to observe white light from NIR sensitization. The presence of $Yb^{3+}$ ion was evident from an intense NIR peak in the absorption spectra. UCL spectra have intense green and red anti-Stoke for NIR $Yb^{3+}$ ion excitation (Dwivedi et al. 2008). Goncalves et al., prepared $Yb^{3+}$-$Er^{3+}$ co-doped $SiO_2$–$TiO_2$ inverse opal structure fabricated by a dip-coating sol-gel process to report UCL spectra through $Er^{3+}$ ions ($^4I_{13/2} \rightarrow {}^4I_{15/2}$) for sensitization of $Yb^{3+}$ ion (Gonçalves et al. 2010). Mahata et al., prepared crystalline $Er^{3+}$-$Yb^{3+}$:$YVO_4$ micro-disc nano-phosphor by a wet-chemical route to report power and temperature-dependent UCL spectra. The thermally coupled states $^2H_{11/2}$ (973 μs) and $^4S_{3/2}$ (681 μs) of $Er^{3+}$ ion have been used for temperature sensing in the 302-520 K range (Mahata et al. 2014).

Sales et al., prepared $Yb^{3+}$-$Er^{3+}$:$BiNbO_4$ orthorhombic crystalline powder with a solid-state reaction process annealed at 850°C to report UCL spectra with prominent green ($^2H_{11/2}$; $^4S_{3/2} \rightarrow {}^4I_{15/2}$) and red ($^4F_{9/2} \rightarrow {}^4I_{15/2}$) transition of the $Er^{3+}$ ion upon 980nm excitation (Sales et al. 2016). Pellegrino et al., prepared $Yb^{3+}$, $Er^{3+}$:$CaF_2$ polycrystalline films on Si, quartz, and glass substrate with the MOCVD route on various substrates using a molten mixture to study UCL spectra with the green and red transitions for the $Er^{3+}$ ion upon 980 nm excitation (Pellegrino et al. 2017). Lojpur et al., prepared $Yb^{3+}$, $Er^{3+}$ ion co-doped $Y_2O_3$ polycrystalline nano-phosphor powder from a polymer complex solution to demonstrate power and concentration ($Yb^{3+}$ion) dependent UCL spectra upon 978 nm excitation (Lojpur, Ahrenkiel, and Dramićanin 2013).

Kaczmarek et al., prepared $Er^{3+}$-$Yb^{3+}$: $LaF_3$ nanoparticles to study possible temperature sensing applications with the help of DCL spectra with ET from $Er^{3+}$ ion to $Yb^{3+}$ ion (Anna M. Kaczmarek et al. 2018).

Table 1.6: List of literature available in $Er^{3+}$-$Yb^{3+}$ ion codoped in different host

| Host | Host | Absorption spectra | DCL spectra $\lambda_{ex}$ (nm) | UCL spectra $\lambda_{ex}$ (nm) | Power (mW) | Temp-erature (K) | Ref |
|---|---|---|---|---|---|---|---|
| **Titania-Silicate** | Thin film | NA | NA | 980 | NA | NA | (Battisha 2007) |
| **Tellurite** | Glass | NA | NA | 980 | 0-500 | NA | (Dwivedi et al. 2008) |
| **$SiO_2$–$TiO_2$** | inverse opal structure | NA | 514, 980 | NA | NA | NA | (Gonçalves et al. 2010) |
| **$Y_2O_3$** | Powder (Cubic-bixbyite) | NA | NA | 978 | 1-2 | NA | (Lojpur et al. 2013) |
| **$CaF_2$** | Si, quartz, and glass substrate | NA | NA | 980 | NA | NA | (Pellegrino et al. 2017) |
| **$LaF_3$** | Powder (NA) | NA | 375 | NA | NA | 15-105 | (Anna M. Kaczmarek et al. 2018) |
| **Yttrium orthovanadate($YVO_4$)** | Phosphor (Tetreagonal) | AVL | 316 | 980 | 2-150 | NA | (Mahata et al. 2014) |
| **$BiNbO_4$** | powder (Ortho-rhombic) | NA | NA | 980 | 100-900 | NA | (Sales et al. 2016) |
| NA: Not Available | | | | AVL: Available | | | |

### 1.7.4. *Zinc Silicate host*

$RE^{3+}$ ions doped in Zinc-Silicate ($ZnO\text{-}SiO_2$) host are tabulated with available structural and morphological data from selected published reports in Table 8. In the table, "$ZnO\text{-}SiO_2$: $RE^{3+}$ (x%)" represents that an x mol% concentration of $RE^{3+}$ ion is admixed in the Zinc and Silicate composite solution.

**Table 1.7: Progress in $RE^{3+}$ ion doping in $ZnO\text{-}SiO_2$ host through different sol-gel synthesis route**

| Dopent | Synthesis | product | XRD | FTIR | TEM | SEM | Ref. |
|---|---|---|---|---|---|---|---|
| **$Tb^{3+}$/ $Eu^{3+}$** | spin-coating | Thin film, xerogel | (■) | (●) | NA | NA | (Zhang, Pita, and Kam 2003) |
| **$Ce^{3+}$** | *ex-situ* sol-gel | powder | (■) | (●) | NA | NA | (Ntwaeaborwa and Holloway 2005) |
| **$Eu^{3+}$** | Sol-gel | Powder | NA | (●) | NA | NA | (Bang et al. 2005) |
| **$Eu^{3+}$** | *in-situ* sol-gel | Glass | NA | NA | NA | NA | (Yu and Nogami 2007) |
| **$Eu^{3+}$** | Sol-gel | Thin film | (■) | NA | ZnO NPs (4-8 nm) | NA | (Lin et al. 2012) |
| **$Tb^{3+}$-$Yb^{3+}$** | Sol-gel | Thin film | (■) | (●) | NA | NA | (Huang and Zhang 2009) |
| **$Yb^{3+}$ / Li** | Facile sol-gel | Glass | NA | NA | (●) | NA | (Xiao et al. 2011) |
| **$Er^{3+}$/$Li^{3+}$** | Facile Sol-gel | Glass | NA | NA | (●) | NA | (Xiao et al. 2012) |
| **$Er^{3+}$-$Al^{2+}$** | Melt quench | Glass | (■) | | (●) | NA | (Ghaemi et al. 2012) |
| **$Ce^{3+}$** | Ex-situ sol-gel, Supercritical | Monolithic aerogel | (■) | NA | NA | NA | (Chelouche, Djouadi, and Aksas 2014) |
| **$Eu^{3+}$** | *in-situ* sol-gel | Thin film | (■) | NA | NA | ZnO NPs | (Tung et al. 2016) |
| **$Eu^{3+}$** | *in-situ* | Glass | (×) | (●) | (●) | NA | (Tran et al. 2017) |
| **$Eu^{3+}$** | Melt-quenched | Glass | (×) | (●) | | (●) | (Khaidir et al. 2019) |

| | | | | | | | |
|---|---|---|---|---|---|---|---|
| **$Er^{3+}$** | *ex-situ* | Thin film | (■) | NA | NA | (■) | (Hien et al. 2019) |
| **Data: Available (●): (x) non crystalline (■) crystalline** | | | | | | | Not available (NA) |

Zhang et al., prepared crystalline thin films on $SiO_2$/Si substrate through spin-coating a transparent $Tb^{3+}$/$Eu^{3+}$ ion-doped ZnO-$SiO_2$ sol-gel solution. The green and red emission peaks for UV exposure ($\lambda_{ex}$=230nm) were reported for thin films (Zhang et al. 2003). In the DTA curve, the second exothermic peaks of the xerogel sample confirmed the formation of ZnO crystallite in the amorphous Silica host, while decomposition of water and combustion of organic components were signified with solo endothermic peaks and first endothermic peak, respectively.

Ntwaeaborwa & Holloway prepared powders from $Ce^{3+}$ ion-doped ZnO-$SiO_2$ *ex-situ* sol-gel solution. PL spectra of the $Ce^{3+}$ ion were observed in the blue region after suppressing the green emission of ZnO NPs (Ntwaeaborwa and Holloway 2005). Bang et al. also prepared $Eu^{3+}$ ion-doped ZnO-$SiO_2$ powder, as mentioned elsewhere (Ntwaeaborwa and Holloway 2005). Emission of green light from ZnO NPs was entirely suppressed when embedded in $SiO_2$ doped with $Eu^{3+}$. The enhanced $Eu^{3+}$ luminescence was reported with energy transfer (ET) from the embedded ZnO NPs and the rise in $Eu^{3+}$ concentration (Bang et al. 2005). Yu and Nogami prepared glass from a $Eu^{3+}$ ion-doped *in-situ* sol-gel ZnO-$SiO_2$ solution-derived xerogel. The enhanced intensity for the emission spectra of $Eu^{3+}$ ion was evident with the increase of ZnO concentration due to the variation of the local environment around dopant ions (Yu and Nogami 2007).

Lin T. et al., prepared $Eu^{3+}$ ion-doped in-situ ZnO-$SiO_2$ solution with varied Zn and fixed $Eu^{3+}$ ion concentration to report concentration and annealing temperature dependence on the luminescence of $Eu^{3+}$ ion. TEM monograph was confirming the presence of ZnO NPs in amorphous $SiO_2$ host (Lin et al. 2012)**.** Huang and Zhang prepared $Tb^{3+}$/$Yb^{3+}$ ion-doped ZnO-$SiO_2$ transparent sol-gel solution to prepare crystalline thin film on $SiO_2$/Si and quartz substrate of thickness 0.4-0.5 μm and average grain size 70nm (Huang and Zhang 2009). DCL spectra through transferring energy to $Yb^{3+}$ ion from $Tb^{3+}$ ion was reported for UV photon excitation where the confirmation of ET was evident from the decrease in decay time from 2.98 ms to 1.91 ms for the $^5D_4 \rightarrow {}^7F_5$ transition of $Tb^{3+}$ ion. TG/DTA curve of the xerogel sample was observed to be consistent for ZnO-$SiO_2$ host irrespective of $RE^{3+}$ ion concentration (Huang and Zhang 2009).

Xiao et al., prepared $Yb^{3+}$ ion-doped ZnO-$SiO_2$ transparent solution where ethanolamine-stabilized ZnO and acid-catalyzed Si-alkoxides for hydrolysis and condensation (Xiao et al. 2011). The PL intensity enhancement (for a peak around 980 nm) was also reported with the rise in $Yb^{3+}$ion concentration for the excitation of UV light (Xiao et al. 2011). The presence of homogeneously distributed ZnO QDs was observed in the silica host matrix from HRTEM image which is highly crystalline with size around 2 to 6 nm with lattice fringes due to appropriate thermal treatment for ZnO crystallization. The SAED pattern, with diffraction rings, were confirming the growth of wurtzite ZnO (Xiao et al. 2011). A schematic diagram of Energy Transfer from ZnO QD in silica host to $Yb^{3+}$ ion was cited (Xiao et al. 2011).

Xiao et al., prepared $Er^{3+}$/$Li^{3+}$ ion-doped ZnO-$SiO_2$ sol-gel transparent solution to prepare bulk composites. Ethanolamine was used to stabilize ZnO solution before admixing it with the acid-catalyzed TEOS solution to complete the hydrolysis and condensation process. PL spectra were optimized at 5 mol% of $Li^{+}$ doping. An SEM image asserted the formation of ZnO QD, which may be the possible reason for enhanced PL intensity through ET from ZnO QD to $RE^{3+}$ ion (Xiao et al. 2012). Ghaemi et al. prepared $Er_2O_3$-doped zinc-alumino-silicate glasses with the melt-quench method. PL spectra with broad emission peaks at 1.54 μm were reported for both the quenched and heat-treated samples (600 & 800 °C) under 518 and 650 nm excitations (Ghaemi et al. 2012).

Chelouche et al. prepared $SiO_2$-ZnO: $Ce^{3+}$nanocomposite by the sol-gel synthesis method from an ex-situ mixture of separately prepared ZnO: $Ce^{3+}$ aerogel powder (crystallite size ca. 78 nm) and TEOS solution to complete hydrolysis and condensation before being annealed at 1200 °C (Chelouche et al. 2014). Ali et al., prepared a ZnO-$SiO_2$ thin film on the silicon substrate (100) from an in-situ solution which turn into a polycrystalline of hexagonal wurtzite ZnO at various annealing temperatures. No $RE^{3+}$ ion were doped in this sample (Mossad Ali et al. 2014).

Tung et al., prepared a thin film on Si substrate from a sol-gel solution where $Eu^{3+}$ ion was doped in ZnO-$SiO_2$ solution. The Zn and $Eu^{3+}$ ion precursor were admixed to the acid-catalyzed silica precursor to modify the surrounding of $Er^{3+}$ion. PL spectra of $Eu^{3+}$ ion were observed to be dependent on three parameters, such as ZnO to $SiO_2$ mol ratio, annealing temperature, and the concentration of $Er^{3+}$ ions. Luminescence of $Eu^{3+}$ was optimized for 1.25 mol% sample annealed at 900 °C, where the hexagonal ZnO structure was observed in the $Eu^{3+}$ ion neighborhood, as in HRTEM image of 0.28 nm crystalline spacing (Tung et al. 2016).

Tran et al., prepared ZnO-$SiO_2$: $Eu^{3+}$ crack-free amorphous transparent *in-situ* sol-gel monolithic glass at 600 °C annealing temperature. The PLE ($\lambda_{em}$= 615nm) and PL ($\lambda_{ex}$ = 394nm and 325nm) spectra were cited for the prepared sample, where an enhancement in the luminescent intensity of $Eu^{3+}$ ions was observed due to the existence $Eu^{3+}$ ions in the neighborhood of ZnO NPs. TEM monographs confirmed the presence of ZnO NPs in the amorphous silica host (Tran et al. 2017).

Khaidir R. et al., reported ZnO-$SiO_2$:$Eu^{3+}$ amorphous glasses prepared with the melt and quench method from recycling renewable sources of waste rice husk, where a shift was observed in the absorption edges towards higher wavelength. The optical band gap enlargement (2.97-4.23 eV) was reported with the formation of larger crystallites in the glass structure (Khaidir et al. 2019). Hien et al., prepared ZnO-$SiO_2$:$Er^{3+}$ (0.3 M) crystalline thin film on a Si substrate with a thickness of approximately 3.3 μm through an *ex-situ* sol-gel process where TEA stabilized ZnO solution was mixed with acid-catalyzed silica precursor to modify the surrounding of $Er^{3+}$ ions. This modification helped in intensifying the emission of $Er^{3+}$ ions in ZnO-$SiO_2$host. PL spectra of the thin film were reported for 325 nm excitation at different annealing temperature and ZnO concentration, where optimization was reported for thin film annealing at 900 °C and 5 mol% ZnO concentrations. The FESEM monograph was observed as crystalline with confirmation of all doping elements in the thin film with a thickness of 3.32 μm (Hien et al. 2019).

### *1.7.5. Titania Silicate host*

$RE^{3+}$ ions doped in titania-silicate ($TiO_2$-$SiO_2$) hosts are tabulated with available structural and morphological data from selective published reports (Table 9). In the table, "$SiO_2$-$TiO_2$: $RE^{3+}$ (x%)" represents that a concentration of x mol% of $RE^{3+}$ ion is added to the Titania and Silicate composite solution.

**Table 1.8: Progress in $RE^{3+}$ ion doping in$TiO_2$-$SiO_2$ host through sol-gel route**

| Dopants | Synthesis | Product | XRD | FTIR | TEM | SEM | Ref. |
|---|---|---|---|---|---|---|---|
| **$Er^{3+}$** | Sol-gel | Thin film/ powder | (■) | NA | NA | NA | (Strohhofer et al. 1998) |
| **$Tb^{3+}$** | Sol-gel | Thin film | NA | NA | NA | NA | (Jenouvrier et al. 2001) |

| | | | | | | | |
|---|---|---|---|---|---|---|---|
| **$Er^{3+}$** | Sol-gel | Powder | NA | NA | NA | NA | (Castan˜eda-Contreras et al. 2006) |
| **$Tb^{3+}$** | Sol-gel | Glass | (■) | NA | NA | NA | (Ismail et al. 2007) |
| **$Eu^{3+}$** | Spin-coating | Thin film | NA | (●) | NA | NA | (Zareba-Grodz et al. 2007) |
| **$Er^{3+}$-$Yb^{3+}$/ $Nd^{3+}$-$Yb^{3+}$** | Spin-coating | Thin film | (■) | (●) | NA | NA | (Battisha 2007) |
| **$La^{3+}$/$Nd^{3+}$/$Sm^{3+}$/$Gd^{3+}$** | Sol-gel | Powder | (■) | NA | NA | NA | (Mohamed and Mkhalid 2010) |
| **$Nd^{3+}$** | Sol-gel | Glass | (x) | (●) | NA | (●) | (Dihingia and Rai 2012) |
| **$Eu^{3+}$/ $Sm^{3+}$** | Sol-gel | powder | (■) | (●) | NA | NA | (Azzouz and Klein 2012) |
| **$Eu^{3+}$** | Dip-coating | Thin film | NA | NA | NA | NA | (Berkani et al. 2012) |
| **$Ho^{3+}$** | Sol-gel | Glass | NA | NA | NA | NA | (Rai and Fanai 2014) |
| **$Er^{3+}$/$Yb^{3+}$** | Sol-Gel | Thin film | (■) | (●) | NA | (●) | (Xiaoqi et al. 2014) |
| **$Eu^{3+}$,$Sm^{3+}$** | Solvo-thermal/Sol-gel | Core-shell | (■) | (●) | NA | (●) | (Chang et al. 2018) |
| **$Er^{3+}$/$Yb^{3+}$-$Eu^{3+}$** | Sol-gel | Xerogel, Powder | NA | NA | NA | NA | (Buarque et al. 2018) |
| **$Eu^{3+}$/$Tb^{3+}$** | Stober/ Hydro-thermal | Core-shell | (■) | (●) | NA | (●) | (Wang et al. 2019) |
| **Data: Available (●) : (x) non crystalline (■) crystalline** | | | | | | | Not available (NA) |

Strohhöfer et al., prepared $Er^{3+}$ion-doped $SiO_2$-$TiO_2$ *ex-situ* sol-gel solution to spin-coat a crystalline thin film annealed at 1000 °C on single-crystal Si-wafers although no luminescence spectra were reported for this combination (Strohhofer et al. 1998). Jenourier et al., prepared $Tb^{3+}$ ion-doped $SiO_2$-$TiO_2$ sol-gel solution as a thin film with and without organic complexes (e.g. sulphosalicylic acid) to report PL spectra where enhancement was observed in the sample with organic complexation (Jenouvrier et al. 2001).

Castañujhneda-Contreras J. et al., prepared luminescent powder annealed at 500 °C from $Er^{3+}$ion-doped $TiO_2$–$SiO_2$ sol-gel solution to report visible UCL spectra with excitation at 979 and 1532 nm. The optimized visible UCL spectra were observed for 2 mol% $Er^{3+}$ ion doping. The structural and morphological studies of these sample were not reported (Castan˜eda-Contreras et al. 2006). Ismail et al., prepared binary glass from $Tb^{3+}$ ion-doped $TiO_2$–$SiO_2$ sol-gel solution to report annealing temperature dependence on PL spectra and the PLE spectra ($\lambda_{emi}$=541nm). The PL intensity for an excitation wavelength ($\lambda_{exc}$) of 325 nm was lowered at a higher annealing temperature. The binary dense glass had anatase phase of $TiO_2$ when annealed at 1000 °C, which was not true for a similar sample annealed at 550 °C (Ismail et al. 2007).

Zaręba-Grodź et al., prepared thin films on quartz glass from $Eu^{3+}$ ion-doped $SiO_2$–$TiO_2$ sol-gel solution to report a decrease in lifetimes of $Eu^{3+}$ ions from 780 μs to 220 μs with a rise in annealing temperature (600–900 °C), which was possibly initiated by agglomeration of $Eu^{3+}$ ions (Zareba-Grodz et al. 2007). Battisha prepared thin films on Si substrate through spin coating two different ex-situ silica-titania sol-gel solutions where $Er^{3+}$ /$Yb^{3+}$ and $Nd^{3+}$ /$Yb^{3+}$ ions are co-doped separately. UCL spectra of these two samples were reported in VIS region for NIR (980 nm and 808 nm) excitation. UCL spectra for thin film annealed at 900 °C were the most intense, which can be related to the formation of smaller size (15 nm) of titania crystallites at the highest annealing temperature with broadening of most intense XRD peak (Battisha 2007).

Mohamed & Mkhalid prepared dense glass through annealing $La^{3+}$/$Nd^{3+}$/$Sm^{3+}$/$Gd^{3+}$ doped sol-gel $TiO_2$–$SiO_2$ xerogel samples at 550 °C to report the effect of $RE^{3+}$ ion doping on the photoactivity of EDTA. The anatase phase of $TiO_2$ in amorphous silica was confirmed from XRD patterns, which was also emphasized in TEM monograph (Mohamed and Mkhalid 2010).

Dihingia and Rai prepared $Nd^{3+}$ion-doped $TiO_2$–$SiO_2$ sol-gel solution to dip-coat as amorphous thin film with no crack where UC and DC spectra of $Nd^{3+}$ ion are reported for different excitation wavelength. FTIR spectra were reported with Ti-O-Si bond in xerogel stage. SEM monographs also showed thin film with no cracks. TG and DTA thermograms of the xerogel sample are interesting where an endothermic peak at 89 °C was indicating the desorption of physically adsorbed water and residual solvents. The exothermic peaks at 129 °C and 211 °C were accredited to the decomposition of residual alkyl groups and near complete combustion or carbonization of organic compounds such as alkyl groups remaining in the solid, respectively. The exothermic peak at 275 °C was observed, due to the carbonization of remaining organic

residues (Dihingia and Rai 2012). Total polymerization with no unreacted organic groups was indicated by the absence of exothermic peak beyond 275 °C. The weight loss occurred in two steps as in the TG curve where the initial loss was owed to the evaporation of a small quantity of adsorbed water and the volatilization and thermal decomposition of the remnant organic solvents; along with the carbonization or the combustion of organic compounds responsible for the second part of weight loss (Dihingia and Rai 2012).

Azzouz and Klein prepared $Eu^{3+}$ and $Sm^{3+}$ ion codoped crystalline $SiO_2$-$TiO_2$ monolithic glass and powder samples with the sol-gel method to report UCL spectra for different excitation wavelengths in the visible region. The XRD results confirmed the growth of crystalline ZnO in the amorphous silica host. The formation of Ti-O-Si bonds was indicated because of the insertion of Ti into Si glass host as in FTIR spectra (Azzouz and Klein 2012). Berkani et al. prepared with $Eu^{3+}$ ion-doped Titania-Silicate sol-gel solution to prepare thin films on Si substrate. PL emission spectra of the sample were reported under laser excitation at 351 nm for sample annealed at different temperatures (Berkani et al. 2012). Rai and Fanai prepared $Ho^{3+}$ ion-doped in silica-titania monolithic glass from annealing xerogel at 500 °C through the sol-gel technique. Different radiative parameters were calculated using J-O parameters of $Ho^{3+}$ ion. PL intensity enhancement of $Ho^{3+}$ ion was reported with rise in Ti concentration at 370 nm excitation (Rai and Fanai 2014).

Xiaoqi et al., prepared $Er^{3+}/Yb^{3+}$ ion-codoped in $SiO_2$-$TiO_2$ sol-gel solution to spin-coat thin films on glass substrate. The visible UCL spectra of $Er^{3+}/Yb^{3+}$ ion pair were reported for NIR laser excitation ($\lambda_{exc}$ ~980nm). FTIR spectra confirmed insertion of Si into Ti host along with the crystallization of the sample. The grain size of the sample was visible from the SEM monograph of $Er^{3+}$–$Yb^{3+}$ co-doped $SiO_2$-$TiO_2$ thin film (Xiaoqi et al. 2014). Chang et al. prepared a multifunctional yolk-shell core-shell $SiO_2@TiO_2$: $Eu^{3+}/Sm^{3+}$ by a surfactant-free solvothermal method to report PL spectra and decay times. The SEM and TEM monographs were observed as spherical nanoparticles of $SiO_2@TiO_2$: $Eu^{3+}/Sm^{3+}$ NPs which were separated from each other (Chang et al. 2018).

Chang et al. prepared $SiO_2@TiO_2$: $Sm^{3+}$ hybrid material through a combination of Stöber sol-gel and solvothermal method to report a material with photocatalytic and luminescence properties (Chang et al. 2019). Buarque et al., prepared $Er^{3+}/Yb^{3+}/Eu^{3+}$ codoped Silica-Titania powder from annealing xerogel up to 700-1000 °C to report UCL and DCL spectra with varying

irradiation from 100 to 4000 mW. UCL spectra of the sample annealed at 800 °C were optimized for 980 nm excitation wavelength at 2400mW (Buarque et al. 2018). Wang et al. prepared a hollow $TiO_2$:$Eu^{3+}$ shell on $SiO_2$: $Tb^{3+}$ nanospheres by Stöber sol-gel method to report color tunability of the sample from green to red with variation of doping concentration of $RE^{3+}$ ions (Wang et al. 2019).

## 1.8. SCOPE OF STUDY

The scope to study UCL and DCL spectra of $Pr^{3+}$-$Yb^{3+}$ ion/ $Nd^{3+}$-$Yb^{3+}$ ion is identified. The $TiO_2$-$SiO_2$ and ZnO-$SiO_2$ binary composite hosts can be synthesized using a modified ex-situ sol gel method for uniform distribution of $RE^{3+}$ ion.

### 1.8.1. $Pr^{3+}$-$Yb^{3+}$ ion pair co-doping in $TiO_2$-$SiO_2$ binary composite

UCL and DCL spectra of the $Pr^{3+}$-$Yb^{3+}$ ion pair are reported in $GdAl_3(BO_3)_4$ phosphor (Zhang and Yang 2007), Yttrium oxyfluoride phosphor (Saeed et al. 2020), $CaYAlO_4$ (CYA) host (Wen and Tanner 2011), $GdF_3$ & $YF_3$ host (Nizamutdinov et al. 2019), Tellurite glass (Dwivedi et al. 2008), $KY_3F_{10}$ glass (Wen and Tanner 2011), $Li_2O$–$ZrO_2$–$SiO_2$ glass (Srinivasa Rao et al. 2011), Lead borate ($PbO$–$B_2O_3$) glass (Wen and Tanner 2011), Lanthanum Aluminum silicate (SAL) glasses (Liang et al. 2020).

However, UCL and DCL spectra of the $Pr^{3+}$-$Yb^{3+}$ ion pair co-doped $TiO_2$-$SiO_2$ composite host (dense glass, phosphor and thin film) have yet to be observed. The luminescence of $Pr^{3+}$-$Yb^{3+}$ ion depends on various properties of the host, such as the synthesis route, symmetry of the host, phonon energy etc. The $TiO_2$-$SiO_2$ composite host has been used for $RE^{3+}$ ion doping, and there is a scope to prepare a host with lower phonon energy using a modified *ex-situ* sol-gel synthesis route of $TiO_2$-$SiO_2$ composite. This synthesis route is mentioned in the preparation of monolayer ARC with $TiO_2$-$SiO_2$ composite by Wang et al., (X. Wang et al. 2013). The co-doping of the $Pr^{3+}$-$Yb^{3+}$ ion pair in $TiO_2$-$SiO_2$ composite is a first time occurrence to our knowledge. The $Pr^{3+}$ ion concentration is fixed to observe optimized luminescence concentration of the $Yb^{3+}$ ion, which has been observed in other host but not $TiO_2$-$SiO_2$ composite. The

excitation power of laser is also a parameter to observe variation in UCL and DCL spectra of the $Pr^{3+}$-$Yb^{3+}$ ion, which has also been observed in other hosts but not in $TiO_2$-$SiO_2$ composite.

### 1.8.2. $Nd^{3+}$-$Yb^{3+}$ ion pair co-doped in ZnO-$SiO_2$ composite

UCL and DCL spectra of $Nd^{3+}$-$Yb^{3+}$ ion pair co-doped pair are reported in Tellurite and Germinate glass (Reisfeld and Kalisky 1981), Lead metaphosphate [$Pb(PO_3)_2$] glass (Liégard et al. 2005), $SiO_2$–$TiO_2$ thin film (Battisha 2007), Yttrium fluoride ($YF_3$) crystalline powder phosphor (Meijer et al. 2010), $LiNbO_3$ crystals (Sun et al. 2013), $YF_3$ phosphor (Pudovkin et al. 2021), fluorophosphate [$BaF_2$-$SrF_2$- $Al(PO_3)_3$ -$AlF_3$ - $YF_3$] glass (Faria et al. 2021).

This ion pair has not yet been co-doped in a ZnO-$SiO_2$ composite host (dense glass, phosphor and thin film). The ZnO-$SiO_2$ composite host has been used for $RE^{3+}$ ion doping. Our main objective is to prepare a host with lower phonon energy by tuning synthesis route of ZnO-$SiO_2$ composite. Hien et al. (Hien et al. 2019) reported an *ex-situ* sol gel synthesis method to prepare $Er^{3+}$ ion doped ZnO-$SiO_2$ crystalline thin film on a Si substrate, and a similar to this synthesis method is adopted for the first time for $Nd^{3+}$-$Yb^{3+}$ ion pair co-doping. The *ex-situ* sol-gel synthesis method is further modified by adding equimolar water to methanol-dissolved silica precursor for the pre-hydrolysis of TEOS with the formation of silicic acid. The stabilizer (MEA) is admixed with Zn precursor to promote ZnO NPs formation. This pre-hydrolysis of $SiO_2$ initiates Zn-O-Si non-bridging oxygen to promote asymmetry in the ZnO-$SiO_2$ composite, as the hydrolysis rate of ZnO is much higher than $SiO_2$. Thus co-doping of $Nd^{3+}$-$Yb^{3+}$ ion pair in the ZnO-$SiO_2$ composite is a first time occurrence to our knowledge. The $Nd^{3+}$ ion concentration will be fixed to observe the optimized luminescence concentration of the $Yb^{3+}$ ion, which has been observed in other host but not in the ZnO-$SiO_2$ composite. The excitation power of the laser is also a parameter to observe variations in UCL and DCL spectra of the $Nd^{3+}$-$Yb^{3+}$ ion, which has also been observed in other hosts but not in the ZnO-$SiO_2$ composite.

## 1.9. CONCLUSION

In summary, this study presents the synthesis and characterization of four novel luminescent materials intended for potential future photonic applications, as elaborated in subsequent chapters. Initially, we utilize SAMPLE I ($Pr^{3+}$-$Yb^{3+}$ ion pair co-doped Titania-Silicate) and

SAMPLE II ($Nd^{3+}$-$Yb^{3+}$ ion pair co-doped Zinc-silicate) solutions as starting materials to fabricate thin film, phosphors, and monolithic glass materials employing a modified *ex-situ* sol-gel synthesis approach. We investigate the UCL and DCL spectra of these materials across varying $Yb^{3+}$ ion concentration while maintaining fixed $Nd^{3+}$ or $Pr^{3+}$ ion concentrations, exploring the optimization of these spectra. The thermal characterizations of samples are observed with TG and DSC to understand thermal stability.

Furthermore, we delve into SAMPLE III ($Pr^{3+}$-$Er^{3+}$ ion pair codoped in Titania-Silicate host) and SAMPLE IV ($Nd^{3+}$-$Er^{3+}$ ions pairs codoped in Zinc-Silicate host) to further investigate the modification of optical properties. We conduct structural characterizations of these samples using FTIR spectroscopy and XRD analysis, while morphological characterizations of these samples are performed with FESEM and FETEM monographs. The chapterization of the research work is presented as follows:

***Chapter 2*** provides a summary of the sol-gel synthesis method and various characterization techniques used in this study.

***Chapter 3*** presents the results of the structural, morphological, thermal and optical characterizations of SAMPLE I ($Pr^{3+}$-$Yb^{3+}$ ion pair co-doped Titania-Silicate) dense glass ceramic and thin film.

***Chapter 4*** presents the results of the structural, morphological, thermal and optical characterizations of SAMPLE II ($Nd^{3+}$-$Yb^{3+}$ ion pair co-doped Zinc-Silicate) dense glass ceramic and thin film.

***Chapter 5*** presents the synthesis of SAMPLE III ($Pr^{3+}$/$Er^{3+}$ ion pair co-doped Titania-Silicate and SAMPLE IV ($Nd^{3+}$/$Er^{3+}$ ion pair co-doped Zinc-Silicate) Dense Glass Ceramic for IR luminescent application materials, where the structural, morphological and optical characterization were performed.

***Chapter 6*** provides concluding remarks on the overall study and suggestions for possible future studies.

**REFERENCE:**


Ahrens, Bernd. 2009. “Down-and Up-Conversion in Fluorozirconate-Based Glasses and Glass Ceramics for Photovoltaic Application.” PADERBORN.

Amin, Peshawa O., Asmaa J. Kadhim, Majida A. Ameen, and Rebar T. Abdulwahid. 2018. “Structural and Optical Properties of Thermally Annealed TiO2–SiO2 Binary Thin Films Synthesized by Sol–Gel Method.” *Journal of Materials Science: Materials in Electronics* 29(18):16010–20. doi: 10.1007/s10854-018-9688-6.

Anna M. Kaczmarek, Mariusz K. Kaczmarek, and Rik Van Deuna. 2018. “Er3+-to-Yb3+ and Pr3+-to-Yb3+ Energy Transfer for Highly Efficient near-Infrared Cryogenic Optical Temperature Sensing.” *Nanoscale* 11(3):1–3. doi: 10.1039/C8NR08348G.

Auzel, F. 1990. “Upconversion Processes in Coupled Ion Systems.” *Journal of Luminescence* 45(1–6):341–45. doi: 10.1016/0022-2313(90)90189-I.

Azzouz, I. M., and Lisa C. Klein. 2012. “Red , Violet and Upconversion Luminescence of Eu / Sm Codoped Sol Gel SiO 2 – TiO 2.” *Optical Materials* 35:292–96. doi: 10.1016/j.optmat.2012.09.006.

Bang, Jungsik, Heesun Yang, and Paul H. Holloway. 2005. “Enhanced Luminescence of SiO 2 : Eu 3 + by Energy Transfer from ZnO Nanoparticles.” *The Journal of Chemical Physics* 123(May 2013):1–4. doi: 10.1063/1.2007647.

Battisha, I. K. 2007. “Visible Up-Conversion Photoluminescence from IR Diode-Pumped SiO2-TiO2 Nano-Composite Films Heavily Doped with Er3+-Yb3+ and Nd3+-Yb3+.” *Journal of Non-Crystalline Solids* 353(18–21):1748–54. doi: 10.1016/j.jnoncrysol.2007.01.043.

Berkani, Oualid, Khelil Latrous, Hicham El, Bruno Capoen, and Mohamed Bouazaoui. 2012. “Effects of Heat Treatment and TiO 2 Content on the Optical Properties of Eu 3 þ Doped TiO 2 – SiO 2 Thin Films.” *Journal of Luminescence* 132:2979–83. doi: 10.1016/j.jlumin.2012.06.019.

Binnemans, Koen. 2009. “Lanthanide-Based Luminescent Hybrid Materials.” *Chemical Review* 109:4283–4374.

Binnemans, Koen. 2015. “Interpretation of Europium ( III ) Spectra.” *Coordination Chemistry Reviews* 295:1–45. doi: 10.1016/j.ccr.2015.02.015.

Brik, Mikhail G., Ž. M. Anti, Katarina Vukovi, and Miroslav D. Drami. 2015. “Judd - Ofelt Analysis of Eu 3 + Emission in TiO 2 Anatase Nanoparticles.” *Materials Transactions* 56(9):1416–18.

Buarque, Juliana M. M., Danilo Manzani, Sérgio Luis Scarpari, Marcelo Nalin, Sidney J. L. Ribeiro, Jennifer Esbenshade, Marco A. Schiavon, and Jefferson L. Ferrari. 2018. “SiO2-TiO2 Doped with Er3+/Yb3+/Eu3+ Photoluminescent Material: A Spectroscopy and Structural Study about Potential Application for Improvement of the Efficiency on Solar Cells.” *Materials Research Bulletin* 107:295–307. doi: 10.1016/j.materresbull.2018.07.007.

Carnall, W. T.; Crosswhite, H.; Crosswhite, H. M. 1977. *Energy Level Structure and Transition Probabilitiesof the Trivalent Lanthanides in LaF3*. Argonne (USA): Rep. Argonne National Laboratory.

Carnall, W. T., P. R. Fields, and K. Rajnak. 1968. "Electronic Energy Levels in the Trivalent Lanthanide Aquo Ions. I. Pr3+, Nd3+, Pm3+, Sm3+, Dy3+, Ho3+, Er3+, and Tm3+." *The Journal of Chemical Physics* 49:4424–42. doi: 10.1063/1.1669893.

Carnall, W. T., G. L. Goodman, K. Rajnak, and R. S. Rana. 1989. "A Systematic Analysis of the Spectra of the Lanthanides Doped into Single Crystal LaF3." *The Journal of Chemical Physics* 90(7):3443–57. doi: 10.1063/1.455853.

Castan˜eda-Contreras, J., M. A. Meneses-Nava, O. Barbosa-Garcı´a, R. A. Rodrı´guez-Rojas, and M. V. Fe´lix. 2006. "Visible Erbium Luminescence in SiO2 – TiO2 – Er3+ Sol – Gel Powders." *Optical Materials* 29:38–42. doi: 10.1016/j.optmat.2006.03.005.

Chang, Meiqi, Yanhua Song, Lei Cui Jie Chen, Zhan Shi, Ye Sheng, and Haifeng Zou. 2018. "Photocatalytic and Photoluminescence Properties of Core- Shell SiO2@TiO2:Eu3+,Sm3+ and Its Etching Products." *ACS Sustainable Chemistry & Engineering* 6(1):223–36. doi: 10.1021/acssuschemeng.7b02285.

Chang, Meiqi, Yanhua Song, Ye Sheng, Jie Chen, and Haifeng Zou. 2017. "Understanding the Remarkable Luminescence Enhancement: Via SiO2 Coating on TiO2:Eu3+ Nanofibers." *Physical Chemistry Chemical Physics* 19(26):17063–74. doi: 10.1039/c7cp01113j.

Chang, Meiqi, Haifeng Zou, Yanhua Song, Jie Chen, Lei Cui, Ye Sheng, and Keyan Zheng. 2019. "Photoluminescence and Photodegradation Properties of SiO2@TiO2:Sm3+ with Different Coating Effects." *Journal of Physics and Chemistry of Solids* 124:100–110. doi: 10.1016/j.jpcs.2018.09.010.

Chelouche, A., D. Djouadi, and A. Aksas. 2014. "Structural Characterization of SiO 2 / Zn 2 SiO 4 : Ce Nanocomposite Obtained by Sol Gel Method." *Journal of the Association of Arab Universities for Basic and Applied Sciences* 15:10–14. doi: 10.1016/j.jaubas.2013.05.002.

Chen, X. P., X. Y. Huang, and Q. Y. Zhang. 2009. "Concentration-Dependent near-Infrared Quantum Cutting in NaYF4: Pr3+, Yb3+phosphor." *Journal of Applied Physics* 106(6):3–7. doi: 10.1063/1.3224906.

Dibaba, Solomon Tiruneh, Xiaoqian Ge, Wei Ren, and Lining Sun. 2019. "Recent Progress of Energy Transfer and Luminescence Intensity Boosting Mechanism in Nd3+-Sensitized Upconversion Nanoparticles." *Journal of Rare Earths* 37(8):791–805. doi: 10.1016/j.jre.2019.02.001.

Dieudonné, B., B. Boulard, G. Alombert-Goget, A. Chiasera, Y. Gao, S. Kodjikian, and M. Ferrari. 2013. "Up- and down-Conversion in Yb3+-Pr3+ Co-Doped Fluoride Glasses and Glass Ceramics." *Journal of Non-Crystalline Solids* 377:105–9. doi: 10.1016/j.jnoncrysol.2012.12.025.

Dihingia, P. J., and S. Rai. 2012. "Synthesis of TiO 2 Nanoparticles and Spectroscopic

Upconversion Luminescence of Nd 3+-Doped TiO 2-SiO 2 Composite Glass." *Journal of Luminescence* 132(5):1243–51. doi: 10.1016/j.jlumin.2011.12.008.

Dwivedi, Y., Anita Rai, and S. B. Rai. 2008. "Intense White Upconversion Emission in Pr / Er / Yb Codoped Tellurite Glass." *Journal of Applied Physics* 104(043509):1–4. doi: 10.1063/1.2969046.

Van Der Ende, Bryan M., Linda Aarts, and Andries Meijerink. 2009. "Lanthanide Ions as Spectral Converters for Solar Cells." *Physical Chemistry Chemical Physics* 11(47):11081–95. doi: 10.1039/b913877c.

Eriksen, Emil H., Soren P. Madsen, Brian Julsgaard, Clarissa L. M. Hofmann, Jan Christoph Goldschmidt, and Peter Balling. 2019. "Enhanced Upconversion via Plasmonic Near-Field Effects: Role of the Particle Shape." *Journal of Optics (United Kingdom)* 21(3). doi: 10.1088/2040-8986/ab0272.

Escudero, Alberto, Ana I. Becerro, Carolina Carrillo-Carrión, Nuria O. Núñez, Mikhail V. Zyuzin, Mariano Laguna, Daniel González-Mancebo, Manuel Ocanã, and Wolfgang J. Parak. 2017. "Rare Earth Based Nanostructured Materials: Synthesis, Functionalization, Properties and Bioimaging and Biosensing Applications." *Nanophotonics* 6(5):881–921. doi: 10.1515/nanoph-2017-0007.

Faria, W. J., T. S. Gonçalves, and Andrea S. S. De Camargo. 2021. "Near Infrared Optical Thermometry in Fluorophosphate Glasses Doped with Nd3+ and Nd3+/Yb3+." *Journal of Alloys and Compounds* 883:160849. doi: 10.1016/j.jallcom.2021.160849.

Fischer, S., J. C. Goldschmidt, P. Löper, G. H. Bauer, R. Brüggemann, K. Krämer, D. Biner, M. Hermle, and S. W. Glunz. 2010. "Enhancement of Silicon Solar Cell Efficiency by Upconversion: Optical and Electrical Characterization." *Journal of Applied Physics* 108(4):1–11. doi: 10.1063/1.3478742.

Ghaemi, Bahram, Gaoling Zhao, Shengchen Huang, Jianxun Wang, and Gaorong Han. 2012. "Structural and Luminescence Properties of Er-Doped Zinc – Alumino – Silicate Glass Ceramic." *J. Am. Ceram. Soc.* 4:1–4. doi: 10.1111/j.1551-2916.2012.05200.x.

Gonçalves, M. Clara, Luis M. Fortes, Rui M. Almeida, Alessandro Chiasera, Andrea Chiappini, Maurizio Ferrari, and Shivakiran Bhaktha. 2010. "Photoluminescence in Er3+/Yb3+-Doped Silica-Titania Inverse Opal Structures." *Journal of Sol-Gel Science and Technology* 55(1):52–58. doi: 10.1007/s10971-010-2212-y.

Guille, A., A. Pereira, C. Martinet, and B. Moine. 2012. "Quantum Cutting in CaYAlO4: Pr3+, Yb3+." *Optics Letters* 37(12):2280. doi: 10.1364/ol.37.002280.

Hehlen, Markus P., Mikhail G. Brik, and Karl W. Kramer. 2013. "50th Anniversary of the Judd – Ofelt Theory : An Experimentalist ' s View of the Formalism and Its Application." *Journal of Luminescence* 136:221–39. doi: 10.1016/j.jlumin.2012.10.035.

Hien, Le Thi Thu, Nguyen Van Dub, Ngo Ngoc Hab, Nguyen Duc Hoab, Tran Ngoc Khiemb, and Nguyen Duc Chiena. 2019. "Optical Materials Photoluminescence Enhancement OF Er

3 + -Doped ZnO / SiO 2 Nanocomposites Fabricated through Two-Step Synthesis." *Optical Materials* 92(April):262–66. doi: 10.1016/j.optmat.2019.04.043.

Huang, X. Y., and Q. Y. Zhang. 2009. "Efficient Near-Infrared down Conversion in Zn2 SiO4: Tb3+, Yb3+ Thin-Films." *Journal of Applied Physics* 105(5):1–5. doi: 10.1063/1.3088890.

Huang, Xiaoyong, Sanyang Han, Wei Huang, and Xiaogang Liu. 2013. "Enhancing Solar Cell Efficiency: The Search for Luminescent Materials as Spectral Converters." *Chemical Society Reviews* 42(1):173–201. doi: 10.1039/c2cs35288e.

Ismail, Adel Ali, Mostafa Abboudi, Paul Holloway, and Hassan El-Shall. 2007. "Photoluminescence from Terbium Doped Silica-Titania Prepared by a Sol-Gel Method." *Materials Research Bulletin* 42(1):137–42. doi: 10.1016/j.materresbull.2006.05.002.

Jenouvrier, P., E. Cela1, C. Coutier, M. Langlet, R. Rimet, and J. Fick. 2001. "Photoluminescence of Terbium-Organic Complex in Aerosol – Gel-Derived Planar Waveguides." *Applied Physics B* 73:463–66. doi: 10.1007/s003400100707.

Khaidir, Rahayu Emilia Mohamed, Yap Wing Fen, Mohd Hafiz Mohd Zaid, Khamirul Amin Matoria, Nur Alia Sheh Omar, Aisyah Zakiah Khirel Azman , Muhammad Fahmi Anuarb, Siti Aisyah Abdul Wahaba, Nur Alia, Sheh Omar, Muhammad Fahmi, Siti Aisyah, Abdul Wahab, Aisyah Zakiah, and Khirel Azman. 2019. "Exploring Eu 3 + -Doped ZnO-SiO 2 Glass Derived by Recycling Renewable Source of Waste Rice Husk for White-LEDs Application." *Results in Physics* 15(July). doi: 10.1016/j.rinp.2019.102596.

Kumar, Pawan, Kanika, Satbir Singh, Rimli Lahon, Abhiram Gundimeda, Govind Gupta, and Bipin Kumar Gupta. 2018. "A Strategy to Design Lanthanide Doped Dual-Mode Phosphor Mediated Spectral Convertor for Solar Cell Applications." *Journal of Luminescence* 196(October 2017):207–13. doi: 10.1016/j.jlumin.2017.12.035.

Kumar, Vinod, O. M. Ntwaeaborwa, T. Soga, Viresh Dutta, and H. C. Swart. 2017. "Rare Earth Doped Zinc Oxide Nanophosphor Powder : A Future Material for Solid State Lighting and Solar Cells." *ACS Photonics* 4:2613–37. doi: 10.1021/acsphotonics.7b00777.

Kumar, Vinod, S. P. Tiwari, O. M. Ntwaeaborwa, and Hendrik C. Swart. 2020. "Spectroscopy of Lanthanide-Doped Oxide Materials." Pp. 345–64 in *Spectroscopy of Lanthanide Doped Oxide Materials*. Elsevier Ltd.

Kunkel, Nathalie, and Philippe Goldner. 2018. "Recent Advances in Rare Earth Doped Inorganic Crystalline Materials for Quantum Information Processing." *Zeitschrift Fur Anorganische Und Allgemeine Chemie* 644(2):66–76. doi: 10.1002/zaac.201700425.

Lee, Jae Won, Sungmin Kong, Woo Sik Kim, and Jinsoo Kim. 2007. "Preparation and Characterization of SiO2/TiO2 Core-Shell Particles with Controlled Shell Thickness." *Materials Chemistry and Physics* 106(1):39–44. doi: 10.1016/j.matchemphys.2007.05.019.

Li, Xiaomin, Rui Wang, Fan Zhang, and Dongyuan Zhao. 2014. "Engineering Homogeneous Doping in Single Nanoparticle To Enhance Upconversion E Ffi Ciency." *Nano Letters* 14:3634–39.

Li, Xiaoyu, and Junhui He. 2013. “Synthesis of Raspberry-Like SiO2 − TiO2 Nanoparticles toward Antire Fl Ective and Self-Cleaning Coatings.” *ACS Applied Materials & Interfaces* 5(11):5282–90. doi: https://doi.org/10.1021/am401124j.

Liang, Leben, Zhifeng Mo, Biao Ju, Changming Xia, and Zhiyun Hou. 2020. “Visible and Near-Infrared Emission Properties of Yb 3 + / Pr 3 + Co-Doped Lanthanum Aluminum Silicate Glass.” *Journal of Non-Crystalline Solids* (November):120578. doi: 10.1016/j.jnoncrysol.2020.120578.

Liang, Leben, Zhifeng Mo, Biao Ju, Changming Xia, and Zhiyun Hou. 2021. “Visible and Near-Infrared Emission Properties of Yb 3 + / Pr 3 + Co-Doped Lanthanum Aluminum Silicate Glass.” *Journal of Non-Crystalline Solids* 557(September 2020):120578. doi: 10.1016/j.jnoncrysol.2020.120578.

Liang, Liangliang, Yumin Liu, Chenghao Bu, Kaimo Guo, Weiwei Sun, Niu Huang, Tao Peng, Bobby Sebo, Mengmei Pan, Wei Liu, Shishang Guo, and Xing Zhong Zhao. 2013. “Highly Uniform, Bifunctional Core/Double-Shell-Structured β-NaYF 4:Er3+, Yb3+@SiO2@TiO2 Hexagonal Sub-Microprisms for High-Performance Dye Sensitized Solar Cells.” *Advanced Materials* 25(15):2174–80. doi: 10.1002/adma.201204847.

Liang, Liangliang, Daniel B. L. Teh, Ngoc Duy Dinh, Weiqiang Chen, Qiushui Chen, Yiming Wu, Srikanta Chowdhury, Akihiro Yamanaka, Tze Chien Sum, Chia Hung Chen, Nitish V. Thakor, Angelo H. All, and Xiaogang Liu. 2019. “Upconversion Amplification through Dielectric Superlensing Modulation.” *Nature Communications* 10(1):1–9. doi: 10.1038/s41467-019-09345-0.

Liégard, F., J. L. Doualan, R. Moncorgé, and M. Bettinelli. 2005. “Nd3+ → Yb3+ Energy Transfer in a Codoped Metaphosphate Glass as a Model for Yb3+ Laser Operation around 980 Nm.” *Applied Physics B: Lasers and Optics* 80(8):985–91. doi: 10.1007/s00340-005-1829-y.

Lin, Tao, Xiao-wei Zhang, Yun-ji Wang, Jun Xu, Neng Wan, and Jian-feng Liu. 2012. “Luminescence Enhancement Due to Energy Transfer in ZnO Nanoparticles and Eu 3 + Ions Co-Doped Silica.” *Thin Solid Films* 520(17):5815–19. doi: 10.1016/j.tsf.2012.04.058.

Liu, Yujia, Yiqing Lu, Xusan Yang, Xianlin Zheng, Shihui Wen, Fan Wang, Xavier Vidal, Jiangbo Zhao, Deming Liu, Zhiguang Zhou, Chenshuo Ma, Jiajia Zhou, James A. Piper, Peng Xi, and Dayong Jin. 2017. “Amplified Stimulated Emission in Upconversion Nanoparticles for Super-Resolution Nanoscopy.” *Nature* 543(7644):229–33. doi: 10.1038/nature21366.

Lluscà, M., J. López-Vidrier, A. Antony, S. Hernández, B. Garrido, and J. Bertomeu. 2014. “Up-Conversion Effect of Er- and Yb-Doped ZnO Thin Films.” *Thin Solid Films* 562:456–61. doi: 10.1016/j.tsf.2014.03.078.

Lojpur, Vesna M., Phillip S. Ahrenkiel, and Miroslav D. Dramićanin. 2013. “Color-Tunable up-Conversion Emission in Y2O3:Yb3+, Er3+ Nanoparticles Prepared by Polymer Complex Solution Method.” *Nanoscale Research Letters* 8(1):1–6. doi: 10.1186/1556-276X-8-131.

Loo, Jacky Fong-chuen, Yi-hsin Chien, Feng Yin, Siu-kai Kong, Ho-pui Ho, and Ken-tye Yong. 2019. “Upconversion and Downconversion Nanoparticles for Biophotonics and Nanomedicine.” *Coordination Chemistry Reviews* 400:213042. doi: 10.1016/j.ccr.2019.213042.

Mahata, Manoj Kumar, Surya Prakash Tiwari, Shriparna Mukherjee, Kaushal Kumar, and Vineet Kumar Rai. 2014. “YVO4:Er3+ /Yb3+ Phosphor for Multifunctional Applications.” *Journal of Optical Society America B* 31(8):1814–21.

Meijer, Janne Mieke, Linda Aarts, Bryan M. Van Der Ende, Thijs J. H. Vlugt, and Andries Meijerink. 2010. “Downconversion for Solar Cells in YF3: Nd3+, Yb 3+.” *Physical Review B - Condensed Matter and Materials Physics* 81(3):1–9. doi: 10.1103/PhysRevB.81.035107.

Mir, Wasim J., Tariq Sheikh, Habibul Arfin, Zhiguo Xia, and Angshuman Nag. 2020. “Lanthanide Doping in Metal Halide Perovskite Nanocrystals: Spectral Shifting, Quantum Cutting and Optoelectronic Applications.” *NPG Asia Materials* 12(1). doi: 10.1038/s41427-019-0192-0.

Mohamed, R. M., and I. A. Mkhalid. 2010. “The Effect of Rare Earth Dopants on the Structure , Surface Texture and Photocatalytic Properties of TiO 2 – SiO 2 Prepared by Sol – Gel Method.” *Journal of Alloys and Compounds* 501:143–47. doi: 10.1016/j.jallcom.2010.04.061.

Mossad Ali, Atif, Adel A. Ismail, Rasha Najmy, and Ali Al-hajry. 2014. “Preparation and Characterization of ZnO – SiO 2 Thin Films as Highly Efficient Photocatalyst.” *Journal of Photochemistry & Photobiology, A: Chemistry* 275:37–46. doi: 10.1016/j.jphotochem.2013.11.002.

Muniz, R. F., V. S. Zanuto, M. S. Gibin, J. V. Gunha, A. Novatski, J. H. Rohling, A. N. Medina, and M. L. Baesso. 2023. “Down- and up-Conversion Processes in Nd3+/Yb3+ Co-Doped Sodium Calcium Silicate Glasses with Concomitant Yb2+ Assessment.” *Journal of Rare Earths* 41(3):342–48. doi: 10.1016/j.jre.2022.01.020.

Nizamutdinov, A. S., S. V Kuznetsov, V. A. Konyushkin, A. N. Nakladov, E. I. Madirov, V. V Voronov, A. R. Khadiev, M. A. Marisov, and V. V Semashko. 2019. “LUMINESCENCE OF GdF 3 : Pr : Yb AND YF 3 : Pr : Yb SOLID SOLUTIONS SYNTHESIZED BY CRYSTALLIZATION FROM THE MELT.” *Journal of Applied Spectroscopy* 86(5):795–801. doi: 10.1007/s10812-019-00895-1.

Ntwaeaborwa, O. M., and P. H. Holloway. 2005. “Enhanced Photoluminescence of Ce 3+ Induced by an Energy Transfer from ZnO Nanoparticles Encapsulated in SiO 2.” *Nanotechnology* 16(6):865–68. doi: 10.1088/0957-4484/16/6/042.

Pellegrino, Anna L., Paolo Cortelletti, Marco Pedroni, Adolfo Speghini, and Graziella Malandrino. 2017. “Nanostructured CaF2:Ln3+ (Ln3+ = Yb3+/Er3+, Yb3+/Tm3+) Thin Films: MOCVD Fabrication and Their Upconversion Properties.” *Advanced Materials Interfaces* 4(18):2–7. doi: 10.1002/admi.201700245.

Prathibha, K. N., R. Hari Krishna, B. V. Nagesh, D. Prakashbabu, B. S. Panigrahi, and R. Ananthanarayanan. 2021. “Investigation of Luminescence Spectroscopic Characteristics in Eu3+-Doped Zn2SiO4 by Judd–Ofelt Parameters.” *Journal of Materials Science: Materials in Electronics* 32(15):20197–210. doi: 10.1007/s10854-021-06524-y.

Pudovkin, M. S., A. K. Ginkel, and E. V. Lukinova. 2021. “Temperature Sensitivity of Nd3+, Yb3+:YF3 Ratiometric Luminescent Thermometers at Different Yb3+ Concentration.” *Optical Materials* 119(April):111328. doi: 10.1016/j.optmat.2021.111328.

Qiu, Jianrong, Kentarou Nouchi, Kiyotaka Miura, Tsuneo Mitsuyu, and Kazuyuki Hirao. 2000. “Room-Temperature Persistent Spectral Hole Burning of x-Ray-Irradiated Sm 3 + -Doped Glass.” *J. Phys.: Condens. Matter* 12:5061–5067.

Raevskaya, A. E., Ya V. Panasiuk, O. L. Stroyuk, S. Ya Kuchmiy, V. M. Dzhagan, A. G. Milekhin, N. A. Yeryukov, L. A. Sveshnikova, E. E. Rodyakina, V. F. Plyusnin, and D. R. T. Zahn. 2014. “Spectral and Luminescent Properties of ZnO-SiO2 Core-Shell Nanoparticles with Size-Selected ZnO Cores.” *RSC Advances* 4(108):63393–401. doi: 10.1039/c4ra07959k.

Rai, Suman, and Andrew L. Fanai. 2014. “Spectroscopic Studies of Ho 3+ Doped SiO 2-TiO 2 Nanoparticle for Photonic Applications.” *Science Vision* 14(3):112–17.

Reisfeld, R., and Y. Kalisky. 1981. “Nd3+ and Yb3+ Germanate and Tellurite Glasses for Fluorescent Solar Energy Collectors.” *Chemical Physics Letters* 80(1):178–83. doi: 10.1016/0009-2614(81)80084-X.

Richards, B. S. 2006. “Enhancing the Performance of Silicon Solar Cells via the Application of Passive Luminescence Conversion Layers.” *Solar Energy Materials and Solar Cells* 90(15):2329–37. doi: 10.1016/j.solmat.2006.03.035.

Saeed, N. A. M., E. Coetsee, and H. C. Swart. 2020. “Down-Conversion of YOF: Pr3+, Yb3+ Phosphor.” *Optical Materials* 110(February):110516. doi: 10.1016/j.optmat.2020.110516.

Sales, A. J. M., D. G. Sousa, H. O. Rodrigues, M. M. Costa, A. S. B. Sombra, and F. N. A. Freire. 2016. “Power Dependent Upconversion in Er 3+/ Yb 3+ Co-Doped BiNbO 4 Phosphors.” *Ceramics International* 42(6):6899–6905. doi: 10.1016/j.ceramint.2016.01.075.

Serrano, D., A. Braud, J. L. Doualan, P. Camy, A. Benayad, V. Ménard, and R. Moncorgé. 2011. “Ytterbium Sensitization in KY3F10: Pr3+, Yb3+ for Silicon Solar Cells Efficiency Enhancement.” *Optical Materials* 33(7):1028–31. doi: 10.1016/j.optmat.2010.07.023.

Smentek, Lidia. 1988. “Theoritical Description of the Spectroscopic Properties of Rare Earth Ions in Crystal.” *Physics Reports* 297:155–237.

Smentek, Lidia, and Brian G. Wybourne. 2000. “Relativistic f ↔ f Transitions in Crystal Fields.” *Journal of Phsics B* 33:3647–51.

Song, Nan, Songbin Liu, Peng Zhang, Junshan He, Qinyuan Zhang, Feng Wang, and Bo Zhou. 2021. “Enhancing Upconversion of Nd3+ through Yb3+-Mediated Energy Cycling towards

Temperature Sensing." *Journal of Rare Earths* 39(12):1506–11. doi: 10.1016/j.jre.2021.06.013.

Soni, Abhishek Kumar, Riya Dey, and Vineet Kumar Rai. 2015. "Stark Sublevels in Tm3+–Yb3+ Codoped Na2Y2B2O7 Nanophosphor for Multifunctional Applications." *RSC Advances* 5:34999–9. doi: 10.1039/C4RA15891A.

Srinivasa Rao, Ch, I. V Kityk, T. Srikumar, G. Naga Raju, V. Ravi Kumar, Y. Gandhi, and N. Veeraiah. 2011. "Spectroscopy Features of Pr 3 + and Er 3 + Ions in Li 2 O – ZrO 2 – SiO 2 Glass Matrices Mixed with Some Sesquioxides." *Journal of Alloys and Compounds* 509:9230–39. doi: 10.1016/j.jallcom.2011.07.001.

Sta, I., M. Jlassi, M. Hajji, M. F. Boujmil, R. Jerbi, M. Kandyla, M. Kompitsas, and H. Ezzaouia. 2014. "Structural and Optical Properties of TiO2 Thin Films Prepared by Spin Coating." *Journal of Sol-Gel Science and Technology* 72(2):421–27. doi: 10.1007/s10971-014-3452-z.

Strohhofer, C., J. Fick, H. C. Vasconcelos, and R. M. Almeida. 1998. "Active Optical Properties of Er-Containing Crystallites in Sol – Gel Derived Glass Films." *Journal of Non-Crystalline Solids* 226:182–91.

Sun, Ting, Ai Hua Li, Chao Xu, Yu Heng Xu, and Rui Wang. 2013. "Energy Transfer Properties of Nd3+→Yb3+ in Nd:Yb:LiNbO3 Crystals." *Optics and Laser Technology* 56:322–25. doi: 10.1016/j.optlastec.2013.09.010.

Tavernaro, Isabella, Christian Cavelius, Henrike Peuschel, and Annette Kraegeloh. 2017. "Bright Fluorescent Silica-Nanoparticle Probes for High-Resolution STED and Confocal Microscopy." *Beilstein Journal of Nanotechnology* 8:1283–96. doi: 10.3762/bjnano.8.130.

Tran, T. T. Va., T. M. Dun. Cao, Quang Vinh Lam, and Van Hieu Le. 2017. "Emission of Eu3 + in SiO2-ZnO Glass and SiO2-SnO2 Glass-Ceramic: Correlation between Structure and Optical Properties of Eu3 + Ions." *Journal of Non-Crystalline Solids* 459:57–62. doi: 10.1016/j.jnoncrysol.2016.12.040.

Tung, Pham Son, Le Thi Thu Hien, Ngo Ngoc Ha, Tran Ngoc Khiem, and Nguyen Duc Chien. 2016. "Influence of Composition , Doping Concentration and Annealing Temperatures on Optical Properties of Eu3+-Doped ZnO–SiO2 Nanocomposites." *Journal of Nanoscience and Nanotechnology* 16(8):7955–58. doi: 10.1166/jnn.2016.12756.

Vasconcelos, Helena Cristina, and Afonso Silva Pinto. 2017. "Fluorescence Properties of Rare-Earth-Doped Sol-Gel Glasses." in *Recent Applications in Sol-Gel Synthesis*, edited by Usha chandra. IntechOpen.

Villanueva-Delgado, Pedro, Karl W. Krämer, and Rafael Valiente. 2015. "Simulating Energy Transfer and Upconversion in β-NaYF4: Yb3+, Tm3+." *Journal of Physical Chemistry C* 119(41):23648–57. doi: 10.1021/acs.jpcc.5b06770.

Walsh, Brian M. 2006. "Judd-Ofelt Theory: Principles and Practices." Pp. 403–33 in *Advances in Spectroscopy for Lasers and Sensing*, edited by B. Di Bartolo and O. Forte. Netherland:

Springer.

Wang, Fangke, Lei Cui, Zhengce An, Xiangting Zhang, Yanhua Song, Ye Sheng, and Haifeng Zou. 2019. “Interfacial Energy Transfer in Hollow Double-Shelled TiO2 : X % Eu3 + @ SiO2 : Y % Tb3 + Nanospheres for Tissue Imaging.” *ACS Applied Nano Materials* 1–28. doi: 10.1021/acsanm.9b01713.

Wang, Feng, and Xiaogang Liu. 2009. “Recent Advances in the Chemistry of Lanthanide-Doped Upconversion Nanocrystals.” *Chemical Society Reviews* 38:976–89. doi: 10.1039/b809132n.

Wang, Xiaodong, Guangming Wu, Bin Zhou, and Jun Shen. 2013. “Thermal Annealing Effect on Optical Properties of Binary TiO 2 -SiO 2 Sol-Gel Coatings.” *Materials* 6:76–84. doi: 10.3390/ma6010076.

Wang, Ye-fu, Gao-yuan Liu, Ling-dong Sun, Jia-wen Xiao, Jia-cai Zhou, Chun-hua Yan, and Wang E. T. Al. 2013. “Nd 3+ -Sensitized Upconversion Nanophosphors : E Ffi Cient In Vivo Bioimaging Probes with Minimized Heating E Ff Ect.” *ACS Nano* 7(8):7200–7206.

Wen, Hongli, and Peter A. Tanner. 2011. “Energy Transfer and Luminescence Studies of Pr3+, Yb 3+ Co-Doped Lead Borate Glass.” *Optical Materials* 33(11):1602–6. doi: 10.1016/j.optmat.2011.04.024.

Wen, Shihui, Jiajia Zhou, Kezhi Zheng, Artur Bednarkiewicz, Xiaogang Liu, and Dayong Jin. 2018. “Advances in Highly Doped Upconversion Nanoparticles.” *Nature Communications* 9(1):1–12. doi: 10.1038/s41467-018-04813-5.

Xiao, F., R. Chen, Y. Q. Shen, Z. L. Dong, H. H. Wang, Q. Y. Zhang, and H. D. Sun. 2012. “Efficient Energy Transfer and Enhanced Infrared Emission in Er-Oped ZnO-SiO 2 Omposites.” *Journal of Physical Chemistry C* 116(24):13458–62. doi: 10.1021/jp304075g.

Xiao, F., R. Chen, Y. Q. Shen, B. Liu, G. G. Gurzadyan, Z. L. Dong, Q. Y. Zhang, and H. D. Sun. 2011. “Infrared Emission Properties and Energy Transfer in ZnO – SiO 2 : Yb 3 + Composites.” *Journal of Alloys and Compounds* 509(November 2018):7794–97. doi: 10.1016/j.jallcom.2011.05.011.

Xiaoqi, Meng, Li Lianqiang, Zou Kaishun, and Liu Juncheng. 2014. “The Effect of SiO2 on TiO2 Up-Conversion Photoluminescence Film.” *Optical Materials* 37(C):367–70. doi: 10.1016/j.optmat.2014.06.027.

Yu, Lixin, and Masayuki Nogami. 2007. “Local Structure and Photoluminescent Characteristics of Eu 3 + in ZnO – SiO 2 Glasses.” *Journel of Sol-Gel Technology* 43:355–60. doi: 10.1007/s10971-007-1581-3.

Zareba-Grodz, Iwona, Robert Pazik, Włodzimierz Tylus, Witold Mielcarek, Krzysztof Hermanowicz, Wiesław Strek, and Krzysztof Maruszewski. 2007. “Europium-Doped Silica – Titania Thin Films Obtained by the Sol – Gel Method.” *Optical Materials* 29:1103–6. doi: 10.1016/j.optmat.2006.05.001.

Zhang, Q. Y., K. Pita, and C. H. Kam. 2003. “Sol – Gel Derived Zinc Silicate Phosphor Films

for Full-Color Display Applications." *Journal of Physics and Chemistry of Solids* 64:333–38.

Zhang, Q. Y., and G. F. Yang. 2007. "Cooperative Downconversion in GdAl3(BO3)4: RE3+, Yb3+ (RE=Pr, Tb, and Tm)." *Applied Physics Letters* 91(5):4–7. doi: 10.1063/1.2757595.

Zhao, Jiangbo, Dayong Jin, Erik P. Schartner, Yiqing Lu, Yujia Liu, Andrei V Zvyagin, Lixin Zhang, Judith M. Dawes, Peng Xi, James A. Piper, Ewa M. Goldys, and Tanya M. Monro. 2013. "Single-Nanocrystal Sensitivity Achieved by Enhanced Upconversion Luminescence." *Nature Nanotechnology* (September):1–6. doi: 10.1038/nnano.2013.171.

Zhou, Bo, Bingyang Shi, Dayong Jin, and Xiaogang Liu. 2015. "Controlling Upconversion Nanocrystals for Emerging Applications." *Nature Nanotechnology* 10(11):924–36. doi: 10.1038/nnano.2015.251.

Zhu, Wenjuan, Daqin Chen, Lei Lei, Ju Xua, and Yuansheng Wang. 2014. "An Active-Core/Active-Shell Structure with Enhanced Quantum-Cutting Luminescence in Pr – Yb Co-Doped Monodisperse Nanoparticles." *Nanoscale Communication* 6(10500):10500–504. doi: 10.1039/C4NR02785J.

# *CHAPTER- 2*

## *EXPERIMENTAL METHODS*

***This chapter is discussing experimental and characterization technique used in the present thesis.***

*Chapter -2*

---

# EXPERIMENTAL METHODS

---

## 2.1. INTRODUCTION

This chapter outlines the experimental processes relevant to the present work. It offers a detailed discussion of the *ex-situ* sol-gel synthesis method, including crucial points for material synthesis, different precursors, and useful instruments. The structural characterization of the materials has been accomplished using X-Ray Diffraction (XRD) analysis and Fourier-transform infrared spectroscopy (FTIR). The morphology has been studied utilizing Transmission Electron Microscopy (TEM) and Scanning Electron Microscopy (SEM). Thermal characterization is performed with Thermo-gravimetry (TG) and Derivative thermo-gravimetry analysis (DTA). The optical characterization of the samples has been carried out by recording Absorption spectra and Photoluminescence spectra. A brief theoretical background of each characterization techniques are covered along with block diagram and image of corresponding instrument.

## 2.2. SYNTHESIS

The *ex-situ* sol-gel method is employed to prepare dense glass, phosphor, and thin film samples. Various aspect of the *ex-situ* sol-gel method are discussed below, which includes precursor, materials, and the procedure to prepare Titania-Silica and Zinc-Silicate binary composites, along with existing modifications in this synthesis process.

### 2.2.1. Precursors and starting material

The following precursors and materials are used in the *ex-situ* sol-gel synthesis method of $RE^{3+}$ ion co-doping in Titania-Silica and Zinc-Silicate host:

- Tetraethyl orthosilicate (Sigma Aldich, 99%; TEOS) as silica source
- Methonal (MeOH) (Merck, 99.8%) as solvent
- De-ionized water (Sigma Aldich, 99%; $H_2O$) initiate hydrolysis
- Nitric Acid ($HNO_3$, Merck 70%; catalyst)
- N,N Dimethyl formamide (DMF) as dying control chemical additive (DCCA) (99.5%)
- RE salts (Sigma Aldich, 99%; ) as source of $RE^{3+}$ ion
- Titanium isopropoxide (TIPO; Sigma Aldich, 99%) as titania precursor
- Isopropanol (PrOH) solvent for TIPO
- Acethylacetone ($CH_3COCH_2COCH_3$; AcAc) as a stabilizer and complexing agent $TiO_2$
- Zinc acetate di-hydrate [$Zn(CH_3COOH)_2 \cdot 2H_2O$; Sigma Aldich, 99% ] is used as source of ZnO dopant
- Monoethanolamine (MEA) as a stabilizer and complexing agent of ZnO
- Ytterbium chloride hexahydrate [$YbCl_3 \cdot 6H_2O$; Sigma Aldich, 99.9%],
- Neodymium chloride hexahydrate [$NdCl_3 \cdot 6H_2O$; Sigma Aldich, 99.9%], are purchased and use as such.

**Important materials for sol-gel synthesis:**

- Glass vessel (15 ml)
- Dropper (1.5 ml)
- Electric muffle furnace
- Magnetic stirrer cum hot plate
- Polypropline container
- Spin Coater
- Substrate (Si wafer, Quartz plate, Borosilicate glass etc), Single side optically polished <100> P-type Silica substrate [Si; Sigma Aldich] are priming and cleaned as discussed in section (2.2.3) before spin coating the solution.

### 2.2.2. SYNTHESIS METHOD

Different material synthesis processes are classified into two main groups: (i) physical and (ii) chemicals processes, as shown in Table 2.1. Different morphologies of the final sample can be obtained through both the physical and chemical synthesis methods. In the physical process, high-temperature and high-pressure environments, along with pure precursors, are required. This makes the synthesis route an optimized one, although it has limited applications due to its cost. On the other hand, the chemical synthesis route is used to create chemical compounds from their precursor. For example, sol-gel, chemical vapor deposition (CVD), sonochemistry, and the hydrothermal method are some of the important chemical synthesis methods.

Table 2.1: List of physical and chemical synthesis process

| **Physical process** | **Chemical process** |
|---|---|
| Laser ablation | Sol-Gel |
| Spray pyrolysis | Sono-chemical |
| Vapor condensation | Microwave assisted |
| Thermal decomposition | Electrochemical |
| Plasma sprayed | Hydro-thermal |
| Sputter deposition | Chemical Vapor Deposition |

Sol-gel is an essential wet chemical synthesis method through which controlled core-shell morphology such as raspberry or nanoparticles is obtained (Rosales and Esquivel 2020). These morphologies can also be achieved through sonochemical and hydrothermal synthesis routes. Laser ablation is a superior physical synthesis route for thin films due to its improved thickness control and particle size (Rosales and Esquivel 2020). In this work, we strictly confine our focus to the *ex-situ* sol-gel synthesis route of $RE^{3+}$ ion doped Titania-Silicate ($SiO_2$-$TiO_2$) and Zinc-Silicate (ZnO-$SiO_2$) hosts, which can be utilized for optimized UCL and DCL spectra of $RE^{3+}$ ion.

#### 2.2.2.1. Sol-Gel process

According to C. J. Brinker and G. W. Scherer, a sound knowledge of different areas of physics (fractal geometry and percolation theory), chemistry ( hydrolysis and condensation), and ceramic (sintering and structural relaxation) is required to understand the basic principles of the sol-gel

method (C. Jefffrey and George W. Scherer 1990). The transformation of a "polymer solution" into "gels" is termed the "sol-gel transition," in the same spirit as suggested by the pioneer, Prof. Pierre-Gilles de Gennes. $RE^{3+}$ ions of different concentrations can be doped into different host glasses (phosphate, borate, silicate, etc) to optimize promising applications. The $RE^{3+}$ ions can be immobilized into sol-gel glasses using three processes (Binnemans 2009): (i) Impregnation, (ii) Doping, and (iii) Chemical immobilization. Impregnation of $RE^{3+}$ ions in a silica glass occurs through the diffusion of a luminescent complex solution with a high concentration into the pores or channels of the silica glass when silica glass is immersed in this solution. Chemical immobilization occurs as organosilicon compounds are added to a sol-gel solution to form coordinate groups of organically modified silicates (ormosils). Doping of $RE^{3+}$ ions in the host is achieved by mixing $RE^{3+}$ ion salts and ligand into the silica sol before gelation, and the $RE^{3+}$ ions are eventually trapped in the silica host matrix during annealing.

There are different processes available to produce Titania –Silicate and Zinc Silicate monolithic glass and thin films. However, this work primarily targets the Sol-Gel method. It is a low-temperature synthesis route compared to the melt quenched method, and it allows for phase separation and crystallization to be avoided (Kozuka 2005).Simple instruments such as a beaker, a stirrer, a hot plate, and a furnace are used to prepare the sol-gel samples . Less expensive pure metal alkoxides are used to obtain a highly pure final product with a homogeneous structure from the aged solution. The aged solution is cast in different form to create bulk samples (monoliths), thin films, and fibers. Correspondingly, the promising encapsulation of organic compounds or metal complexes can enhance the photostability of organic luminophores.

**Silica host:**

The Silica has been used as a host of $RE^{3+}$ ions for a long time, benefiting from its thermal and chemical stability. The preparation of a silica host typically involves four stages: (i) hydrolysis & condensation, (ii) gelation, (iii) aging, and (iv) drying, sequentially as shown in Fig 4. A discussion of each of these four steps is necessary to understand the preparation of $RE^{3+}$ ion-doped silica samples.

*Hydrolysis and Condensation*

The silica precursor [e.g., Tetra-orthosilicate, $Si(OC_2H_5)_4$, TEOS] is typically admixed with DI water, using a alcohol as mutual solvent to obtain a solution of homogeneous nature for the hydrolysis and condensation of TEOS, even though they are immiscible (TEOS and water). The

hydrolysis of TEOS is slower due to the bulkier ethoxy groups, compared to other silica precursor. The molar ratio of TEOS to water is usually maintained as 1:4 to complete the hydrolysis of TEOS to Si-$(OH)_4$ as seen in Eq. (2.1).

$$(OC_2H_5)_3\text{-Si-}(OC_2H_5) + 4H_2O \rightarrow HO\text{-Si-}(OH)_3 + \text{Ethanol } (OC_2H_5) \quad (2.1)$$

$$(OC_2H_5)_3\text{-Si-}(OC_2H_5) + H_2O \rightarrow HO\text{-Si-}(OC_2H_5)_3 + \text{Ethanol } (OC_2H_5) \quad (2.2)$$

The hydrolysis of TEOS is also performed partially through fixing initial molar ratio of TEOS: water as 1:1.The silanol groups (Si-OH) and alcohol evolves in partial hydrolysis of TEOS as in Eq. (2.1). The Silicic acid [$(OC_2H_5)_3$-Si-OH; alkyl = $C_2H_5$] take part in condensation reactions for bridging oxygen (BO) formation as Si-O-Si siloxane bonds in Eq. (2.2) (Binnemans 2009). A straight forward chemical reaction for the hydrolysis and condensation of a TEOS is as follows,

$$(OC_2H_5)_3\text{-Si-OH} + HO\text{-Si-}(OC_2H_5)_3 \rightarrow (OC_2H_5)_3\text{-Si-O-Si-}(OC_2H_5)_3 + \text{Water} \quad (2.3)$$

The hydrolysis and condensation of TEOS occurs in both acidic and basic mediums. These two mediums are worth mentioning because the dimension and shape of silica particles change depending on the reaction medium. The hydrolysis of TEOS in the presence of acids [e.g. Nitric acid ($HNO_3$) and Hydrochloric acid (HCl), ] as catalysts initiates the protonation of the Si-alkoxide. It is accompanied by a nucleophilic attack by a $H_2O$ molecule, resulting in the formation of a penta-coordinated intermediate and the exclusion of an alcohol molecule. This process leads to the formation of smaller sol particles and gel network in acidic conditions due to the faster hydrolysis rate compared to the condensation rate, as shown in Eq. (2.1) (Binnemans 2009). On the other hand, TEOS can also be hydrolyzed in the presence of a base catalyst [e.g. Ammonium Hydroxide, Sodium Hydroxide (NaOH), Potassium Hydroxide (KOH), etc]. Stober et al., prepared monodisperse silica spheres by hydrolyzing TEOS in an ammonia (basic) solution of water and alcohol (C. Jefffrey and George W. Scherer 1990). Different amounts of alcohol, ammonia, and water are used as parameters to modify the size of spherical silica particle, which is useful for preparing core@shell nanomaterials.

The colloidal particles are formed during the hydrolysis of the TEOS precursor and in the initial phases of the condensation reaction. These suspended particles in a liquid are known as sol (Binnemans 2009). This sol then converts into a gel in the next step through additional polymerization reactions and interconnection of the network (Binnemans 2009).

***Gelation process***

The gelation process is essentially the conversion of sol into gel. This process increases the viscosity of the liquid medium due to additional polymerization reactions and the interconnection of the network of colloidal particle network (Binnemans 2009). Gel formation converts the fluid into a stiff 3-D structure with an interstitial liquid phase (Binnemans 2009). The gelation mechanisms of $SiO_2$ are completed in two phases (C. Jefffrey and George W. Scherer 1990). Initially, a transparent wet gel is formed in the reaction with the structural frame of (-Si-O-Si-) expanding in 3D. This 3-D network of Si-O-Si bond continues into the second phase until the last bond in the gel stage. Silicon is observed as relatively less susceptible to nucleophilic attacks than transition metals due to its partial positive charge [$\delta$(Si)= +0.32], making the gelation of silica solution a slower process. The viscosity of the solution abruptly increases with the gelation of silica sol.

***Aging & Drying***

Gels are usually kept in sealed vessels to avoid the evaporation of the solvent, allowing for the continuation of condensation reactions and cross-linking among the network to promote strength and reduce the risk of fracture (C. Jefffrey and George W. Scherer 1990). Three different products are obtained during the removal of the remaining liquid through drying gel: xerogel, aerogel, and cryogel among others.

**Thermal drying: xerogel**

The conventional thermal drying of the gel in a specific temperature range (27-200 °C) is termed as xerogel. In xerogel state, the shrinking of the gel is accompanied by additional cross-linkage when the unreacted -OR and -OH groups approach close proximity as the network collapses (Binnemans 2009). The drying process accelerates the evaporation of the liquid phase along with volume shrinkage, although a significant amount of liquid remains trapped in the pores (Binnemans 2009). The formation of cracks during annealing can present challenge in preparing high-quality monolithic xerogels (Binnemans 2009).

***Supercritical drying: Aerogel***

Supercritical drying of the sol beyond the critical pressure and temperature of the liquid phase in an autoclave initiates a detachment of liquid phase, resulting in the formation of aerogel. Aerogel is a good insulator with very low densities but is seldom utilized as the host for luminescent metal ions or organic molecules (Binnemans 2009).

***Freeze Drying: Cryogel***

Cryogel is obtained from the sol when the liquid phase of the gel is extracted at a much lower temperature using a vacuum. It is a sublimation phase of the solvent.

***Annealing***

Annealing of xerogel and aerogel is performed to remove the remaining liquid phase in the interconnected porous network at higher temperature (T > 200 °C). This process promotes the oxidation of remnant hydroxyl groups (Kozuka 2005), which could otherwise efficiently quench luminescence. During annealing, the remaining water and organic components in the network are eliminated at high temperatures, along with the relaxation of the gel structure to a dense state through viscous sintering (Binnemans 2009). These dense glasses are typically amorphous in nature but become polycrystalline at higher annealing temperature, forming what is known as glass ceramic.

The silica sol is also used to prepare thin film using a spin-coating or dip-coating route on a heat-resistant substrate. Heat-resistant substrates such as silica wafers, quartz wafers, and microscopic glass slide are used for optical tests and compositional analysis. In the spin-coating method, an excess quantity of sol solution is dropped on the substrate and spread under centrifugal force, typically maintained at speeds ranging from 1000 to 10000 rpm, until the desired film thickness is accomplished (Binnemans 2009). The volatile solvent evaporates concurrently, with the film's thickness depending on the factors such as spinning rate, solution concentration and viscosity, and the solvent used. In the dip coating method, the substrate is immersed in the sol and then gradually withdrawn (Binnemans 2009). In thin film, the stress induced is roughly equal to the tension in the liquid ($P \approx \sigma_x$), and during annealing, it becomes equal to the capillary stress, typically resulting in film cracking (C. Jefffrey and George W. Scherer 1990). $RE^{3+}$ ions are typically doped in small amounts in the silica solution to prepare dense glass and thin film for optoelectronic applications.

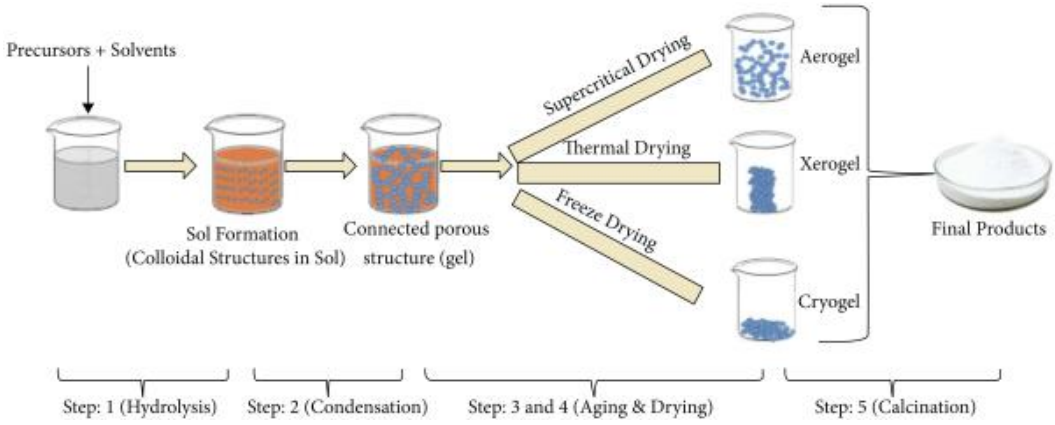


Fig. 2.1: Schematic sol-gel process (Bokov et al. 2021)

### 2.2.2.2. Host modifier

The sol-gel synthesis method of silica ($SiO_2$**)** glass host has been discussed in detail in the earlier sections. The sol-gel synthesis method is comparatively inexpensive and offers good control of particle size, high homogeneity, and uniform morphology (Esposito 2019), (Mhlongo 2011) etc. The introduction of the network modifier (e.g.$TiO_2$ (Halin et al. 2017) and ZnO (Agustín-Sáenz et al. 2018) ) in silica host is intended to promote lower phonon energy and lower symmetry. The formation of non-bridging oxygen (NBO) offers an efficient absorption (Lee et al. 2017), and luminescence of $RE^{3+}$ ion. The *ex-situ* sol-gel method is particularly emphasized here, due its utility for crafting dense glass, phosphor, and thin film samples doped with $RE^{3+}$ ions in ZnO-$SiO_2$ and $TiO_2$-$SiO_2$ binary composite host.

#### 2.2.2.2.1. $SiO_2$-$TiO_2$ binary host for $RE^{3+}$ ion doping

The homo-condensation of the silicate is slow with respect to the hetero-condensation of the reaction (C. Jefffrey and George W. Scherer 1990). This faster hydrolysis−condensation rate of Ti-alkoxides [(TIPO; $Ti(OC_3H_7)_4$] is going to promote the creation and segregation of bulky inhomogeneous $TiO_2$ sol particles with the addition of water into a mixture of TEOS+TIPO solution (Chen, Huang, and Perng 2012). An admixture of separately prepared silica sols and titania sols is used to remove the difficulties in controlling titania dimension and morphology in the sol−gel method (Chen et al. 2012). Chen et al., reported a homogeneous final solution with an admixture of Acetylacetone (AcAc)-stabilized TIPO (exothermic reaction) to pre-hydrolysis

TEOS. The hydrolysis rate of TIPO is slow down as AcAc removes *i-Pr* [-($C_3H_7$)] ligand and Ti coordination number raise from four to five as in Eq. (2.1) (Chen et al. 2012).

$$Ti\text{-}[(OC_3H_7]_4 + AcAc \rightarrow (AcAc)\text{-}Ti\text{-}[(OC_3H_7)]_3 + (\text{-}OC_3H_7) \quad (2.4)$$

The admixing of equimoles of water and TEOS generates more reactive Silicic acid [ $(OR)_3Si{-}OH$] where Silicic acid can react with AcAc-Ti-$(OC_3H_7)_3$ and favorably forms heterometal Si−O−Ti (Battisha 2007) oxides bond (NBO). The chemical reaction of Silicic Acid and AcAc-Ti-$(OC_3H_7)_3$ lead to Si-O-Ti (NBO) bond as follow (Chen et al. 2012),

$$[(OC_2H_5)]_3\text{-}Si\text{-}OH + (AcAc)\text{-}Ti\text{-}[(OC_3H_7)]_3 \rightarrow [(OC_2H_5)]_3\text{-}Si\text{-}O\text{-}Ti[(OC_3H_7)]_3 \quad (2.5)$$

Battisha I. K. , reported TIPO dissolved with AcAc and Acetic Acid (AcOH) under continuous stirring before PrOH was added to react with AcOH to generate $H_2O$ (Battisha 2007),

$$PrOH + AcOH \rightarrow PrOAc + H_2O \quad (2.6)$$

Chen et al. conducted a homogeneous esterification reaction to synthesize a $TiO_2$ solution. The process began with the pre-hydrolysis of TEOS using an equimolar ratio of TEOS to $H_2O$ (1:1 molar ratio). In the final stage, additional water was added to facilitate the formation of more Ti–O–Si bonds (Chen et al. 2012). The mixed solutions have a transparent brownish-purple ($SiO_2$-$TiO_2$) color. This transparent $TiO_2$-$SiO_2$ sol is further used to dope $RE^{3+}$ ion of different concentration.

### 2.2.2.2.2. ZnO-$SiO_2$ binary host for $RE^{3+}$ ion doping

The ZnO-$SiO_2$ binary samples are usually made from a mixed solution of ZnO and $SiO_2$ solution where ZnO and $SiO_2$ solutions are prepared separately (*ex-situ*) (Haque and Mahalakshmi 2013) or together (*in-situ*) to mold the final solution for synthesis. The Zinc Acetate dihydrate [$Zn(CH_3COO)_2.2H_2O$] is hydrolyzed in the alcoholic medium in presence of a complexing agent/stabilizer [e.g Tetra-ethanolamine (TEA) (Haque and Mahalakshmi 2013), Diethanolamine (DEA) (Hien et al. 2019), mono-ethanolamine (MEA)] to enhance the conversion of zinc hydroxide into zinc oxide and reducing ***the agglomeration of ZnO particle.*** C¸ opurog˘lu et al., reported colloids growth from an initial solution of Zinc Acetate dehydrate, Isopropanol, and MEA from cluster families such as basic zinc acetate [tetrahedral oxy-acetate $Zn_4O(C_2H_3O_2)_6$),

or $Zn_{10}O_4(C_2H_3O_2)_{12}$]; hydroxy double salt [hydroxy-acetate $Zn_5(OH)_8(C_2H_3O_2)_2(H_2O)_2$]; and alkoxy [(RO)-acetate ($ROZnC_2H_3O_2)_n$) in the absence of water for hydrolysis and condensation reaction (Çopuroğlu et al. 2016). Haque & Mahalakshmi, prepared wurtzite ZnO NPs from TEA [$N(CH_2CH_2OH)_3$] stabilized Zinc Acetate dehydrate and NaOH solution (Haque and Mahalakshmi 2013).

$$Zn(CH_3COO)_2.2H_2O+TEA \rightarrow [Zn(TEA)]+2CH_3COO^- \quad (2.7)$$

$$[Zn(TEA)] \rightarrow Zn^{2+}+TEA \quad (2.8)$$

The reaction parameters (temperature, pH, and synthetic methods) decide the final precipitation of zinc(II) hydroxide [$Zn(OH)_2$] or Zincate [$Zn(OH)^{2-}_4$ ] of ZnO NPs (Haque and Mahalakshmi 2013).

$$Zn^{2+}+2OH^- \rightarrow Zn(OH)_2 \downarrow \quad (2.9)$$

$$Zn(OH)_2 \rightarrow ZnO+H_2O\uparrow \quad (2.10)$$

The final transparent ZnO suspension can be excited with a UV lamp, where green emission from it confirms the formation of ZnO NP. Subsequently, the $SiO_2$ solution and ZnO solutions were mixed to form a homogeneous mixture of ZnO-$SiO_2$ binary sol material. This transparent ZnO-$SiO_2$ sol is used to dope $RE^{3+}$ ion of different concentration.

After admixing $RE^{3+}$ ion of different concentration, these two solutions are further cab be used as intial solution for dip coating or spin coating on a clean glass or silica substrate or left undisturbed to convert into a xerogel of various sizes and shapes. The homogeneousness of the hybrid thin film has also been relied on the dimension and functionality of the silica and titania/zinc sol particles where sol particles of smaller size offer more homogeneous film through less structural and compositional fluctuations (Chen et al. 2012). The acidity of final solution determines the functional behaviour of the sol particles whereas the quantity of DI water can influence the adhesion of the sol particles (Chen et al. 2012).

### 2.2.2.2.3. **Thin film preparation**

The final solution is used to spin- or dip- coated on clean substrate (Si wafer, Quartz wafer, glass etc). The substrates were cautiously cleaned with following steps;

a. The substrates are immersed in soap solution under ultrasonic bath (5 min).

b. Next, along with HCl in an ultrasonic bath for 10 minute.

c. Three additional rounds were conducted to the Si-substrate with DI water (1 min each) to eliminate the impurities of acid agent.

d. The substrate is systematically scrubbed with acetone for 15 min and propanol for 10 min in an ultrasonic wash in separate rounds to eliminate any adsorbed gases or impurities.

e. To remove native oxide layer and passivate Si wafer, substrate is immersed in HF (5%) solution for 20-30 s. Native oxide is etched and dangling Si bond (hydrophilic θ=10) are terminated by hydrogen atoms (more hydrophobic θ=70).

f. Rinsed in DI water and dried up at room temperature.

## 2.3. PHYSICAL CHARACTERIZATION

The physical characterization of dense glass ceramic materials includes estimation of density, porosity, and refractive index measurements, which are discussed as follows:

### 2.3.1. Density and porosity

Archimedes' principle serves as the basis for determining the density of dense glass ceramic. According to this principle, "the up thrust acting on a material submerged in a fluid, whether fully or partially, is equivalent to the weight of the fluid displaced by the material". To estimate the experimental density ($d_{exp}$) of the dense glass samples, one should measure both the weight and volume of the dense glass material in the air utilizing the following relationship:

$$d_{exp} = \frac{W_a}{W_a - W_w} \tag{2.11}$$

In this equation, $W_a$ represents the weight of the material in air, and $W_w$ represent the weight of material in the liquid.

Additionally, the porosity of a sample can be termed as the relative volume of the pores within the dense glass material. The porosity is estimated for any given material as follows:

$$p = \frac{d_x - d_{exp}}{d_x} \times 100\% \quad \textbf{(2.12)}$$

Here, $d_x$ represents the relative density of the sample, and $d_{exp}$ stands for the experimental density of the material.

### 2.3.2. Measurement of refractive index

To measure the refractive index of dense glass, one can employ the Brewster angle. According to Brewster, when unpolarized light strikes the surface of the dense glass material, the refracted light becomes partially polarized, and the refracted ray is perpendicular to reflected rays. The relationship between the Brewster angle ($\theta_B$) and index of refraction (n) is given by:

$$\tan \theta_B = \frac{n_2}{n_1} \quad \textbf{(2.13)}$$

In this equation, $n_1$ and $n_2$ denote the refractive indices of the medium and the material, correspondingly. Here, the refractive index of air ($n_1$ =1) is considered. Therefore, at maximum polarization, the angle of incidence is solely dependent on the refractive index. Consequently, the refractive index of the as-synthesized material (n), can be calculated as follows:

$$\tan \theta_B = n \quad \textbf{(2.14)}$$

The experimental arrangement, featuring a laser source, polarizer, and sample mounted for rotation, and the Brewster angle, is used to derive the refractive index of material with the help of Eq. (2.11).

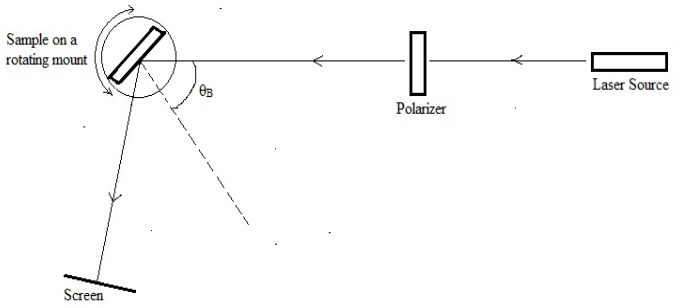


Figure 2.2: Experimental arrangement for refractive index estimation

**Ellipsometer**

Furthermore, an ellipsometer is employed as an optical method for inspecting the dielectric properties of thin film, including the complex refractive index or dielectric function. It quantifies the transformation in polarization upon transmission or reflection and equates it to a model.

The complex reflectance ratio (ρ) is defined as the ratio between the amplitude of p-polarized ($r_p$) and s-polarized ($r_s$) light, normalized to the initial values near the Brewster angle. It is parameterized by the amplitude component (Ψ) and phase difference (Δ) as follow:

$$\rho = \frac{r_p}{r_s} = \tan\Psi \times e^{i\Delta} \quad \textbf{(2.15)}$$

### 2.3.3. Effective mass approximation (EMA):

The dimension of nanoparticles in dense glass ceramic sample is determined with the Effective Maas Approximation (EMA) formula to ascertain in the average size of these nanoparticles. Optical absorption in the form of a photon with energy exceeding the bandgap energy of the semiconductor is required to generate a hole-electron pair. The accessibility of electrons within the solid is impacted by the binding energy of exciton and the screening of the hole. When $ZnO/TiO_2$ nanoparticles exhibit a shift towards a bluer color in their excitation energy, it is attributed to a quantum size effect. The effect is produced by the broadening of the bandgap of finite size. For more comprehensive understanding of the Effective Mass Approximation formula, Brus (1984) elucidates the theory behind the blue shift (Brus 1986). He presented the energy, denoted as E(r), which is dependent on the radius (R) of the nanoparticles, as follows (neglecting polarization energy and coulomb potential):

$$E_R = E_o + \frac{\hbar\pi^2}{R^2}\left(\frac{1}{\mu_e} + \frac{1}{\mu_h}\right) \quad \textbf{(2.16)}$$

Here the above symbols in Equation (2.15) have usual meanings.

## 2.4. STRUCTURAL AND MORPHOLOGICAL STUDIES

The structural studies were carried out by utilizing XRD technique and FTIR spectroscopy. The morphological analysis of prepared samples is accomplished with FESEM and FETEM analyses. Brief theoretical backgrounds of all the techniques are covered along with block diagram and image of corresponding instrument.

### 2.4.1. ATR-FTIR Spectroscopy

FTIR spectroscopy is the most advantageous procedure to identify organic and inorganic chemicals, along with chemical bonds, for example hydrogen bonding interactions, in solid and liquid form. The vibration of different molecules only lies within the IR range and thus this is an appropriate technique to detect presence of different molecular species. FTIR spectrometer uses two coherent but bifurcated IR beams passing through a beam splitter before producing an interference pattern, which is similar to the Michelson Interferometer. The transmitted and reflected beams reach a fixed mirror and movable mirror respectively, and recombine after passing through a beam splitter before passing through the sample and detector respectively as in Fig 2.3 (a). Here, constructive and destructive interference patterns are produced due to the introduced path difference. Each sample absorbs only specific frequencies, which is evident from the shape of the interference pattern (interferogram). The sample-specific variation with wavelength creates a characteristic spectrum of the sample. FTIR spectroscopy is a collection of data that is converted from an interference pattern to spectrum using a detector. There are two sampling technique available to plot IR absorption of a sample.

- Attenuated Total Reflection (ATR)
- KBr pellet method

#### 2.4.1.1. Instrument

ATR-FTIR Spectrometer [model IRAffinity-1S; SHIMADZU; USA) is equipped with ATR sampling technique to plot IR absorption of a sample without using cumbersome KBr pellet method. ATR-FTIR Spectrometer has a resolution of approximately 2 $cm^{-1}$ in diffuse reflectance (DR) mode within the vibrational frequency scanning range (400-4000 $cm^{-1}$).

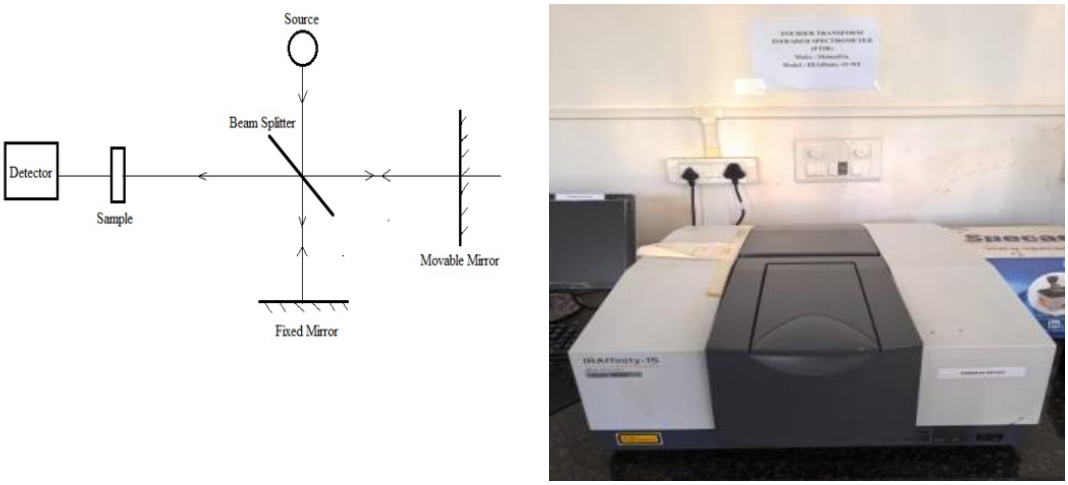


Figure 2.3: (a) Schematic diagrams and (b) Image of FTIR spectrophotometer

### 2.4.2. XRD Technique

Powder XRD technique is used to determine crystal structures and lattice parameters; measure crystallite size of material; identify as compounds and phases. A scattered monochromatic x-ray is passed through the sample with wavelength (λ) comparable to the spacing between the atoms in most inorganic materials.

**Bragg's Law:**

When monochromatic X-rays are directed at atoms confined within a crystal lattice, each atom emits scattered radiation at the exact same wavelength. The crystal lattice acts as a series of parallel reflecting planes. At a definite angle of incidence, the maximum intensity of the reflected beam is observed when the path difference (2dsinθ) between two waves reflected from two distinct planes is an integral times of the wavelength. This relationship can be expressed mathematically as follows:

$$2d\sin\theta = n\lambda \qquad (2.17)$$

The parallel planes of atom points is separated by a spacing (d) for two subsequent planes where a narrow x-ray beam is incident on the first plane at glancing angle θ [Figure 2.3 ( a)]. Here *2dsinθ* is the total path difference for x-ray beam with order of the scattered beam n (=1, 2, 3…α). The reinforcement happens between two rays to produce maximum intensity.

**Laue pattern**

The rotational averaging of scattered radiation hints to smooth diffraction rings around the axis of beam whereas discrete Laue spots are monitored in single crystal diffraction. The scattering angle (2θ) is the angle between the the ring and the beam axis. The directions of probable diffractions rely on the shape and size of the unit cell of the material. The intensities of the diffracted waves count on the types and distribution of atoms in the crystal structure.

**Debye-Scherrer's equation**

The dimension of the crystallites ($d_{hkl}$) is evaluated from the Debye-Scherrer's equation as the half-width of the diffraction peak (β) is inversely proportional to parameter that is a degree of the crystallites size. Mathematically,

$$d_{hkl} = \frac{0.94\,\lambda}{\beta \cos\theta} \tag{2.18}$$

The actual crystallite sizes of the synthesized samples are estimated based on line broadening of XRD peaks. The lattice strain also initiate broadening of X-ray peaks for particles with size below 20 nm whereas narrow peak width is observed for the crystallite with average diameter ca.100nm.

The area under the peaks contain information regarding the number of crystallites, the process whose calculation depends on integral breadth (area/height) is of significant value for precise crystallite size measurements.

**Uniform deformation model (UDM)**

The crystal strain is expected to be homogeneous in all crystallographic directions, thus taking into account the isotropic nature of the crystal, where the properties of the materials are invariant of the direction along which they are estimated.

**Williamson-Hall equation**

The W-H equation helps in plotting $4sin\theta$ (x-axis) vs $\beta_{hkl}cos\theta$ (y-axis) to measure the crystallite size and micro-strain produce in the crystal structure:

$$\beta_{hkl} = \frac{K\lambda}{d\cos\theta} + 4\epsilon\tan\theta \quad (2.19)$$

The size of the crystallite is calculated from the intercept of the y-axis in linearly fitted data, whereas the strain from the slope of the fit.

**Advantages**:

- The sample preparation is simple
- swiftness of measurement
- the ability to evaluate mixed phases,
- "in situ" structure determination

**ICDD reference database (JCPDS file)**

The identification of compound and phase is convenient through search and match software which associates experimental data with standard patterns from the ICDD reference database (JCPDS file).

### 2.4.2.1. Instrument

The 9 kW Powder X-Ray Diffractometer [model: Smartlab; Rigaku Technologies; Japan] is used to record XRD with CuKα radiation ($\lambda_{ex}$=0.15406nm) at different glancing angle (ω= 0.5 and 0.2 $A^0$) at CIF, IIT Guwahati.

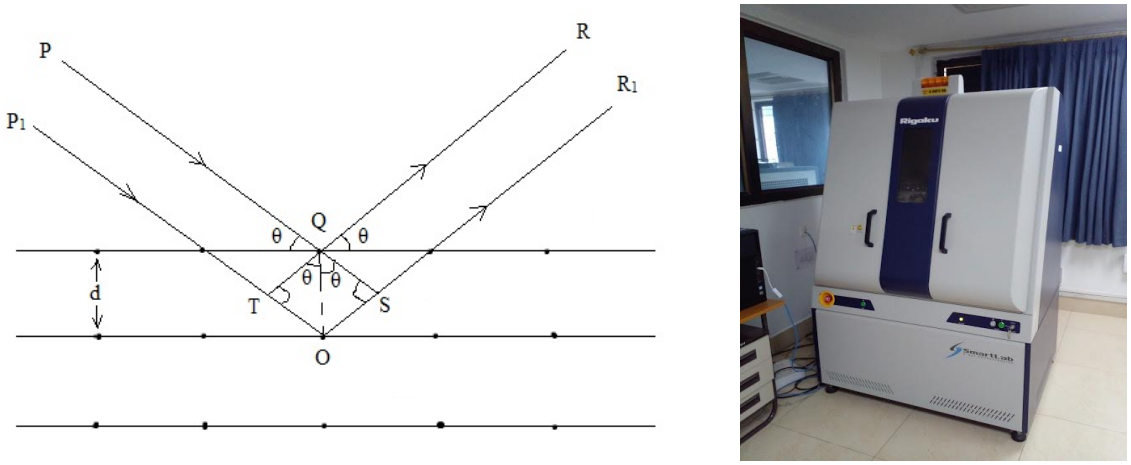


Figure 2.4: (a) Incident and diffracted radiation from crystal planes (b) Image of X-Ray diffractometer.

### 2.4.3. THE MORPHOLOGICAL CHARACTERIZATION

The morphological characterizations were carried out by utilizing FESEM and FETEM analyses. A brief theoretical background of each characterization technique is covered along with block diagram and image of corresponding instrument.

#### 2.4.3.1. FETEM analysis

FETEM is an instrumental technique employed to capture the morphological features of prepared samples. This electron microscope operates across four distinct stages. FETEM provides information about the sample in both real space (imaging mode) and reciprocal space (diffraction mode) by utilizing a focused electron beam, rather than visible light, to "image" and collect data pertaining to the structure and composition of the specimen.

**Principle and Operation**

FETEM relies on the de-Broglie wavelength of energetic electrons, where a smaller de-Broglie wavelength results in higher-resolution images compared to a compound microscope. The schematic diagram of FETEM comprises four stages, as depicted in Figure 2.5(b). In the initial stage, an electron gun generates a beam of electrons, which is then accelerated to the specimen with the help of a positive electrical potential ranging from 80 to 300 keV. This electron stream is subsequently focused through the use of metal apertures and magnetic lenses referred to as “condenser lenses,” resulting in the formation of a monochromatic, narrow, and focused beam. The beam impinges on the specimen, with a portion of it being transmitted through the sample. This transmitted portion is further focused utilizing a set of lenses known as “objective lenses,” resulting in the creation of an image. In the third stage, intermediate and projector lenses assist in enlarging the image, relying on the desired enlargement. The phosphorous image screen has been employed to render the image visible. The image strikes screen, and light is generated, enabling the operator to observe the image. Darker regions within the image correspond to thicker or denser areas of the sample (here fewer electrons were transmitted), while lighter areas characterize thinner or less dense regions (here large number of electrons were transmitted).

**TEM Sample preparation**

A crucial aspect of FETEM involves sample preparation, where the thickness of TEM samples must be less than 100 nm. Typically, a solution is drop-cast onto a 3.1 mm-diameter copper TEM grid and allowed to dry. The high-vacuum environment within TEM imposes specific requirements on the sample, like as the samples must be dry and capable of withstanding exposure to high-energy electron beams.

**High resolution TEM (HRTEM)**

HRTEM delivers high-magnification images of samples at the atomic scale by exploiting the interference of both transmitted and scattered electron beams. This technique allows for the easy observation of 2D projections of crystals with defects, with the lattice spacing of inorganic materials typically on the order of $10^{-10}$ m. HRTEM operates by tilting a thin slice of crystal including a low-index direction is precisely making an angle 90ºC to the electron beam. The alignment result in all lattice planes approximately parallel to the electron beam, which facilitates diffraction from the entire lattice plane. The diffraction pattern in two dimensions can be understood as the result of performing a Fourier transform on the periodic potential experienced by the electron. Within the objective lens, each diffracted beams is recombined with the primary beam, leading to an extended representation of the periodic potential at approximately a $10^6$ –fold magnification.

**Energy dispersive X-ray spectrometer (EDS)**

EDS is an invaluable tool for determining the chemical composition of samples with minimal quantities. Each, element possesses a characteristic x-ray spectrum that can be employed for identification. The EDS detector includes a crystal that absorbs inward x-rays' energy through ionization, generating free electrons within the crystal, thereby producing a signal of electrical charge. The absorption of x-ray transforms the energy of distinct x-rays into electrical voltages of relative size, with the electrical pulses corresponding to the characteristic x-rays emitted by the elements.

#### 2.4.3.1.1. Instrument

FETEM instrument used is JEOL 2100F (USA) at CIF, IIT Guwahati. This microscope operates in Bright-Field mode, Dark-Field mode, HRTEM mode, SAED and Convergent Beam Electron Diffraction (CBED) modes. The JEOL 2100 features a single-tilt stage with a maximum Tilt Angle of ± $80^{o}$ in Goinometer, here UHR pole section functions at a highest accelerating voltage ($V_{max}$) of 200kV. The $LaB_6$ filament operates in the pressure range of $10^{-5}$ to $10^{-6}$ Pa in a vacuum, with a 0.14 nm lattice resolution and a 0.12 nm point-to-point resolution. A Gatan digital camera is coupled with JEOL 2100 for digital image processing with a largest magnification of 1.5 million. Additionally, it features an anti-contamination device (ACD) operates with liquid nitrogen to avert filament contamination from volatile material. The OXFORD EDS system is integrated to the FETEM for mapping and elemental analysis of the sample.

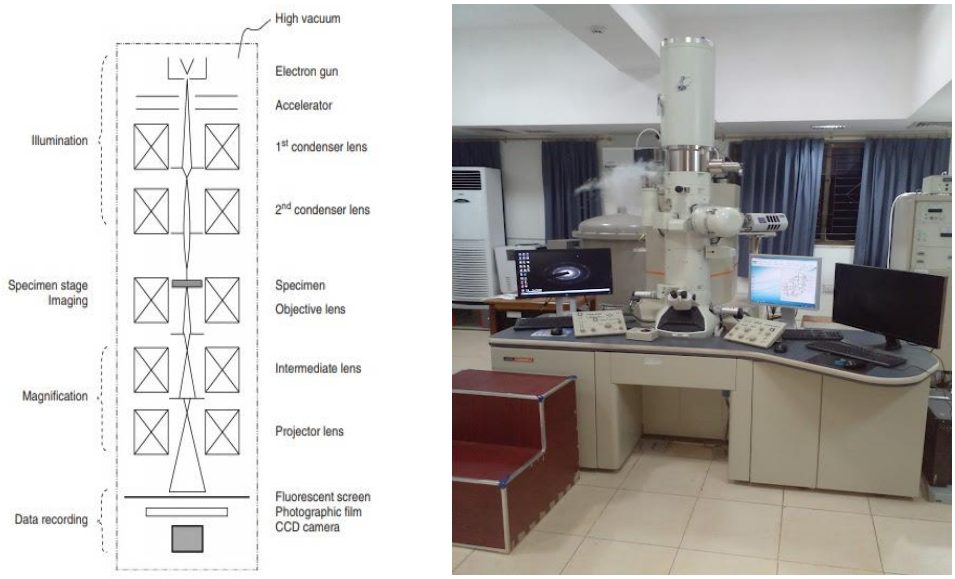


Figure 2.5: (a) Schematic diagram (b) Image of FETEM (IITG)

#### 2.4.3.2. FESEM analysis

FESEM is an advanced electron microscope utilized for producing high resolution images of small-sized samples. It operates by scanning a focused beam of electrons with an energy range spanning from 0.2 -40 electronvolts (eV). To achieve this, the electron beam is precisely focused

to a diameter ranging from 0.4 nm to 5 nm using one or two condenser lenses. Different pairs of scanning coils or pairs of deflector plates are stereotypically positioned in the terminal lens, which control the electron beam's movement along the x and y axes. The scanning action allows the beam to transverse the sample's surface in a raster pattern, covering a rectangular area. As the beam of primary electrons interact with the sample, it experiences a repetitive random scattering and absorption, primarily within a teardrop-shaped region within the specimen known as the interaction volume. This interaction volume covers from below 100 nanometers to approximately 5 micrometer beneath the surface and varies in size based on factors such as the landing energy of the electrons, the atomic number of the specimen, and the the specimen's density. The exchange of energy among the electron beam and the material consequences, several phenomena, including the emission of secondary electrons through inelastic scattering, the reflection of high-energy electrons by elastic scattering, and the emission of electromagnetic (EM) radiation. Specialized detectors are employed to capture and detect each of these signals. Additionally, the amount of beam current absorbed by the specimen is measured and utilized to generate images that depict the distribution of specimen current. To visualize and analyze the signals, electronic amplifiers of various kinds used. The distinctions in signal intensity are exhibited as brightness variation on a monitor of computer or, a cathode ray tube (for vintage models). Each pixel of the computer's video memory is synchronized with the position of beam on the material, creating a distribution map of the emitted signal's intensity within the scanned area of the material. In modern FESEM systems, images are stored as digital data on a computer, but in older models, high-resolution cathode ray tubes were used for capturing images through photography.

#### 2.4.3.2.1. Instrument

FESEM [Model: Sigma; Make: Zeiss, USA] are used to record monographs of samples in CIF, IIT Guwahati, which is capable of magnification around 10-300000x with spatial resolution of 0.1 nm. The OXFORD EDS is attached with FESEM for EDS mapping and elemental analysis of the sample.

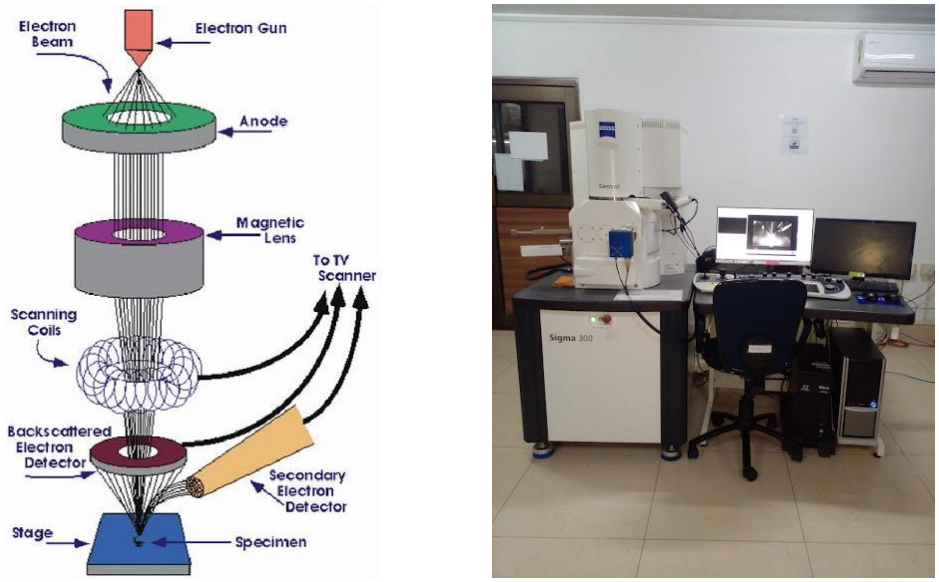


Figure 2.6: (a) Schematic diagram (b) Image of FESEM (IITG)

## 2.5. THERMAL ANALYSIS

The thermal studies were carried out by utilizing Thermo-gravimetry analysis and Derivative thermo-gravimetry analysis. A brief theoretical background of each characterization technique is covered along with block diagram and image of corresponding instrument.

### 2.5.1. Thermo gravimetric -Derivative thermo gravimetry analysis

Thermo gravimetric (TG) analysis is basically a tool for studying the change in the mass of a sample as a function of temperature. Derivative thermogravimetry analysis (DTA) represents how the mass change grows or reduces with temperature. With the help of this technique, the evaporation temperatures of the different constituents of samples, as well as the amount of weight loss due to temperature, can be determined. TG analysis continuously measures the mass of the sample while the temperature varies over time. It contains a balance capable of measuring with high precision and a sample holder inside a furnace. The temperature of the furnace can be controlled by programming. The temperature is gradually raised at a constant rate during the experiment. A sample purge gas (inert or reactive) is used to maintain the environment around the sample, it drifts over the sample and exits through an exhaust. The data for TG analysis for

the sample is collected from the thermal decomposition of the sample. Then it is expressed as a variation of mass or % of mass of the sample (Y-axis) with temperature (X-axis). This curve is known as the TGA curve. The first-order derivative of the TGA curve is referred to as the DTA curve. The DTA curve is used to determine inflection points, i.e., maximum or minimum change in the TGA curve.

### 2.5.1.1 Instrument

TGA/DTG analysis had been done with the help of a thermal analyzer (Model: TGA-4000 from Perkin Elmer, UK) in the Analytical lab, School of Energy Science & Technology, IITG. The temperature range of the instrument is 15-900 °C.

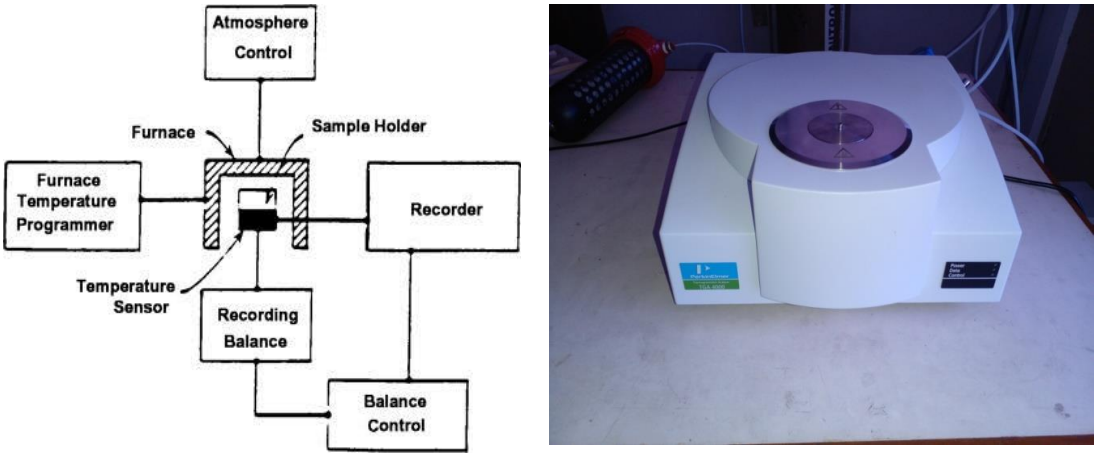


Figure 2.7: (a) Schematic diagram of TG/DTA thermal analyzer (b) Image of TGA-4000 from PerkinElmer (IITG)

## 2.6. OPTICAL CHARACTERIZATION

The optical studies were carried out by utilizing absorption spectra and photoluminescence spectra. A brief theoretical background of each characterization technique is covered along with block diagram and image of corresponding instrument.

### 2.6.1. Ultraviolet-Visible (UV-VIS & NIR) absorption spectroscopy

**Beer-Lambert's law**

In UV-VIS & NIR absorption spectroscopy, an electron is excited from the valence band (VB) to conduction band (CB) with the absorption of a photon in UV-VIS or NIR range. It can be utilized to estimate the value of the optical bandgap, where the absorption coefficient (α) is calculated using the relation,

$$\alpha = \frac{2.303 \times \log(absorption)}{thickness\ of\ the\ sample} \tag{2.20}$$

**Tauc Plot**

The association between the absorption coefficient (α) and the incident photon energy (hν) can be presented as:

$$\alpha h\nu = A\left(h\nu - E_g\right)^n \tag{2.21}$$

Here, A is a constant, and $E_g$ stand for the bandgap energy of the material. Here direct band gap (n = ½) and indirect band gap (n = 2) material have different value of n, where the optical bandgap is estimated by extrapolating the straight line portion of Tauc plot.

### 2.6.2. Photoluminescence (PL) Spectra

PL spectra are emissions from luminescent materials where electrons in the materials are excited from the VB to the CB by gaining the photon energy from the excitation source, which is greater than the band gap of the materials. It is a non-destructive characterization technique used to study the electronic structure of the band gap in semiconductor materials, along with the characteristic of structural and compositional defects within the materials, such as the existence of involuntary dopants and surface-associated defects. The presence of impurity levels and their

position can also be identified from PL spectra. The light sources are aligned at an angle of $90^{o}$ geometry to the sample, as in Fig 2.7 (b).In direct band gap semiconductors ($TiO_2$), the electrons in the conduction band promptly relax by emitting photons of energy equivalent to the band gap of the material. Electrons could potentially recombine with defects and perturbations within the lattice structure of the material, including valence band holes. These extra energy states might influences the characteristics of the emitted photons.

The UCL and DCL mechanisms have already been discussed in chapter 1, section 1.3. UCL and DCL spectra are basically PL spectra measurement, which are measured using a spectrometer using a monochromatic excitation source (e.g. $\lambda_{ex}$ = 980 or 808nm).

**CIE diagram**

The CIE 1931 color co-ordinates were the first to perceive the quantitative relations amid distributions of wavelengths in the visible EM spectrum and the physiological perception of colors in a human eye. The mathematical relations that describe these color spaces are crucial tools for color management and are vital when dealing with illuminated displays, color inks, and image processing devices for instance digital cameras. The CIE diagram represents each possible color with a pair of numerical co-ordinates (x, y), representing hue and saturation (also called colorfulness), respectively. The mixing of different colors of light can be observed, and the purity of the resultant color from luminescent material are also be determined geometrically from the CIE diagram.

**Life time measurement**

The rate of depopulation of an excited state can be represented by its life time. The longer the lifetime of a radiative transition, the more suitable the system is for laser applications. The lifetime of an excited state of $RE^{3+}$ ions varies from 50 μs to 10 ms in different matrices. In general, the lifetime of $RE^{3+}$ ions are estimated in two different ways: calculated (here defined as radiative) lifetime and experimental lifetime. The radiative lifetime of a particular upper state is calculated using J-O theory, whereas the experimental lifetime is evaluated from the time co-related PL spectra. The radiative lifetime estimated from the J-O theory is always greater than experimental lifetime because it contains the non radiative contributions like cross relaxation,

multi-phonon relaxation etc. The PL quantum efficiency can be expressed as the ratio of experimental lifetime ($\tau$) to the radiative life time ($\tau_{rad}$) of a particular metastable state.

### 2.6.3. Photoluminescence excitation (PLE) Spectra

PLE spectra represent the transformation in PL intensity as a function of the wavelength of the excitation light. Here wavelength of the emission monochromator ($\lambda_{em}$) is fixed to an identified PL emission wavelength from the material, and the wavelength of the excitation monochromator is scanned across the anticipated excitation range, recording the PL intensity on the detector as a function of excitation wavelength. If the material complies with Kash's Rule and Vavilov's rule, then the PLE spectrum will be indistinguishable to the absorption spectrum. PLE spectra can, therefore, be termed as PL-sensed absorption spectra.

### 2.6.4. Instrumentation

The optical characterizations of the dense glass ceramic materials are performed using following instruments.

#### 2.6.4.1. Spectrometer (iHR320)

The optical absorption spectra are acquired at room temperature by employing a spectrometer, specifically the iHR320 model from Horiba Scientific, in conjunction with the with the Syner JY$^{TM}$ software. The spectroscopic system was configured with a medium scan speed and a sampling interval of 0.5 within the wavelength range of 200-800 nm. The iHR320 spectrometer is equipped with integrating acquisition and data analysis capabilities. The iHR320 model incorporates a CCD detector and lacks an internal light source. Therefore, an external light source, in the form of an incandescent bulb, was utilized to cover the entire spectral range from visible to the infrared (IR) region for the purpose of recording absorption spectra. Due to the inherent weakness of UV emissions from the bulb, it was not suitable for capturing absorption spectra in that specific region.

For the acquisition of absorption spectra, the external light source was positioned and directed through the monochromator, as illustrated in Figure 2.8 (a). The monochromator's was carefully adjusted to allow the light to pass through, subsequently reaching the detector. The

detector, equipped with a CCD, then discerned the intensity of the incident light at various wavelengths within a predefined range.

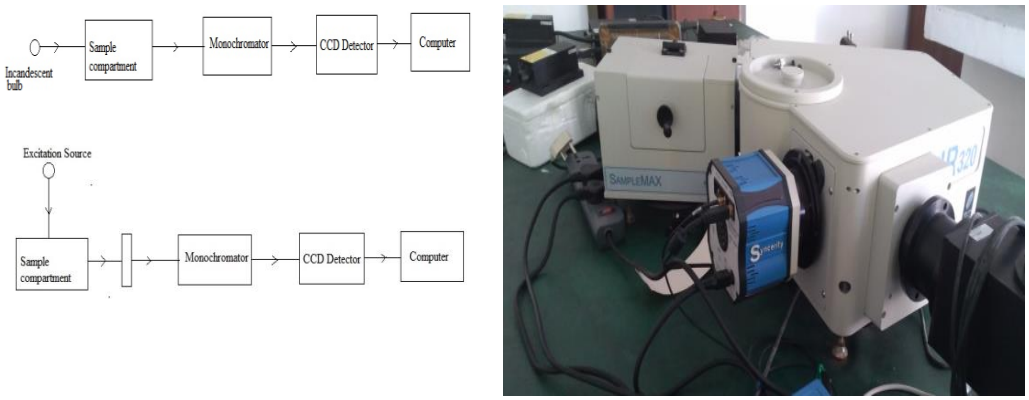


Figure 2.8: Schematic diagram of the recording (a) Absorption and (b) PL spectra(c) Image of iHR320 imaging spectrometer (MZU).

### 2.6.4.2. Horiba Fluromax 4

A 150 W Xenon lamp laser of wavelength of 350 nm is used as the excitation source. PL is collected by a collimating lens, where a photomultiplier tube measures the PL intensity over the range of wavelengths. For PL spectra, light sources of 370nm and 430nm of diode laser of max power 2 watt is utilized at $90^{o}$ geometry to the sample.

## 2.7. **CONCLUSION**

This chapter explores into a comprehensive discussion of the ex-situ sol-gel method, with a particular emphasis on its utility for crafting dense glass, phosphor, and thin film samples doped with $RE^{3+}$ ions in doped ZnO-$SiO_2$ and $TiO_2$-$SiO_2$ binary composite. Additionally the chapter provides a detailed explanation of various physical, structural, morphological and thermal analysis techniques employed for the sample characterization. Notably, optical characterization

take center stage in this research and the discussion touches upon the recording of absorption and emission spectra in a concise manner.

## REFERENCE


Agustín-Sáenz, Cecilia, José Ángel Sánchez-García, Maider Machado, Marta Brizuela, Oihana Zubillaga, and Agnieszka Tercjak. 2018. "Broadband Antireflective Coating Stack Based on Mesoporous Silica by Acid-Catalyzed Sol-Gel Method for Concentrated Photovoltaic Application." *Solar Energy Materials and Solar Cells* 186(February):154–64. doi: 10.1016/j.solmat.2018.06.040.

Battisha, I. K. 2007. "Visible Up-Conversion Photoluminescence from IR Diode-Pumped SiO2-TiO2 Nano-Composite Films Heavily Doped with Er3+-Yb3+ and Nd3+-Yb3+." *Journal of Non-Crystalline Solids* 353(18–21):1748–54. doi: 10.1016/j.jnoncrysol.2007.01.043.

Binnemans, Koen. 2009. "Lanthanide-Based Luminescent Hybrid Materials." *Chemical Review* 109:4283–4374.

Bokov, Dmitry, Abduladheem Turki Jalil, Supat Chupradit, Wanich Suksatan, Mohammad Javed Ansari, Iman H. Shewael, Gabdrakhman H. Valiev, and Ehsan Kianfar. 2021. "Nanomaterial by Sol-Gel Method: Synthesis and Application." *Advances in Materials Science and Engineering* 2021. doi: 10.1155/2021/5102014.

Brus, Louis. 1986. "Electronic Wave Functions in Semiconductor Clusters: Experiment and Theory." *Journal of Physical Chemistry* 90(12):2555–60. doi: 10.1021/j100403a003.

C. Jefffrey and George W. Scherer. 1990. *Sol-Gel Science, The Physics and Chemistry of Sol-Gel Processing*. London: Academic Press, Inc.

Chen, Hsueh Shih, Sheng Hsin Huang, and Tsong Pyng Perng. 2012. "Preparation and Characterization of Molecularly Homogeneous Silica-Titania Film by Sol-Gel Process with Different Synthetic Strategies." *ACS Applied Materials and Interfaces* 4(10):5188–95. doi: 10.1021/am301113a.

Çopuroğlu, Mehmet, Lee Huat Kelly Koh, Gabriel M. Crean, and Shane O'Brien. 2016. "Comparative Characterisation of Zinc Oxide Thin Films Prepared from Zinc Acetate with or without Water of Hydration via the Sol – Gel Method." *Journal of Sol-Gel Science and Technology* 52:432–38. doi: 10.1007/s10971-009-2016-0.

Esposito, Serena. 2019. "'Traditional' Sol-Gel Chemistry as a Powerful Tool for the Preparation of Supported Metal and Metal Oxide Catalysts." *Materials* 12(4):1–25. doi: 10.3390/ma12040668.

Halin, D. S. C., M. M. A. B. Abdullah, N. Mahmed, S. N. A. Abdul Malek, P. Vizureanu, and A. W. Azhari. 2017. "Synthesis and Characterization of TiO2/SiO2 Thin Film via Sol-Gel Method." *IOP Conference Series: Materials Science and Engineering* 209(1). doi: 10.1088/1757-899X/209/1/012002.

Haque, Md Azimul, and S. Mahalakshmi. 2013. "Effect of Triethanolamine on Zinc Oxide Nanoparticles." *Materials Focus* 2(6):469–74. doi: 10.1166/mat.2013.1117.

Hien, Le Thi Thu, Nguyen Van Dub, Ngo Ngoc Hab, Nguyen Duc Hoab, Tran Ngoc Khiemb,

and Nguyen Duc Chiena. 2019. “Optical Materials Photoluminescence Enhancement OF Er 3 + -Doped ZnO / SiO 2 Nanocomposites Fabricated through Two-Step Synthesis.” *Optical Materials* 92(April):262–66. doi: 10.1016/j.optmat.2019.04.043.

Kozuka, Hiromitsu. 2005. *Handbook of Sol-Gel Science and Technology: Processing, Characterization, and Applications*. Vol. I,II,III. edited by Sumio Sakka. New York: Kluwer Academic Publisher.

Lee, Chee Sun, Khamirul Amin Matori, Sidek Hj Ab Aziz, Halimah Mohamed Kamari, Ismayadi Ismail, and Mohd Hafiz Mohd Zaid. 2017. “Fabrication and Characterization of Glass and Glass-Ceramic from Rice Husk Ash as a Potent Material for Opto-Electronic Applications.” *Journal of Materials Science: Materials in Electronics* 28(23):17611–21. doi: 10.1007/s10854-017-7699-3.

Mhlongo. 2011. “Luminescence Investigation of Trivalent Rare Earth Ions in Sol-Gel Derived SiO2 and ZnO Co- Doped SiO2:Pr3+.” University of Free State.

Rosales, Alicia, and Karen Esquivel. 2020. “SiO2@TiO2 Composite Synthesis and Its Hydrophobic Applications: A Review.” *Catalysts* 10(2):1–17. doi: 10.3390/catal10020171.

*CHAPTER- 3*

# STRUCTURAL, MORPHOLOGICAL, THERMAL AND OPTICAL CHARACTERIZATION OF $Pr^{3+}$ - $Yb^{3+}$ ION CODOPED TITANIA- SILICATE DENSE GLASS

***This chapter is focused on synthesis method of STPYX-DGC and -TF along with structural, morphological, thermal and optical characterization of these samples.***

*Chapter- 3*

---

**Structural, morphological, thermal and optical characterization of $Pr^{3+}$-$Yb^{3+}$ ion co-doped Titania- Silicate dense glass ceramic and thin film**

---

## 3.1. INTRODUCTION:

Herein, $Pr^{3+}$ (0.7 mol%) and $Yb^{3+}$ (X mol%; X= 0.0, 0.7, 1.5, 3.0) ions co-doped titania-silicate (STPYX) solution were prepared through ex-situ sol-gel method. The STPYX final solutions were further used to prepare dense glass-ceramic (DGC) and thin film (TF) samples. The structural characterization of the STPY07-DGC sample was performed using the X-ray diffraction (XRD) pattern and Fourier transformations infrared spectroscopy at different annealing temperatures to investigate the structural evolution of the sample at different annealing temperatures. The morphological characterization of the STPYX-DGC and -TF samples were analyzed via Transmission electron microscopy (TEM) and Scanning electron microscopy (SEM) respectively. The energy dispersion spectroscopy (EDS) was used to understand the doping purity of the samples. The thermal characterization of the STPY07 xerogel was performed using thermogravimetric (TG) analyzer and differential scanning calorimetry (DSC) to record the difference in the amount of heat required to increase the temperature with respect to the copper crucible as a reference material. Finally optical properties of these as-synthesized STPYX-DGC materials were studied using absorption and photoluminescence spectroscopy in this chapter.

## 3.2. SYNTHESIS: $RE^{3+}$ ion co-doped $TiO_2$-$SiO_2$ binary composite

The *ex-situ* sol-gel synthesis of the STPYX-DGC materials were initiated with two separate solutions, namely "SOL-B: stabilized-$TiO_2$" and "SOL-A: activated-$SiO_2$". The SOL-B and SOL-A were admixed in 1:9 mol ratios respectively to ensure final solution for $RE^{3+}$ ion doping (Fig. 3.1). The admixing of mutually immiscible TEOS and water leads to inevitable phase separation during the hydrolysis-condensation of $SiO_2$ compound. Here, the pre-mixing of TEOS in alcoholic medium promotes the dispersion of both TEOS and water, thereby helping to prevent phase separation (Livage 2004), (Chen, Huang, and Perng 2012). The equimolar ratio of TEOS and water (r =1) was retained in initial stage to promote pre-hydrolysis TEOS. The SOL A was prepared by admixing TEOS: EtOH: $H_2O$: $HNO_3$ = 1: 30: 1: 0.5 molar ratios and stirred vigorously for 90 min at 60 $^0$C. In "AcAc-stablized $TiO_2$" solution, TIPO was added initially to PrOH to avoid evaporation where AcAc was added as a stabilizer. The dropwise addition of AcAc reacts exothermally and produces a clear orange solution. The equi-molar ratio was maintained for AcAc and TIPO. The $TiO_2$ solution is stirred for 20 min at room temperature to get a stable jelly-like sol. The pH of the solutions is maintained at 1.5 to reduce the time of gelation by maintaining the viscosity of the solution. The composite $SiO_2$-$TiO_2$ binary solution was further stirred vigorously for one hour and the remaining water is slowly added to maintain 1:4 molar ratio of Si: DI water for completion of the hydrolysis and condensation. The salt of $Pr^{3+}$ and $Yb^{3+}$ ions were dissolved in MeOH in final stage before admixing to the $SiO_2$-$TiO_2$ composite solution under uninterrupted stirring for 60 min.

The final solution (SOL-C) was poured in to a polypropylene container to convert into the STPYX-xerogel materials within three weeks of aging at room temperature. The annealing of the STPYX-xerogel materials were performed in two steps where the materials were dried gradually in hot air oven up to 235°C before heating ca. 900 ºC for one hour in an electric muffle furnace at the cooling rate of 1.0 °C/min. Here STPY00, STPY07, STPY15, and STPY30 are representing STPYX-DGC materials with fixed $Pr^{3+}$ (0.7 mol%) ion and varying $Yb^{3+}$ ion molar concentration (X mol%; X= 0.0, 0.7, 1.5 and 3.0 ) respectively with respect to the total 9.98 mmol of $SiO_2$-$TiO_2$ binary solution.

.

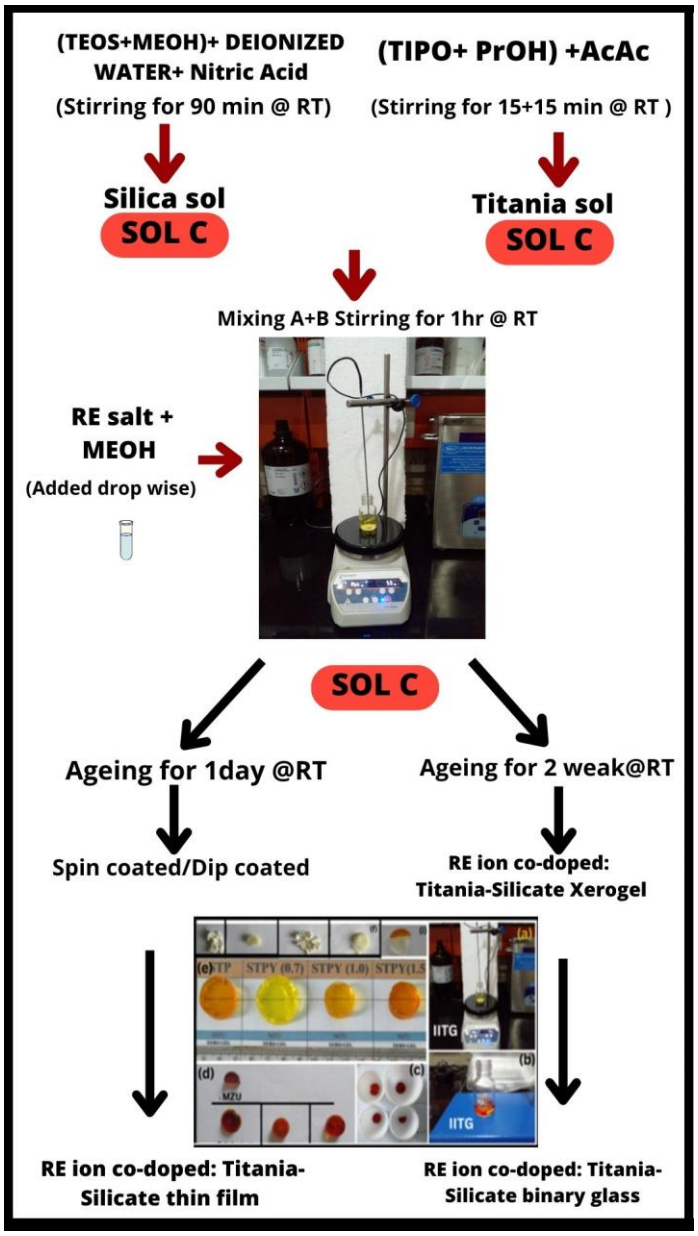


Figure 3.1: Schematic diagram of (a) *ex-situ* sol-gel preparation (inset) Image of the STPYX-DGC materials

The STPYX-TF samples were prepared on cleaned Si wafer from final STPYX solution after aging for one week. The spin-coating of these thin films are performed at 3000 rpm for 30 sec with successive baking at 90 °C before annealing at higher temperature. The cleaning and priming of Si substrate is followed as mentioned elsewhere (Shi et al. 2016). Here STPYX were annealed at three different temperatures (900 °C, 700 °C and 235 °C).

## 3.3. STRUCTURAL CHARACTERIZATION

The structural characterization was performed with ATR-FTIR spectroscopy and XRD pattern at different annealing temperatures to highlight the structural growth.

### 3.3.1. XRD analysis

XRD measurement of the STPY07-DGC material annealed at three different annealing temperature (235, 700, 900 ºC) have a broad diffraction peak at 15° and 30° which is relatable to the amorphous nature of the $SiO_2$ component as in Fig. 3.2.

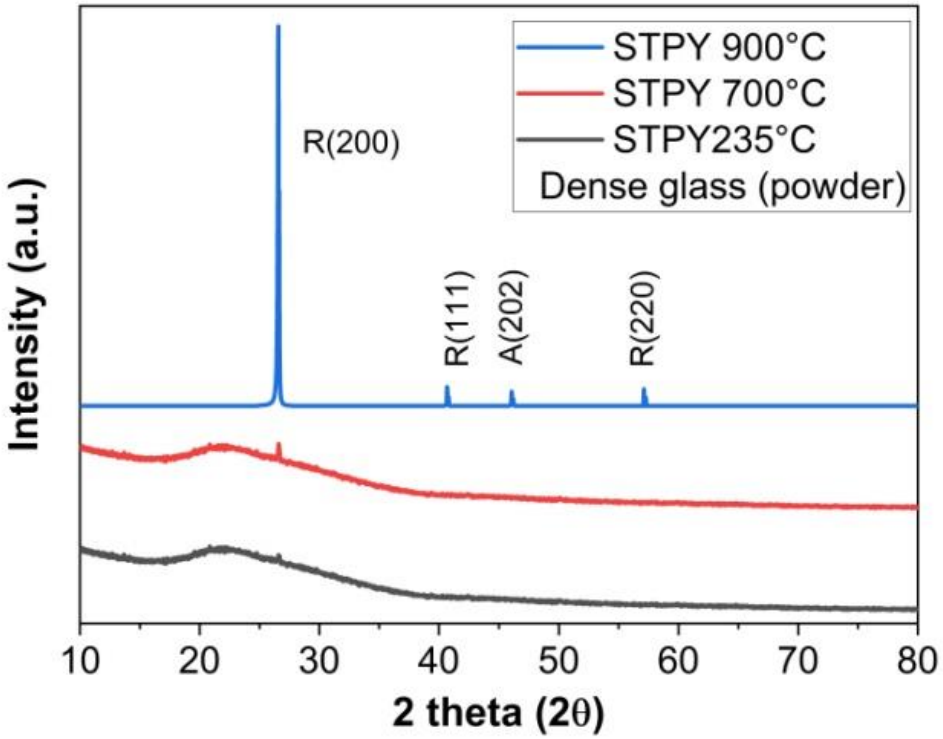


Figure 3.2: XRD spectra of the STPYX-DGC samples at different annealing temperature.

The crystalline growth of $TiO_2$ at higher annealing temperature (< 900 ºC) suppresses the amorphous nature of the as-synthesized material (El-Bashir 2017), (Amin et al. 2018). No amorphous diffraction peak of the α-cristobalite phase was observed for the STPY07-DGC material The diffraction peaks of $TiO_2$ nano-crystallites as rutile (200), rutile (111), anatase (202), and rutile (220) phase have been observed for two thetas (2θ) values at 26.64°, 40.64°, 46.08° and, 56.1° respectively as reported elsewhere (Ismail et al. 2007). The enhancement of intensity was observed with the escalation in annealing temperature. The temperature-dependent crystalline quality improvement of the $TiO_2$ compound can enhance the photoluminescence of

immovable $RE^{3+}$ ions in the crystalline host. Thus as-synthesized and -annealed STPY07-DGC material is converted into glass-ceramic at 900 ºC.

The STPYX-TF samples were observed as amorphous although Si substrate peaks (Fig 3.3) are observed due to the formation of cracks at higher annealing temperatures which is also confirmed by the SEM monograph. A shift in high annealing temperature is observed due to the possible formation of Anatasa phase (101) of $TiO_2$ which only can be confirmed if the film is annealed at a higher annealing temperature as mentioned elsewhere (Amin et al. 2018).

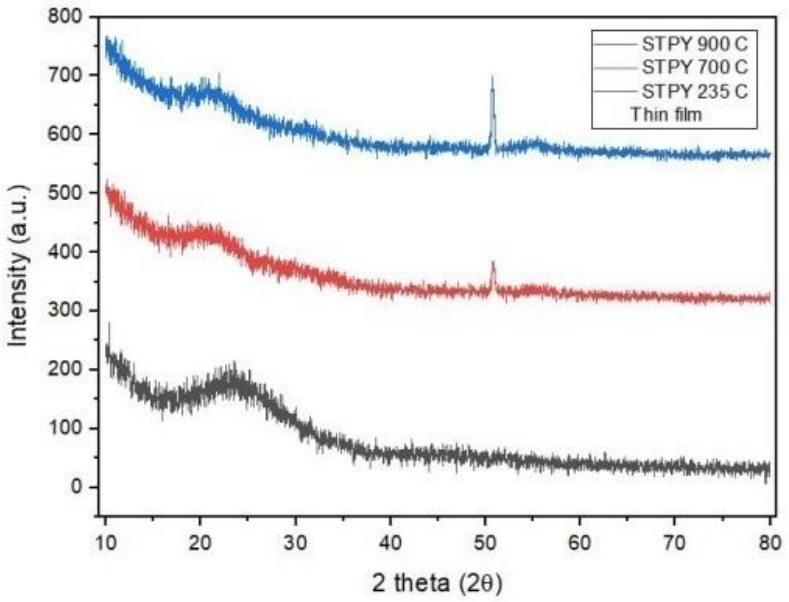


Figure 3.3: XRD spectra of STPY07-TF thin film at different annealing temperature.

The amorphous silica peak shift toward left and become narrow with rise in annealing temperature due to the crystallization. Thus homogeneous and regular dispersion of Ti and Si atoms in the composite solution is promoting Ti–O–Si bond along with $TiO_2$ particle in amorphous $SiO_2$ to offer a better host for $RE^{3+}$ ion doping (Amin et al. 2018).

### 3.3.2. ATR-FTIR Spectra

Figure 3 shows ATR-FTIR spectra of STPY07-xerogel and -DGC sample annealed at different temperature as in Fig 3.4. The FTIR absorption bands for the xerogel material around 3356 $cm^{-1}$ (Buarque et al. 2018) and 1658 $cm^{-1}$ due to the telescopic and angular vibrations of the $OH^-$ bond respectively (Sun et al. 2020). The removal of surface adsorbed water in the material annealed at higher temperatures (ca. 235, 700 and 900 ºC) is useful against hydroxyl-quenching (Wang et al. 2013). The Si–O–Si bonds with symmetric ($\upsilon_s$) and asymmetric ($\upsilon_{as}$) vibration were observed

from the absorption band around 779 and 1064 $cm^{-1}$ respectively (Chang et al. 2018), (Wang et al. 2013). The formation of $TiO_2$ crystallite is confirmed with corresponding peaks at 448 $cm^{-1}$ for Ti-O-Ti bridging stretching mode.

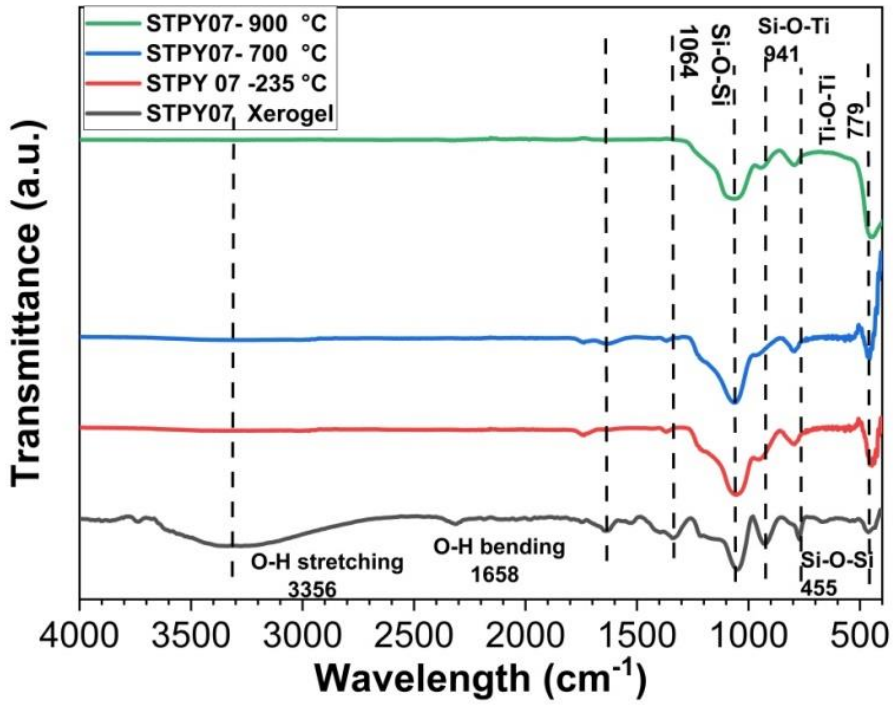


Figure 3.4: ATR-FTIR spectra of the STPY07-DGC sample at different annealing temperature.

The important result of this characterization is stretching vibration at 941 $cm^{-1}$ which can be attributed to the Si–O–Ti bond (non-bridging oxygen) formation during condensation reaction (Wang et al. 2013) and stretching mode [ $\tilde{\nu}Si\text{-}O_d$ ] of dangling Si-O (Chang et al. 2018). These results confirm the existence of oxygen-related defects in the host matrix which considerably impacts the luminescence properties of the STPY07-DGC materials.

Table 3.1: FTIR peak positions and its different assignments for STPY07-DGC samples

| Wavenumber ($cm^{-1}$) | Assignment | Observation intensity |
|---|---|---|
| **524** | Si-O, asymmetric stretching vibrations, O-Si-O stretching [*] | Strong, broad |
| **540** | NBO (Non-bridging oxygen) [*] | No peak |
| **612** | | |
| **671** | Si-O of $SiO_4$ symmetric bending [*] | No peak |
| **771** | OH | |
| **925** | Si-OH, $SiO^-$ group, Si-O-Ti bonds (Weisenbach et al. 1991), (Wang et al. 2013), | Strong |
| **1041** | Si-O-Si bonds (Wang et al. 2013), $SiO_2$ asymmetric stretching [*] | Intense peak |
| **1334** | Ti-O-Ti [*] | Minor peak |
| **3271** | OH stretching vibration of different Si-OH species and water molecule (Wang et al. 2013) | Broad, strong |

The presence of $RE^{3+}$ ion was not confirmed in the structural analysis $RE^3$which may be due to the lower concentration of $RE^{3+}$ ion in the host matrix structure or complete dissolution of $^+$ ion without agglomeration (J. et al. 2020).

## 3.4. Morphological characterization

The morphological characterizations of the STPY07-DGC and -TF samples were performed using the FETEM and FESEM analysis respectively.

### 3.4.1. FETEM analysis

FETEM micrographs of the annealed STPY07-DGC material were shown in Fig. 3.5 (a-b); the agglomeration of the composite is endorsed along with the occurrence of $TiO_2$ crystallite in the $SiO_2$ matrix. The observed border fogging confirms the existing connections among the silica particles (Wang et al. 2018). The amorphous nature of $SiO_2$ was confirmed with the diffuse nature of the selected area electron diffraction (SAED) pattern as in Fig 5 (c). Three bright spots in the SAED pattern were related to the anatase and rutile phase of $TiO_2$ nano-crystallites although the domination of amorphous $SiO_2$ over lower concentration of crystalline $TiO_2$

screened complete crystalline growth. The rise in annealing temperature and concentration of $TiO_2$ doping are developing crystalline nature although we fixed $TiO_2$ concentration (10 mol% of $SiO_2$) for the composite solution (Minehan, Messing, and Pantano 1989). The presence of Si, O, Ti, Pr, and Yb in the as-synthesized material was confirmed via FETEM-EDS spectra as in Fig 5(d).

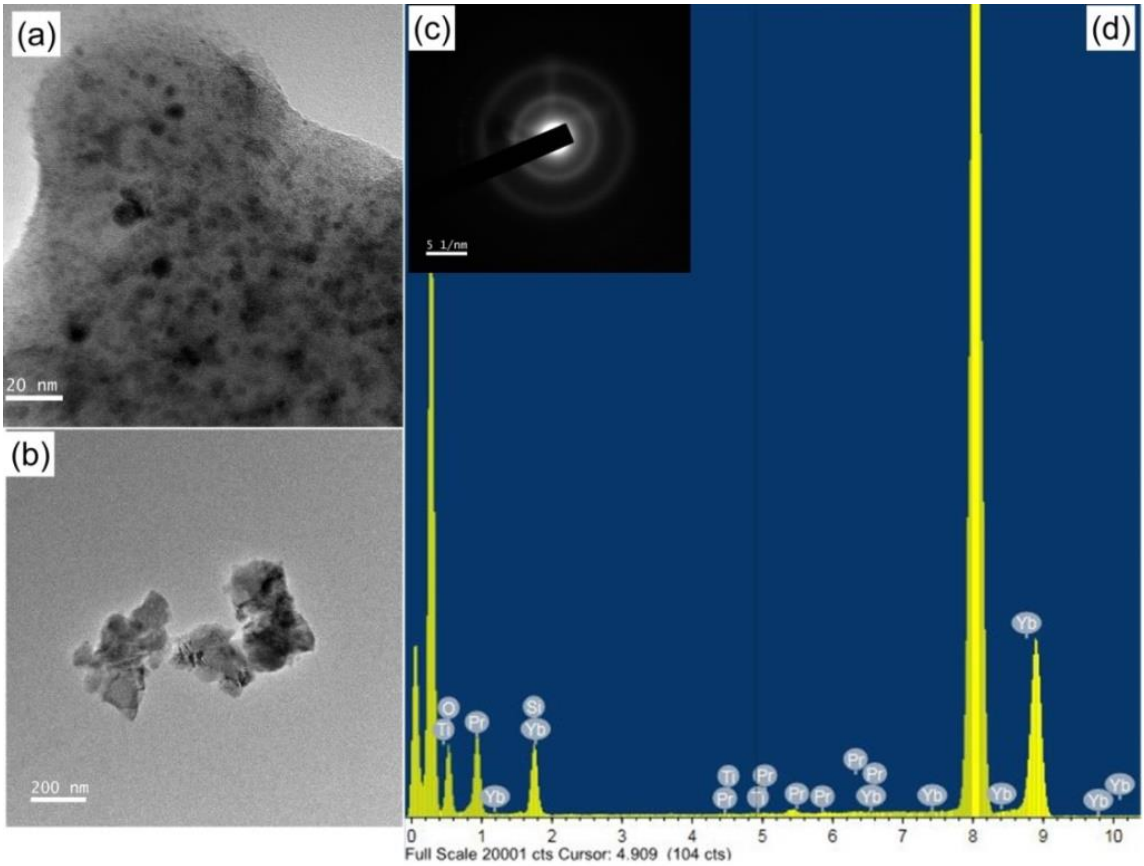


Figure 3.**5**: FETEM image at magnification bar at (a) 20nm (b) 200 nm, (c) SAED pattern, (d) EDS spectra of the annealed STPY07-DGC material.

### 3.4.2. FESEM analysis

FESEM micrographs of the STPY07-TF are reported with different scale bars as in Figure 3.6 (a-c). The large flaky size and large cracks with inhomogeneous distribution are observed throughout the coatings which is a consequence of high annealing temperature as it induces surface tension between the film and the air along with rise in capillary forces and generation of cracks on the surface (Halin et al. 2017). Figure 3.6 (b) and (c) are taken from the edges of the

samples and centre of flaky respectively. The porous nature of STPY07-TF can enhance the required antireflection and transmission properties of promising upconversion and downconversion layer on Si-solar cell.

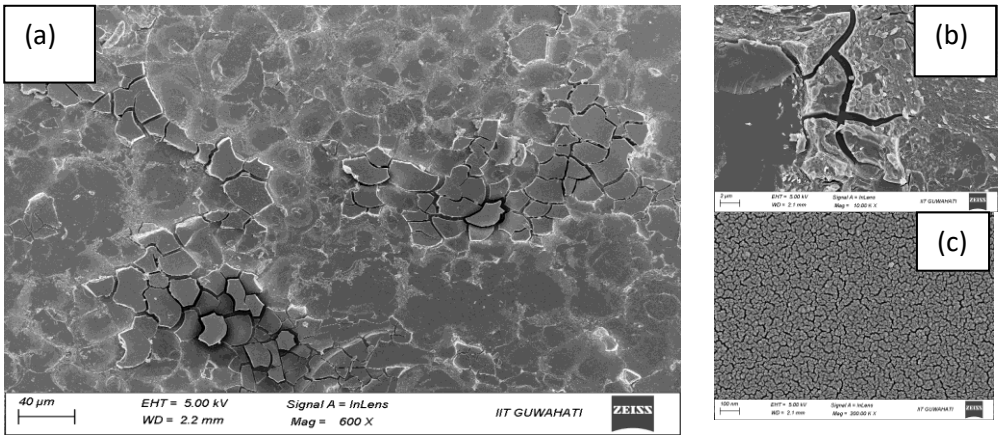


Figure 3.6 (a, b, c): SEM image of STPY07-TF annealed at 900 °C

SEM-EDS analysis of STPY07-TF was performed to investigate the presence of Si, Ti, O, Yb and Pr in the thin film which is confirmed as 51.6, 46.7, 0.8, 0.7 and 0.2 atomic % respectively as in Fig. 3.7.

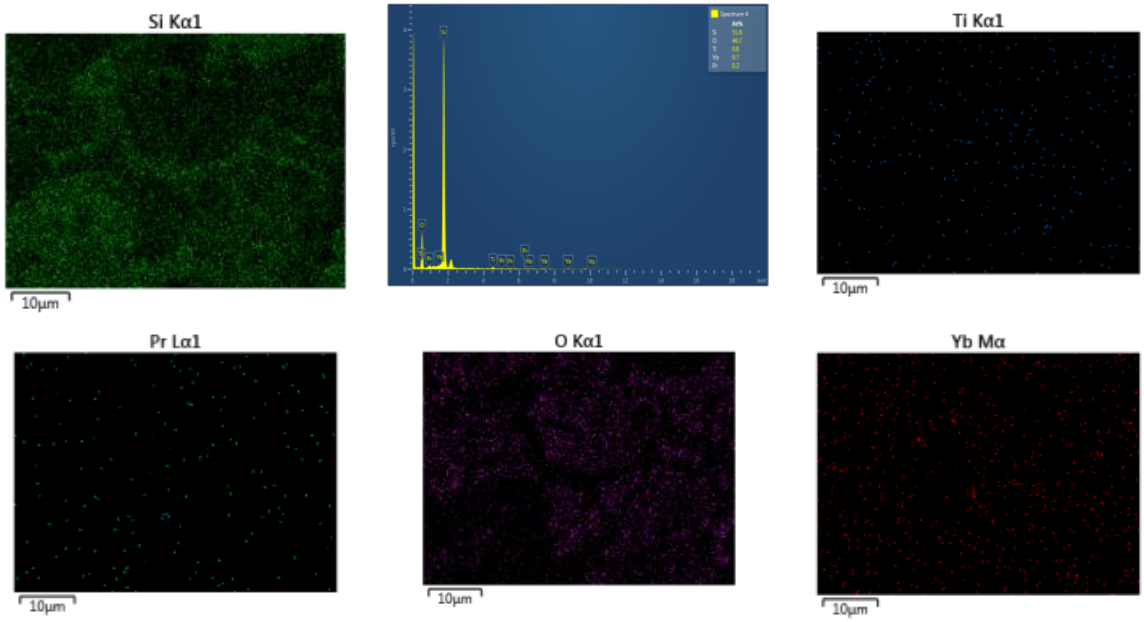


Figure 3.7: SEM-EDS image of the STPY07-TF annealed at 900 °C

SEM-EDS component mapping image of the STPY07-TF sample is cited with the location-specific identification of Ti, Si, O, Yb, and Pr in the thin film which are visually confirmed although component distribution is not very homogeneous due to evaporation of adsorbed water and trapped solvents present during coating.

## 3.5. THERMAL CHARACTERIZATION

The TG and DSC analyses of the STPY07-xerogel material with temperature rise are shown in Figure 3.8 (a, b). The TG curve depicts a gradual weight loss of around ~17% up to the remaining 83% mass for the original. The prominent exothermic peak in the DSC curve at around 70 ºC is due to the evaporation of adsorbed and absorbed water as shown in Fig. 3.8 (b) (Kakoti et al. 2019), (Zieliński et al. 2017). The glass transition temperature ($T_g$) at 60°C is an important parameter where the xerogel starts converting into dense glass. The decomposition of ethoxy and butoxy groups occurs in the 80-150 °C temperature range with a second exothermic peak in the DSC curve (Kakoti et al. 2019).

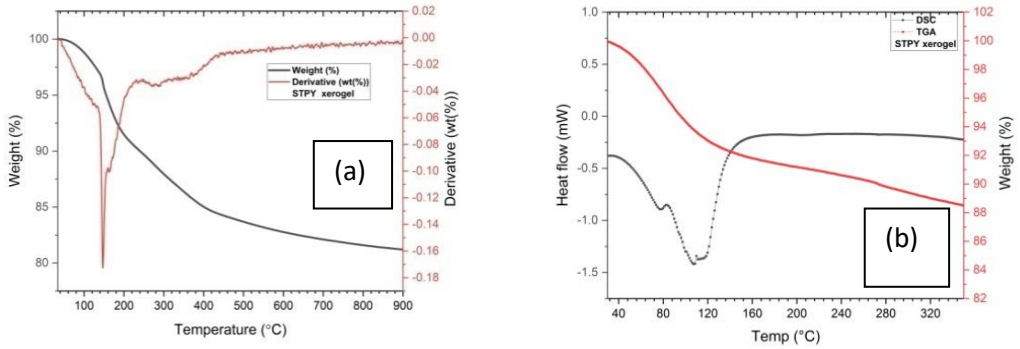


Figure 3.8: (a) TG-DTA and (b) TG-DSC curve of the STPY07- xerogel

The thermal stability of the STPY07-DSC material at higher temperatures is confirmed with an almost straight curve in the range ca. 450–900 °C. The nature of TG curves is independent of $RE^{3+}$ ion doping concentration (J. et al. 2020). The optical characterization of the STPYX-DGC material was performed in two ways. Initially, absorption spectra of the material were recorded to signify the possible excitation channels. In the next phase, the samples were excited with specific excitation wavelength to obtain the photoluminescence spectra. The

excitation wavelengths of photoluminescence studies were chosen to maximize the material's absorption cross-section.

## 3.6. Optical characterization

### 3.6.1. Absorption spectra

Fig. 3.9 shows that the absorption peaks of the STPY07-DGC material can easily be assigned to the earlier recorded spectra (Dwivedi, Rai, and Rai 2008). The absorption peaks have been confirmed for excitation of 4f electron from the ground state of $Pr^{3+}$ ions for a transition from ground state [$^3H_4$ ] to different excited state [$^3P_J$ (J=0,1,2), $^1D_2$]. The absorption peaks at 980 nm is relatable to the $^2F_{7/2} \rightarrow ^2F_{5/2}$ transition of $Yb^{3+}$ ion with the shoulder at 1060 nm due to the stark splitting of $^2F_{5/2}$ state (Liang et al. 2021), (Dwivedi et al. 2008) as depicted in schematic diagram Fig 3.12.

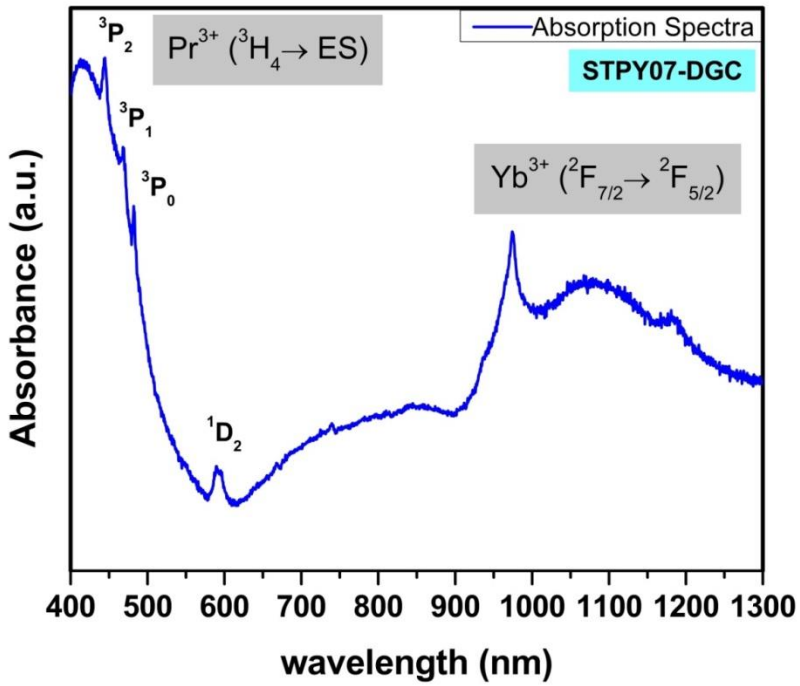


Figure 3.9: Absorption spectra of the STPY07-DGC material

### 3.6.2. Upconversion luminescence spectra

Fig. 3.10 shows a novel ultra-broadband UCL spectra of the STPYX-DGC materials for excitation photon of wavelength ($\lambda_{ex}$= 980 nm) for different $Yb^{3+}$ ion concentration. The broadband $^3P_1 \rightarrow {}^3H_J$ (450-750 nm), $^3P_0 \rightarrow {}^3F_{J=3,4,5}$ (450-750 nm) and $^3P_0 \rightarrow {}^1G_4$ (ca. 900 nm) transitions of $Pr^{3+}$ ion are assigned to the earlier recorded UCL spectra (Nizamutdinov et al. 2019), (Zou et al. 2016). The broad emission does hamper clear identification of the contribution of the $^3P_1 \rightarrow {}^3H_J$ transitions. The optimized UCL has been observed for material with $Yb^{3+}$ ion concentration of 1.5 mol%. The gradual intensity enhancement has been observed with an initial increase in $Yb^{3+}$ ion concentration to 1.5mol% and successively falls with further rise in $Yb^{3+}$ ion concentration. The transfer of energy from $Yb^{3+}$ to $Pr^{3+}$ ion is usually low due to the cross-relaxation between $Pr^{3+}$ ion (Dieudonné et al. 2013). The possibilities of energy back transfer from $Pr^{3+}$ ion to $Yb^{3+}$ and concentration quenching of $Yb^{3+}$ ion has been impacting quantum yield of UCL process (Dieudonné et al. 2013).

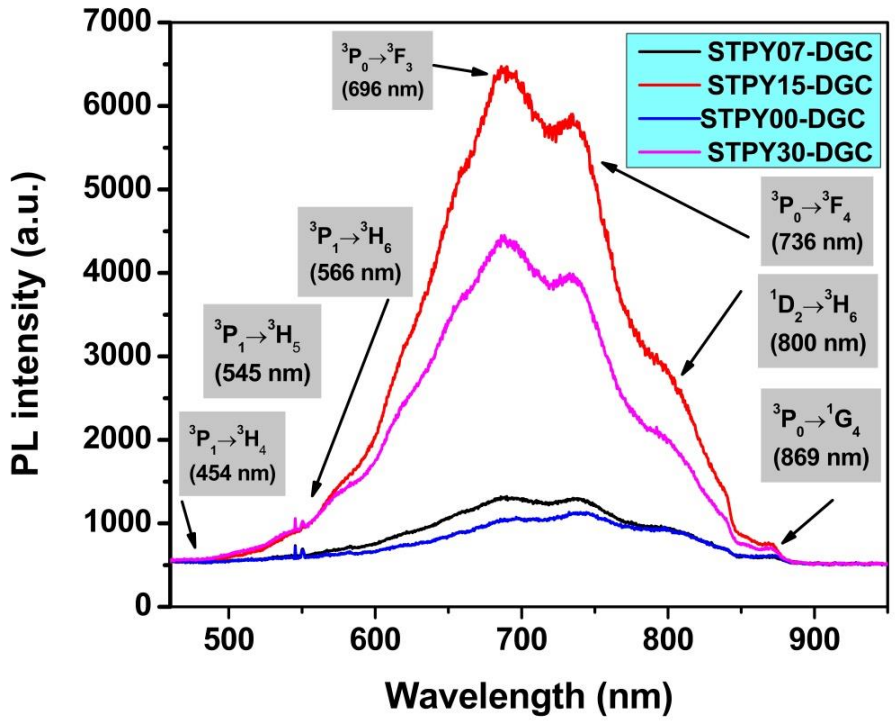


Figure 3.10: UCL spectra of the STPYX-DGC samples under 980nm excitation

### 3.6.3. Downconversion luminescence spectra

The DCL spectra of the STPYX-DGC materials were reported in the UV-VIS region, utilizing an excitation wavelength of $\lambda_{ex}$ = 450 nm (ca. 222222 $cm^{-1}$) corresponding to the $Pr^{3+}$: $^3H_4 \rightarrow {}^3P_2$ transition. The emission peaks typically stem from $^3P_0 \rightarrow {}^3H_{4,5,6}$ and $^3P_0 \rightarrow {}^3F_{2,3,4}$ transitions, along with the weaker $^1D_2 \rightarrow {}^3H_{4,5,6}$ transitions of the $Pr^{3+}$ ion, as illustrated in Fig 3.11 (Chen, Huang, and Zhang 2009) (Saeed, Coetsee, and Swart 2020). Non-radiative relaxation among the $^3P_2$ and $^3P_0$ multiplates occurs due to the narrow energy gap (Chen et al. 2009). The co-doping of $Yb^{3+}$ ion was anticipated to facilitate quantum cutting (QC) of one visible photon into two NIR photons, but this phenonomenon is not observed in the PL spectra of the $Pr^{3+}$ -$Yb^{3+}$ ion pairs (Wen and Tanner 2011). The maximum phonon energy of the $SiO_2$-$TiO_2$ binary host (ca. 1100 $cm^{-1}$) and the relatively small energy difference between the $^3P_0$ and $^1D_2$ states (ca. 3780 $cm^{-1}$) allow bridging the energy gap by three photons, initiating multiphonon relaxation from $^3P_0$ to $^1D_2$ multiplets (Wen and Tanner 2011).

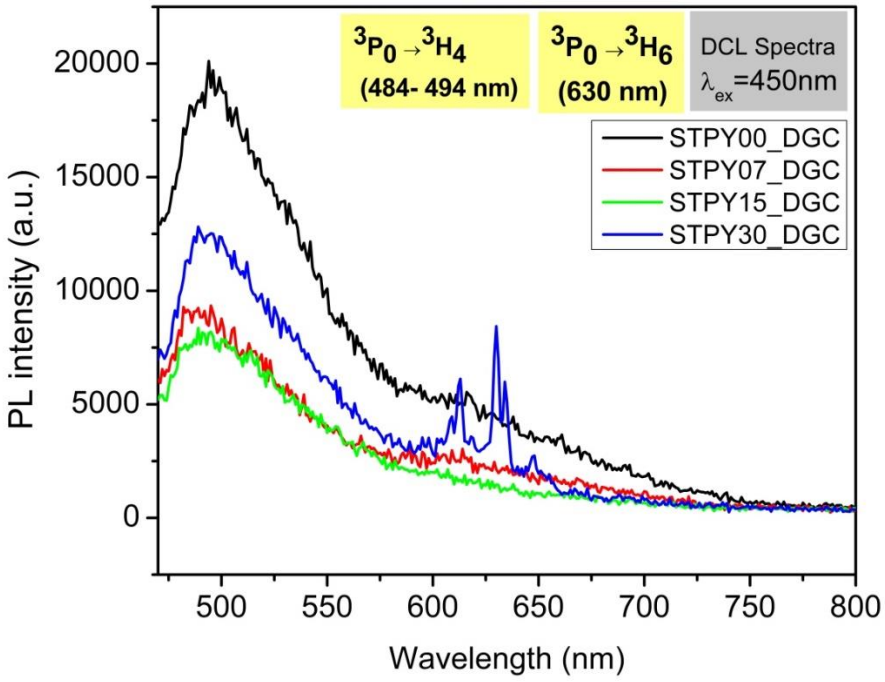


Figure 3.11: DCL spectra of the STPYX-DGC materials for 450 nm excitation

### 3.6.4. Results and discussion

#### 3.6.4.1. Judd–Ofelt (J-O) parameters

In accordance with the J–O theory (Judd and Lindgren 1961) (Ofelt 1962), the analysis of radiative transitions associated with the $4f^2$ configuration of $Pr^{3+}$ is rooted on the absorption spectra of $Pr^{3+}$ ion (Fig. 5) (Hehlen, Brik, and Kramer 2013), (Hua et al. 2017). The J–O intensity parameters [$\Omega_\lambda$ ($\lambda$ = 2, 4, and 6)] for $Pr^{3+}$ within the STPY07-DGC sample are determined through a least square fitting approach, utilizing both the experimentally derived oscillator strength ($f_{exp}$) and the calculated oscillator strength ($f_{cal}$), using the obtained squared matrix elements (Carnall, Fields, and Wybourne 1965). The intensity parameter $\Omega_2$ is notably susceptible to the asymmetry and covalency of the $RE^{3+}$ ions, while $\Omega_4$ and $\Omega_6$ are linked to the bulk property and rigidity of the materials, respectively. Higher values of $\Omega_2$ represent a pronouncedly asymmetrical and strongly covalent environment, owed to the presence of $TiO_2$, which changes the ligand field of $Pr^{3+}$ and thus achieves intense fluorescence emission (Hua et al. 2017).

Table 3.2: J-O intensity parameters and oscillator strengths of $Pr^{3+}$ ion

| **Transitions $^3H_4\rightarrow$** | **Wavelength (nm)** | **Energy ($cm^{-1}$)** | **$f_{exp}$ ($\times10^{-6}$)** | **$f_{exp}$ ($\times10^{-6}$)** | **$\Omega_2$** | **$\Omega_4$ ($10^{-20}$ $cm^2$)** | **$\Omega_6$** |
|---|---|---|---|---|---|---|---|
| $^1D_2$ | 589 | 16957 | 1.3302 | 0.7411 | | | |
| $^3P_o$ | 482 | 20705 | 0.4903 | 0.3088 | 7.014 | 0.4850 | 3.472 |
| $^3P_1$ | 469 | 21315 | 0.8305 | 0.9766 | | | |
| $^3P_2$ | 444 | 22487 | 1.6136 | 1.8073 | | | |
| | | | | | | | |
| Refractive Index =1.67 | (2J+1) = 9 | Thickness = 0.2 cm Radius = 0.8cm | | Concentration of $Pr^{3+}$ ion = 0.1280 mol/L | | | RMS= 0.6152 |

The comparison of J-O parameters of the $Pr^{3+}$ ion is tabulated in Table 3.3. Here $\Omega_2$ is sensitive to the structure and is also correlated with the symmetry and degree of covalency in the chemical bonds among the $Pr^{3+}$ ion and the coordinating ligands (Bokatial and Rai 2012). The relatively high value of $\Omega_6$ is correlated with the less rigid $TiO_2$-$SiO_2$ host matrix (Hehlen et al. 2013). The larger spectroscopic quality factor ($\Omega_4/\Omega_6$) indicates higher stimulated emission cross-section and lower photoluminescence intensity.

Table 3.3: Comparison of calculated Judd-Ofelt intensity parameters

| Host | $\Omega_2$ | $\Omega_4$ | $\Omega_6$ | $\Omega_4/\Omega_6$ |
|---|---|---|---|---|
| **Present work** | 7.014 | 0.4850 | 3.4728 | 0.1396 |
| **Tellurite** (Hua et al. 2017) | 2.07 | 3.23 | 3.56 | 0.6264 |
| **CdS- $SiO_2$** (Bokatial and Rai 2010) | 10.58 | 7.4 | 0.95 | 7.79 |

The assessment of radiative properties, such as probabilities of spontaneous emission ($A_{rad}$), luminescence branching ratios (β), and radiative lifetime ($\tau_{rad}$), for the optical transitions of $Pr^{3+}$ in the STPY07-DGC can be obtained using the J-O intensity parameters, which is presented in Table 3.4.

**Table 3.4: Radiative parameters**

| Transition | | Wavelength (nm) | Energy ($cm^{-1}$) | $A_R$ ($s^{-1}$) | $\beta_R$ (%) | τ (μs) |
|---|---|---|---|---|---|---|
| $^3P_1\rightarrow$ | $^3H_4$ | 468 | 21367 | 748.10 | 7.62 | 101.88 |
| | $^3H_5$ | 519 | 19267 | 1289.41 | 13.13 | |
| | $^3H_6$ | 586 | 17064 | 357.74 | 3.64 | |
| | $^3F_2$ | 611 | 16366 | 2991.1 | 30.47 | |
| | $^3F_3$ | 668 | 14970 | 5167.89 | 52.65 | |
| | $^3F_4$ | 687 | 14556 | 366.28 | 3.74 | |
| | | | $A_T$ = | 9814.68 $s^{-1}$ | | |
| $^1D_6\rightarrow$ | $^3H_4$ | 595 | 16806 | 216.25 | 10.40 | 481.28 |
| | $^3H_5$ | 678 | 14749 | 3.48 | 0.16 | |
| | $^3H_6$ | 800 | 12500 | 67.81 | 3.26 | |
| | $^3F_2$ | 842 | 11806 | 124.95 | 1.27 | |
| | $^3F_3$ | 956 | 10460 | 101.90 | 4.90 | |
| | $^3F_4$ | 995 | 10050 | 1563.37 | 75.24 | |
| | | | $A_T$ = | 2077.79 $s^{-1}$ | | |
| | | | $A_T$ ($s^{-1}$) = | 1297.86 μs | | |
| $^3P_0\rightarrow$ | $^3F_4$ | 718 | 13661 | 131.33 | 3.32 | 253.47 |
| | $^3F_2$ | 635 | 15748 | 2931.56 | 74.30 | |
| | $^3H_6$ | 608 | 16447 | 186.62 | 4.73 | |
| | $^3H_4$ | 482 | 20746 | 695.65 | 17.62 | |
| | | | $A_T$ = | 3945.18 $s^{-1}$ | | |

### 3.6.4.2. Energy transfer upconversion (ETU)

ETU mechanism of the $Pr^{3+}$-$Yb^{3+}$ ions pair is helpful in the transfer of energy among this activator to sensitizer ion pair as in Fig 3.12. In ground state absorption (GSA) of two NIR photon leads to excitation of $Yb^{3+}$ and $Pr^{3+}$ ions to respective excited state. The absorption of photon through the $^2F_{7/2} \rightarrow {}^2F_{5/2}$ transition path of $Yb^{3+}$ ion ends up transferring energy to a nearby ion at excited state. Thus excited electron of $Pr^{3+}$ ion jumps up from $^1G_4$ (10176 $cm^{-1}$) state to $^3P_0$ (20683 $cm^{-1}$) state. The population of $^3P_1$ (21302 $cm^{-1}$) state is also observed from emission spectra where thermal energy play critical role. Thus excited electron at $^3P_0$ and $^3P_1$ states may come to ground state ($^3H_4$) by emitting a photon of higher energy as shown in figure below. The intensity enhancement of UCL has a direct relationship with presence of more available $Yb^{3+}$ ion around each $Pr^{3+}$ ion which usually increases with the doping concentration of $Yb^{3+}$ ion. Here $Yb^{3+}$ ion plays a role of efficient activator by absorbing photon of 980 nm and transfer it into a nearby $Pr^{3+}$ ion. Further, rise in $Yb^{3+}$ ion concentration has negatively influenced luminescence because the excess acceptor ion ($Yb^{3+}$) promotes transfer of energy to a nearby acceptor ($Yb^{3+}$) ion in the ground state.

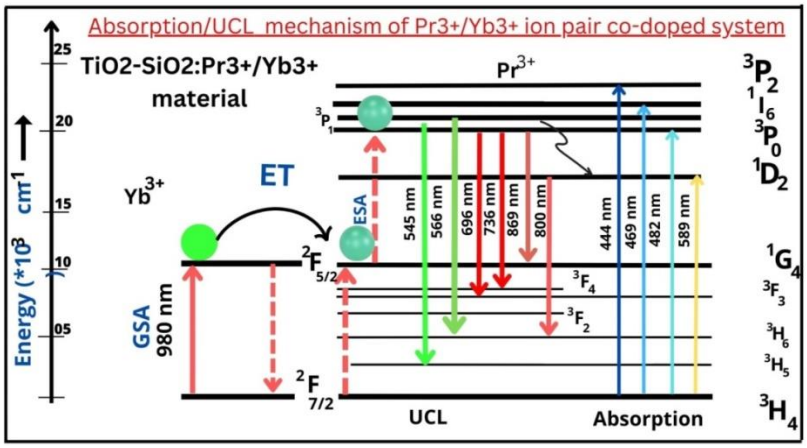


Figure 3.12: Schematic ETU mechanisms of $Pr^{3+}$-$Yb^{3+}$ ion pair in the STPYX-DGC material

The investigation on concentration dependence indicates that the UCL spectra are most effective when the concentration of $Yb^{3+}$ ions is twice that of $Pr^{3+}$ ions in the sample. Consequently, having two $Yb^{3+}$ ions surrounding one $Pr^{3+}$ ion enhances the desired luminescence

outcomes. However, a subsequent rise in the concentration of $Yb^{3+}$ ions adversely affects the intensity of the UCL spectra.

### 3.6.4.3. CIE-chromaticity diagram

Fig. 3.13 presents the CIE chromaticity coordinates of corresponding UCL of the STPYX-DGC materials. The change in CIE coordinates with respect to $Yb^{3+}$ ion concentration towards red region endorses color tunability of the as-synthesized material.

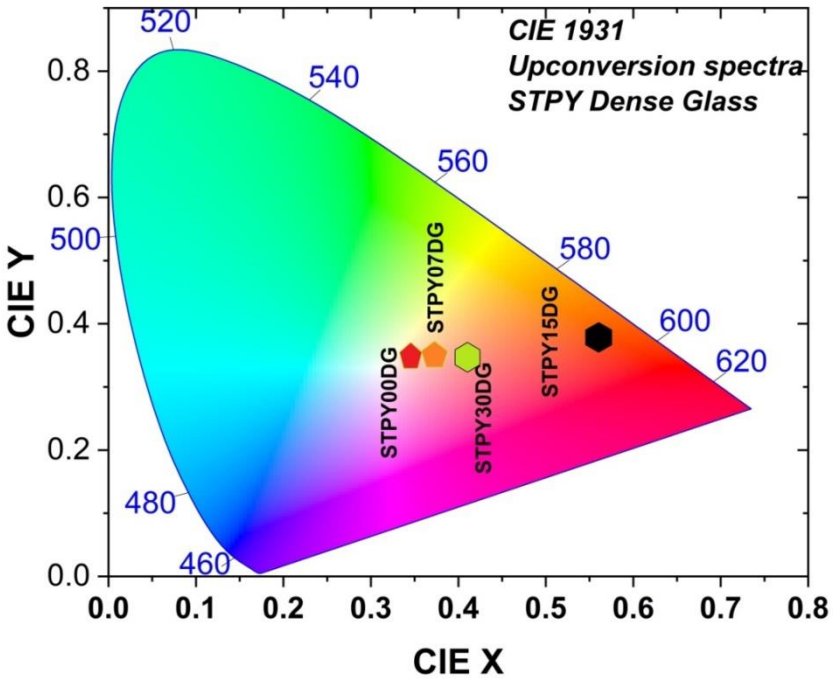


Figure 3.13: CIE chromaticity diagram of the STPYX-DGC material at different $Yb^{3+}$ ion concentration (Color is indicative only)

### 3.6.4.4. Confocal PL microscopy

Figure 3.14 represents confocal PL mapping of the STPY15-DGC material at 980 nm excitation wavelengths, observed as the most intense among all other as-synthesized materials. It also cites a non-uniform UCL intensity distribution due to the uneven topological surface of the material in powder form. Thus, PL mapping results of the STPY15-DGC materials endorse throughout spatial UCL emission (Kumar et al. 2018).

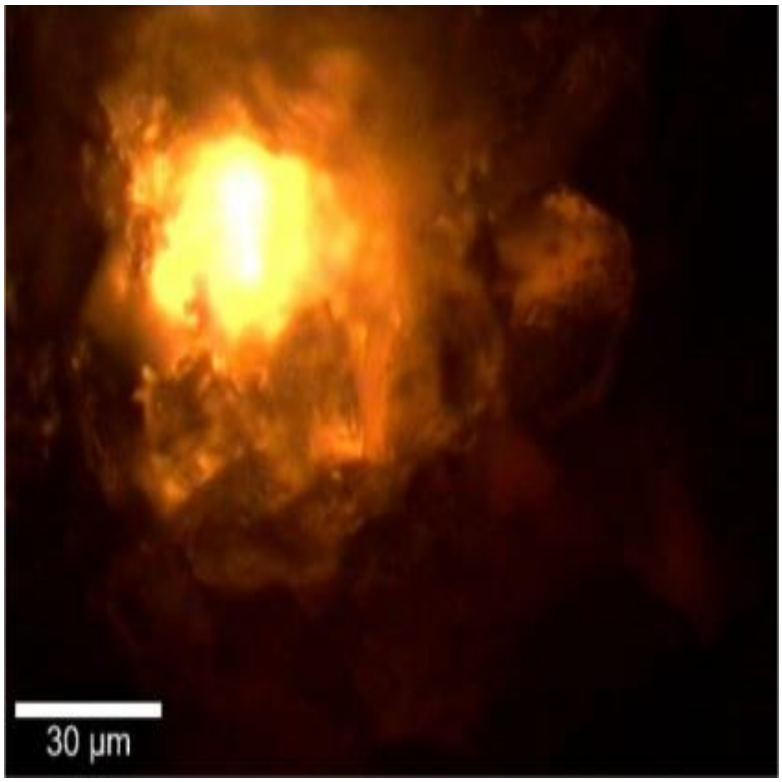


Figure 3.14: PL confocal mapping of the STPY15-DGC material

## 3.7. CONCLUSIONS

In conclusion, the STPY07-DGC and -TF materials have been successfully synthesized using an improved *ex-situ* sol-gel method and annealed at three different annealing temperatures (235, 700 & 900 ºC). The absence of OH- molecules with increasing annealing temperatures offers an advantage against the hydroxyl quenching of luminescence. The formation of a pure oxide phase, as well as non-bridging oxygen (Ti-O-Si) bonds, promotes an asymmetric $TiO_2$-$SiO_2$ binary host.

The presence of anatase and rutile phases of $TiO_2$ nano-crystallites in an amorphous $SiO_2$ background at higher annealing temperatures supports the luminescence of $Pr^{3+}$ and $Yb^{3+}$ ions in a crystalline environment, where the $RE^{3+}$ ions are immobilized in crystalline surroundings. The existence of the $Pr^{3+}$ and $Yb^{3+}$ ion pair was confirmed by the EDS spectra. Based on TG/DSC analyses, the material was found to be thermally stable, with thermal decomposition identified at 80 and 120 ºC. Therefore, the material can remain stable even in adverse environmental conditions. From optical analysis, an ultra-broadband UCL of the STPYX-DGC materials was obtained for the first time, optimized for the STPY15-DSC material. PL confocal mapping of the STPY15-DGC material confirms UCL throughout the space material in powder form. The concentration of $Yb^{3+}$ ion has been observed as a color-tunable factor of UCL spectra from white to red. The obtained outcomes endorse that the STPY15-DGC material is optically active and capable of ultra-broadband red UCL for near-infrared excitation at 980nm, suitable for diverse photonic applications such as solar photovoltaic, thermal sensor, lighting and display device, soft robotics, soft electronics etc. The as-synthesized STPYE07-DGC material has been observed as optically active with possible application in various photonic applications.

## REFERENCES


Amin, Peshawa O., Asmaa J. Kadhim, Majida A. Ameen, and Rebar T. Abdulwahid. 2018. "Structural and Optical Properties of Thermally Annealed TiO2–SiO2 Binary Thin Films Synthesized by Sol–Gel Method." *Journal of Materials Science: Materials in Electronics* 29(18):16010–20. doi: 10.1007/s10854-018-9688-6.

Bokatial, L., and S. Rai. 2010. "Optical Properties and Up-Conversion of Pr 3 + Doped CdS Nanoparticles in Sol – Gel Glasses." *Journal of Luminescence* 130(10):1857–62. doi: 10.1016/j.jlumin.2010.04.022.

Bokatial, Litul, and S. Rai. 2012. "Optical Properties of Sm 3 + Ions in Sol-Gel Derived Alumino-Silicate Glasses." *J Opt* 41(June):94–103. doi: 10.1007/s12596-012-0069-x.

Buarque, Juliana M. M., Danilo Manzani, Sérgio Luis Scarpari, Marcelo Nalin, Sidney J. L. Ribeiro, Jennifer Esbenshade, Marco A. Schiavon, and Jefferson L. Ferrari. 2018. "SiO2-TiO2 Doped with Er3+/Yb3+/Eu3+ Photoluminescent Material: A Spectroscopy and Structural Study about Potential Application for Improvement of the Efficiency on Solar Cells." *Materials Research Bulletin* 107:295–307. doi: 10.1016/j.materresbull.2018.07.007.

Carnall, W. T., P. R. Fields, and B. G. Wybourne. 1965. "Spectral Intensities of the Trivalent Lanthanides and Actinides in Solution. I. Pr3+, Nd3+, Er3+, Tm3+, and Yb3+." *The Journal of Chemical Physics* 42:3797–3806. doi: 10.1063/1.1695840.

Chang, Meiqi, Yanhua Song, Lei Cui Jie Chen, Zhan Shi, Ye Sheng, and Haifeng Zou. 2018. "Photocatalytic and Photoluminescence Properties of Core- Shell SiO2@TiO2:Eu3+,Sm3+ and Its Etching Products." *ACS Sustainable Chemistry & Engineering* 6(1):223–36. doi: 10.1021/acssuschemeng.7b02285.

Chen, Hsueh Shih, Sheng Hsin Huang, and Tsong Pyng Perng. 2012. "Preparation and Characterization of Molecularly Homogeneous Silica-Titania Film by Sol-Gel Process with Different Synthetic Strategies." *ACS Applied Materials and Interfaces* 4(10):5188–95. doi: 10.1021/am301113a.

Chen, X. P., X. Y. Huang, and Q. Y. Zhang. 2009. "Concentration-Dependent near-Infrared Quantum Cutting in NaYF4: Pr3+, Yb3+phosphor." *Journal of Applied Physics* 106(6):3–7. doi: 10.1063/1.3224906.

Dieudonné, B., B. Boulard, G. Alombert-Goget, A. Chiasera, Y. Gao, S. Kodjikian, and M. Ferrari. 2013. "Up- and down-Conversion in Yb3+-Pr3+ Co-Doped Fluoride Glasses and Glass Ceramics." *Journal of Non-Crystalline Solids* 377:105–9. doi: 10.1016/j.jnoncrysol.2012.12.025.

Dwivedi, Y., Anita Rai, and S. B. Rai. 2008. "Intense White Upconversion Emission in Pr / Er / Yb Codoped Tellurite Glass." *Journal of Applied Physics* 104(043509):1–4. doi: 10.1063/1.2969046.

El-Bashir, S. M. 2017. "Physical Properties Nd3+ Doped (SiO2-TiO2) Monolithic Glass for Photoresistor Applications." *Materials Research Express* 4(11):0–6.

Halin, D. S. C., M. M. A. B. Abdullah, N. Mahmed, S. N. A. Abdul Malek, P. Vizureanu, and A. W. Azhari. 2017. "Synthesis and Characterization of TiO2/SiO2 Thin Film via Sol-Gel Method." *IOP Conference Series: Materials Science and Engineering* 209(1). doi: 10.1088/1757-899X/209/1/012002.

Hehlen, Markus P., Mikhail G. Brik, and Karl W. Kramer. 2013. "50th Anniversary of the Judd – Ofelt Theory : An Experimentalist ' s View of the Formalism and Its Application." *Journal of Luminescence* 136:221–39. doi: 10.1016/j.jlumin.2012.10.035.

Hua, Chenxiao, Xin Zhao, Yue Bun, and Hai Lin. 2017. "Pr3+ Doped Tellurite Glasses Incorporated with Silver Nanoparticles for Laser Illumination." *RSC Adv.* 7:55691–701. doi: 10.1039/c7ra11594f.

Ismail, Adel Ali, Mostafa Abboudi, Paul Holloway, and Hassan El-Shall. 2007. "Photoluminescence from Terbium Doped Silica-Titania Prepared by a Sol-Gel Method." *Materials Research Bulletin* 42(1):137–42. doi: 10.1016/j.materresbull.2006.05.002.

J., Manju Gopinath R., Subash Gopi, Sanu Mathew Simon, A. C. Saritha, P. R. Biju, and N. V Unnikrishnan. 2020. "Spectroscopic Analysis of Eu3+ Doped Silica– Titania– Polydimethylsiloxane Hybrid ORMOSILs." *RSC Adv.* 10:20057–66. doi: 10.1039/d0ra03073b.

Judd, B. R., and I. Lindgren. 1961. "Theory of Zeeman Effect in the Ground Multiplets of Rare-Earth Atoms." *Physical Review* 122(6):1802–12. doi: 10.1103/PhysRev.122.1802.

Kakoti, D., P. Dutta, P. Gogoi, N. Dehingia, N. Rajkonwar, A. Boruah, A. T. T. Mostako, P. K. Saikia, and P. K. Gogoi. 2019. "Effect of ZnS Nanoparticles on the Judd-Ofelt and Radiative Parameters of Sm3+ Ions in Sol-Gel Silica Matrix." *Journal of Luminescence* 211(April):401–12. doi: 10.1016/j.jlumin.2019.03.063.

Kumar, Pawan, Kanika, Satbir Singh, Rimli Lahon, Abhiram Gundimeda, Govind Gupta, and Bipin Kumar Gupta. 2018. "A Strategy to Design Lanthanide Doped Dual-Mode Phosphor Mediated Spectral Convertor for Solar Cell Applications." *Journal of Luminescence* 196(October 2017):207–13. doi: 10.1016/j.jlumin.2017.12.035.

Liang, Leben, Zhifeng Mo, Biao Ju, Changming Xia, and Zhiyun Hou. 2021. "Visible and Near-Infrared Emission Properties of Yb 3 + / Pr 3 + Co-Doped Lanthanum Aluminum Silicate Glass." *Journal of Non-Crystalline Solids* 557(September 2020):120578. doi: 10.1016/j.jnoncrysol.2020.120578.

Livage, J. 2004. *BASIC PRINCIPLES of SOL-GEL CHEMISTRY*. Technologi. edited by M. A. Aegerter and M. Mennig. Boston, MA: Springer.

Minehan, W. T., G. L. Messing, and C. G. Pantano. 1989. "Titania-Silica Glasses Prepared by Sintering Alkoxide Derived Spherical Colloids." *Journal of Non-Crystalline Solids* 108(2):163–68. doi: 10.1016/0022-3093(89)90579-6.

Nizamutdinov, A. S., S. V Kuznetsov, V. A. Konyushkin, A. N. Nakladov, E. I. Madirov, V. V Voronov, A. R. Khadiev, M. A. Marisov, and V. V Semashko. 2019. "LUMINESCENCE

OF GdF 3 : Pr : Yb AND YF 3 : Pr : Yb SOLID SOLUTIONS SYNTHESIZED BY CRYSTALLIZATION FROM THE MELT." *Journal of Applied Spectroscopy* 86(5):795–801. doi: 10.1007/s10812-019-00895-1.

Ofelt, G. S. 1962. "Intensities of Crystal Spectra of RareEarth Ions." *The Journal of Chemical Physics* 37(May 2012):511–20. doi: 10.1063/1.1701366.

Saeed, N. A. M., E. Coetsee, and H. C. Swart. 2020. "Down-Conversion of YOF: Pr3+, Yb3+ Phosphor." *Optical Materials* 110(February):110516. doi: 10.1016/j.optmat.2020.110516.

Shi, Gang, Jie Chen, Likui Wang, Dawei Wang, Jingguo Yang, Ying Li, Liping Zhang, Caihua Ni, and Lifeng Chi. 2016. "Titanium Oxide/Silicon Moth-Eye Structures with Antireflection, p–n Heterojunctions, and Superhydrophilicity." *Langmuir* 32(41):10719–24. doi: 10.1021/acs.langmuir.6b03117.

Sun, Xiaoyu, Xiaozhuang Xu, Guanyu Song, Jielei Tu, Lei Li, Pinyuan Yan, Weinan Zhang, and Kai Hu. 2020. "Preparation of MgF2/SiO2 Coating with Broadband Antireflective Coating by Using Sol–Gel Combined with Electron Beam Evaporation." *Optical Materials* 101(November 2019):2–10. doi: 10.1016/j.optmat.2020.109739.

Wang, Shuangyue, Hongwei Yan, Dengji Li, Liang Qiao, Shaobo Han, Xiaodong Yuan, and Wei Liu. 2018. "TEM and STEM Studies on the Cross- Sectional Morphologies of Dual- / Tri-Layer Broadband SiO 2 Antireflective Films." *Nanoscale Research Letters* 13(49):0–8. doi: 10.1186/s11671-018-2442-4.

Wang, Xiaodong, Guangming Wu, Bin Zhou, and Jun Shen. 2013. "Thermal Annealing Effect on Optical Properties of Binary TiO 2 -SiO 2 Sol-Gel Coatings." *Materials* 6:76–84. doi: 10.3390/ma6010076.

Weisenbach, Lon, Brian J. J. Zeinski, John O. Kelly, Jeanne Morreale, Ronald L. Roncone, and James J. Burke. 1991. "The Influence of Processing Variables on the Optical Properties of SiO2-Ti02 Planar Waveguides." *Submolecular Glass Chemistry and Physics* 1590:50–58.

Wen, Hongli, and Peter A. Tanner. 2011. "Energy Transfer and Luminescence Studies of Pr3+, Yb 3+ Co-Doped Lead Borate Glass." *Optical Materials* 33(11):1602–6. doi: 10.1016/j.optmat.2011.04.024.

Zieliński, Michał, Bogdan Czajka, Mariusz Pietrowski, Iwona Tomska-Foralewska, Emilia Alwin, Monika Kot, and Maria Wojciechowska. 2017. "MgO-MgF2 System Obtained by Sol–Gel Method as an Immobilizing Agent of the Electrolyte Applied in the High Temperature Cells." *Journal of Sol-Gel Science and Technology* 84(2):368–74. doi: 10.1007/s10971-017-4495-8.

Zou, Zehua, Lin Feng, Cheng Cao, Jiachi Zhang, and Yuhua Wang. 2016. "Near-Infrared Quantum Cutting Long Persistent Luminescence." *Scientific Reports* 6(May):1–7. doi: 10.1038/srep24884.

*CHAPTER- 4*

# STRUCTURAL, MORPHOLOGICAL, THERMAL AND OPTICAL CHARACTERIZATION of *EX-SITU* SOL-GEL SYNTHESIZED $Nd^{3+}$ - $Yb^{3+}$ ION CODOPED ZINC- SILICATE (SZNYX) DENSE GLASS CERAMIC

***This chapter is focused on synthesis of SZNYX-DGC and -TF along with structural, morphological, thermal and optical characterization of these samples.***

*Chapter- 4*

---

**Structural, morphological, thermal and optical characterization of *ex-situ* sol-gel synthesized $Nd^{3+}$-$Yb^{3+}$ ion co-doped Zinc- Silicate dense glass and thin-film**

---

## 4.1. INTRODUCTION:

Herein, $Nd^{3+}$ (0.7 mol%) and $Yb^{3+}$ (X mol%; X= 0.0, 0.7, 1.5, 3.0) ions co-doped zinc-silicate (SZNYX) solution were prepared through ex-situ sol-gel method. The SZNYX final solutions were further used to prepare dense glass-ceramic (DGC) and thin film (TF) samples. The structural characterization of the SZNY07-DGC sample was performed using the X-ray diffraction (XRD) pattern and Fourier transformations infrared spectroscopy at different annealing temperatures to investigate the structural evolution of the sample at different annealing temperatures. The morphological characterization of the SZNYX-DGC and -TF samples were analyzed via Transmission electron microscopy (TEM) and Scanning electron microscopy (SEM) respectively. The energy dispersion spectroscopy (EDS) was used to understand the doping purity of the samples. The thermal characterization of the SZNY07 xerogel was performed using thermogravimetric (TG) analyzer and differential scanning calorimetry (DSC) to record the difference in the amount of heat required to increase the temperature with respect to the copper crucible as a reference material. Finally, optical properties of the resulting STPYX-DGC materials were investigated using absorption and photoluminescence spectroscopy.

## 4.2. SYNTHESIS: $RE^{3+}$ ion co-doped $ZnO$-$SiO_2$ binary composite

The SZNYX solutions were prepared with an *ex-situ* sol-gel route where two different solutions of "MEA stabilized-ZnO" and "activated-$SiO_2$" were admixed to have ZnO-$SiO_2$ composite solutions. The phase separation is inevitable during the

hydrolysis-condensation process because TEOS and water are not miscible with each other. Pre-mixing of TEOS with MeOH improves dispersion in water. The pH of the solution was kept below 1.5 to maintain the viscosity. The mol ratio of TEOS to water (r=1) was maintained initially to prepare "activated-$SiO_2$". The "activated-$SiO_2$" solution was stirred vigorously for 90 min at 60 $^0$C. The molar ratio TEOS: MeOH: $H_2O$: $HNO_3$ = 1: 30: 1: 0.5 was maintained for the $SiO_2$ solution. "MEA stabilized -ZnO" solution was prepared by admixing zinc acetate di-hydrate to MeOH where MEA was added dropwise as a stabilizer under continuous stirring for 15 min at 60 °C to transform into a jelly-like solution. The molar ratio for zinc acetate di-hydrate and MEA is maintained at 3:1. The "MEA stabilized-ZnO" and "activated-$SiO_2$" solutions were admixed to have final solutions of 1:9 mol ratio Finally, $Nd^{3+}$ and $Yb^{3+}$ ions salt was dissolved in MeOH before being admixed to the mixture under continuous stirring for another hour. The DI water was added in the final stage to maintain Si: water (1:4) molar ratio to complete the hydrolysis and condensation. The final solution was transformed into the SZNYX-xerogel samples in a sealed container after three weeks at room temperature. The xerogel samples were initially dried slowly from room temperature to 235 °C in a hot air oven and then annealed further up to 900 °C at the rate of 1 °C per min in an electric muffle furnace. The xerogel samples were dried slowly up to 235 °C in a hot air oven and then annealed to form dense glass through annealing up to 900 °C at the rate of 1°C per min for 1hr in a muffle furnace. Here SZNY00, SZN07, SZNY15, and SZNY30 are representing the SZNYX-DGC samples with $Yb^{3+}$ ion molar concentration X= 0.0, 0.7, 1.5, and 3.0 mol% of total mol of [Si+Zn] in the binary solution respectively.

The SZNYX-TF samples were prepared on cleaned Si wafer from final SZNYX solution after aging for one week. The spin-coating of these thin films are performed at 3000 rpm for 30 sec with successive baking at 90 °C before annealing at higher temperature. The cleaning and priming of Si substrate is followed as mention elsewhere (Shi et al. 2016) . Here SZNY were annealed at three different temperatures (900 °C, 700 °C and 235 °C).

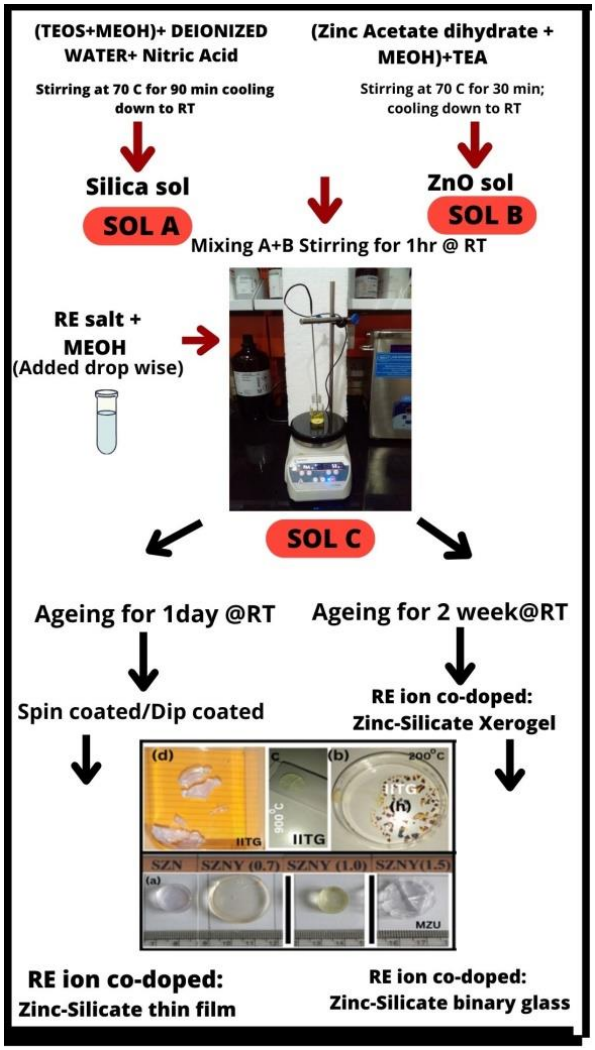


Figure 4.1: Schematic diagram of preparation of the SZNY binary host

## 4.3. STRUCTURAL CHARACTERIZATION

The structural characterization of the SZNY07-DGC and -TF samples were performed using the X-ray diffraction (XRD) pattern and Fourier transformations infrared spectroscopy.

### 4.3.1. XRD analysis

The XRD patterns of the SZNY07-DGC sample annealed at different temperatures were obtained as shown in Fig. 4.2. It has an amorphous halo between 15° and 30° which is a characteristic of the $SiO_2$ component of the host matrix. The peaks of ZnO crystallites are weakly visible because of the low concentration of ZnO (El-Bashir 2017) or the low annealing temperature (Amin et al. 2018). The XRD pattern

revealed different peaks at 2θ = 20.86° (012), 26.64° (220), 35.16° (042), 39.42° (104), 40.28° (502), 40.72° (241), 42.44° (502), 45.82° (600), 50.12° (161), 54.10° (054), 59.62° (006), 64.3° (306), 68.8° (345), and 75.7° (713), indexed as α-$Zn_2SiO_4$ crystal phase as in Fig 4.2 (Chandraboss et al. 2013). The intensity enhancement of the diffraction peak is observed for the SZNY07-DGC sample with the rise in annealing temperature which is a clear indication of crystalline quality improvement (Tung et al. 2016). The formation of a tetragonal willemite $Zn_2SiO_4$ structure with R-3(148) has been confirmed after comparison with JCPDS card No: 00-008-0492. The SZNY07-DGC sample is converted into glass-ceramic at 235 °C with the rise in annealing temperature. The annealing temperature is related to the conversion from the amorphous to the crystalline phase. These results are further extended to other as-synthesized samples. The presence of the optical center ($Nd^{3+}/Yb^{3+}$ ion) in the ZnO neighborhood promotes luminescence enhancement (Bang et al. 2005), (Hien et al. 2019).

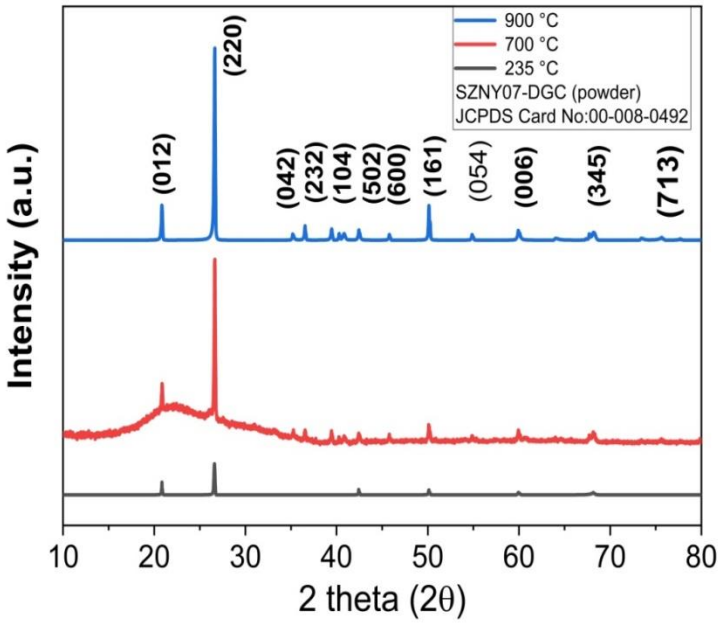


Figure 4.2: XRD pattern of the SZNY07-DGC sample annealed at different temperature

The XRD pattern of the SZNY07-TF samples, annealed at 235, 700 and 900 °C were observed with peaks at 2θ = 20.86°, 26.64°, 35.16°, 36.6°, 39.42°, 40.28°, 40.72°, 42.44°, 45.82°, 50.12°, 54.10°, 59.62°, 64.3°, 67.9°, 68.8°, 73.8° 75.7° and 75.7° which can be indexed as α-$Zn_2SiO_4$ crystal phase as in Fig 4.3 (b) (Chang et al. 2018). The crystalline growth in SZPY07-TF sample annealed at 235 C was hindered either due to the with lower thickness or lower annealing temperature which may further affect the detection sensitivity of XRD instrument (Amin et al. 2018). The SZNY-TF sample annealed at 700 and 900 ºC were crystalline in nature.

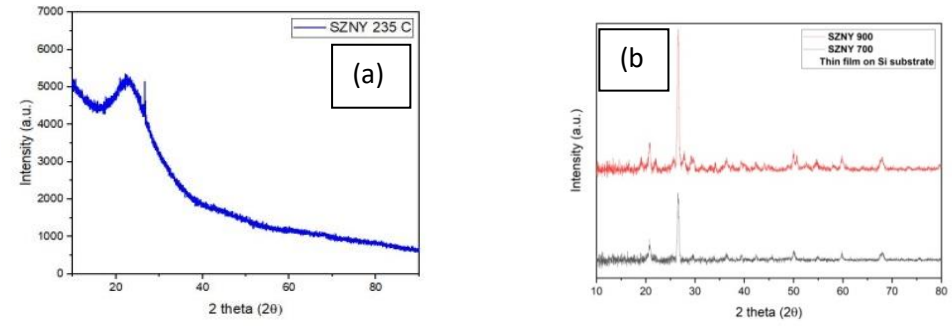


Figure 4.3: XRD pattern of the SZNY07-TF samples annealed at (a) 235 $^{o}$C (b) 700 & 900$^{o}$ C.

### 4.3.2. ATR-FTIR Spectra

The ATR-FTIR spectroscopy has been used as an effective tool for analyzing the chemical and structural changes of the SZNY07-DGC sample annealed at different temperatures in the range of 400-4000 $cm^{-1}$ (Fig. 4.4). The absorption bands at ~ 3356 and 1658 $cm^{-1}$ occur due to the stretching and bending vibrations of surface adsorbed water and OH groups respectively which slowly removed with a rise in annealing temperature. The Si–O–Si bonds with asymmetric stretching of bridging oxygen (BO) are observed at around 1054 $cm^{-1}$ (Lee et al. 2017). The overlapping of the intense band of bending vibration δ(Si-O-Si) at 440 $cm^{-1}$ and the D2 band at 603 $cm^{-1}$ of amorphous $SiO_2$ are creating difficulties in distinguishing the characterized vibrations of ZnO in the SZNY07-DGC sample from Fig 4.4 (Tran et al. 2017). The

interface of zinc silicate has been evident from the materialization of a shoulder at 950 $cm^{-1}$ because of Zn-O-Si vibration, it also stands for the penetration of Zn into the Si glass matrix (Raevskaya et al. 2014), (Galedari and Rahmani 2017). The formation of non-bridging oxygen (NBO) promotes absorption enhancement along with alteration of absorption edge and decrease in band gap (Lee et al. 2017) which is evident from the sharpness of peaks towards the lower wavenumber region. The ATR-FTIR results confirm the complete removal of hydroxyl impurity and the presence of oxygen-related defects in the host matrix which significantly influences the luminescence properties of the SZNY07-DGC sample.

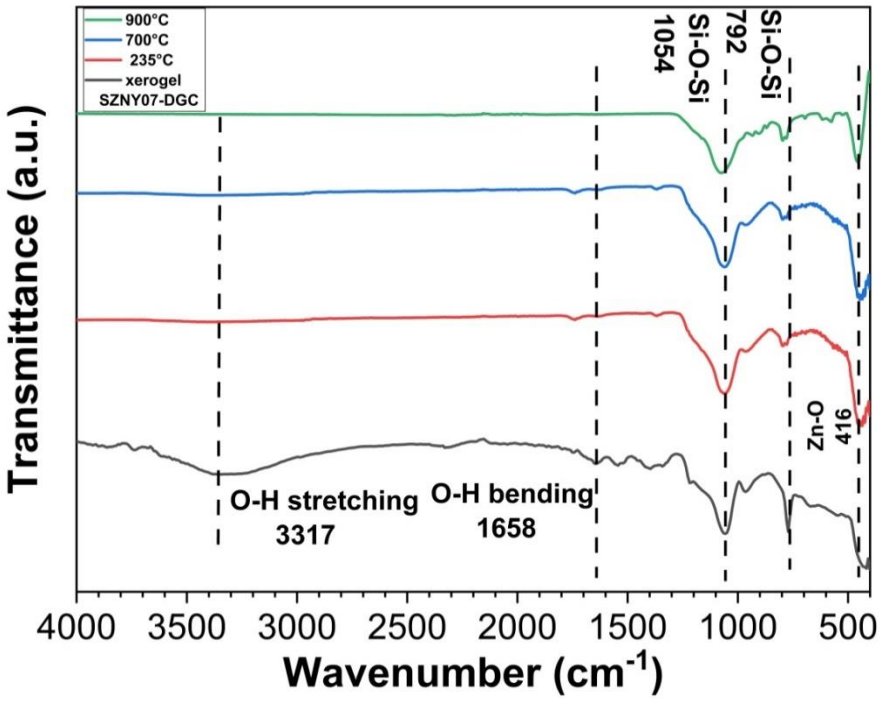


Figure 4.4: ATR-FTIR spectra of the SZNY07-DGC sample annealed at different temperatures

The presence of $RE^{3+}$ ions in the as-synthesized samples has not been confirmed by structural characterization as the homogeneous distribution of $RE^{3+}$ ions do not offer any structural modification on the host matrix (J. et al. 2020). Thus as-obtained results can be extended for all other samples with different $Yb^{3+}$ ion concentrations.

Table 4.1: FTIR peak positions and its different assignments in the SZNY07-DGC sample

| Wavenumber ($cm^{-1}$) | Assignment | Observation |
|---|---|---|
| **509** | Si-O, asymmetric stretching vibrations, O-Si-O stretching (Helmiyati and Suci 2019), (D1) are assigned to symmetric breathing modes of four membered rings of SiO2 tetrahedral, | Strong, broad |
| **547** | NBO (Non-bridging oxygen) [*] | |
| **612** | (D2) are assigned to symmetric breathing modes of three membered rings of $SiO_2$ tetrahedral | |
| **671** | Zn-O-Zn stretching mode (Mossad Ali et al. 2014), Si-O of $SiO_4$ symmetric bending [*] | |
| **771** | O-Si-O stretching modes (Tran et al. 2017) | |
| **810** | Si-O-Si deformation (Mossad Ali et al. 2014) | |
| **879** | | |
| **950-964** | Zn-O-Si bending vibrations (Mossad Ali et al. 2014), stretching vibration of Si-OH (Tran et al. 2017), | Strong |
| **1056** | TO vibration mode of the asymmetric stretching of Si-O-Si bond (Mossad Ali et al. 2014), $SiO_2$ asymmetric stretching (Kumar et al. 2013) | Intense peak |
| **1219** | | |
| **1342-1396** | Zn-O stretching vibration in wurtzite hexagonal-type ZnO crystal (Tran et al. 2017) | Minor peak |
| **1543** | ZnO-OH band (Kumar et al. 2013), C=C (Helmiyati and Suci 2019) | |
| **3325** | Stretching vibration of different Si-OH (Mossad Ali et al. 2014) bonds and H-OH bonds (X. Wang et al. 2013) | Broad, strong |

## 4.4. MORPHOLOGICAL CHARACTERIZATION

The morphological characterization of the SZNY07-DGC and -TF samples were performed using the TEM and SEM analysis.

### 4.4.1. FETEM analysis

The FETEM micrographs of the SZNY07-DGC sample were recorded to observe the morphology of DGC where agglomeration of composite have been confirmed as well as the presence of ZnO nano-crystallite in $SiO_2$ matrix as in Fig. 4.5 (a). The SAED pattern of the SZNY07-DGC sample has been observed as the growth of the ZnO crystallites as in Fig. 4.5 (b). The HRTEM image further confirms interplanar spacing of 0.28 nm in ZnO nano-crystallites as in Fig 4.5 (c). These results from the FETEM monograph are in also agreement with the XRD outcome. The EDS spectra of the SZNY15-DGC sample is found to be consistent with the elements (Si, O, Zn, $Nd^{3+}$, $Yb^{3+}$) supposed to be present in the sample as in Fig 4.5 (d), which is also true for other as-synthesized samples.

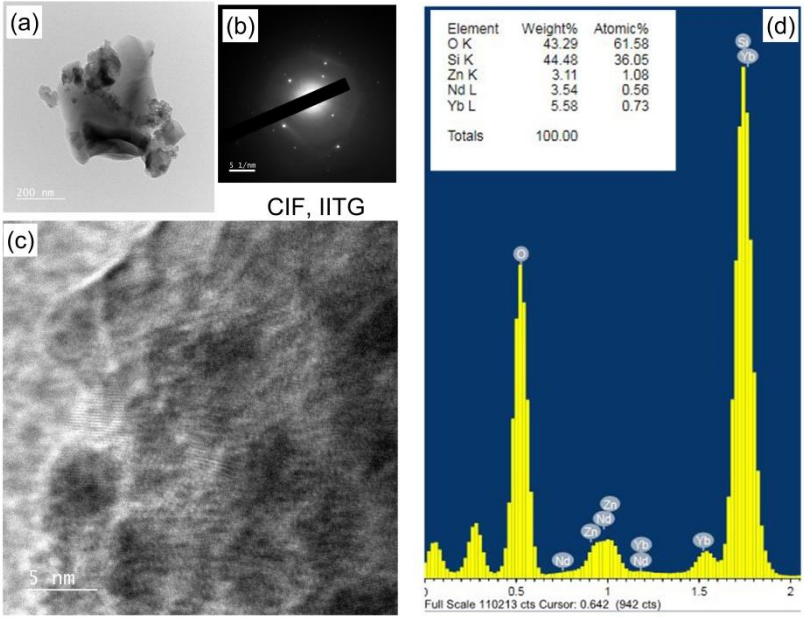


Figure 4.5: TEM image of SZNY07-DGC sample annealed at 900 °C

### 4.4.2. FESEM analysis

FESEM micrograph of SZNY900C thin is reported with asymmetrical nanoflower with cracks on the surface with scale 200 nm but in different magnification (100kX and 150kX) as in Fig. 4.6. EDX analysis of SZNY thin film was performed to

investigate the presence of Si, O, Zn, Yb and, Nd in the fabricated samples as 2.09, 0.25 and 0.59 atomic % confirmed respectively as in Fig. 4.6.

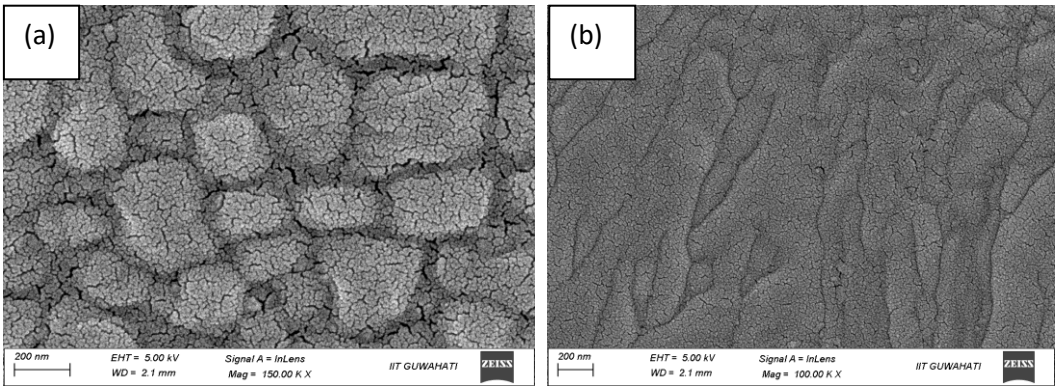


Figure 4.**6**: (a, b) SEM image of the SZNY thin film annealed at 900 °C

EDS component mapping image of STPY thin film is performed to investigate the location specific identification of Zn, Si, O, Yb and Nd in the thin film which are visually confirmed although component distribution are nearly homogeneous as pores are created with evaporation of adsorbed water and trapped solvents present during coating which can benefit SZNY thin film as upconversion and downconversion layer in Si solar cell.

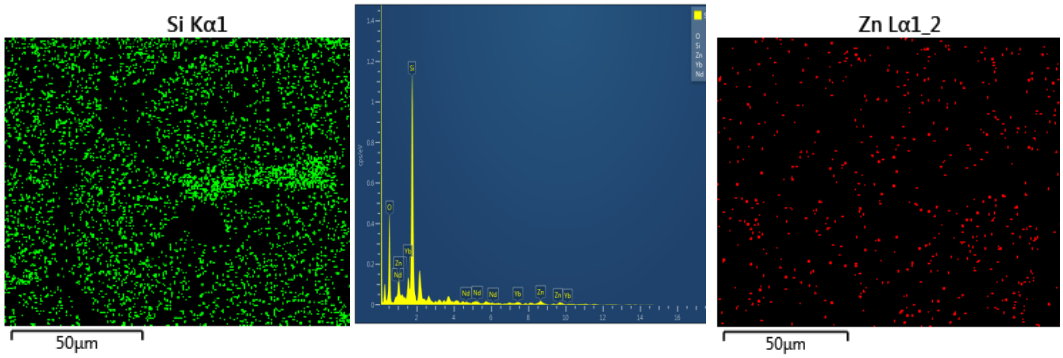

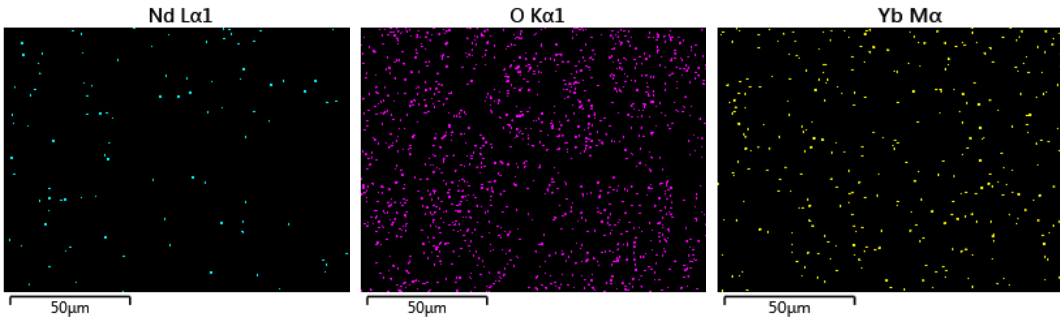


Figure 4.7: SEM-EDS image of SZNY thin film annealed at 900 °C

## 4.5. THERMAL CHARACTERIZATION

TG and DTA of the $ZnO\text{-}SiO_2$: $Nd^{3+}/Yb^{3+}$ xerogel is performed in the nitrogen atmosphere up to 900 °C to report thermal stability as in Fig. 5. The TG curve depicts a weight loss of the material in two phases as initially, 30% weight loss occurred on heating to ca. 120 °C as in inset of Fig 4.8. Two exothermic peaks in the DSC curve are observed at around 139 °C and 189 °C along with an endothermic peak at around 119 °C.

$ZnO\text{-}SiO_2$: $Nd^{3+}/Yb^{3+}$ material was found to be thermally stable with an almost straight curve in the range 220–900 °C which is also indicating phase transformation of the material. The evaporation of adsorbed water and trapped solvents in the matrix are the possible reasons for this loss (Zieliński et al. 2017). The evaporation of chemically bound water, decomposition of surface-bound hydroxide groups, and other byproducts of the reaction is evident from the first phase of mass loss with a broad endothermic peak around 70-120 °C. The first exothermic peak at 140 ºC is co-related to the combustion of trapped organic solvents which is also seen as a 30% loss of mass in the TG-DTA curve. The second exothermic peak at 200°C is co-related to the complete pyrolysis of zinc alkoxide and the energy required for it to sinter into ZnO crystallite as observed by XRD (Fig. 4.2) with nearly no change in mass (Tseng et al. 2012). We assume that the nature of TG curves for $RE^{3+}$ ion concentration is not a factor as the matrix structure remains unaffected with low $RE^{3+}$ ion doping (J. et al. 2020), (Xu, Keefe, and Perry 2004).

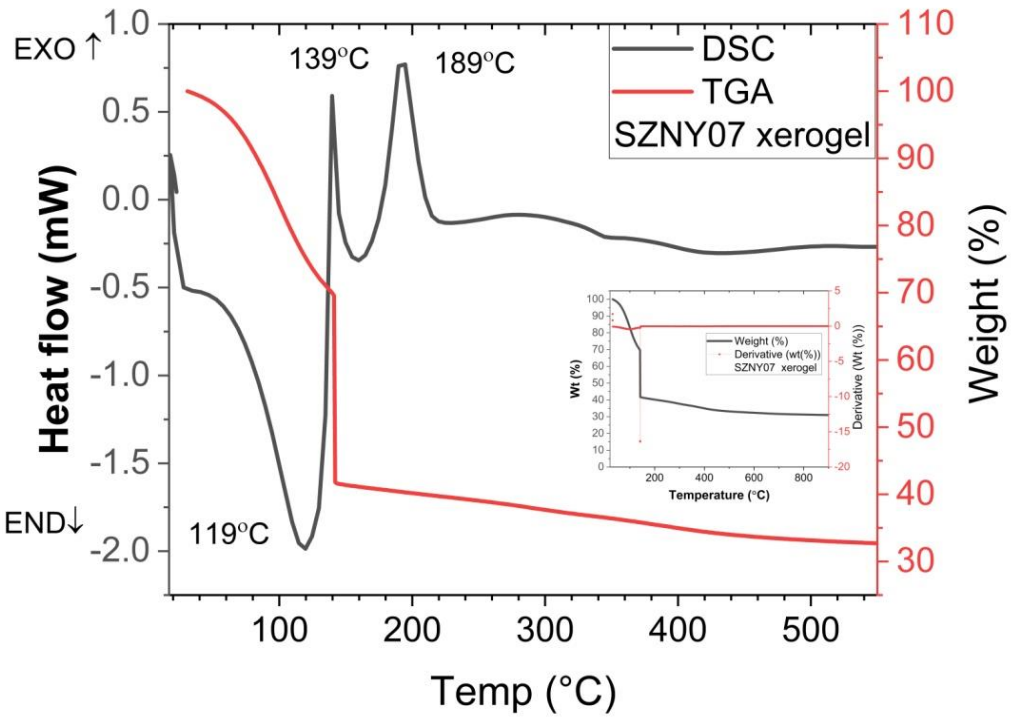


Figure 4.8: TG –DSC curve of the SZNY07 xerogel. Inset TG-DTA curve

## 4.6. OPTICAL CHARACTERIZATION

Optical characterization of the SZNYX-DGC material was performed in two steps. Initially absorption spectra of the material were recorded to identify possible excitation channels. In the next phase, the samples were excited with specific excitation wavelengths to obtain photoluminescence spectra. Excitation wavelengths for photoluminescence studies were chosen to maximize the material's absorption cross-section.

### 4.6.1. Absorption spectra

The absorption spectra of the $ZnO\text{-}SiO_2$: $Nd^{3+}/Yb^{3+}$ material were recorded in the VIS & NIR region with the excitation of 4f electrons from the ground state of $Nd^{3+}$ ($^4I_{9/2} \rightarrow ES$) and $Yb^{3+}$($^2F_{7/2} \rightarrow {}^2F_{5/2}$ ) ions, as shown in Fig 4.9. Various transitions of $Nd^{3+}$ ions from the GS to different ES were observed, such as $^4I_{9/2} \rightarrow {}^4F_{3/2}$ (867nm),

$^4F_{3/2}$ + $^2H_{9/2}$ (808 nm); $^4S_{3/2}$ +$^4F_{7/2}$ (743 nm); $^4F_{9/2}$ (680 nm); $^2H_{11/2}$ (623 nm); $^4G_{5/2}$ + $^2G_{7/2}$ (581 nm); $^4G_{7/2}$ + $^4G_{9/2}$ + $^2K_{13/2}$ (524 nm). The absorption peaks at 980 nm correspond to the $^2F_{7/2}\rightarrow{}^2F_{5/2}$ transition of $Yb^{3+}$ ions. The most intense absorption peaks of $Nd^{3+}$ ion were observed from the $^4I_{9/2} \rightarrow {}^4F_{5/2}$ + $^2H_{9/2}$ transition (808 nm). Thus our as-synthesized ZnO-$SiO_2$: $Nd^{3+}$/$Yb^{3+}$ material can be excited by a laser source of wavelength ($\lambda_{ex}$) 980 nm and 808 nm to obtain photoluminescence spectra.

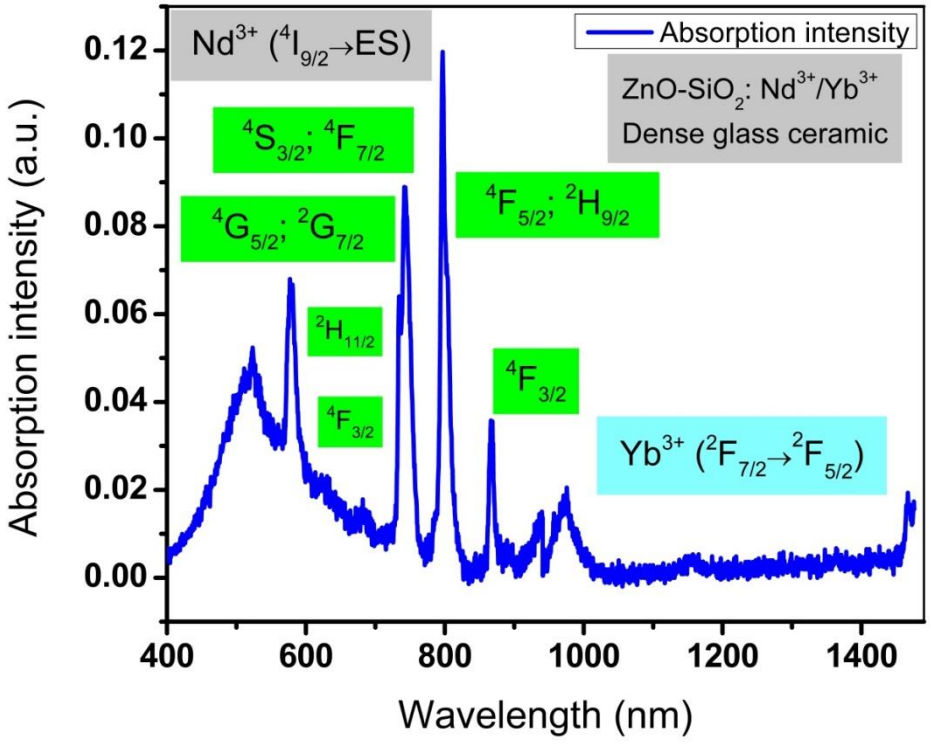


Figure 4.9: Absorption spectra of the SZNY07-DGC materials

### 4.6.2. Upconversion luminescence spectra

The UCL spectra of the SZNYX-DGC samples were observed in visible (VIS) and near-infrared (NIR) regions using a 980 nm excitation source as in Fig. 4.10. The contribution of $Nd^{3+}$ ion is observed in UCL spectra with the transition of $^4F_J$ (J= 7/2,

5/2,3/2) → $^4I_{9/2}$ (752, 808, 870 nm) and $^4G_{7/2}$ → $^4I_{9/2}$ (540 nm) & $^4I_{11/2}$ (601 nm) which is only possible because of energy transfer from $Yb^{3+}$ ion [$^2F_{7/2}$→$^2F_{5/2}$] to $Nd^{3+}$ ions as in Fig 4.12. The intensity of UCL spectra is gradually increased with an increase in $Yb^{3+}$ ion concentration which is maximized for the SZNY15-DGC sample. The gradual quenching with the rise in $Yb^{3+}$ ion concentration to 3.0 mol% has been correlated to concentration quenching. The presence of $Yb^{3+}$ ions in the neighborhood of $Nd^{3+}$ ion contributes to the enhancement of UCL of $Nd^{3+}$ ion through the transfer of energy which is initially absorbed by $Yb^{3+}$ ion. The concentration quenching is observed at higher $Yb^{3+}$ ion concentrations due to the ET among $Yb^{3+}$ ions in the ground state. The UCL intensity can enhance with high-power laser irradiation which is yet to record. The UCL was observed for the SZNY00-DGC sample with no resonating energy level of $Nd^{3+}$ ions at an excitation wavelength of 980 nm whereas the same observation was made in case of $Nd^{3+}$ ion doped $Y_2O_3$ phosphor material without $Yb^{3+}$ ion due to $Er^{3+}$ ion impurity (Sukul and Kumar 2016). Although we believe that thermal energy plays a supporting role to excite an electron to metastable state in this case.

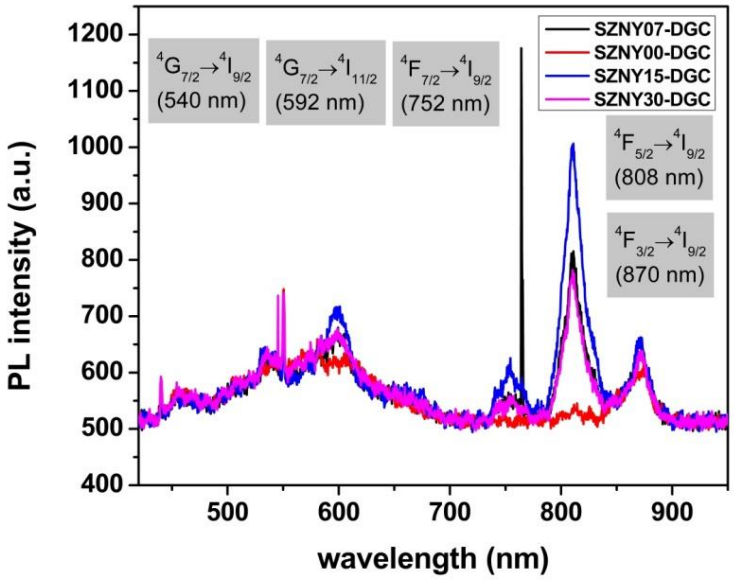


Fig. 4.**10**. UCL spectra of the SZNYX-DGC materials under 980nm excitation

### 4.6.3. Downconversion luminescence spectra

The DCL spectra of the SZNYX-DGC samples are presented in the UV-VIS region with $\lambda_{ex}$ = 450 nm (approximately 222222 $cm^{-1}$), corresponding to the $Nd^{3+}$: $^4I_{9/2} \rightarrow {}^2P_{1/2}$ transition. The emission peaks typically arise from $^2P_{1/2} \rightarrow {}^4I_{9/2}$; $^4F_J$ (J= 7/2, 5/2,3/2) $\rightarrow {}^4I_{9/2}$ and $^4G_{7/2} \rightarrow {}^4I_{9/2}$ & $^4I_{11/2}$. However, in this specific sample, only two emission peaks for $Nd^{3+}$ ion [$^4F_{7/2} \rightarrow {}^4I_{15/2}$] and $Yb^{2+}$ ion [ 4f→5d] has been observed, as shown in Fig. 4.11 (Muniz et al. 2023). The presence of $Yb^{3+}$ ions in the as-synthesized materials is confirmed by the emission peak at 614 nm for the 4f→5d transition. Co-doping of $Yb^{3+}$ ions was expected to facilitate quantum cutting (QC) of one visible photon into two NIR photons. However, this phenomenon is not observed in the PL spectra of the $Nd^{3+}$ -$Yb^{3+}$ ion pairs (Wen and Tanner 2011). The maximum phonon energy of ZnO-$SiO_2$ binary host (ca. 1100 $cm^{-1}$) and the relatively small energy difference between the various energy levels of $Nd^{3+}$ ion enable bridging the energy gap to initiate multiphonon relaxation (Wen and Tanner 2011).

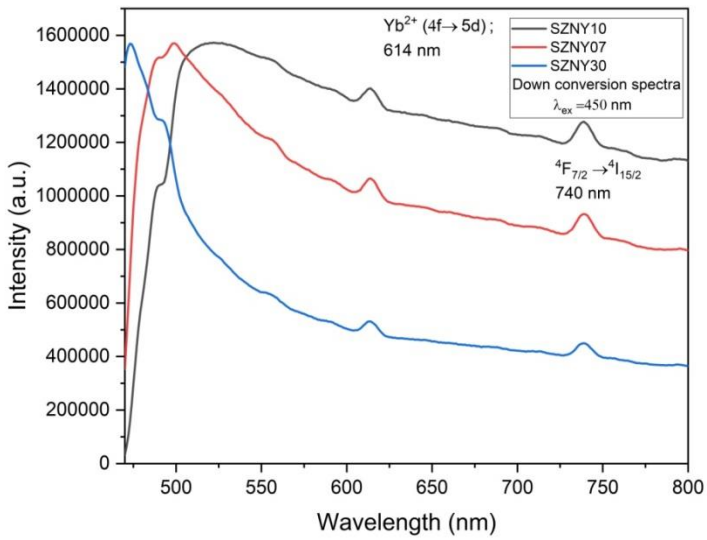


Figure 4.11: DCL spectra of the SZNYX-DGC sample under 450 nm excitation source

### 4.6.4. Results and discussion

#### 4.6.4.1. Judd–Ofelt (J-O) parameters

According to the J-O theory (Judd and Lindgren 1961), (Ofelt 1962), the radiative transitions belonging to the $4f^2$ configuration of $Nd^{3+}$ can be analyzed based on the absorption spectra of $Nd^{3+}$ ion (Fig. 4.1). The J–O intensity parameters $\Omega_\lambda$ ($\lambda$ = 2, 4, and 6) for $Nd^{3+}$ in the SZNY07-DGC sample are derived by the least square fitting of oscillator strength derived from experiment ($f_{exp}$) and calculation ($f_{cal}$) oscillator strength using as obtained squared matrix elements (Carnall et al. 1968).

**Table 4.2: Judd-Ofelt intensity parameters and oscillator strengths of $Nd^{3+}$ ion**

| **Transitions $^4I_{9/2}\rightarrow$** | **Wave-length (nm)** | **Energy ($cm^{-1}$)** | **$f_{exp}$ ($\times10^{-6}$)** | **$f_{exp}$ ($\times10^{-6}$)** | $\Omega_2$ | $\Omega_4$ ($10^{-20}$ $cm^2$) | $\Omega_6$ |
|---|---|---|---|---|---|---|---|
| $^4F_{3/2}$ | 866 | 11541 | 0.4743 | 0.7045 | | | |
| $^4F_{5/2}$ + $^2H_{9/2}$ | 797 | 12546 | 2.2706 | 2.4599 | | | |
| $^4S_{3/2}$ + $^4F_{7/2}$ | 743 | 13455 | 2.4773 | 2.4489 | 7.4258 | 1.3166 | 1.6884 |
| $^4G_{5/2}$ + $^2G_{7/2}$ | 577 | 17331 | 1.6099 | 2.2961 | | | |
| $^4G_{7/2}$+$^4G_{9/2}$+ $^2K_{13/2}$ | 523 | 19107 | 3.4425 | 2.6317 | | | |
| **Refractive Index = 1.62** | | | | Concentration of $Nd^{3+}$ ion = | | | |
| **Thickness = 0.18 cm** | | | | 0.2477 mol/L | | | |
| **Radius = 0.7cm** | | | | Degeneracy (2J+1)=10 | | | |

The comparison of J-O parameters of $Nd^{3+}$ ion is tabulated in Table 4.3. The second intensity parameter ($\Omega_2$) has been acknowledged as sensitive to the asymmetrical host and the covalency of the $RE^{3+}$ ions whereas $\Omega_4$ and $\Omega_6$ are co-related to the bulk property and rigidity of the materials, correspondingly (Hua et al. 2017). The higher $\Omega_2$ represent strong asymmetrical and higher covalent environment owed to the introduction of ZnO altering the ligand field of $Nd^{3+}$, thus accomplishing the intense PL emission (Hua et al. 2017).

Table 4.3: Comparison of calculated Judd-Ofelt intensity parameters

| Host | $\Omega_2$ | $\Omega_4$ | $\Omega_6$ | $\Omega_4/\Omega_6$ |
|---|---|---|---|---|
| **Present work** | 3.4894 | 1.770 | 2.500 | 0.7081 |
| **$TiO_2$-$SiO_2$**(Dihingia and Rai 2012) | 14.807 | 0.9 | 3.9 | 0.2307 |

The radiative properties such as spontaneous emission probabilities ($A_{rad}$), luminescence branching ratios (β), and radiative lifetime ($\tau_{rad}$) for the optical transitions of $Nd^{3+}$ in the SZNY07-DGC sample is estimated using J-O intensity parameters in Table 4.4.

Table 4.4: Radiative parameters of the SZNY07-DGC sample

| Transition | | Wavelength (nm) | Energy ($cm^{-1}$) | $A_R$ ($s^{-1}$) | $\beta_R$ (%) | τ (μs) |
|---|---|---|---|---|---|---|
| $^4G_{7/2}$ → | $^4I_{9/2}$ | 540 | 18518 | 1405.69 | 23.39 | 166.39 |
| | $^4I_{11/2}$ | 592 | 16891 | 4396.92 | 73.16 | |
| | $^4I_{13/2}$ | 601 | 16638 | 149.74 | 2.49 | |
| | $^4I_{15/2}$ | 700 | 14285 | 57.45 | 0.95 | |
| | | | $A_T$ ($s^{-1}$) = | 6009.81 μs | | |
| $^4F_{7/2}$ → | $^4I_{9/2}$ | 752 | 13333 | 510.82 | 39.35 | 77.04 |
| | $^4I_{11/2}$ | **808** | 12376 | 438.40 | 33.77 | |
| | $^4I_{13/2}$ | 840 | 11904 | 204.34 | 15.74 | |
| | $^4I_{15/2}$ | 1338 | 7473 | 144.28 | 11.11 | |
| | | | $A_T$ ($s^{-1}$) = | 1297.86 μs | | |
| $^4F_{5/2}$ → | $^4I_{9/2}$ | **808** | 12376 | 515.92 | 64.55 | 1246.42 |
| | $^4I_{11/2}$ | 948 | 10548 | 93.36 | 7.19 | |
| | $^4I_{13/2}$ | 1164 | 8591 | 161.20 | 12.42 | |
| | $^4I_{15/2}$ | 1535 | 6514 | 29.79 | 2.29 | |
| | | | $A_T$ ($s^{-1}$) = | 802.29 μs | | |
| $^4F_{3/2}$ → | $^4I_{9/2}$ | 878 | 12376 | 161.57 | 38.92 | 2409.39 |
| | $^4I_{11/2}$ | 1051 | 9514 | 209.54 | 50.48 | |
| | $^4I_{13/2}$ | 1329 | 7524 | 41.77 | 10.06 | |
| | $^4I_{15/2}$ | 1827 | 5473 | 2.15 | 0.51 | |
| | | | $A_T$ ($s^{-1}$) = | 415.05 μs | | |

### 4.6.4.2. Cooperative sensitization upconversion

UCL of the $Nd^{3+}$-$Yb^{3+}$ ions pair is only possible because of the ET from $Yb^{3+}$ to $Nd^{3+}$ ions. Since the excitation wavelength at 980 nm is not in resonance with any transition of $Nd^{3+}$ ion starting from the ground state, but certainly with the $^2F_{7/2} \rightarrow {}^2F_{5/2}$ transition of $Yb^{3+}$ ion (Muniz et al. 2023). The two different paths of ET from the $Yb^{3+}$ ion to the $Nd^{3+}$ ion are phonons-assisted (energy transfer PAET) and CSU (Muniz et al. 2023). In the CSU process, two-NIR photons each of ca. 10000 $cm^{-1}$ are absorbed by two nearby activators ($Yb^{3+}$ ) ions whereas one electron is transferring energy to the other in ES (sensitizer) before relaxing to the initial energy state. The schematic CSU of the $Nd^{3+}$-$Yb^{3+}$ ion pair is cited in Fig. 4.12. Here sensitizer is capable of occupying the energy state of $^4G_{7/2}$ of $Nd^{3+}$ ion (ca. 20000 $cm^{-1}$) and thus the emission of a photon of higher energy is possible to GS.

The concentration-dependent study reveals that UCL spectra are optimized for a sample with a $Yb^{3+}$ ion concentration twice that of the $Nd^{3+}$ ion. Therefore, the presence of two $Yb^{3+}$ ions around one $Nd^{3+}$ ion can enhance the desired luminesce result. However, a further increase in the $Yb^{3+}$ ion concentration has a negative impact on the intensity of UCL spectra.

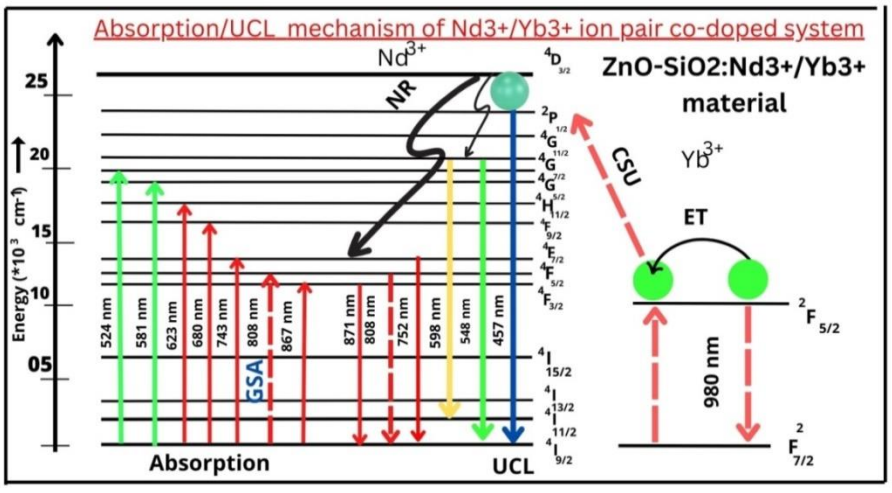

Fig. 4.12. Schematic diagram of the CSU mechanism in $Yb^{3+}$-$Nd^{3+}$ ion pair

#### 4.6.4.3. CIE-chromaticity diagram

The Commission International d' Eclairage (CIE) coordinates (0.34, 0.35) of corresponding UCL of the SZNYX-DGC samples have been obtained for different $Yb^{3+}$ ion concentrations as in Fig 4.13. The CIE coordinate in the white region doesn't changes with a varying $Yb^{3+}$ ion concentration. Thus PL color coordinates are not tunable through the modification of the concentration of $Yb^{3+}$ ion.

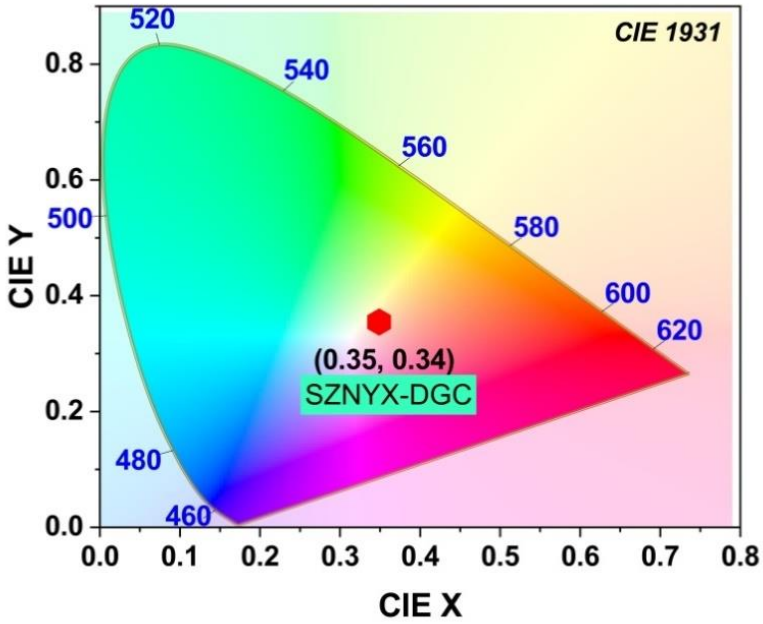


Fig. 4.13. CIE 1931 chromaticity diagram of the SZNYX-DGC sample

#### 4.6.4.3. Confocal PL microscopy

PL confocal mapping of the SZNY15-DSC sample has been performed at two different locations of the powdered sample with an excitations source of the wavelength of 980 nm [Fig. 4. 14]. The intensity of PL emission was not similar in

the two different locations. This non-uniform PL emission arises due to the uneven topological surface of samples in powder form. It reveals that the UCL of the sample is obtained at every point for the SZNY15-DGC sample which is also true for other as-synthesized samples (Kumar et al. 2018).

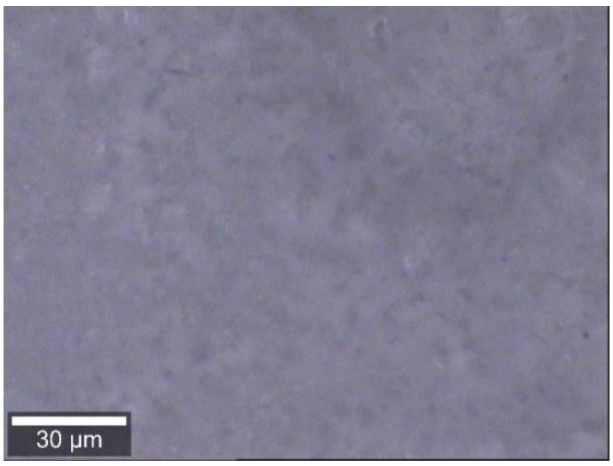


Fig. 4.14. PL confocal mapping of the SZNY15-DGC sample

## 4.7. CONCLUSIONS

Thus modified *ex-situ* sol-gel process has been useful to synthesis the SZNY07-DGC and -TF. These glass and thin film were observed to be crystalline in nature due to annealing temperature. The transparent dense glasses are free from OH molecule with higher phonon energy which promotes hydroxyl quenching of $RE^{3+}$ ion. The $Nd^{3+}$ and $Yb^{3+}$ ion are well distributed all over the thin film although voids are unavoidable from evaporation of adsorbed water and trapped solvents. Thus promotion of $Nd^{3+}$ and $Yb^{3+}$ ion codoped in Zinc-Silicate asymmetrical host with non-bridging oxygen (Zn-O-Si) is reported through this modified sol-gel synthesis route for future optoelectronic applications. FETEM are embedded in an amorphous silica matrix, with an interplanar spacing of 0.24 nm. TG and DSC analysis provide insights into the thermal behavior of the material. The synthesized materials exhibited white UCL spectra under 980nm excitation; with the optimum UCL

intensity observed for the SZNY15-DSC samples. PL confocal mapping of the SZNY15-DGC sample revealed non-uniform luminescence due to the uneven topological surface in powder form.

The optical activity of the SZNY15-DGC material, with both UCL and DCL properties, makes it promising candidates for various photonic applications such as display devices, photovoltaic solar cells, temperature sensors, bio-sensing etc.

## REFERENCES


Agustín-Sáenz, Cecilia, José Ángel Sánchez-García, Maider Machado, Marta Brizuela, Oihana Zubillaga, and Agnieszka Tercjak. 2018. "Broadband Antireflective Coating Stack Based on Mesoporous Silica by Acid-Catalyzed Sol-Gel Method for Concentrated Photovoltaic Application." *Solar Energy Materials and Solar Cells* 186(February):154–64. doi: 10.1016/j.solmat.2018.06.040.

Ahrens, Bernd. 2009. "Down-and Up-Conversion in Fluorozirconate-Based Glasses and Glass Ceramics for Photovoltaic Application." PADERBORN.

Amin, Peshawa O., Asmaa J. Kadhim, Majida A. Ameen, and Rebar T. Abdulwahid. 2018. "Structural and Optical Properties of Thermally Annealed TiO2–SiO2 Binary Thin Films Synthesized by Sol–Gel Method." *Journal of Materials Science: Materials in Electronics* 29(18):16010–20. doi: 10.1007/s10854-018-9688-6.

Anna M. Kaczmarek, Mariusz K. Kaczmarek, and Rik Van Deuna. 2018. "Er3+-to-Yb3+ and Pr3+-to-Yb3+ Energy Transfer for Highly Efficient near-Infrared Cryogenic Optical Temperature Sensing." *Nanoscale* 11(3):1–3. doi: 10.1039/C8NR08348G.

Auzel, F. 1990. "Upconversion Processes in Coupled Ion Systems." *Journal of Luminescence* 45(1–6):341–45. doi: 10.1016/0022-2313(90)90189-I.

Azzouz, I. M., and Lisa C. Klein. 2012. "Red , Violet and Upconversion Luminescence of Eu / Sm Codoped Sol Gel SiO 2 – TiO 2." *Optical Materials* 35:292–96. doi: 10.1016/j.optmat.2012.09.006.

Bang, Jungsik, Heesun Yang, and Paul H. Holloway. 2005. "Enhanced

Luminescence of SiO 2 : Eu 3 + by Energy Transfer from ZnO Nanoparticles." *The Journal of Chemical Physics* 123(May 2013):1–4. doi: 10.1063/1.2007647.

Battisha, I. K. 2007. "Visible Up-Conversion Photoluminescence from IR Diode-Pumped SiO2-TiO2 Nano-Composite Films Heavily Doped with Er3+-Yb3+ and Nd3+-Yb3+." *Journal of Non-Crystalline Solids* 353(18–21):1748–54. doi: 10.1016/j.jnoncrysol.2007.01.043.

Berkani, Oualid, Khelil Latrous, Hicham El, Bruno Capoen, and Mohamed Bouazaoui. 2012. "Effects of Heat Treatment and TiO 2 Content on the Optical Properties of Eu 3 þ Doped TiO 2 – SiO 2 Thin Films." *Journal of Luminescence* 132:2979–83. doi: 10.1016/j.jlumin.2012.06.019.

Binnemans, Koen. 2009. "Lanthanide-Based Luminescent Hybrid Materials." *Chemical Review* 109:4283–4374.

Binnemans, Koen. 2015. "Interpretation of Europium ( III ) Spectra." *Coordination Chemistry Reviews* 295:1–45. doi: 10.1016/j.ccr.2015.02.015.

Bokatial, L., and S. Rai. 2010. "Optical Properties and Up-Conversion of Pr 3 + Doped CdS Nanoparticles in Sol – Gel Glasses." *Journal of Luminescence* 130(10):1857–62. doi: 10.1016/j.jlumin.2010.04.022.

Bokatial, Litul, and S. Rai. 2012. "Optical Properties of Sm 3 + Ions in Sol-Gel Derived Alumino-Silicate Glasses." *J Opt* 41(June):94–103. doi: 10.1007/s12596-012-0069-x.

Bokov, Dmitry, Abduladheem Turki Jalil, Supat Chupradit, Wanich Suksatan, Mohammad Javed Ansari, Iman H. Shewael, Gabdrakhman H. Valiev, and Ehsan Kianfar. 2021. "Nanomaterial by Sol-Gel Method: Synthesis and Application." *Advances in Materials Science and Engineering* 2021. doi: 10.1155/2021/5102014.

Brik, Mikhail G., Ž. M. Anti, Katarina Vukovi, and Miroslav D. Drami. 2015. "Judd - Ofelt Analysis of Eu 3 + Emission in TiO 2 Anatase Nanoparticles." *Materials Transactions* 56(9):1416–18.

Brus, Louis. 1986. "Electronic Wave Functions in Semiconductor Clusters: Experiment and Theory." *Journal of Physical Chemistry* 90(12):2555–60. doi: 10.1021/j100403a003.

Buarque, Juliana M. M., Danilo Manzani, Sérgio Luis Scarpari, Marcelo Nalin,

Sidney J. L. Ribeiro, Jennifer Esbenshade, Marco A. Schiavon, and Jefferson L. Ferrari. 2018. “SiO2-TiO2 Doped with Er3+/Yb3+/Eu3+ Photoluminescent Material: A Spectroscopy and Structural Study about Potential Application for Improvement of the Efficiency on Solar Cells.” *Materials Research Bulletin* 107:295–307. doi: 10.1016/j.materresbull.2018.07.007.

C. Jefffrey and George W. Scherer. 1990. *Sol-Gel Science, The Physics and Chemistry of Sol-Gel Processing*. London: Academic Press, Inc.

Carnall, W. T.; Crosswhite, H.; Crosswhite, H. M. 1977. *Energy Level Structure and Transition Probabilitiesof the Trivalent Lanthanides in LaF3*. Argonne (USA): Rep. Argonne National Laboratory.

Carnall, W. T., P. R. Fields, and K. Rajnak. 1968. “Electronic Energy Levels in the Trivalent Lanthanide Aquo Ions. I. Pr3+, Nd3+, Pm3+, Sm3+, Dy3+, Ho3+, Er3+, and Tm3+.” *The Journal of Chemical Physics* 49:4424–42. doi: 10.1063/1.1669893.

Carnall, W. T., P. R. Fields, and B. G. Wybourne. 1965. “Spectral Intensities of the Trivalent Lanthanides and Actinides in Solution. I. Pr3+, Nd3+, Er3+, Tm3+, and Yb3+.” *The Journal of Chemical Physics* 42:3797–3806. doi: 10.1063/1.1695840.

Carnall, W. T., G. L. Goodman, K. Rajnak, and R. S. Rana. 1989. “A Systematic Analysis of the Spectra of the Lanthanides Doped into Single Crystal LaF3.” *The Journal of Chemical Physics* 90(7):3443–57. doi: 10.1063/1.455853.

Castan˜eda-Contreras, J., M. A. Meneses-Nava, O. Barbosa-Garcı´a, R. A. Rodrı´guez-Rojas, and M. V. Fe´lix. 2006. “Visible Erbium Luminescence in SiO2 – TiO2 – Er3+ Sol – Gel Powders.” *Optical Materials* 29:38–42. doi: 10.1016/j.optmat.2006.03.005.

Chandraboss, V. L., B. Karthikeyan, J. Kamalakkannan, S. Prabha, and S. Senthilvelan. 2013. “Sol-Gel Synthesis of TiO2/SiO2 and ZnO/SiO2 Composite Films and Evaluation of Their Photocatalytic Activity towards Methyl Green.” *Journal of Nanoparticle* 2013(507161):1–7.

Chang, Meiqi, Yanhua Song, Lei Cui Jie Chen, Zhan Shi, Ye Sheng, and Haifeng Zou. 2018. “Photocatalytic and Photoluminescence Properties of Core- Shell SiO2@TiO2:Eu3+,Sm3+ and Its Etching Products.” *ACS Sustainable Chemistry*

*& Engineering* 6(1):223–36. doi: 10.1021/acssuschemeng.7b02285.

Chang, Meiqi, Yanhua Song, Ye Sheng, Jie Chen, and Haifeng Zou. 2017. "Understanding the Remarkable Luminescence Enhancement: Via SiO2 Coating on TiO2:Eu3+ Nanofibers." *Physical Chemistry Chemical Physics* 19(26):17063–74. doi: 10.1039/c7cp01113j.

Chang, Meiqi, Haifeng Zou, Yanhua Song, Jie Chen, Lei Cui, Ye Sheng, and Keyan Zheng. 2019. "Photoluminescence and Photodegradation Properties of SiO2@TiO2:Sm3+ with Different Coating Effects." *Journal of Physics and Chemistry of Solids* 124:100–110. doi: 10.1016/j.jpcs.2018.09.010.

Chelouche, A., D. Djouadi, and A. Aksas. 2014. "Structural Characterization of SiO 2 / Zn 2 SiO 4 : Ce Nanocomposite Obtained by Sol Gel Method." *Journal of the Association of Arab Universities for Basic and Applied Sciences* 15:10–14. doi: 10.1016/j.jaubas.2013.05.002.

Chen, Hsueh Shih, Sheng Hsin Huang, and Tsong Pyng Perng. 2012. "Preparation and Characterization of Molecularly Homogeneous Silica-Titania Film by Sol-Gel Process with Different Synthetic Strategies." *ACS Applied Materials and Interfaces* 4(10):5188–95. doi: 10.1021/am301113a.

Chen, X. P., X. Y. Huang, and Q. Y. Zhang. 2009. "Concentration-Dependent near-Infrared Quantum Cutting in NaYF4: Pr3+, Yb3+phosphor." *Journal of Applied Physics* 106(6):3–7. doi: 10.1063/1.3224906.

Çopuroğlu, Mehmet, Lee Huat Kelly Koh, Gabriel M. Crean, and Shane O'Brien. 2016. "Comparative Characterisation of Zinc Oxide Thin Films Prepared from Zinc Acetate with or without Water of Hydration via the Sol – Gel Method." *Journal of Sol-Gel Science and Technology* 52:432–38. doi: 10.1007/s10971-009-2016-0.

Deshmukh, Pratik, S. Satapathy, Anju Ahlawat, MK Tiwari, and A. K. Karnal. 2018. "Fabrication and Characterization of Er , Nd Codoped Transparent Ceramic : A Dual Mode Photo-Luminescence Emitter." *Journal of Alloys and Compounds* 754:32–38.

Dibaba, Solomon Tiruneh, Xiaoqian Ge, Wei Ren, and Lining Sun. 2019. "Recent Progress of Energy Transfer and Luminescence Intensity Boosting Mechanism in Nd3+-Sensitized Upconversion Nanoparticles." *Journal of Rare Earths*

37(8):791–805. doi: 10.1016/j.jre.2019.02.001.

Dieudonné, B., B. Boulard, G. Alombert-Goget, A. Chiasera, Y. Gao, S. Kodjikian, and M. Ferrari. 2013. “Up- and down-Conversion in Yb3+-Pr3+ Co-Doped Fluoride Glasses and Glass Ceramics.” *Journal of Non-Crystalline Solids* 377:105–9. doi: 10.1016/j.jnoncrysol.2012.12.025.

Dihingia, P. J., and S. Rai. 2012. “Synthesis of TiO 2 Nanoparticles and Spectroscopic Upconversion Luminescence of Nd 3+-Doped TiO 2-SiO 2 Composite Glass.” *Journal of Luminescence* 132(5):1243–51. doi: 10.1016/j.jlumin.2011.12.008.

Dwivedi, Y., Anita Rai, and S. B. Rai. 2008. “Intense White Upconversion Emission in Pr / Er / Yb Codoped Tellurite Glass.” *Journal of Applied Physics* 104(043509):1–4. doi: 10.1063/1.2969046.

El-Bashir, S. M. 2017. “Physical Properties Nd3+ Doped (SiO2-TiO2) Monolithic Glass for Photoresistor Applications.” *Materials Research Express* 4(11):0–6.

Van Der Ende, Bryan M., Linda Aarts, and Andries Meijerink. 2009. “Lanthanide Ions as Spectral Converters for Solar Cells.” *Physical Chemistry Chemical Physics* 11(47):11081–95. doi: 10.1039/b913877c.

Eriksen, Emil H., Soren P. Madsen, Brian Julsgaard, Clarissa L. M. Hofmann, Jan Christoph Goldschmidt, and Peter Balling. 2019. “Enhanced Upconversion via Plasmonic Near-Field Effects: Role of the Particle Shape.” *Journal of Optics (United Kingdom)* 21(3). doi: 10.1088/2040-8986/ab0272.

Escudero, Alberto, Ana I. Becerro, Carolina Carrillo-Carrión, Nuria O. Núñez, Mikhail V. Zyuzin, Mariano Laguna, Daniel González-Mancebo, Manuel Ocanã, and Wolfgang J. Parak. 2017. “Rare Earth Based Nanostructured Materials: Synthesis, Functionalization, Properties and Bioimaging and Biosensing Applications.” *Nanophotonics* 6(5):881–921. doi: 10.1515/nanoph-2017-0007.

Esposito, Serena. 2019. “‘Traditional’ Sol-Gel Chemistry as a Powerful Tool for the Preparation of Supported Metal and Metal Oxide Catalysts.” *Materials* 12(4):1–25. doi: 10.3390/ma12040668.

Faria, W. J., T. S. Gonçalves, and Andrea S. S. De Camargo. 2021. “Near Infrared Optical Thermometry in Fluorophosphate Glasses Doped with Nd3+ and

Nd3+/Yb3+.” *Journal of Alloys and Compounds* 883:160849. doi: 10.1016/j.jallcom.2021.160849.

Fischer, S., J. C. Goldschmidt, P. Löper, G. H. Bauer, R. Brüggemann, K. Krämer, D. Biner, M. Hermle, and S. W. Glunz. 2010. “Enhancement of Silicon Solar Cell Efficiency by Upconversion: Optical and Electrical Characterization.” *Journal of Applied Physics* 108(4):1–11. doi: 10.1063/1.3478742.

Galedari, Naghmeh Abuali, and Mohammad Rahmani. 2017. “Preparation , Characterization , and Application of ZnO @ SiO 2 Core – Shell Structured Catalyst for Photocatalytic Degradation of Phenol.” *Environmental Science and Pollution Research* 24(14):12655–63. doi: 10.1007/s11356-016-7888-2.

Ghaemi, Bahram, Gaoling Zhao, Shengchen Huang, Jianxun Wang, and Gaorong Han. 2012. “Structural and Luminescence Properties of Er-Doped Zinc – Alumino – Silicate Glass Ceramic.” *J. Am. Ceram. Soc.* 4:1–4. doi: 10.1111/j.1551-2916.2012.05200.x.

Gonçalves, M. Clara, Luis M. Fortes, Rui M. Almeida, Alessandro Chiasera, Andrea Chiappini, Maurizio Ferrari, and Shivakiran Bhaktha. 2010. “Photoluminescence in Er3+/Yb3+-Doped Silica-Titania Inverse Opal Structures.” *Journal of Sol-Gel Science and Technology* 55(1):52–58. doi: 10.1007/s10971-010-2212-y.

Guille, A., A. Pereira, C. Martinet, and B. Moine. 2012. “Quantum Cutting in CaYAlO4: Pr3+, Yb3+.” *Optics Letters* 37(12):2280. doi: 10.1364/ol.37.002280.

Halin, D. S. C., M. M. A. B. Abdullah, N. Mahmed, S. N. A. Abdul Malek, P. Vizureanu, and A. W. Azhari. 2017. “Synthesis and Characterization of TiO2/SiO2 Thin Film via Sol-Gel Method.” *IOP Conference Series: Materials Science and Engineering* 209(1). doi: 10.1088/1757-899X/209/1/012002.

Haque, Md Azimul, and S. Mahalakshmi. 2013. “Effect of Triethanolamine on Zinc Oxide Nanoparticles.” *Materials Focus* 2(6):469–74. doi: 10.1166/mat.2013.1117.

Hehlen, Markus P., Mikhail G. Brik, and Karl W. Kramer. 2013. “50th Anniversary of the Judd – Ofelt Theory : An Experimentalist ’ s View of the Formalism and Its Application.” *Journal of Luminescence* 136:221–39. doi:

10.1016/j.jlumin.2012.10.035.

Helmiyati, Helmiyati, and R. P. Suci. 2019. “Nanocomposite of Cellulose-ZnO / SiO2 as Catalyst Biodiesel Methyl Ester from Virgin Coconut Oil.” *AIP Conference Proceedings* (April 2020). doi: 10.1063/1.5132490.

Hien, Le Thi Thu, Nguyen Van Dub, Ngo Ngoc Hab, Nguyen Duc Hoab, Tran Ngoc Khiemb, and Nguyen Duc Chiena. 2019. “Optical Materials Photoluminescence Enhancement OF Er 3 + -Doped ZnO / SiO 2 Nanocomposites Fabricated through Two-Step Synthesis.” *Optical Materials* 92(April):262–66. doi: 10.1016/j.optmat.2019.04.043.

Hua, Chenxiao, Xin Zhao, Yue Bun, and Hai Lin. 2017. “Pr3+ Doped Tellurite Glasses Incorporated with Silver Nanoparticles for Laser Illumination.” *RSC Adv.* 7:55691–701. doi: 10.1039/c7ra11594f.

Huang, X. Y., and Q. Y. Zhang. 2009. “Efficient Near-Infrared down Conversion in Zn2 SiO4: Tb3+, Yb3+ Thin-Films.” *Journal of Applied Physics* 105(5):1–5. doi: 10.1063/1.3088890.

Huang, Xiaoyong, Sanyang Han, Wei Huang, and Xiaogang Liu. 2013. “Enhancing Solar Cell Efficiency: The Search for Luminescent Materials as Spectral Converters.” *Chemical Society Reviews* 42(1):173–201. doi: 10.1039/c2cs35288e.

Ismail, Adel Ali, Mostafa Abboudi, Paul Holloway, and Hassan El-Shall. 2007. “Photoluminescence from Terbium Doped Silica-Titania Prepared by a Sol-Gel Method.” *Materials Research Bulletin* 42(1):137–42. doi: 10.1016/j.materresbull.2006.05.002.

J., Manju Gopinath R., Subash Gopi, Sanu Mathew Simon, A. C. Saritha, P. R. Biju, and N. V Unnikrishnan. 2020. “Spectroscopic Analysis of Eu3+ Doped Silica–Titania–Polydimethylsiloxane Hybrid ORMOSILs.” *RSC Adv.* 10:20057–66. doi: 10.1039/d0ra03073b.

Jenouvrier, P., E. Cela1, C. Coutier, M. Langlet, R. Rimet, and J. Fick. 2001. “Photoluminescence of Terbium-Organic Complex in Aerosol – Gel-Derived Planar Waveguides.” *Applied Physics B* 73:463–66. doi: 10.1007/s003400100707.

Judd, B. R., and I. Lindgren. 1961. “Theory of Zeeman Effect in the Ground

Multiplets of Rare-Earth Atoms." *Physical Review* 122(6):1802–12. doi: 10.1103/PhysRev.122.1802.

Kakoti, D., P. Dutta, P. Gogoi, N. Dehingia, N. Rajkonwar, A. Boruah, A. T. T. Mostako, P. K. Saikia, and P. K. Gogoi. 2019. "Effect of ZnS Nanoparticles on the Judd-Ofelt and Radiative Parameters of Sm3+ Ions in Sol-Gel Silica Matrix." *Journal of Luminescence* 211(April):401–12. doi: 10.1016/j.jlumin.2019.03.063.

Khaidir, Rahayu Emilia Mohamed, Yap Wing Fen, Mohd Hafiz Mohd Zaid, Khamirul Amin Matoria, Nur Alia Sheh Omar, Aisyah Zakiah Khirel Azman , Muhammad Fahmi Anuarb, Siti Aisyah Abdul Wahaba, Nur Alia, Sheh Omar, Muhammad Fahmi, Siti Aisyah, Abdul Wahab, Aisyah Zakiah, and Khirel Azman. 2019. "Exploring Eu 3 + -Doped ZnO-SiO 2 Glass Derived by Recycling Renewable Source of Waste Rice Husk for White-LEDs Application." *Results in Physics* 15(July). doi: 10.1016/j.rinp.2019.102596.

Kozuka, Hiromitsu. 2005. *Handbook of Sol-Gel Science and Technology: Processing, Characterization, and Applications*. Vol. I,II,III. edited by Sumio Sakka. New York: Kluwer Academic Publisher.

Kumar, Pawan, Kanika, Satbir Singh, Rimli Lahon, Abhiram Gundimeda, Govind Gupta, and Bipin Kumar Gupta. 2018. "A Strategy to Design Lanthanide Doped Dual-Mode Phosphor Mediated Spectral Convertor for Solar Cell Applications." *Journal of Luminescence* 196(October 2017):207–13. doi: 10.1016/j.jlumin.2017.12.035.

Kumar, Vijay Bhooshan, Madhavi Annamanedi, Muvva Durga Prashad, Kalle M. Arunasree, Yitzhak Mastai, Aharon Gedanken, Pradip Paik, and Received: 2013. "Synthesis of Mesoporous SiO 2 – ZnO Nanocapsules : Encapsulation of Small Biomolecules for Drugs and '" SiOZO-Plex "' for Gene Delivery." *Journal Nanopart Res* 15:1–13. doi: 10.1007/s11051-013-1904-y.

Kumar, Vinod, O. M. Ntwaeaborwa, T. Soga, Viresh Dutta, and H. C. Swart. 2017. "Rare Earth Doped Zinc Oxide Nanophosphor Powder : A Future Material for Solid State Lighting and Solar Cells." *ACS Photonics* 4:2613–37. doi: 10.1021/acsphotonics.7b00777.

Kumar, Vinod, S. P. Tiwari, O. M. Ntwaeaborwa, and Hendrik C. Swart. 2020.

"Spectroscopy of Lanthanide-Doped Oxide Materials." Pp. 345–64 in *Spectroscopy of Lanthanide Doped Oxide Materials*. Elsevier Ltd.

Kunkel, Nathalie, and Philippe Goldner. 2018. "Recent Advances in Rare Earth Doped Inorganic Crystalline Materials for Quantum Information Processing." *Zeitschrift Fur Anorganische Und Allgemeine Chemie* 644(2):66–76. doi: 10.1002/zaac.201700425.

Lee, Chee Sun, Khamirul Amin Matori, Sidek Hj Ab Aziz, Halimah Mohamed Kamari, Ismayadi Ismail, and Mohd Hafiz Mohd Zaid. 2017. "Fabrication and Characterization of Glass and Glass-Ceramic from Rice Husk Ash as a Potent Material for Opto-Electronic Applications." *Journal of Materials Science: Materials in Electronics* 28(23):17611–21. doi: 10.1007/s10854-017-7699-3.

Lee, Jae Won, Sungmin Kong, Woo Sik Kim, and Jinsoo Kim. 2007. "Preparation and Characterization of SiO2/TiO2 Core-Shell Particles with Controlled Shell Thickness." *Materials Chemistry and Physics* 106(1):39–44. doi: 10.1016/j.matchemphys.2007.05.019.

Li, Xiangtan, Binhua Yang, Junjie Zhang, Lili Hu, and Liyan Zhang. 2014. "Energy Transfer between Er3+ and Pr3+ for 2.7 Mm Fiber Laser Material." *Fibers* 2:24–33. doi: 10.3390/fib2010024.

Li, Xiaomin, Rui Wang, Fan Zhang, and Dongyuan Zhao. 2014. "Engineering Homogeneous Doping in Single Nanoparticle To Enhance Upconversion E Ffi Ciency." *Nano Letters* 14:3634–39.

Li, Xiaoyu, and Junhui He. 2013. "Synthesis of Raspberry-Like SiO2 − TiO2 Nanoparticles toward Antire Fl Ective and Self-Cleaning Coatings." *ACS Applied Materials & Interfaces* 5(11):5282–90. doi: https://doi.org/10.1021/am401124j.

Li, Z. Q., X. D. Li, Q. Q. Liu, X. H. Chen, Z. Sun, C. Liu, X. J. Ye, and S. M. Huang. 2012. "Core/Shell Structured NaYF 4:Yb 3+/Er 3+/Gd +3 Nanorods with Au Nanoparticles or Shells for Flexible Amorphous Silicon Solar Cells." *Nanotechnology* 23(2):1–8. doi: 10.1088/0957-4484/23/2/025402.

Liang, Leben, Zhifeng Mo, Biao Ju, Changming Xia, and Zhiyun Hou. 2020. "Visible and Near-Infrared Emission Properties of Yb 3 + / Pr 3 + Co-Doped Lanthanum Aluminum Silicate Glass." *Journal of Non-Crystalline Solids*

(November):120578. doi: 10.1016/j.jnoncrysol.2020.120578.

Liang, Leben, Zhifeng Mo, Biao Ju, Changming Xia, and Zhiyun Hou. 2021. "Visible and Near-Infrared Emission Properties of Yb 3 + / Pr 3 + Co-Doped Lanthanum Aluminum Silicate Glass." *Journal of Non-Crystalline Solids* 557(September 2020):120578. doi: 10.1016/j.jnoncrysol.2020.120578.

Liang, Liangliang, Yumin Liu, Chenghao Bu, Kaimo Guo, Weiwei Sun, Niu Huang, Tao Peng, Bobby Sebo, Mengmei Pan, Wei Liu, Shishang Guo, and Xing Zhong Zhao. 2013. "Highly Uniform, Bifunctional Core/Double-Shell-Structured β-NaYF 4:Er3+, Yb3+@SiO2@TiO2 Hexagonal Sub-Microprisms for High-Performance Dye Sensitized Solar Cells." *Advanced Materials* 25(15):2174–80. doi: 10.1002/adma.201204847.

Liang, Liangliang, Daniel B. L. Teh, Ngoc Duy Dinh, Weiqiang Chen, Qiushui Chen, Yiming Wu, Srikanta Chowdhury, Akihiro Yamanaka, Tze Chien Sum, Chia Hung Chen, Nitish V. Thakor, Angelo H. All, and Xiaogang Liu. 2019. "Upconversion Amplification through Dielectric Superlensing Modulation." *Nature Communications* 10(1):1–9. doi: 10.1038/s41467-019-09345-0.

Liégard, F., J. L. Doualan, R. Moncorgé, and M. Bettinelli. 2005. "Nd3+ → Yb3+ Energy Transfer in a Codoped Metaphosphate Glass as a Model for Yb3+ Laser Operation around 980 Nm." *Applied Physics B: Lasers and Optics* 80(8):985–91. doi: 10.1007/s00340-005-1829-y.

Lin, Tao, Xiao-wei Zhang, Yun-ji Wang, Jun Xu, Neng Wan, and Jian-feng Liu. 2012. "Luminescence Enhancement Due to Energy Transfer in ZnO Nanoparticles and Eu 3 + Ions Co-Doped Silica." *Thin Solid Films* 520(17):5815–19. doi: 10.1016/j.tsf.2012.04.058.

Liu, Quan, Yinsheng Xu, Qi Xia, Weiwei Li, Xianghua Zhang, Quan Liu, Yinsheng Xu, Qi Xia, Weiwei Li, and Xianghua Zhang. 2023. "Intense 2 . 7 Mu m Emission of Er3 + / Pr3 + Doped Ga5Ge20Sb10S65 Chalcogenide Glass." *Journal of the American Ceramic Society* 106(10):5743–53. doi: 10.1111/jace.19181.

Liu, Yujia, Yiqing Lu, Xusan Yang, Xianlin Zheng, Shihui Wen, Fan Wang, Xavier Vidal, Jiangbo Zhao, Deming Liu, Zhiguang Zhou, Chenshuo Ma, Jiajia Zhou, James A. Piper, Peng Xi, and Dayong Jin. 2017. "Amplified Stimulated

Emission in Upconversion Nanoparticles for Super-Resolution Nanoscopy." *Nature* 543(7644):229–33. doi: 10.1038/nature21366.

Livage, J. 2004. *BASIC PRINCIPLES of SOL-GEL CHEMISTRY*. Technologi. edited by M. A. Aegerter and M. Mennig. Boston, MA: Springer.

Lluscà, M., J. López-Vidrier, A. Antony, S. Hernández, B. Garrido, and J. Bertomeu. 2014. "Up-Conversion Effect of Er- and Yb-Doped ZnO Thin Films." *Thin Solid Films* 562:456–61. doi: 10.1016/j.tsf.2014.03.078.

Lojpur, Vesna M., Phillip S. Ahrenkiel, and Miroslav D. Dramićanin. 2013. "Color-Tunable up-Conversion Emission in Y2O3:Yb3+, Er3+ Nanoparticles Prepared by Polymer Complex Solution Method." *Nanoscale Research Letters* 8(1):1–6. doi: 10.1186/1556-276X-8-131.

Loo, Jacky Fong-chuen, Yi-hsin Chien, Feng Yin, Siu-kai Kong, Ho-pui Ho, and Ken-tye Yong. 2019. "Upconversion and Downconversion Nanoparticles for Biophotonics and Nanomedicine." *Coordination Chemistry Reviews* 400:213042. doi: 10.1016/j.ccr.2019.213042.

Lv, Zhijia, Longhai Jin, Yue Cao, Hao Zhang, Dongzhi Xue, Na Yin, Tianqi Zhang, Yinghui Wang, Jianhua Liu, Xiaogang Liu, and Hongjie Zhang. 2022. "A Nanotheranostic Agent Based on Nd 3 + -Doped YVO 4 with Blood-Brain-Barrier Permeability for NIR-II Fl Uorescence Imaging / Magnetic Resonance Imaging and Boosted Sonodynamic Therapy of Orthotopic Glioma." *Light: Science & Applications* 11(116):1–10. doi: 10.1038/s41377-022-00794-9.

Mahata, Manoj Kumar, Surya Prakash Tiwari, Shriparna Mukherjee, Kaushal Kumar, and Vineet Kumar Rai. 2014. "YVO4:Er3+ /Yb3+ Phosphor for Multifunctional Applications." *Journal of Optical Society America B* 31(8):1814–21.

Meijer, Janne Mieke, Linda Aarts, Bryan M. Van Der Ende, Thijs J. H. Vlugt, and Andries Meijerink. 2010. "Downconversion for Solar Cells in YF3: Nd3+, Yb 3+." *Physical Review B - Condensed Matter and Materials Physics* 81(3):1–9. doi: 10.1103/PhysRevB.81.035107.

Mhlongo. 2011. "Luminescence Investigation of Trivalent Rare Earth Ions in Sol-Gel Derived SiO2 and ZnO Co- Doped SiO2:Pr3+." University of Free State.

Minehan, W. T., G. L. Messing, and C. G. Pantano. 1989. "Titania-Silica Glasses

Prepared by Sintering Alkoxide Derived Spherical Colloids." *Journal of Non-Crystalline Solids* 108(2):163–68. doi: 10.1016/0022-3093(89)90579-6.

Mir, Wasim J., Tariq Sheikh, Habibul Arfin, Zhiguo Xia, and Angshuman Nag. 2020. "Lanthanide Doping in Metal Halide Perovskite Nanocrystals: Spectral Shifting, Quantum Cutting and Optoelectronic Applications." *NPG Asia Materials* 12(1). doi: 10.1038/s41427-019-0192-0.

Mohamed, R. M., and I. A. Mkhalid. 2010. "The Effect of Rare Earth Dopants on the Structure , Surface Texture and Photocatalytic Properties of TiO 2 – SiO 2 Prepared by Sol – Gel Method." *Journal of Alloys and Compounds* 501:143–47. doi: 10.1016/j.jallcom.2010.04.061.

Mossad Ali, Atif, Adel A. Ismail, Rasha Najmy, and Ali Al-hajry. 2014. "Preparation and Characterization of ZnO – SiO 2 Thin Films as Highly Efficient Photocatalyst." *Journal of Photochemistry & Photobiology, A: Chemistry* 275:37–46. doi: 10.1016/j.jphotochem.2013.11.002.

Muniz, R. F., V. S. Zanuto, M. S. Gibin, J. V. Gunha, A. Novatski, J. H. Rohling, A. N. Medina, and M. L. Baesso. 2023. "Down- and up-Conversion Processes in Nd3+/Yb3+ Co-Doped Sodium Calcium Silicate Glasses with Concomitant Yb2+ Assessment." *Journal of Rare Earths* 41(3):342–48. doi: 10.1016/j.jre.2022.01.020.

Naresh, V., and S. Buddhudu. 2015. "Analysis of Visible-NIR Emission and Photoluminescence Quenching in Er3+lasses: Bi2O3-AIF3-TeO2-B2O3." *Journal, Glasses European Science, Glass Part, Technology* 56(6):255–62. doi: 10.13036/17533562.56.5.255.

Nizamutdinov, A. S., S. V Kuznetsov, V. A. Konyushkin, A. N. Nakladov, E. I. Madirov, V. V Voronov, A. R. Khadiev, M. A. Marisov, and V. V Semashko. 2019. "LUMINESCENCE OF GdF 3 : Pr : Yb AND YF 3 : Pr : Yb SOLID SOLUTIONS SYNTHESIZED BY CRYSTALLIZATION FROM THE MELT." *Journal of Applied Spectroscopy* 86(5):795–801. doi: 10.1007/s10812-019-00895-1.

Ntwaeaborwa, O. M., and P. H. Holloway. 2005. "Enhanced Photoluminescence of Ce 3+ Induced by an Energy Transfer from ZnO Nanoparticles Encapsulated in SiO 2." *Nanotechnology* 16(6):865–68. doi: 10.1088/0957-4484/16/6/042.

Ofelt, G. S. 1962. “Intensities of Crystal Spectra of RareEarth Ions.” *The Journal of Chemical Physics* 37(May 2012):511–20. doi: 10.1063/1.1701366.

Pellegrino, Anna L., Paolo Cortelletti, Marco Pedroni, Adolfo Speghini, and Graziella Malandrino. 2017. “Nanostructured CaF2:Ln3+ (Ln3+ = Yb3+/Er3+, Yb3+/Tm3+) Thin Films: MOCVD Fabrication and Their Upconversion Properties.” *Advanced Materials Interfaces* 4(18):2–7. doi: 10.1002/admi.201700245.

Pisarski, Wojciech A., Joanna Pisarska, Marta Kuwik, Marcin Kochanowicz, Jacek Żmojda, Piotr Miluski, Agata Baranowska, Jan Dorosz, Magdalena Leśniak, and Dominik Dorosz. 2020. “Fluoroindate Glasses Co-doped with Pr3+/Er3+ for Near-infrared Luminescence Applications.” *Scientific Reports* 10(0123456789):1–16. doi: 10.1038/s41598-020-77943-w.

Prathibha, K. N., R. Hari Krishna, B. V. Nagesh, D. Prakashbabu, B. S. Panigrahi, and R. Ananthanarayanan. 2021. “Investigation of Luminescence Spectroscopic Characteristics in Eu3+-Doped Zn2SiO4 by Judd–Ofelt Parameters.” *Journal of Materials Science: Materials in Electronics* 32(15):20197–210. doi: 10.1007/s10854-021-06524-y.

Pudovkin, M. S., A. K. Ginkel, and E. V. Lukinova. 2021. “Temperature Sensitivity of Nd3+, Yb3+:YF3 Ratiometric Luminescent Thermometers at Different Yb3+ Concentration.” *Optical Materials* 119(April):111328. doi: 10.1016/j.optmat.2021.111328.

Qiu, Jianrong, Kentarou Nouchi, Kiyotaka Miura, Tsuneo Mitsuyu, and Kazuyuki Hirao. 2000. “Room-Temperature Persistent Spectral Hole Burning of x-Ray-Irradiated Sm 3 + -Doped Glass.” *J. Phys.: Condens. Matter* 12:5061–5067.

Raevskaya, A. E., Ya V. Panasiuk, O. L. Stroyuk, S. Ya Kuchmiy, V. M. Dzhagan, A. G. Milekhin, N. A. Yeryukov, L. A. Sveshnikova, E. E. Rodyakina, V. F. Plyusnin, and D. R. T. Zahn. 2014. “Spectral and Luminescent Properties of ZnO-SiO2 Core-Shell Nanoparticles with Size-Selected ZnO Cores.” *RSC Advances* 4(108):63393–401. doi: 10.1039/c4ra07959k.

Rai, Suman, and Andrew L. Fanai. 2014. “Spectroscopic Studies of Ho 3+ Doped SiO 2-TiO 2 Nanoparticle for Photonic Applications.” *Science Vision* 14(3):112–17.

Reisfeld, R., and Y. Kalisky. 1981. “Nd3+ and Yb3+ Germanate and Tellurite Glasses for Fluorescent Solar Energy Collectors.” *Chemical Physics Letters* 80(1):178–83. doi: 10.1016/0009-2614(81)80084-X.

Richards, B. S. 2006. “Enhancing the Performance of Silicon Solar Cells via the Application of Passive Luminescence Conversion Layers.” *Solar Energy Materials and Solar Cells* 90(15):2329–37. doi: 10.1016/j.solmat.2006.03.035.

Rosales, Alicia, and Karen Esquivel. 2020. “SiO2@TiO2 Composite Synthesis and Its Hydrophobic Applications: A Review.” *Catalysts* 10(2):1–17. doi: 10.3390/catal10020171.

Saeed, N. A. M., E. Coetsee, and H. C. Swart. 2020. “Down-Conversion of YOF: Pr3+, Yb3+ Phosphor.” *Optical Materials* 110(February):110516. doi: 10.1016/j.optmat.2020.110516.

Sales, A. J. M., D. G. Sousa, H. O. Rodrigues, M. M. Costa, A. S. B. Sombra, and F. N. A. Freire. 2016. “Power Dependent Upconversion in Er 3+/ Yb 3+ Co-Doped BiNbO 4 Phosphors.” *Ceramics International* 42(6):6899–6905. doi: 10.1016/j.ceramint.2016.01.075.

Serrano, D., A. Braud, J. L. Doualan, P. Camy, A. Benayad, V. Ménard, and R. Moncorgé. 2011. “Ytterbium Sensitization in KY3F10: Pr3+, Yb3+ for Silicon Solar Cells Efficiency Enhancement.” *Optical Materials* 33(7):1028–31. doi: 10.1016/j.optmat.2010.07.023.

Shi, Gang, Jie Chen, Likui Wang, Dawei Wang, Jingguo Yang, Ying Li, Liping Zhang, Caihua Ni, and Lifeng Chi. 2016. “Titanium Oxide/Silicon Moth-Eye Structures with Antireflection, p–n Heterojunctions, and Superhydrophilicity.” *Langmuir* 32(41):10719–24. doi: 10.1021/acs.langmuir.6b03117.

Smentek, Lidia. 1988. “Theoritical Description of the Spectroscopic Properties of Rare Earth Ions in Crystal.” *Physics Reports* 297:155–237.

Smentek, Lidia, and Brian G. Wybourne. 2000. “Relativistic f ↔ f Transitions in Crystal Fields.” *Journal of Phsics B* 33:3647–51.

Song, Nan, Songbin Liu, Peng Zhang, Junshan He, Qinyuan Zhang, Feng Wang, and Bo Zhou. 2021. “Enhancing Upconversion of Nd3+ through Yb3+-Mediated Energy Cycling towards Temperature Sensing.” *Journal of Rare Earths* 39(12):1506–11. doi: 10.1016/j.jre.2021.06.013.

Soni, Abhishek Kumar, Riya Dey, and Vineet Kumar Rai. 2015. “Stark Sublevels in Tm3+–Yb3+ Codoped Na2Y2B2O7 Nanophosphor for Multifunctional Applications.” *RSC Advances* 5:34999–9. doi: 10.1039/C4RA15891A.

Srinivasa Rao, Ch, I. V Kityk, T. Srikumar, G. Naga Raju, V. Ravi Kumar, Y. Gandhi, and N. Veeraiah. 2011. “Spectroscopy Features of Pr 3 + and Er 3 + Ions in Li 2 O – ZrO 2 – SiO 2 Glass Matrices Mixed with Some Sesquioxides.” *Journal of Alloys and Compounds* 509:9230–39. doi: 10.1016/j.jallcom.2011.07.001.

Sta, I., M. Jlassi, M. Hajji, M. F. Boujmil, R. Jerbi, M. Kandyla, M. Kompitsas, and H. Ezzaouia. 2014. “Structural and Optical Properties of TiO2 Thin Films Prepared by Spin Coating.” *Journal of Sol-Gel Science and Technology* 72(2):421–27. doi: 10.1007/s10971-014-3452-z.

Strohhofer, C., J. Fick, H. C. Vasconcelos, and R. M. Almeida. 1998. “Active Optical Properties of Er-Containing Crystallites in Sol – Gel Derived Glass Films.” *Journal of Non-Crystalline Solids* 226:182–91.

Sukul, Prasenjit Prasad, and Kaushal Kumar. 2016. “Near-Infrared (808 and 980 Nm) Excited Photoluminescence Study in Nd-Doped Y2O3 Phosphor for Bio-Imaging.” *Methods and Applications in Fluorescence* 4(44005):1–9. doi: 10.1088/2050-6120/4/4/044005.

Sun, Ting, Ai Hua Li, Chao Xu, Yu Heng Xu, and Rui Wang. 2013. “Energy Transfer Properties of Nd3+→Yb3+ in Nd:Yb:LiNbO3 Crystals.” *Optics and Laser Technology* 56:322–25. doi: 10.1016/j.optlastec.2013.09.010.

Sun, Xiaoyu, Xiaozhuang Xu, Guanyu Song, Jielei Tu, Lei Li, Pinyuan Yan, Weinan Zhang, and Kai Hu. 2020. “Preparation of MgF2/SiO2 Coating with Broadband Antireflective Coating by Using Sol–Gel Combined with Electron Beam Evaporation.” *Optical Materials* 101(November 2019):2–10. doi: 10.1016/j.optmat.2020.109739.

Tavernaro, Isabella, Christian Cavelius, Henrike Peuschel, and Annette Kraegeloh. 2017. “Bright Fluorescent Silica-Nanoparticle Probes for High-Resolution STED and Confocal Microscopy.” *Beilstein Journal of Nanotechnology* 8:1283–96. doi: 10.3762/bjnano.8.130.

Tran, T. T. Va., T. M. Dun. Cao, Quang Vinh Lam, and Van Hieu Le. 2017.

"Emission of Eu3 + in SiO2-ZnO Glass and SiO2-SnO2 Glass-Ceramic: Correlation between Structure and Optical Properties of Eu3 + Ions." *Journal of Non-Crystalline Solids* 459:57–62. doi: 10.1016/j.jnoncrysol.2016.12.040.

Tseng, Yung-kuan, Ming-hung Chuang, Yen-cheng Chen, and Chao-hsien Wu. 2012. "Synthesis of 1D, 2D, and 3D ZnO Polycrystalline Nanostructures Using the Sol-Gel Method." *Journal of Nanotechnology* 2012:1–9. doi: 10.1155/2012/712850.

Tung, Pham Son, Le Thi Thu Hien, Ngo Ngoc Ha, Tran Ngoc Khiem, and Nguyen Duc Chien. 2016. "Influence of Composition , Doping Concentration and Annealing Temperatures on Optical Properties of Eu3+-Doped ZnO–SiO2 Nanocomposites." *Journal of Nanoscience and Nanotechnology* 16(8):7955–58. doi: 10.1166/jnn.2016.12756.

Vasconcelos, Helena Cristina, and Afonso Silva Pinto. 2017. "Fluorescence Properties of Rare-Earth-Doped Sol-Gel Glasses." in *Recent Applications in Sol-Gel Synthesis*, edited by Usha chandra. IntechOpen.

Villanueva-Delgado, Pedro, Karl W. Krämer, and Rafael Valiente. 2015. "Simulating Energy Transfer and Upconversion in β-NaYF4: Yb3+, Tm3+." *Journal of Physical Chemistry C* 119(41):23648–57. doi: 10.1021/acs.jpcc.5b06770.

Walsh, Brian M. 2006. "Judd-Ofelt Theory: Principles and Practices." Pp. 403–33 in *Advances in Spectroscopy for Lasers and Sensing*, edited by B. Di Bartolo and O. Forte. Netherland: Springer.

Wang, Fangke, Lei Cui, Zhengce An, Xiangting Zhang, Yanhua Song, Ye Sheng, and Haifeng Zou. 2019. "Interfacial Energy Transfer in Hollow Double-Shelled TiO2 : X % Eu3 + @ SiO2 : Y % Tb3 + Nanospheres for Tissue Imaging." *ACS Applied Nano Materials* 1–28. doi: 10.1021/acsanm.9b01713.

Wang, Feng, and Xiaogang Liu. 2009. "Recent Advances in the Chemistry of Lanthanide-Doped Upconversion Nanocrystals." *Chemical Society Reviews* 38:976–89. doi: 10.1039/b809132n.

Wang, Qun, Changyuan Xu, Fengjiao Zhao, and Hongming Yin. 2024. "Energy Transfer Er3+-Nd3+ Co-Doped in Tellurate via Energy Level Match." *Current Applied Physics* 65:68–74.

Wang, Shuangyue, Hongwei Yan, Dengji Li, Liang Qiao, Shaobo Han, Xiaodong

Yuan, and Wei Liu. 2018. “TEM and STEM Studies on the Cross- Sectional Morphologies of Dual- / Tri-Layer Broadband SiO 2 Antireflective Films.” *Nanoscale Research Letters* 13(49):0–8. doi: 10.1186/s11671-018-2442-4.

Wang, Xiaodong, Guangming Wu, Bin Zhou, and Jun Shen. 2013. “Thermal Annealing Effect on Optical Properties of Binary TiO 2 -SiO 2 Sol-Gel Coatings.” *Materials* 6:76–84. doi: 10.3390/ma6010076.

Wang, Ye-fu, Gao-yuan Liu, Ling-dong Sun, Jia-wen Xiao, Jia-cai Zhou, Chun-hua Yan, and Wang E. T. Al. 2013. “Nd 3+ -Sensitized Upconversion Nanophosphors : E Ffi Cient In Vivo Bioimaging Probes with Minimized Heating E Ff Ect.” *ACS Nano* 7(8):7200–7206.

Weisenbach, Lon, Brian J. J. Zeinski, John O. Kelly, Jeanne Morreale, Ronald L. Roncone, and James J. Burke. 1991. “The Influence of Processing Variables on the Optical Properties of SiO2-Ti02 Planar Waveguides.” *Submolecular Glass Chemistry and Physics* 1590:50–58.

Wen, Hongli, and Peter A. Tanner. 2011. “Energy Transfer and Luminescence Studies of Pr3+, Yb 3+ Co-Doped Lead Borate Glass.” *Optical Materials* 33(11):1602–6. doi: 10.1016/j.optmat.2011.04.024.

Wen, Shihui, Jiajia Zhou, Kezhi Zheng, Artur Bednarkiewicz, Xiaogang Liu, and Dayong Jin. 2018. “Advances in Highly Doped Upconversion Nanoparticles.” *Nature Communications* 9(1):1–12. doi: 10.1038/s41467-018-04813-5.

Xiao, F., R. Chen, Y. Q. Shen, Z. L. Dong, H. H. Wang, Q. Y. Zhang, and H. D. Sun. 2012. “Efficient Energy Transfer and Enhanced Infrared Emission in Er-Oped ZnO-SiO 2 Omposites.” *Journal of Physical Chemistry C* 116(24):13458–62. doi: 10.1021/jp304075g.

Xiao, F., R. Chen, Y. Q. Shen, B. Liu, G. G. Gurzadyan, Z. L. Dong, Q. Y. Zhang, and H. D. Sun. 2011. “Infrared Emission Properties and Energy Transfer in ZnO – SiO 2 : Yb 3 + Composites.” *Journal of Alloys and Compounds* 509(November 2018):7794–97. doi: 10.1016/j.jallcom.2011.05.011.

Xiaoqi, Meng, Li Lianqiang, Zou Kaishun, and Liu Juncheng. 2014. “The Effect of SiO2 on TiO2 Up-Conversion Photoluminescence Film.” *Optical Materials* 37(C):367–70. doi: 10.1016/j.optmat.2014.06.027.

Xu, Jian, S. O. Keefe, and Carole C. Perry. 2004. “The Preparation and

Characterization of Sol – Gel Zinc Silicate Glass Particles with Pyramid Shape and Millimetre Size." *Journal of Material Chemistry* 14:1744–48.

Yu, Lixin, and Masayuki Nogami. 2007. "Local Structure and Photoluminescent Characteristics of Eu 3 + in ZnO – SiO 2 Glasses." *Journel of Sol-Gel Technology* 43:355–60. doi: 10.1007/s10971-007-1581-3.

Zareba-Grodz, Iwona, Robert Pazik, Włodzimierz Tylus, Witold Mielcarek, Krzysztof Hermanowicz, Wiesław Strek, and Krzysztof Maruszewski. 2007. "Europium-Doped Silica – Titania Thin Films Obtained by the Sol – Gel Method." *Optical Materials* 29:1103–6. doi: 10.1016/j.optmat.2006.05.001.

Zhang, Q. Y., K. Pita, and C. H. Kam. 2003. "Sol – Gel Derived Zinc Silicate Phosphor Films for Full-Color Display Applications." *Journal of Physics and Chemistry of Solids* 64:333–38.

Zhang, Q. Y., and G. F. Yang. 2007. "Cooperative Downconversion in GdAl3(BO3)4: RE3+, Yb3+ (RE=Pr, Tb, and Tm)." *Applied Physics Letters* 91(5):4–7. doi: 10.1063/1.2757595.

Zhao, Jiangbo, Dayong Jin, Erik P. Schartner, Yiqing Lu, Yujia Liu, Andrei V Zvyagin, Lixin Zhang, Judith M. Dawes, Peng Xi, James A. Piper, Ewa M. Goldys, and Tanya M. Monro. 2013. "Single-Nanocrystal Sensitivity Achieved by Enhanced Upconversion Luminescence." *Nature Nanotechnology* (September):1–6. doi: 10.1038/nnano.2013.171.

Zhou, Bo, Bingyang Shi, Dayong Jin, and Xiaogang Liu. 2015. "Controlling Upconversion Nanocrystals for Emerging Applications." *Nature Nanotechnology* 10(11):924–36. doi: 10.1038/nnano.2015.251.

Zhu, Wenjuan, Daqin Chen, Lei Lei, Ju Xua, and Yuansheng Wang. 2014. "An Active-Core/Active-Shell Structure with Enhanced Quantum-Cutting Luminescence in Pr – Yb Co-Doped Monodisperse Nanoparticles." *Nanoscale Communication* 6(10500):10500–504. doi: 10.1039/C4NR02785J.

Zieliński, Michał, Bogdan Czajka, Mariusz Pietrowski, Iwona Tomska-Foralewska, Emilia Alwin, Monika Kot, and Maria Wojciechowska. 2017. "MgO-MgF2 System Obtained by Sol–Gel Method as an Immobilizing Agent of the Electrolyte Applied in the High Temperature Cells." *Journal of Sol-Gel Science and Technology* 84(2):368–74. doi: 10.1007/s10971-017-4495-8.

Zou, Zehua, Lin Feng, Cheng Cao, Jiachi Zhang, and Yuhua Wang. 2016. “Near-Infrared Quantum Cutting Long Persistent Luminescence.” *Scientific Reports* 6(May):1–7. doi: 10.1038/srep24884.

*CHAPTER- 5*

# $Pr^{3+}/Er^{3+}$ AND $Nd^{3+}/Er^{3+}$ PAIR CO-DOPED TITANIA-SILICATE AND ZINC-SILICATE DENSE GLASS CERAMIC FOR IR LUMINESCENT APPLICATION

***This chapter is focused on the Erbium-Praseodymium and Erbium-Neodymium ions pair co-doping in Titania-Silicate and Zinc-Silicate dense glass ceramic materials***

*Chapter -5*

---

# $Pr^{3+}/Er^{3+}$ and $Nd^{3+}/Er^{3+}$ pair co-doped Titania-Silicate and Zinc-Silicate Dense Glass Ceramic for IR luminescent application

---

## 5.1. Introduction

The rare-earth (RE) ion based luminescent materials can emit light in the mid-IR region. A sensitizer RE ion can transfer absorption photon energy to another RE ion to amplify its emission intensity. The co-doping of different $RE^{3+}$ ions can mitigate cross-relaxation processes between same pair of RE ion through tuning their ionic interaction, which allow high concentration of $RE^{3+}$ doping. The mid-IR laser holds promise for various applications including military countermeasures (Liu et al. 2023), remote sensing, and laser microsurgery (Xiangtan Li et al. 2014). Similarly, optical fiber amplifiers are utilized across different bands such as O-band (1260-1360 nm ), E-band (1360-1460 nm ), S-band (1460-1560 nm ), C-band (1560-1660 nm ), and L-band (1660-1760 nm ) (Pisarski et al. 2020). Recent interest has surges in fluorescence imaging technology, particularly in the second NIR bio window (1000-1700 nm), owing to its advantageous features like high spatial resolution and minimum tissue absorption and scattering (Lv et al. 2022).

Notably, Praseodymium ion ($Pr^{3+}$) and Neodymium ion ($Nd^{3+}$), when paired separately with Erbium ion ($Er^{3+}$) show promise for broadband NIR luminescence with including a wavelength range from 1.2 μm to 1.7 μm. $Pr^{3+}$ effectively sensitizes $Er^{3+}$ emission at 1.5 and 2.7 μm wavelengths. The broad near-IR luminescence mainly originates from transitions in $Pr^{3+}$: $^{l}D_2 \rightarrow {}^{1}G_4$, $Er^{3+}$:$^{4}I_{13/2} \rightarrow {}^{4}I_{15/2}$ and $Er^{3+}$:$^{4}I_{11/2} \rightarrow {}^{4}I_{13/2}$ resulting in emission lines around 1.48 and 2.7 μm (Pisarski et al. 2020). Similarly, $Nd^{3+}$ has been observed with transitions in the NIR region such as

$Nd^{3+}$:$^4F_{3/2} \rightarrow {}^4I_{9/2}$, $Nd^{3+}$:$^4F_{3/2} \rightarrow {}^4I_{11/2}$, $Nd^{3+}$:$^4F_{3/2} \rightarrow {}^4I_{13/2}$ etc. Typically, $Er^{3+}$ ions emit at characteristic emission bands centered at approximately 525 nm ($^4I_{15/2} \rightarrow {}^2H_{11/2}$) (Dwivedi et al. 2008), and 640 nm ($^4I_{15/2} \rightarrow {}^4F_{9/2}$) respectively in visible region. Thus addition of $Er^{3+}$ ions with $Pr^{3+}$ and $Nd^{3+}$ alters the optical properties of the material, offering potential applications in photonics.

For c-Si solar cell, the NIR downconversion materials are suitable which can convert near UV (300-400 nm) part of solar spectrum to photon of 1000-1100 nm (band gap 1.12 eV) (Deshmukh et al. 2018).

Erbium/Neodymium ion ($Nd^{3+}/Er^{3+}$) pairs have been doped in Yttrium Oxide (Deshmukh et al. 2018), Tellurate glass (Wang et al. 2024), etc. Similarly, Erbium-Praseodymium ion ($Er^{3+}/Pr^{3+}$) pairs have been doped in different glasses such as Fluoroindate (Pisarski et al. 2020), Germinate glass (Xiangtan Li et al. 2014), Chalcogenide glass (Liu et al. 2023) etc. Thus both of these pairs have interesting applications in photonics as they cover a wide range of absorption and emission with multiple emission peaks in UV-VIS and NIR region. However, the phenomenon of $Er^{3+}/Pr^{3+}$ and $Er^{3+}/Nd^{3+}$ pair doping in $TiO_2$-$SiO_2$ and ZnO-$SiO_2$ dense glass material remains unexplored. The incorporation of different $RE^{3+}$ ion pairs in Titania-Silicate or Zinc silicate dense glass ceramic could yield luminescent materials with similar intrinsic luminescent properties.

Here, we prepared two novel luminescent materials using $Er^{3+}/Pr^{3+}$ and $Nd^{3+}/Er^{3+}$ pairs. The idea behind the doping of $Er^{3+}/Pr^{3+}$ ion in a Titania-Silicate host and $Nd^{3+}/Er^{3+}$ ions in a Zinc-Silicate host arises to observe possible modifications in structural, morphological and optical properties. The synthesis procedure of Titania-Silicate or Zinc silicate host for $RE^{3+}$ ion doping was kept intact as mentioned in previous chapters. The $Er^{3+}/Pr^{3+}$ ion pairs are co-doped in titania-silicate dense glass ceramic using the same novel *ex-situ* sol-gel method as used in the STPYX-DGC material (Chapter 3). Similarly, $Nd^{3+}/Er^{3+}$ ion pairs are co-doped in Zinc-silicate dense glass ceramic using another novel *ex-situ* sol-gel method as mentioned in the SZNYX-DGC material (Chapter 4). The absorption and photoluminescence properties of the as-synthesized material were recorded to mark optical property modifications after the addition of $Er^{3+}$ ions which may have potential applications in photonics.

## 5.2. Synthesis: $Pr^{3+}/Er^{3+}$ ion pair in Titania-Silicate dense glass ceramic material

The co-doping of low concentrations (0.7 mol% each) of $Er^{3+}$ ion and $Pr^{3+}$ ions pair in Titania-Silicate ($Er^{3+}/Pr^{3+}$:**$TiO_2$-$SiO_2$**) dense glass material was performed using the similar novel *ex-situ* sol-gel method as discussed in section 3.1 of chapter 3, where we replaced $Yb^{3+}$ ions with $Er^{3+}$ ions. The structural, morphological and optical properties of the as-synthesized material were investigated as follows.

### 5.2.1. Structural Characterization

The structural characterization of the $Er^{3+}/Pr^{3+}$:$TiO_2$-$SiO_2$ dense glass ceramic material annealed at 900 ºC was performed with ATR-FTIR spectroscopy and XRD patterns to highlight the structural growth.

#### 5.2.1.1. XRD analysis

XRD measurements (Figure 5.1) of the $Er^{3+}/Pr^{3+}$:$TiO_2$-$SiO_2$ dense glass material annealed at 900 ºC showed crystalline growth of $TiO_2$, which suppresses the amorphous nature of the silica host (El-Bashir 2017), (Amin et al. 2018). The diffraction peaks of $TiO_2$ nano-crystallites, such as rutile (200), rutile (111), anatase (202), and rutile (220) phases, were observed at two thetas (2θ) values, namely 26.64°, 40.64°, 46.08° and, 56.1° respective ely, as reported elsewhere (Ismail et al. 2007). The average crystallite size of $TiO_2$ crystal in $SiO_2$ host was calculated from the most prominent peak corresponding to (200) using Scherrer equation of about 59 nm (Li and He 2013). We can conclude that the as-synthesized and annealed $Er^{3+}/Pr^{3+}$:$TiO_2$-$SiO_2$ dense glass material is in glass-ceramic form, similar to the STPY07-DGC sample reported in chapter 3.

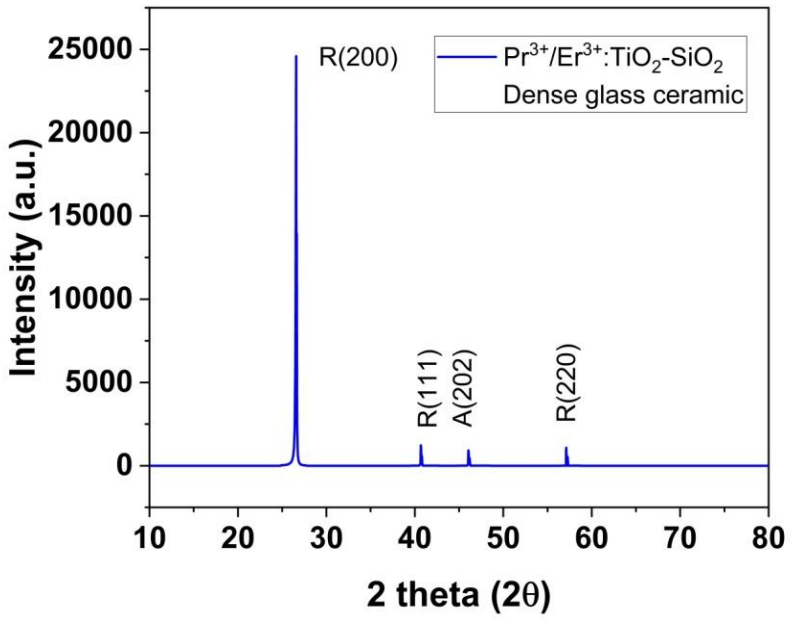


Figure 5.1: XRD spectra of the $Er^{3+}/Pr^{3+}$:$TiO_2$-$SiO_2$ dense glass material annealing at 900 ºC.

Thus, the homogeneous and regular dispersion of Ti and Si atoms in the composite solution promotes Ti–O–Si bonds along with $TiO_2$ particles in the amorphous $SiO_2$ to offer a better host for $RE^{3+}$ ion doping (Amin et al. 2018). The presence of $RE^{3+}$ ions ($Pr^{3+}/Er^{3+}$) has not been observed in the as-synthesized material.

### 5.2.1.2. ATR-FTIR Spectra

Figure 5.2 shows the ATR-FTIR spectra of the $Er^{3+}/Pr^{3+}$:$TiO_2$-$SiO_2$ dense glass material annealed at 900 ºC. The FTIR absorption bands for the material around 3356 $cm^{-1}$ (Buarque et al. 2018) and 1658 $cm^{-1}$ have probably been removed due to the telescopic and angular vibrations of the $OH^-$ group bond, while the broad absorption band at 955 $cm^{-1}$ corresponds to the Si-O-Si asymmetric stretching stretching vibrations in the amorphous silica glass. The finding is in agreement with the observation made in the STPY07-DGC sample (Sun et al. 2020). The removal of surface adsorbed water in the material annealed at 900 ºC is useful against hydroxyl-quenching (X. Wang et al. 2013). The absorption bands around 1267 and 1032 $cm^{-1}$

are attributed to the Si-O-Ti bonds (X. Wang et al. 2013), (Chang et al. 2018). Thus presence of $RE^{3+}$ ions has not been observed in the ATR-FTIR spectrum.

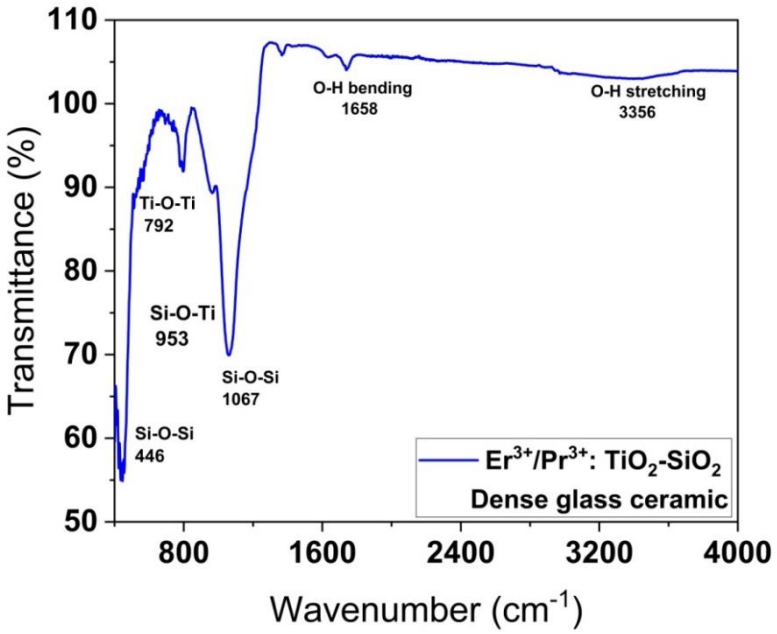


Figure 5.2: ATR-FTIR spectra of the $Er^{3+}/Pr^{3+}$:$TiO_2$-$SiO_2$ dense glass material annealing at 900ºC.

### 5.2.2. Morphological characterization

The morphological characterization of the as-synthesized $Er^{3+}/Pr^{3+}$:$TiO_2$-$SiO_2$ dense glass ceramic material annealed at 900ºC was carried out using TEM analysis to determine the particle size and distribution.

#### 5.2.2.1. TEM analysis

The TEM micrograph (Figure 5.3(a)) of the $Er^{3+}/Pr^{3+}$:$TiO_2$-$SiO_2$ dense glass material annealed at 900 C shows the presence of $TiO_2$ nano-crystallites along with an amorphous $SiO_2$ matrix. The average particle size of $TiO_2$ nano-crystallites was found to be approximately 55-59 nm, which agree with reported literature (J. et al. 2020), (Wang et al. 2018).

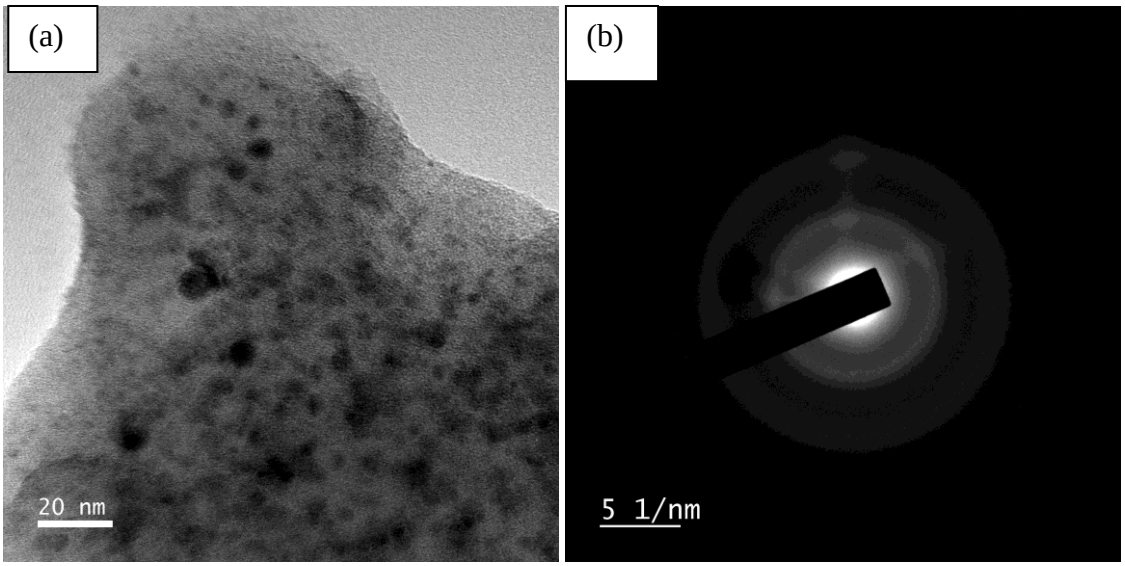


Figure 5.**3**: (a) FETEM image with magnification bar at 200 nm (b) SAED pattern of the annealed $Er^{3+}/Pr^{3+}$:$TiO_2$-$SiO_2$ dense glass ceramic material annealed at 900 ºC.

The amorphous nature of $SiO_2$ was further confirmed with the diffuse nature of the selected area electron diffraction (SAED) pattern as in Fig 5.3(b). The bright spots in the SAED pattern were not observed due to $TiO_2$ nano-crystallites which may be due to the domination of amorphous $SiO_2$ over lower concentration of crystalline $TiO_2$ screened complete crystalline growth (Minehan et al. 1989).

### 5.2.3. Optical characterization

The optical properties of the $Er^{3+}/Pr^{3+}$:$TiO_2$-$SiO_2$ dense glass ceramic materials annealed at 900ºC were evaluated through UV-Vis-NIR absorption and photoluminescence spectroscopy.

#### 5.2.3.1. UV-Vis-NIR Absorption spectra

The UV-Vis-NIR absorption spectrum (Figure 5.4) of the $Er^{3+}/Pr^{3+}$:$TiO_2$-$SiO_2$ dense glass ceramic material shows different absorption bands in the UV-VIS & NIR region for excitation of 4f electrons from ground state of $Er^{3+}$ ($^4I_{15/2}$), $Pr^{3+}$ ($^3H_4$ ), and $Yb^{3+}$($^2F_{7/2}$) ion (Fig 5.4). The presence of $Er^{3+}$ ion in the $Er^{3+}/Pr^{3+}$:$TiO_2$-$SiO_2$ dense glass ceramic material has been validated with additional peaks around 450 nm ($^4I_{15/2}\rightarrow{}^4F_{5/2}$), 521 nm ($^4I_{15/2}\rightarrow{}^2H_{11/2}$) (Dwivedi et al. 2008), 653 nm ($^4I_{15/2}\rightarrow{}^4F_{9/2}$) (Naresh and Buddhudu 2015), 799 nm ($^4I_{15/2}\rightarrow{}^4I_{9/2}$) and 942 nm ($^4I_{15/2}\rightarrow{}^4I_{11/2}$)

(Naresh and Buddhudu 2015). The absorption spectra of the $Er^{3+}/Pr^{3+}$:$TiO_2$-$SiO_2$ sample has two important intense peaks at 450 which can be used to pump the material for obtaining emission in visible range. Both, $Er^{3+}$ and $Pr^{3+}$ ions can absorb photon of wavelength 450 nm. Here presence of $Pr^{3+}$ ion is already validated with peaks around 450 nm, 477 nm, 591 nm, as already discussed in Chapter 3. The intensity enhancement of absorption peaks of $Nd^{3+}$ ion has been observed for co-doping of $Er^{3+}$ ion when compared with the absorption spectra of the $Er^{3+}/Pr^{3+}$:$TiO_2$-$SiO_2$ dense glass ceramic material in Fig 3.7.

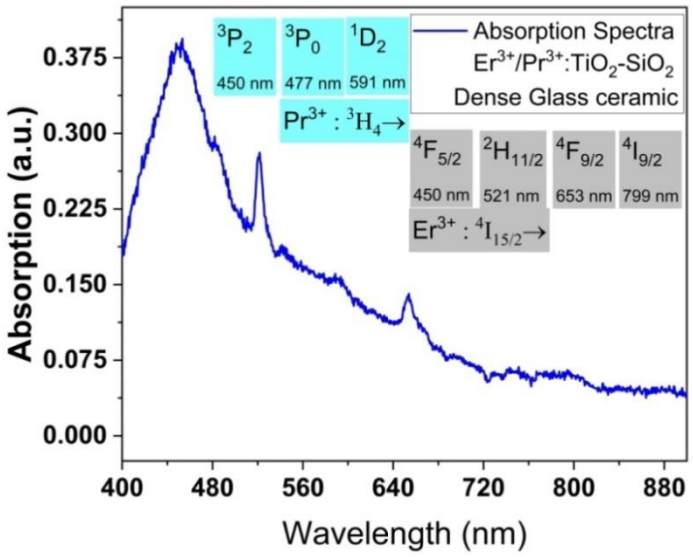


Fig. 5.4. Absorption spectra of the $Er^{3+}/Pr^{3+}$:$TiO_2$-$SiO_2$ dense glass material

### 5.2.3.2. Downconversion luminescence spectra

The DCL spectrum (Figure 5.5) of the $Er^{3+}/Pr^{3+}$:$TiO_2$-$SiO_2$ dense glass ceramic material exibits multiple emission peaks in the visible and NIR regions, which can be attributed to the radiative transitions of $Er^{3+}$ and $Pr^{3+}$ ($^2F_{7/2}$) ions embedded in $TiO_2$-$SiO_2$ matrix. The excited electron relaxes to lower energy after emitting the absorption energy from incident photon of wavelength 450 nm. The characteristic emission peaks of $Er^{3+}$ ions are observed around 514 nm ($^4F_{7/2}\rightarrow{}^4I_{15/2}$) (Pisarski et al. 2020), 538 nm ($^2H_{11/2}\rightarrow{}^4I_{15/2}$) (Mahata et al. 2014), (Li et al. 2012), 559 nm ($^4S_{3/2}\rightarrow{}^4I_{15/2}$) (Sales et al. 2016) and 659 nm ($^4F_{9/2}\rightarrow{}^4I_{15/2}$) (Lojpur et al. 2013).

Similarly the transition due to the $Pr^{3+}$ ion has also been validated with peaks around 545 nm ($^3P_1 \rightarrow {}^3H_5$), 566 nm ($^3P_1 \rightarrow {}^3H_4$), 598 nm ($^1D_2 \rightarrow {}^3H_4$), 657 nm ($^3P_0 \rightarrow {}^3F_2$), and 723 nm ($^3P_0 \rightarrow {}^3F_4$) etc.

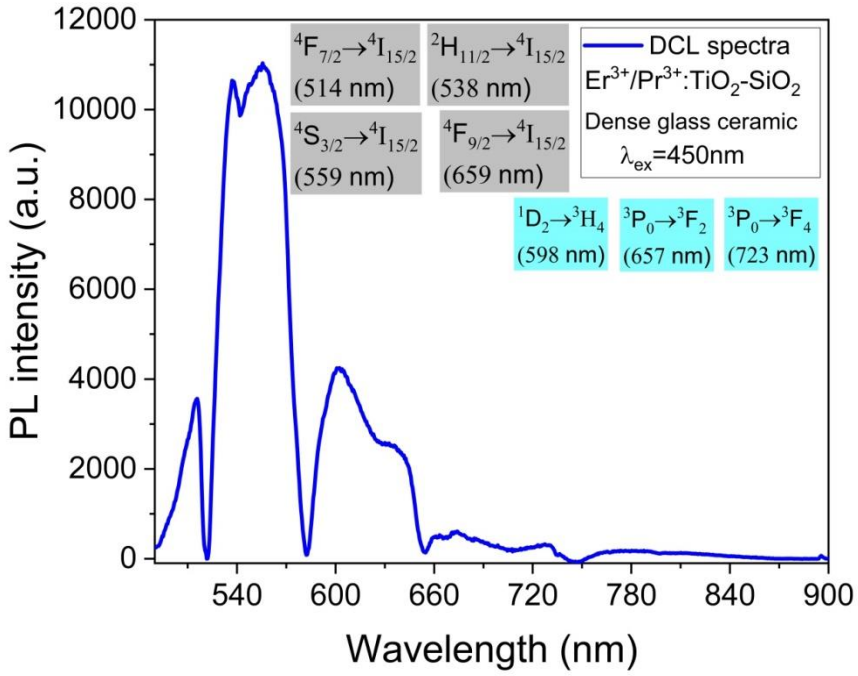


Fig. 5.5. DCL spectra of the $Er^{3+}/Pr^{3+}$:$TiO_2$-$SiO_2$ dense glass material under 450 nm excitation

### 5.2.3.3. Luminescence mechanism of $Pr^{3+}/Er^{3+}$ ion pair

The schematic energy level diagram of the $Pr^{3+}/Er^{3+}$ ion is drawn as in Fig 5.6. From absorption spectra, the as-synthesized $Er^{3+}/Pr^{3+}$:$TiO_2$-$SiO_2$ dense glass ceramic material can absorb photon of different wavelengths as in Fig 5.7. The excitation of 450 nm, helps in populating through the two absorption channel at 450 nm via GSA I ($Er^{3+}$: $^4I_{15/2} \rightarrow {}^4F_{5/2}$) and GSA II ($Pr^{3+}$: $^3H_4 \rightarrow {}^3P_2$). In DCL mechanism, excited energy is possibly transferred through several radiative and nonradiative channels and their mechanism are proposed under 450 nm excitation of Er/Pr ion pair. The energy transfer (ET) process among $Pr^{3+}/Er^{3+}$ ion pair in $TiO_2$-$SiO_2$ host were identified and

shown in Table 1. In GSA I process, a portion of excitation energy can be possibly transfer to $^3P_2$ state of $Pr^{3+}$ ion by transfer of energy (ET) whereas the remaining part of the energy depopulate non-radiatively to the $^4F_{7/2}$ level of $Er^{3+}$ ions. Similar explanation can be put forward for GSA II process.

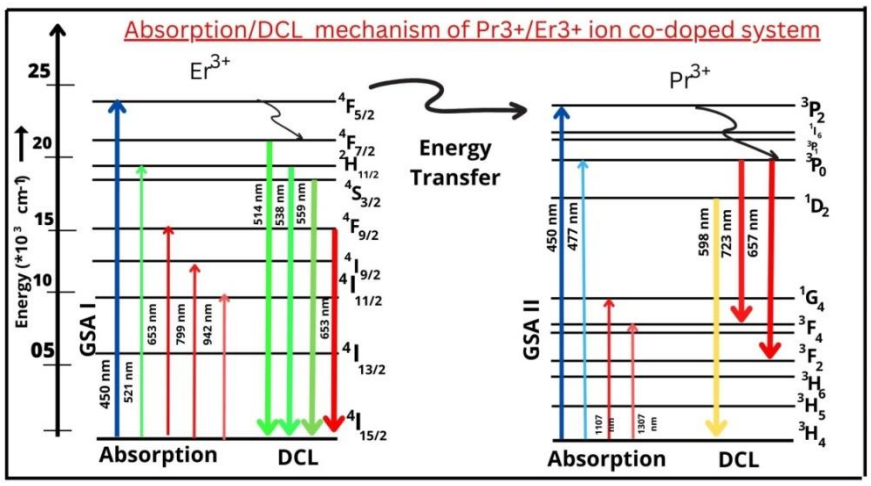


Figure 5.6: Schematic absorption and DCL mechanisms of the $Er^{3+}/Pr^{3+}$:$TiO_2$-$SiO_2$ dense glass material

The different transition peaks of DCL spectra of $Er^{3+}/Pr^{3+}$:$TiO_2$-$SiO_2$ dense glass material is listed along with respective FWHM, branching ratio, and different possible applications:

Table 5.1 : Different transition in PL spectra of the $Er^{3+}/Pr^{3+}$:$TiO_2$-$SiO_2$ dense glass material for excitation wavelength 450 nm

| $Ln^{3+}$ | Transitions | Wavelength (nm) | Wavenumber ($cm^{-1}$) | FWHM (nm) | Branching Ratio (β) (%) |
|---|---|---|---|---|---|
| $Pr^{3+}$ | $^1D_2 \rightarrow {}^3H_4$ | 598 nm | 16722 | 67 | 28 |

| | | | | | |
|---|---|---|---|---|---|
| | $^3P_0 \rightarrow {}^3F_2$ | 657 nm | 15220 | 24 | 07 |
| | $^3P_0 \rightarrow {}^3F_4$ | 723 nm | 13831 | 13 | 09 |
| $Er^{3+}$ | $^4F_{7/2} \rightarrow {}^4I_{15/2}$ | 514 nm | 19455 | 41 | 15 |
| | $^2H_{11/2} \rightarrow {}^4I_{15/2}$ | 538 nm | 18587 | 14 | 13 |
| | $^4S_{3/2} \rightarrow {}^4I_{15/2}$ | 559 nm | 17889 | 23 | 21 |
| | $^4F_{9/2} \rightarrow {}^4I_{15/2}$ | 659 nm | 15174 | 75 | 07 |

### 5.2.3.4. CIE diagram

The Commission International d' Eclairage (CIE) coordinates (0.422, 0.506) of corresponding DCL spectra of the $Er^{3+}/Pr^{3+}$:$TiO_2$-$SiO_2$ dense glass material have been obtained as in Fig 5.7.

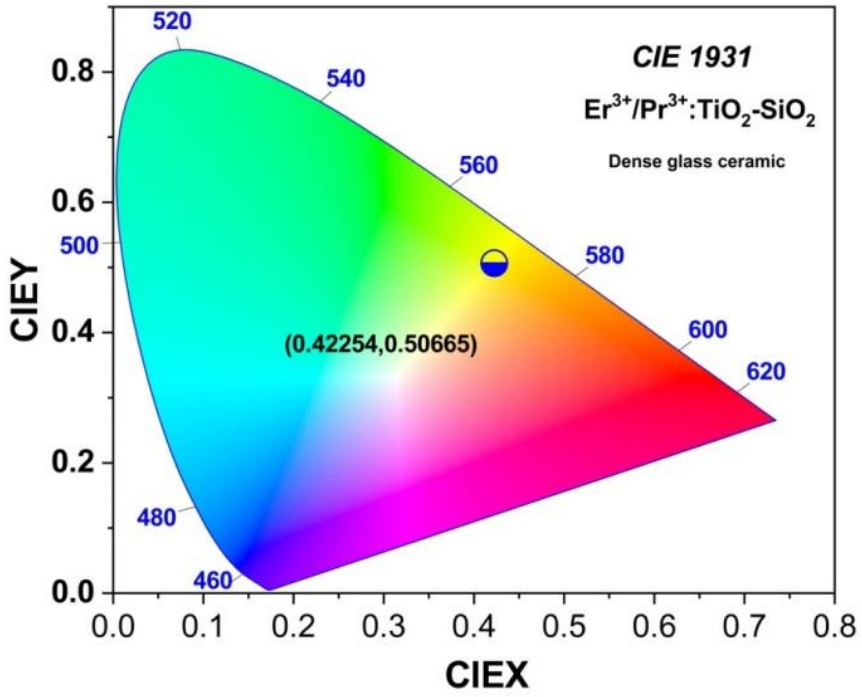


Fig. 5.7: CIE 1931 chromaticity diagram of DCL emission of the $Er^{3+}/Pr^{3+}$:$TiO_2$-$SiO_2$ dense glass material

## 5.3. Synthesis of $Nd^{3+}/Er^{3+}$ ions pair in Zinc-Silicate dense glass ceramic material

The co-doping of low concentration (0.7 mol% each) of $Er^{3+}$ and $Nd^{3+}$ ions in Zinc-Silicate ($Er^{3+}/Nd^{3+}$:ZnO-$SiO_2$) dense glass ceramic material was synthesized with the similar novel *ex-situ* sol-gel method as discussed in section 4.2 of Chapter 4 where we replace $Yb^{3+}$ ion with $Er^{3+}$. The structural, morphological and optical properties of the as-synthesized material were investigated as follows.

### 5.3.2. Structural Characterization

The structural characterization of the $Er^{3+}/Nd^{3+}$:ZnO-$SiO_2$ dense glass material annealed at 900ºC was accomplished using the X-ray diffraction (XRD) pattern and Fourier transformations infrared spectroscopy (FTIR) to highlight structural growth.

### 5.3.2.1. XRD analysis

The XRD analysis of the $Er^{3+}/Nd^{3+}$:ZnO-$SiO_2$ dense glass material annealed at 900 ºC were depicted distinct peaks at various 2θ angles 20.87° (012), 26.65° (220), 35.19° (042), 39.43° (104), 40.29° (502), 40.75° (241), 42.43° (502), 45.87° (600), 50.16° (161), 54.11° (054), 59.64° (006), 64.31° (306), 68.7° (345), and 75.5° (713), which were identified as belonging to the α-$Zn_2SiO_4$ crystalline phase as shown in Figure 5.8 (Chandraboss et al. 2013). Through comparison with JCPDS card No: 00-008-0492, the formation of a tetragonal willemite $Zn_2SiO_4$ structure with R-3(148) was confirmed. Subsequent annealing of as-synthesized material at 900 °C led to the conversion of the ZnO-$SiO_2$ host material into dense glass-ceramic. The average crystallite size of ZnO crystal in $SiO_2$ host was calculated from the most prominent peak corresponding to (220) using Scherrer equation of about 26 nm (Kakoti et al. 2019). Despite the absence of direct observation of optical center ($Nd^{3+}/Er^{3+}$) in the vicinity of ZnO lattice from XRD analysis, it promotes luminescence enhancement (Bang et al. 2005), (Hien et al. 2019).

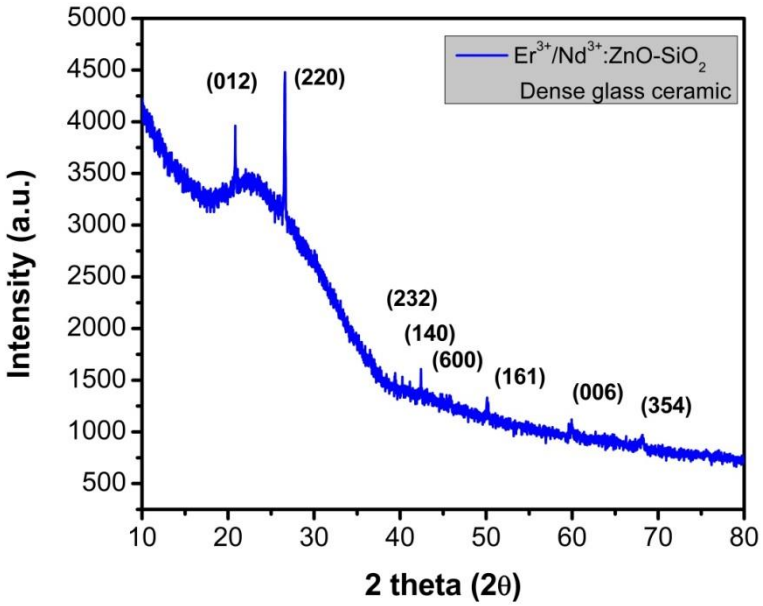


Figure 5.8: XRD pattern of the $Er^{3+}/Nd^{3+}$:ZnO-$SiO_2$ dense glass material annealed at

900 ºC

### 5.3.2.2. ATR-FTIR Spectra

ATR-FTIR spectroscopy was used to investigate chemical and structural transformation in the $Er^{3+}/Nd^{3+}$:ZnO-$SiO_2$ material following annealing at 900 ºC, spanning the spectral range of 400-4000 $cm^{-1}$ (Figure 5.9). Absorption bands near 3356 $cm^{-1}$ and 1658 $cm^{-1}$, attributed to stretching and bending vibrations of surface adsorbed water and OH groups respectively, were absent at 900 ºC, indicating their complete removal. The presence of Si–O–Si bonds, characterized by asymmetric stretching of bridging oxygen (BO), was observed at approximately 1054 $cm^{-1}$ (Lee et al. 2017). Challenges in distinguishing ZnO vibrations in the $Er^{3+}/Nd^{3+}$:ZnO-$SiO_2$ sample arose from the overlap between the intense band of bending vibration δ(Si-O-Si) at 440 $cm^{-1}$ and the D2 band at 603 $cm^{-1}$ of amorphous $SiO_2$ (Tran et al. 2017). The appearance of a shoulder at 950 $cm^{-1}$ indicated the interference of zinc silicate, signifying Zn-O-Si vibration and penetration of Zn into the Si glass matrix (Raevskaya et al. 2014), (Galedari and Rahmani 2017). The generation of non-bridging oxygen (NBO) species were evident, promoting absorption enhancement, altering the absorption edge, and reducing the band gap, as evident from the sharpening of peaks towards the lower wavenumber region (Lee et al. 2017). ATR-FTIR analysis confirmed the elimination of hydroxyl impurities and revealed the presence of oxygen-related defects in the host matrix, which significantly impact the luminescence properties of the $Er^{3+}/Nd^{3+}$:ZnO-$SiO_2$ sample.

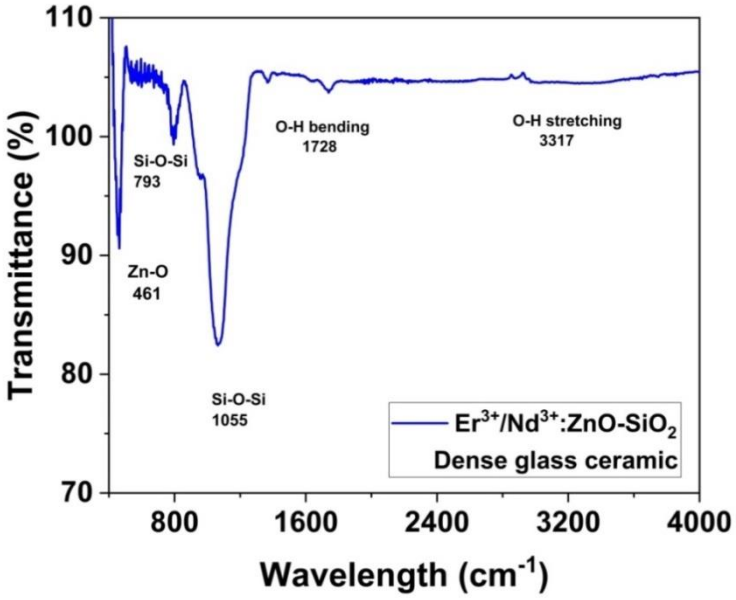


Figure 5. **9**: ATR-FTIR spectra of the $Er^{3+}/Nd^{3+}$:ZnO-$SiO_2$ dense glass material annealed at 900 ºC.

Structural characterization of the as-synthesized material has not confirmed the presence of $RE^{3+}$ ions, as their homogeneous distribution does not include any discernible structural modification on the host matrix (J. et al. 2020).

### 5.3.3. MORPHOLOGICAL CHARACTERIZATION

The morphological characterization of the $Er^{3+}/Nd^{3+}$:ZnO-$SiO_2$ dense glass material was performed using the FETEM analysis.

#### 5.3.3.1. FETEM analysis

The FETEM micrographs of the $Er^{3+}/Nd^{3+}$:ZnO-$SiO_2$ dense glass material sample were captured to examine its morphology. These micrograph revealed the presence of composite agglomeration and the existence of ZnO nano-crystallites in $SiO_2$ matrix, as depicted in Fig. 5.10 (a,b). The growth of the ZnO crystallites with interplanner spacing of 27 nm is confirmed from HRTEM image.

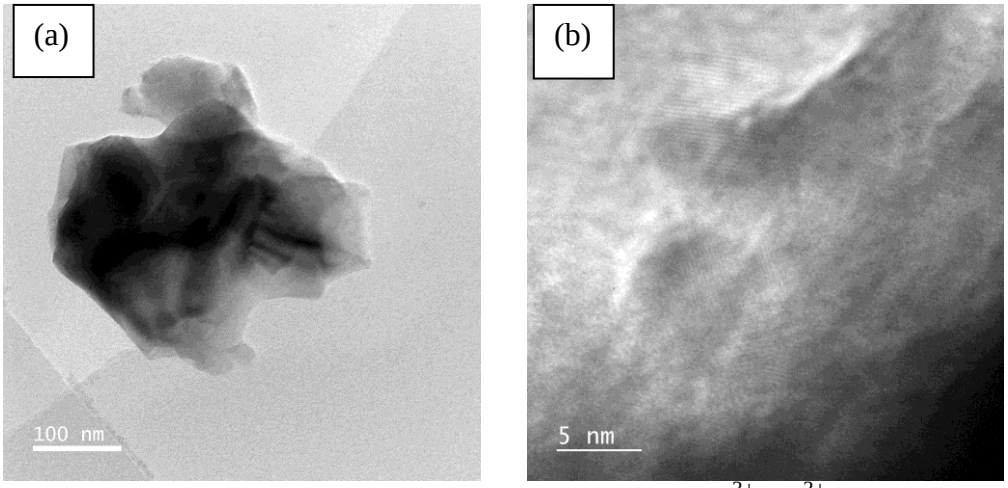


Figure 5.**10**: (a) FETEM image (b) HRTEM image of the $Er^{3+}/Nd^{3+}$:ZnO-$SiO_2$ dense glass material annealed at 900 °C

The SAED pattern of the $Er^{3+}/Nd^{3+}$:ZnO-$SiO_2$ dense glass material has further confirmed the growth of the ZnO crystallites as in Figure 5.11.

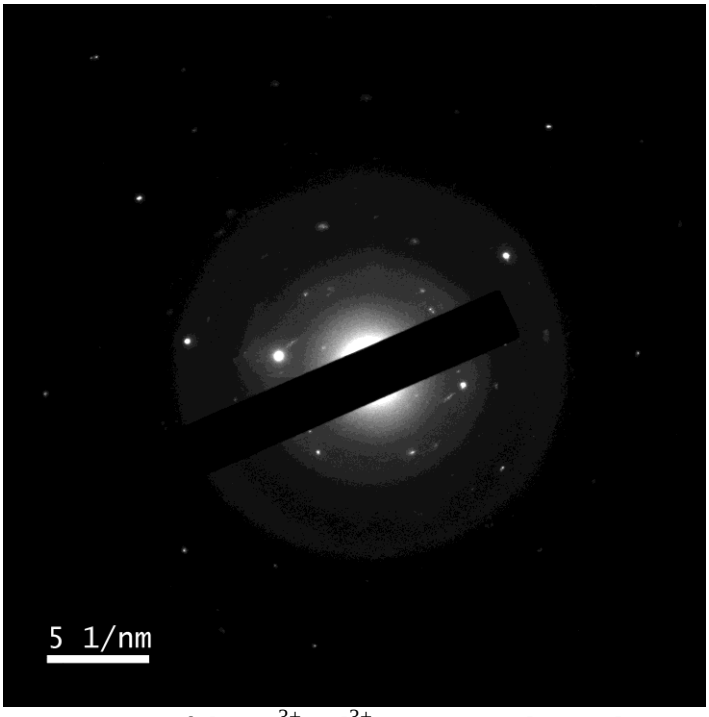


Figure 5.**11**: SAED pattern of the $Er^{3+}/Nd^{3+}$:ZnO-$SiO_2$ dense glass material annealed at 900 °C

### 5.3.4. Optical characterization

The optical characterization of the $Er^{3+}/Nd^{3+}$:ZnO-$SiO_2$ dense glass material has been studied using absorption and photoluminescence spectra where existing report were used to confirm the transition related to the $Er^{3+}$ and $Nd^{3+}$ ions.

#### 5.3.4.1. Absorption spectra

The absorption spectra of the $Er^{3+}/Nd^{3+}$:ZnO-$SiO_2$ dense glass material were recorded in UV-VIS & NIR absorption peak for excitation of 4f electron from ground state of $Er^{3+}$ ($^4I_{15/2}$), $Nd^{3+}$ ($^4I_{9/2}$) and $Yb^{3+}$ ($^2F_{7/2}$) ion as in Figure 5.12. The presence of $Er^{3+}$ ion in the $Er^{3+}/Nd^{3+}$:ZnO-$SiO_2$ material has been validated with peaks due to transition from ground state ($^4I_{15/2}$), around 488 nm ($^4I_{15/2}\rightarrow{}^4F_{7/2}$), 523 nm ($^4I_{15/2}\rightarrow{}^2H_{11/2}$), 542 nm ($^4I_{15/2}\rightarrow{}^4S_{3/2}$), 654 nm ($^4I_{15/2}\rightarrow{}^4F_{9/2}$), 799 nm ($^4I_{15/2}\rightarrow{}^4I_{9/2}$) transition. The simultaneous presence of absorption peaks of $Nd^{3+}$ ($^4I_{9/2}\rightarrow{}^4G_{7/2}$; $^4G_{5/2}$; $^4F_{5/2}+{}^2H_{9/2}$) ion has also observed as seen in the $Er^{3+}/Nd^{3+}$:ZnO-$SiO_2$ dense glass material in Fig 4.7. The intensity enhancement of absorption peaks of $Nd^{3+}$ ion was observed for co-doping of $Er^{3+}$ ion.

The absorption spectra of the $Er^{3+}/Nd^{3+}$:ZnO-$SiO_2$ dense glass material has two important intense peaks at 580 and 808 nm which can be used to pump the material for obtaining emission in visible range.

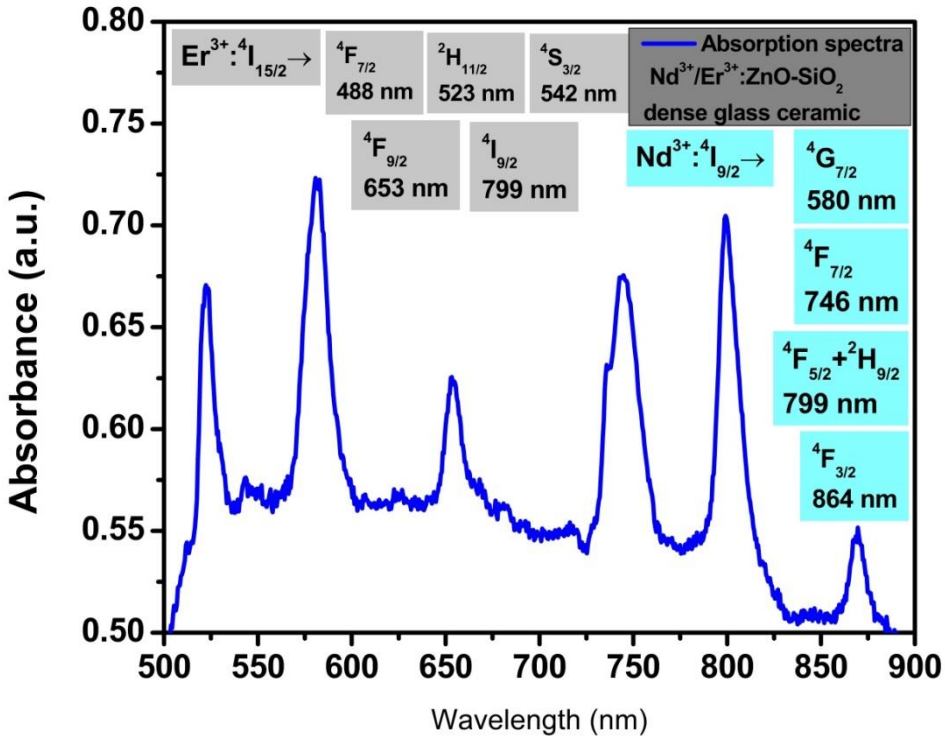


Fig. 5.12 Absorption spectra of the $Er^{3+}/Nd^{3+}$:ZnO-$SiO_2$ dense glass material

### 5.3.4.2. Downconversion luminescence spectra

DCL spectra of the $Er^{3+}/Nd^{3+}$:ZnO-$SiO_2$ dense glass material was recorded for excitation wavelength 450 nm as in Fig 5.13. Both, $Er^{3+}$ ($^4I_{15/2} \rightarrow {}^4I_{9/2}$) and $Nd^{3+}$ ($^3H_4 \rightarrow {}^4F_{9/2}$) ions have absorption peak at this specific excitation wavelength. Here emission peaks from $Er^{3+}$ ion is validated with peaks around 489 nm ($^4F_{17/2} \rightarrow {}^4I_{15/2}$), 518 nm ($^2H_{11/2} \rightarrow {}^4I_{15/2}$) (Deshmukh et al. 2018), 560 nm ($^4S_{3/2} \rightarrow {}^4I_{15/2}$) and 673 nm ($^4F_{9/2} \rightarrow {}^4I_{15/2}$) (Naresh and Buddhudu 2015). Similarly the transition due to the $Nd^{3+}$ ion has also been validated with peaks around 539 nm ($^4G_{7/2} \rightarrow {}^4I_{9/2}$), 602 nm ($^4G_{7/2} \rightarrow {}^4I_{11/2}$), 665 nm ($^4G_{7/2} \rightarrow {}^4I_{9/2}$), and 760 nm ($^4G_{7/2} \rightarrow {}^4I_{15/2}$) etc (Muniz et al. 2023).

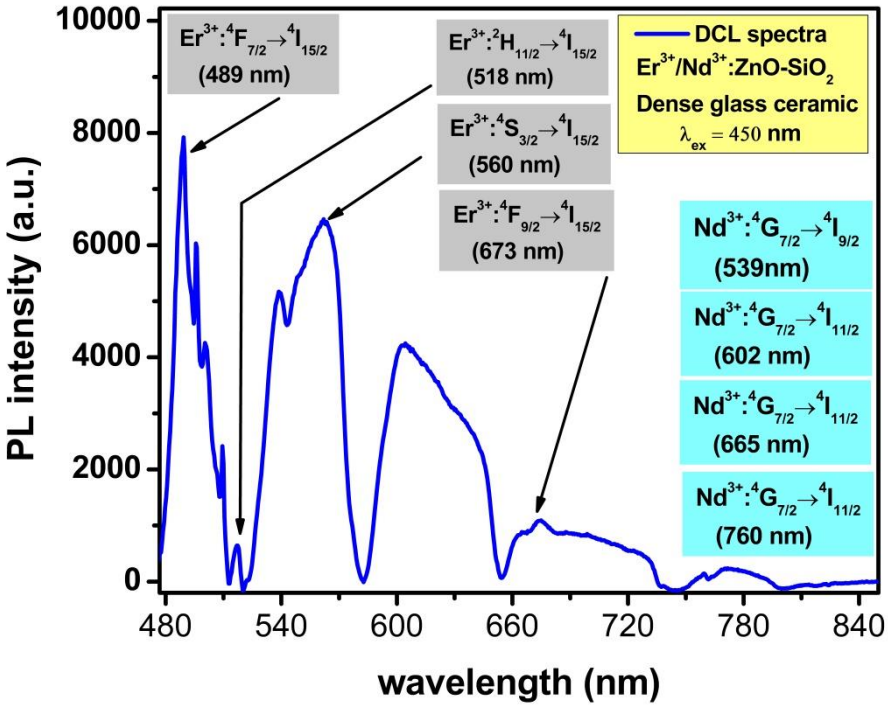


Fig. 5.13: DCL spectra of the $Er^{3+}/Nd^{3+}$:ZnO-$SiO_2$ dense glass material under 450 nm excitation

**DCL** spectra of the $Er^{3+}/Nd^{3+}$ ion paired in ZnO-$SiO_2$ dense glass material was recorded with excitation wavelength 808 nm sh in Figure 5.14. Both, $Er^{3+}$ ($^4I_{15/2}$ → $^4I_{9/2}$) and $Nd^{3+}$ ($^3H_4$→$^4F_{9/2}$) ions have absorption peak at this specific excitation wavelength. The $^4F_{3/2}$ →$^4I_{11/2}$ transition of $Nd^{3+}$ ion can been validated with peaks around 1050-1150 nm. . The emission of photon of lower energy was observed, for example 921 nm ($Nd^{3+}$:$^4F_{3/2}$ →$^4I_{9/2}$), 1057 nm ($Nd^{3+}$:$^4F_{3/2}$ →$^4I_{11/2}$), 1079 nm ($Nd^{3+}$:$^4F_{3/2}$ →$^4I_{13/2}$), 1006 nm ($Er^{3+}$:$^4I_{11/2}$ →$^4I_{15/2}$), 1104 nm ($Er^{3+}$:$^4S_{3/2}$ →$^4I_{11/2}$), 1338 nm ($Er^{3+}$:$^4I_{13/2}$ →$^4I_{15/2}$).

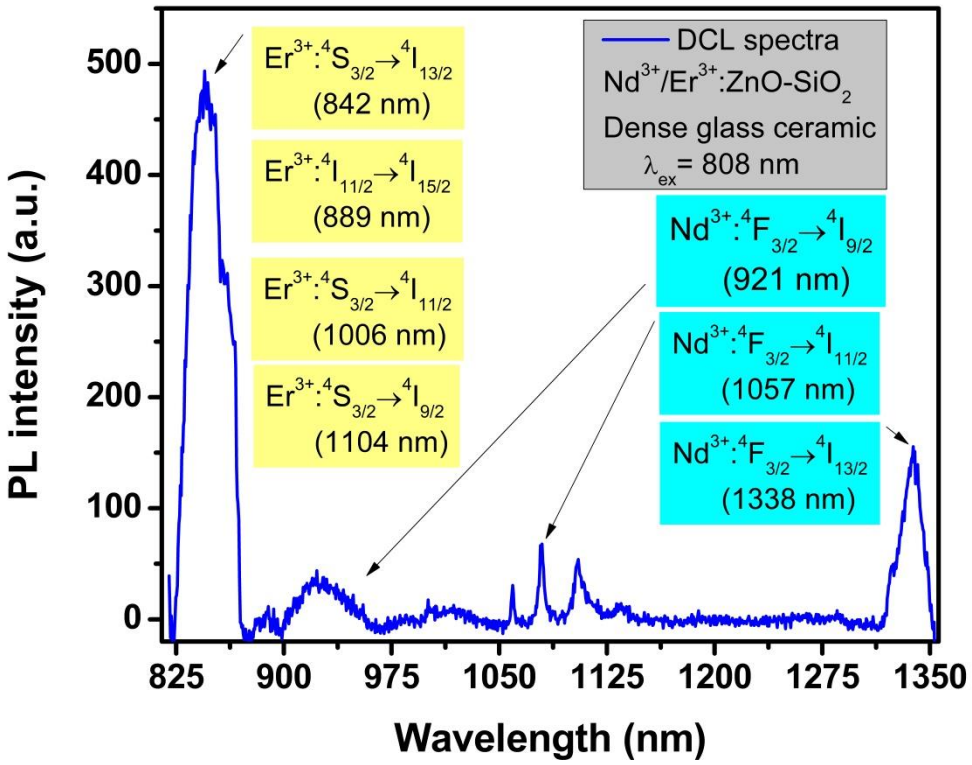


Fig. 5.14: DCL spectra of the $Er^{3+}/Nd^{3+}$:ZnO-$SiO_2$ dense glass material under 808 nm excitation

### 5.3.4.3. Luminescence mechanism of $Nd^{3+}/Er^{3+}$ ion pair

The schematic energy level diagram of the $Nd^{3+}/Er^{3+}$ ion is drawn as in Fig 5.15. From absorption spectra, the as-synthesized $Er^{3+}/Nd^{3+}$:ZnO-$SiO_2$ dense glass ceramic material can absorb photon in the spectral range of 480 to 870 nm. The excitation of as-synthesized sample using laser source of 450 nm, through several radiative and nonradiative channels and their mechanism are proposed for the Er/Nd ion pair. The energy transfer process between Nd/Er ion pair in ZnO-$SiO_2$ host were identified and shown in Table 2. This excitation source helps in populating through the two absorption channels at 450 nm via GSA I ($Er^{3+}$: $^4I_{15/2}\rightarrow{}^4F_{5/2}$) and GSA II ($Nd^{3+}$:$^4I_{9/2}\rightarrow{}^2K_{15/2}$). The partial excitation energy through GSA I process can

possibly transfer non-radiatively to $^4G_{5/2}$ state of $Nd^{3+}$ ion by energy transfer (ET) whereas the remaining part of the energy depopulate non-radiatively to the $^4F_{7/2}$ level of $Er^{3+}$ ions. Similar explanation can be put forward for GSA II process.

DCL mechanism of the $Er^{3+}/Nd^{3+}$:ZnO-$SiO_2$ dense glass material was also observed for 808 nm excitation in the near infrared region. Here absorption of excitation photons (808nm) promotes the electron in the ground state of $Er^{3+}$: ($^4I_{15/2} \rightarrow {}^4I_{9/2}$) and $Nd^{3+}$:($^4I_{9/2} \rightarrow {}^4F_{5/2}$) ion to excited state correspondingly through GSA process. These electrons in excited state were further relaxed to ground state of respective ion through a non-radiative or radiative process.

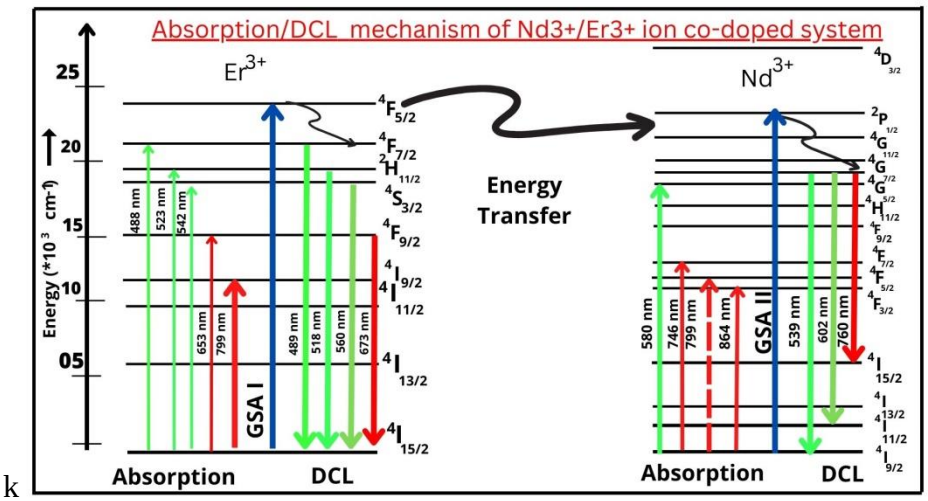


k

Fig. 5.15. Schematic diagram of the absorption and DCL mechanism in the $Er^{3+}/Nd^{3+}$:ZnO-$SiO_2$ dense glass material

The different transition peaks of DCL spectra of $Er^{3+}/Nd^{3+}$:ZnO-$SiO_2$ dense glass material are listed along with respective FWHM and branching ratio:

Table 5.2 : Selective transitions of PL spectra of the $Er^{3+}/Nd^{3+}$:ZnO-$SiO_2$ dense glass material

| $Ln^{3+}$ | Transitions | Wavelength | Wavenumber | Excitation wavelength | FWHM | Branching Ratio (β) |
|---|---|---|---|---|---|---|

| | | (nm) | ($cm^{-1}$) | (nm) | (nm) | (%) |
|---|---|---|---|---|---|---|
| $Nd^{3+}$ | $^4G_{7/2}\rightarrow{}^4I_{9/2}$ | 539 | 18552 | 450 | 28 | 21.31 |
| | $^4G_{7/2}\rightarrow{}^4I_{11/2}$ | 602 | 16611 | | 42 | 24.03 |
| | $^4G_{7/2}\rightarrow{}^4I_{13/2}$ | 665 | 15037 | | 25 | 4.54 |
| | $^4G_{7/2}\rightarrow{}^4I_{15/2}$ | 760 | 13157 | | 32 | 5.91 |
| | $^4F_{3/2}\rightarrow{}^4I_{9/2}$ | 921 | 10875 | 808 | 26 | 46.64 |
| | $^4F_{3/2}\rightarrow{}^4I_{13/2}$ | 1338 | 7473 | | 14 | 2.08 |
| $Er^{3+}$ | $^4F_{7/2}\rightarrow{}^4I_{15/2}$ | 489 | 20449 | 450 | 10.5 | 11.31 |
| | $^2H_{11/2}\rightarrow{}^4I_{15/2}$ | 518 | 19305 | | 10 | 0.19 |
| | $^4S_{3/2}\rightarrow{}^4I_{15/2}$ | 560 | 17857 | | 15 | 11.22 |
| | $^4F_{9/2}\rightarrow{}^4I_{15/2}$ | 673 | 14858 | | 47 | 4.51 |
| | $^4S_{3/2}\rightarrow{}^4I_{13/2}$ | 842 | 11876 | 808 | 28 | 30.9 |
| | $^4S_{3/2}\rightarrow{}^4I_{9/2}$ | 1006 | 9940 | | 0.1 | 3.0 |
| | $^4S_{3/2}\rightarrow{}^4I_{9/2}$ | 1079 | 9267 | | 0.16 | 10.49 |

Here branching ratio of different transition for the $Er^{3+}/Nd^{3+}$:ZnO-$SiO_2$ dense glass material was estimated separately for 450 nm and 808 nm excitation.

### 5.3.4.4. CIE diagram

The Commission International d' Eclairage (CIE) coordinates (0.33, 0.38) of corresponding DCL spectra of the $Er^{3+}/Nd^{3+}$:ZnO-$SiO_2$ dense glass material have been obtained as in Figure 6.16.

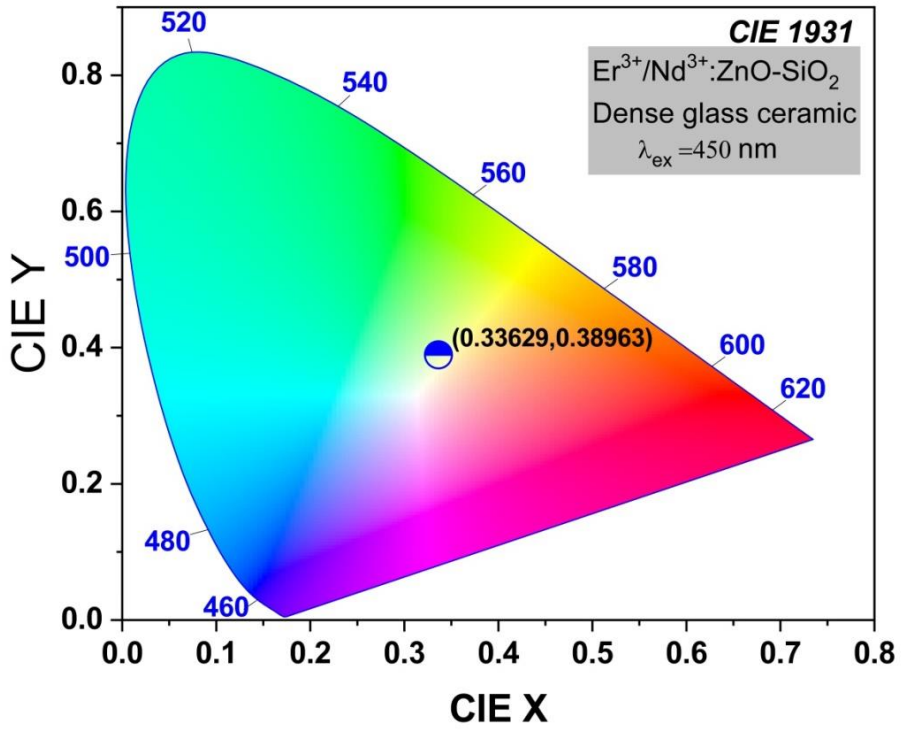


Fig. 5.16: CIE 1931 chromaticity diagram of the $Er^{3+}/Nd^{3+}$:ZnO-$SiO_2$ dense glass material

## 5.4. Conclusion

Here, two novel (distinct) luminescent materials (SAMPLE III & IV) are developed by incorporating different $RE^{3+}$ ion pairs ($Er^{3+}/Pr^{3+}$ and $Er^{3+}/Nd^{3+}$) into *ex-situ* sol-gel derived Titania-Silicate or Zinc-Silicate dense glass ceramics host. Here, *ex-situ* sol-gel techniques of host synthesis have been unmodified except different $RE^{3+}$ ion concentration was used. The focus of this work was to show that the co-doping

$Er^{3+}/Pr^{3+}$ and $Er^{3+}/Nd^{3+}$ ions in respective host can rectify optical properties without altering structural and morphological properties of host. These ion pairs are chosen as the co-doping has potential to tune their ionic interaction, which allow high concentration of $RE^{3+}$ doping for their potential in photonics. Structural, morphological, and optical characterizations are conducted on both materials. Both the pair was observed absorption and emission properties spanning UV-VIS and NIR regions. For the $Er^{3+}/Pr^{3+}$:$TiO_2$-$SiO_2$ material, XRD analysis confirms crystalline growth of $TiO_2$, while ATR-FTIR spectra show Si-O-Ti bonds without observable $RE^{3+}$ ions. TEM analysis reveals $TiO_2$ nano-crystallites within an amorphous $SiO_2$ matrix. In UV-VIS-NIR absorption and DCL spectra, different peaks of $Er^{3+}$ and $Pr^{3+}$ were observed. Similarly, for $Er^{3+}/Nd^{3+}$:ZnO-$SiO_2$, XRD confirms the formation of $\alpha$-$Zn_2SiO_4$, while ATR-FTIR shows Si-O-Si bonds and Zn-O-Si vibrations. TEM analysis confirms ZnO crystallites in the $SiO_2$ matrix. Similarly, in UV-Vis-NIR absorption and DCL spectra, different peaks of $Er^{3+}$ and $Nd^{3+}$ were observed.

Luminescence spectra results from both materials highlight their potential for diverse photonic applications such as optical amplifiers, lasers, and photonic devices. Further optimization of synthesis parameters and characterization of optical properties are essential to enhance luminescent efficiency and overall performance.

REFERENCE

Agustín-Sáenz, Cecilia, José Ángel Sánchez-García, Maider Machado, Marta Brizuela, Oihana Zubillaga, and Agnieszka Tercjak. 2018. “Broadband Antireflective Coating Stack Based on Mesoporous Silica by Acid-Catalyzed Sol-Gel Method for Concentrated Photovoltaic Application.” *Solar Energy Materials and Solar Cells* 186(February):154–64. doi: 10.1016/j.solmat.2018.06.040.

Ahrens, Bernd. 2009. “Down-and Up-Conversion in Fluorozirconate-Based Glasses and Glass Ceramics for Photovoltaic Application.” PADERBORN.

Amin, Peshawa O., Asmaa J. Kadhim, Majida A. Ameen, and Rebar T. Abdulwahid. 2018. “Structural and Optical Properties of Thermally Annealed TiO2–SiO2 Binary Thin Films Synthesized by Sol–Gel Method.” *Journal of Materials*

*Science: Materials in Electronics* 29(18):16010–20. doi: 10.1007/s10854-018-9688-6.

Anna M. Kaczmarek, Mariusz K. Kaczmarek, and Rik Van Deuna. 2018. "Er3+-to-Yb3+ and Pr3+-to-Yb3+ Energy Transfer for Highly Efficient near-Infrared Cryogenic Optical Temperature Sensing." *Nanoscale* 11(3):1–3. doi: 10.1039/C8NR08348G.

Auzel, F. 1990. "Upconversion Processes in Coupled Ion Systems." *Journal of Luminescence* 45(1–6):341–45. doi: 10.1016/0022-2313(90)90189-I.

Azzouz, I. M., and Lisa C. Klein. 2012. "Red , Violet and Upconversion Luminescence of Eu / Sm Codoped Sol Gel SiO 2 – TiO 2." *Optical Materials* 35:292–96. doi: 10.1016/j.optmat.2012.09.006.

Bang, Jungsik, Heesun Yang, and Paul H. Holloway. 2005. "Enhanced Luminescence of SiO 2 : Eu 3 + by Energy Transfer from ZnO Nanoparticles." *The Journal of Chemical Physics* 123(May 2013):1–4. doi: 10.1063/1.2007647.

Battisha, I. K. 2007. "Visible Up-Conversion Photoluminescence from IR Diode-Pumped SiO2-TiO2 Nano-Composite Films Heavily Doped with Er3+-Yb3+ and Nd3+-Yb3+." *Journal of Non-Crystalline Solids* 353(18–21):1748–54. doi: 10.1016/j.jnoncrysol.2007.01.043.

Berkani, Oualid, Khelil Latrous, Hicham El, Bruno Capoen, and Mohamed Bouazaoui. 2012. "Effects of Heat Treatment and TiO 2 Content on the Optical Properties of Eu 3 þ Doped TiO 2 – SiO 2 Thin Films." *Journal of Luminescence* 132:2979–83. doi: 10.1016/j.jlumin.2012.06.019.

Binnemans, Koen. 2009. "Lanthanide-Based Luminescent Hybrid Materials." *Chemical Review* 109:4283–4374.

Binnemans, Koen. 2015. "Interpretation of Europium ( III ) Spectra." *Coordination Chemistry Reviews* 295:1–45. doi: 10.1016/j.ccr.2015.02.015.

Bokatial, L., and S. Rai. 2010. "Optical Properties and Up-Conversion of Pr 3 + Doped CdS Nanoparticles in Sol – Gel Glasses." *Journal of Luminescence* 130(10):1857–62. doi: 10.1016/j.jlumin.2010.04.022.

Bokatial, Litul, and S. Rai. 2012. "Optical Properties of Sm 3 + Ions in Sol-Gel Derived Alumino-Silicate Glasses." *J Opt* 41(June):94–103. doi: 10.1007/s12596-012-0069-x.

Bokov, Dmitry, Abduladheem Turki Jalil, Supat Chupradit, Wanich Suksatan, Mohammad Javed Ansari, Iman H. Shewael, Gabdrakhman H. Valiev, and Ehsan Kianfar. 2021. “Nanomaterial by Sol-Gel Method: Synthesis and Application.” *Advances in Materials Science and Engineering* 2021. doi: 10.1155/2021/5102014.

Brik, Mikhail G., Ž. M. Anti, Katarina Vukovi, and Miroslav D. Drami. 2015. “Judd - Ofelt Analysis of Eu 3 + Emission in TiO 2 Anatase Nanoparticles.” *Materials Transactions* 56(9):1416–18.

Brus, Louis. 1986. “Electronic Wave Functions in Semiconductor Clusters: Experiment and Theory.” *Journal of Physical Chemistry* 90(12):2555–60. doi: 10.1021/j100403a003.

Buarque, Juliana M. M., Danilo Manzani, Sérgio Luis Scarpari, Marcelo Nalin, Sidney J. L. Ribeiro, Jennifer Esbenshade, Marco A. Schiavon, and Jefferson L. Ferrari. 2018. “SiO2-TiO2 Doped with Er3+/Yb3+/Eu3+ Photoluminescent Material: A Spectroscopy and Structural Study about Potential Application for Improvement of the Efficiency on Solar Cells.” *Materials Research Bulletin* 107:295–307. doi: 10.1016/j.materresbull.2018.07.007.

C. Jefffrey and George W. Scherer. 1990. *Sol-Gel Science, The Physics and Chemistry of Sol-Gel Processing*. London: Academic Press, Inc.

Carnall, W. T.; Crosswhite, H.; Crosswhite, H. M. 1977. *Energy Level Structure and Transition Probabilitiesof the Trivalent Lanthanides in LaF3*. Argonne (USA): Rep. Argonne National Laboratory.

Carnall, W. T., P. R. Fields, and K. Rajnak. 1968. “Electronic Energy Levels in the Trivalent Lanthanide Aquo Ions. I. Pr3+, Nd3+, Pm3+, Sm3+, Dy3+, Ho3+, Er3+, and Tm3+.” *The Journal of Chemical Physics* 49:4424–42. doi: 10.1063/1.1669893.

Carnall, W. T., P. R. Fields, and B. G. Wybourne. 1965. “Spectral Intensities of the Trivalent Lanthanides and Actinides in Solution. I. Pr3+, Nd3+, Er3+, Tm3+, and Yb3+.” *The Journal of Chemical Physics* 42:3797–3806. doi: 10.1063/1.1695840.

Carnall, W. T., G. L. Goodman, K. Rajnak, and R. S. Rana. 1989. “A Systematic Analysis of the Spectra of the Lanthanides Doped into Single Crystal LaF3.”

*The Journal of Chemical Physics* 90(7):3443–57. doi: 10.1063/1.455853.

Castan˜eda-Contreras, J., M. A. Meneses-Nava, O. Barbosa-Garcı´a, R. A. Rodrı´guez-Rojas, and M. V. Fe´lix. 2006. "Visible Erbium Luminescence in SiO2 – TiO2 – Er3+ Sol – Gel Powders." *Optical Materials* 29:38–42. doi: 10.1016/j.optmat.2006.03.005.

Chandraboss, V. L., B. Karthikeyan, J. Kamalakkannan, S. Prabha, and S. Senthilvelan. 2013. "Sol-Gel Synthesis of TiO2/SiO2 and ZnO/SiO2 Composite Films and Evaluation of Their Photocatalytic Activity towards Methyl Green." *Journal of Nanoparticle* 2013(507161):1–7.

Chang, Meiqi, Yanhua Song, Lei Cui Jie Chen, Zhan Shi, Ye Sheng, and Haifeng Zou. 2018. "Photocatalytic and Photoluminescence Properties of Core- Shell SiO2@TiO2:Eu3+,Sm3+ and Its Etching Products." *ACS Sustainable Chemistry & Engineering* 6(1):223–36. doi: 10.1021/acssuschemeng.7b02285.

Chang, Meiqi, Yanhua Song, Ye Sheng, Jie Chen, and Haifeng Zou. 2017. "Understanding the Remarkable Luminescence Enhancement: Via SiO2 Coating on TiO2:Eu3+ Nanofibers." *Physical Chemistry Chemical Physics* 19(26):17063–74. doi: 10.1039/c7cp01113j.

Chang, Meiqi, Haifeng Zou, Yanhua Song, Jie Chen, Lei Cui, Ye Sheng, and Keyan Zheng. 2019. "Photoluminescence and Photodegradation Properties of SiO2@TiO2:Sm3+ with Different Coating Effects." *Journal of Physics and Chemistry of Solids* 124:100–110. doi: 10.1016/j.jpcs.2018.09.010.

Chelouche, A., D. Djouadi, and A. Aksas. 2014. "Structural Characterization of SiO 2 / Zn 2 SiO 4 : Ce Nanocomposite Obtained by Sol Gel Method." *Journal of the Association of Arab Universities for Basic and Applied Sciences* 15:10–14. doi: 10.1016/j.jaubas.2013.05.002.

Chen, Hsueh Shih, Sheng Hsin Huang, and Tsong Pyng Perng. 2012. "Preparation and Characterization of Molecularly Homogeneous Silica-Titania Film by Sol-Gel Process with Different Synthetic Strategies." *ACS Applied Materials and Interfaces* 4(10):5188–95. doi: 10.1021/am301113a.

Chen, X. P., X. Y. Huang, and Q. Y. Zhang. 2009. "Concentration-Dependent near-Infrared Quantum Cutting in NaYF4: Pr3+, Yb3+phosphor." *Journal of Applied Physics* 106(6):3–7. doi: 10.1063/1.3224906.

Çopuroğlu, Mehmet, Lee Huat Kelly Koh, Gabriel M. Crean, and Shane O'Brien. 2016. "Comparative Characterisation of Zinc Oxide Thin Films Prepared from Zinc Acetate with or without Water of Hydration via the Sol – Gel Method." *Journal of Sol-Gel Science and Technology* 52:432–38. doi: 10.1007/s10971-009-2016-0.

Deshmukh, Pratik, S. Satapathy, Anju Ahlawat, MK Tiwari, and A. K. Karnal. 2018. "Fabrication and Characterization of Er , Nd Codoped Transparent Ceramic : A Dual Mode Photo-Luminescence Emitter." *Journal of Alloys and Compounds* 754:32–38.

Dibaba, Solomon Tiruneh, Xiaoqian Ge, Wei Ren, and Lining Sun. 2019. "Recent Progress of Energy Transfer and Luminescence Intensity Boosting Mechanism in Nd3+-Sensitized Upconversion Nanoparticles." *Journal of Rare Earths* 37(8):791–805. doi: 10.1016/j.jre.2019.02.001.

Dieudonné, B., B. Boulard, G. Alombert-Goget, A. Chiasera, Y. Gao, S. Kodjikian, and M. Ferrari. 2013. "Up- and down-Conversion in Yb3+-Pr3+ Co-Doped Fluoride Glasses and Glass Ceramics." *Journal of Non-Crystalline Solids* 377:105–9. doi: 10.1016/j.jnoncrysol.2012.12.025.

Dihingia, P. J., and S. Rai. 2012. "Synthesis of TiO 2 Nanoparticles and Spectroscopic Upconversion Luminescence of Nd 3+-Doped TiO 2-SiO 2 Composite Glass." *Journal of Luminescence* 132(5):1243–51. doi: 10.1016/j.jlumin.2011.12.008.

Dwivedi, Y., Anita Rai, and S. B. Rai. 2008. "Intense White Upconversion Emission in Pr / Er / Yb Codoped Tellurite Glass." *Journal of Applied Physics* 104(043509):1–4. doi: 10.1063/1.2969046.

El-Bashir, S. M. 2017. "Physical Properties Nd3+ Doped (SiO2-TiO2) Monolithic Glass for Photoresistor Applications." *Materials Research Express* 4(11):0–6.

Van Der Ende, Bryan M., Linda Aarts, and Andries Meijerink. 2009. "Lanthanide Ions as Spectral Converters for Solar Cells." *Physical Chemistry Chemical Physics* 11(47):11081–95. doi: 10.1039/b913877c.

Eriksen, Emil H., Soren P. Madsen, Brian Julsgaard, Clarissa L. M. Hofmann, Jan Christoph Goldschmidt, and Peter Balling. 2019. "Enhanced Upconversion via Plasmonic Near-Field Effects: Role of the Particle Shape." *Journal of Optics*

*(United Kingdom)* 21(3). doi: 10.1088/2040-8986/ab0272.

Escudero, Alberto, Ana I. Becerro, Carolina Carrillo-Carrión, Nuria O. Núñez, Mikhail V. Zyuzin, Mariano Laguna, Daniel González-Mancebo, Manuel Ocanã, and Wolfgang J. Parak. 2017. "Rare Earth Based Nanostructured Materials: Synthesis, Functionalization, Properties and Bioimaging and Biosensing Applications." *Nanophotonics* 6(5):881–921. doi: 10.1515/nanoph-2017-0007.

Esposito, Serena. 2019. "'Traditional' Sol-Gel Chemistry as a Powerful Tool for the Preparation of Supported Metal and Metal Oxide Catalysts." *Materials* 12(4):1–25. doi: 10.3390/ma12040668.

Faria, W. J., T. S. Gonçalves, and Andrea S. S. De Camargo. 2021. "Near Infrared Optical Thermometry in Fluorophosphate Glasses Doped with Nd3+ and Nd3+/Yb3+." *Journal of Alloys and Compounds* 883:160849. doi: 10.1016/j.jallcom.2021.160849.

Fischer, S., J. C. Goldschmidt, P. Löper, G. H. Bauer, R. Brüggemann, K. Krämer, D. Biner, M. Hermle, and S. W. Glunz. 2010. "Enhancement of Silicon Solar Cell Efficiency by Upconversion: Optical and Electrical Characterization." *Journal of Applied Physics* 108(4):1–11. doi: 10.1063/1.3478742.

Galedari, Naghmeh Abuali, and Mohammad Rahmani. 2017. "Preparation , Characterization , and Application of ZnO @ SiO 2 Core – Shell Structured Catalyst for Photocatalytic Degradation of Phenol." *Environmental Science and Pollution Research* 24(14):12655–63. doi: 10.1007/s11356-016-7888-2.

Ghaemi, Bahram, Gaoling Zhao, Shengchen Huang, Jianxun Wang, and Gaorong Han. 2012. "Structural and Luminescence Properties of Er-Doped Zinc – Alumino – Silicate Glass Ceramic." *J. Am. Ceram. Soc.* 4:1–4. doi: 10.1111/j.1551-2916.2012.05200.x.

Gonçalves, M. Clara, Luis M. Fortes, Rui M. Almeida, Alessandro Chiasera, Andrea Chiappini, Maurizio Ferrari, and Shivakiran Bhaktha. 2010. "Photoluminescence in Er3+/Yb3+-Doped Silica-Titania Inverse Opal Structures." *Journal of Sol-Gel Science and Technology* 55(1):52–58. doi: 10.1007/s10971-010-2212-y.

Guille, A., A. Pereira, C. Martinet, and B. Moine. 2012. "Quantum Cutting in

CaYAlO4: Pr3+, Yb3+." *Optics Letters* 37(12):2280. doi: 10.1364/ol.37.002280.

Halin, D. S. C., M. M. A. B. Abdullah, N. Mahmed, S. N. A. Abdul Malek, P. Vizureanu, and A. W. Azhari. 2017. "Synthesis and Characterization of TiO2/SiO2 Thin Film via Sol-Gel Method." *IOP Conference Series: Materials Science and Engineering* 209(1). doi: 10.1088/1757-899X/209/1/012002.

Haque, Md Azimul, and S. Mahalakshmi. 2013. "Effect of Triethanolamine on Zinc Oxide Nanoparticles." *Materials Focus* 2(6):469–74. doi: 10.1166/mat.2013.1117.

Hehlen, Markus P., Mikhail G. Brik, and Karl W. Kramer. 2013. "50th Anniversary of the Judd – Ofelt Theory : An Experimentalist ' s View of the Formalism and Its Application." *Journal of Luminescence* 136:221–39. doi: 10.1016/j.jlumin.2012.10.035.

Helmiyati, Helmiyati, and R. P. Suci. 2019. "Nanocomposite of Cellulose-ZnO / SiO2 as Catalyst Biodiesel Methyl Ester from Virgin Coconut Oil." *AIP Conference Proceedings* (April 2020). doi: 10.1063/1.5132490.

Hien, Le Thi Thu, Nguyen Van Dub, Ngo Ngoc Hab, Nguyen Duc Hoab, Tran Ngoc Khiemb, and Nguyen Duc Chiena. 2019. "Optical Materials Photoluminescence Enhancement OF Er 3 + -Doped ZnO / SiO 2 Nanocomposites Fabricated through Two-Step Synthesis." *Optical Materials* 92(April):262–66. doi: 10.1016/j.optmat.2019.04.043.

Hua, Chenxiao, Xin Zhao, Yue Bun, and Hai Lin. 2017. "Pr3+ Doped Tellurite Glasses Incorporated with Silver Nanoparticles for Laser Illumination." *RSC Adv.* 7:55691–701. doi: 10.1039/c7ra11594f.

Huang, X. Y., and Q. Y. Zhang. 2009. "Efficient Near-Infrared down Conversion in Zn2 SiO4: Tb3+, Yb3+ Thin-Films." *Journal of Applied Physics* 105(5):1–5. doi: 10.1063/1.3088890.

Huang, Xiaoyong, Sanyang Han, Wei Huang, and Xiaogang Liu. 2013. "Enhancing Solar Cell Efficiency: The Search for Luminescent Materials as Spectral Converters." *Chemical Society Reviews* 42(1):173–201. doi: 10.1039/c2cs35288e.

Ismail, Adel Ali, Mostafa Abboudi, Paul Holloway, and Hassan El-Shall. 2007.

"Photoluminescence from Terbium Doped Silica-Titania Prepared by a Sol-Gel Method." *Materials Research Bulletin* 42(1):137–42. doi: 10.1016/j.materresbull.2006.05.002.

J., Manju Gopinath R., Subash Gopi, Sanu Mathew Simon, A. C. Saritha, P. R. Biju, and N. V Unnikrishnan. 2020. "Spectroscopic Analysis of Eu3+ Doped Silica–Titania–Polydimethylsiloxane Hybrid ORMOSILs." *RSC Adv.* 10:20057–66. doi: 10.1039/d0ra03073b.

Jenouvrier, P., E. Cela1, C. Coutier, M. Langlet, R. Rimet, and J. Fick. 2001. "Photoluminescence of Terbium-Organic Complex in Aerosol – Gel-Derived Planar Waveguides." *Applied Physics B* 73:463–66. doi: 10.1007/s003400100707.

Judd, B. R., and I. Lindgren. 1961. "Theory of Zeeman Effect in the Ground Multiplets of Rare-Earth Atoms." *Physical Review* 122(6):1802–12. doi: 10.1103/PhysRev.122.1802.

Kakoti, D., P. Dutta, P. Gogoi, N. Dehingia, N. Rajkonwar, A. Boruah, A. T. T. Mostako, P. K. Saikia, and P. K. Gogoi. 2019. "Effect of ZnS Nanoparticles on the Judd-Ofelt and Radiative Parameters of Sm3+ Ions in Sol-Gel Silica Matrix." *Journal of Luminescence* 211(April):401–12. doi: 10.1016/j.jlumin.2019.03.063.

Khaidir, Rahayu Emilia Mohamed, Yap Wing Fen, Mohd Hafiz Mohd Zaid, Khamirul Amin Matoria, Nur Alia Sheh Omar, Aisyah Zakiah Khirel Azman , Muhammad Fahmi Anuarb, Siti Aisyah Abdul Wahaba, Nur Alia, Sheh Omar, Muhammad Fahmi, Siti Aisyah, Abdul Wahab, Aisyah Zakiah, and Khirel Azman. 2019. "Exploring Eu 3 + -Doped ZnO-SiO 2 Glass Derived by Recycling Renewable Source of Waste Rice Husk for White-LEDs Application." *Results in Physics* 15(July). doi: 10.1016/j.rinp.2019.102596.

Kozuka, Hiromitsu. 2005. *Handbook of Sol-Gel Science and Technology: Processing, Characterization, and Applications*. Vol. I,II,III. edited by Sumio Sakka. New York: Kluwer Academic Publisher.

Kumar, Pawan, Kanika, Satbir Singh, Rimli Lahon, Abhiram Gundimeda, Govind Gupta, and Bipin Kumar Gupta. 2018. "A Strategy to Design Lanthanide Doped Dual-Mode Phosphor Mediated Spectral Convertor for Solar Cell Applications."

*Journal of Luminescence* 196(October 2017):207–13. doi: 10.1016/j.jlumin.2017.12.035.

Kumar, Vijay Bhooshan, Madhavi Annamanedi, Muvva Durga Prashad, Kalle M. Arunasree, Yitzhak Mastai, Aharon Gedanken, Pradip Paik, and Received: 2013. "Synthesis of Mesoporous SiO 2 – ZnO Nanocapsules : Encapsulation of Small Biomolecules for Drugs and '" SiOZO-Plex "' for Gene Delivery." *Journal Nanopart Res* 15:1–13. doi: 10.1007/s11051-013-1904-y.

Kumar, Vinod, O. M. Ntwaeaborwa, T. Soga, Viresh Dutta, and H. C. Swart. 2017. "Rare Earth Doped Zinc Oxide Nanophosphor Powder : A Future Material for Solid State Lighting and Solar Cells." *ACS Photonics* 4:2613–37. doi: 10.1021/acsphotonics.7b00777.

Kumar, Vinod, S. P. Tiwari, O. M. Ntwaeaborwa, and Hendrik C. Swart. 2020. "Spectroscopy of Lanthanide-Doped Oxide Materials." Pp. 345–64 in *Spectroscopy of Lanthanide Doped Oxide Materials*. Elsevier Ltd.

Kunkel, Nathalie, and Philippe Goldner. 2018. "Recent Advances in Rare Earth Doped Inorganic Crystalline Materials for Quantum Information Processing." *Zeitschrift Fur Anorganische Und Allgemeine Chemie* 644(2):66–76. doi: 10.1002/zaac.201700425.

Lee, Chee Sun, Khamirul Amin Matori, Sidek Hj Ab Aziz, Halimah Mohamed Kamari, Ismayadi Ismail, and Mohd Hafiz Mohd Zaid. 2017. "Fabrication and Characterization of Glass and Glass-Ceramic from Rice Husk Ash as a Potent Material for Opto-Electronic Applications." *Journal of Materials Science: Materials in Electronics* 28(23):17611–21. doi: 10.1007/s10854-017-7699-3.

Lee, Jae Won, Sungmin Kong, Woo Sik Kim, and Jinsoo Kim. 2007. "Preparation and Characterization of SiO2/TiO2 Core-Shell Particles with Controlled Shell Thickness." *Materials Chemistry and Physics* 106(1):39–44. doi: 10.1016/j.matchemphys.2007.05.019.

Li, Xiangtan, Binhua Yang, Junjie Zhang, Lili Hu, and Liyan Zhang. 2014. "Energy Transfer between Er3+ and Pr3+ for 2.7 Mm Fiber Laser Material." *Fibers* 2:24–33. doi: 10.3390/fib2010024.

Li, Xiaomin, Rui Wang, Fan Zhang, and Dongyuan Zhao. 2014. "Engineering Homogeneous Doping in Single Nanoparticle To Enhance Upconversion E Ffi

Ciency.” *Nano Letters* 14:3634–39.

Li, Xiaoyu, and Junhui He. 2013. “Synthesis of Raspberry-Like SiO2 − TiO2 Nanoparticles toward Antire Fl Ective and Self-Cleaning Coatings.” *ACS Applied Materials & Interfaces* 5(11):5282–90. doi: https://doi.org/10.1021/am401124j.

Li, Z. Q., X. D. Li, Q. Q. Liu, X. H. Chen, Z. Sun, C. Liu, X. J. Ye, and S. M. Huang. 2012. “Core/Shell Structured NaYF 4:Yb 3+/Er 3+/Gd +3 Nanorods with Au Nanoparticles or Shells for Flexible Amorphous Silicon Solar Cells.” *Nanotechnology* 23(2):1–8. doi: 10.1088/0957-4484/23/2/025402.

Liang, Leben, Zhifeng Mo, Biao Ju, Changming Xia, and Zhiyun Hou. 2020. “Visible and Near-Infrared Emission Properties of Yb 3 + / Pr 3 + Co-Doped Lanthanum Aluminum Silicate Glass.” *Journal of Non-Crystalline Solids* (November):120578. doi: 10.1016/j.jnoncrysol.2020.120578.

Liang, Leben, Zhifeng Mo, Biao Ju, Changming Xia, and Zhiyun Hou. 2021. “Visible and Near-Infrared Emission Properties of Yb 3 + / Pr 3 + Co-Doped Lanthanum Aluminum Silicate Glass.” *Journal of Non-Crystalline Solids* 557(September 2020):120578. doi: 10.1016/j.jnoncrysol.2020.120578.

Liang, Liangliang, Yumin Liu, Chenghao Bu, Kaimo Guo, Weiwei Sun, Niu Huang, Tao Peng, Bobby Sebo, Mengmei Pan, Wei Liu, Shishang Guo, and Xing Zhong Zhao. 2013. “Highly Uniform, Bifunctional Core/Double-Shell-Structured β-NaYF 4:Er3+, Yb3+@SiO2@TiO2 Hexagonal Sub-Microprisms for High-Performance Dye Sensitized Solar Cells.” *Advanced Materials* 25(15):2174–80. doi: 10.1002/adma.201204847.

Liang, Liangliang, Daniel B. L. Teh, Ngoc Duy Dinh, Weiqiang Chen, Qiushui Chen, Yiming Wu, Srikanta Chowdhury, Akihiro Yamanaka, Tze Chien Sum, Chia Hung Chen, Nitish V. Thakor, Angelo H. All, and Xiaogang Liu. 2019. “Upconversion Amplification through Dielectric Superlensing Modulation.” *Nature Communications* 10(1):1–9. doi: 10.1038/s41467-019-09345-0.

Liégard, F., J. L. Doualan, R. Moncorgé, and M. Bettinelli. 2005. “Nd3+ → Yb3+ Energy Transfer in a Codoped Metaphosphate Glass as a Model for Yb3+ Laser Operation around 980 Nm.” *Applied Physics B: Lasers and Optics* 80(8):985–91. doi: 10.1007/s00340-005-1829-y.

Lin, Tao, Xiao-wei Zhang, Yun-ji Wang, Jun Xu, Neng Wan, and Jian-feng Liu. 2012. “Luminescence Enhancement Due to Energy Transfer in ZnO Nanoparticles and Eu 3 + Ions Co-Doped Silica.” *Thin Solid Films* 520(17):5815–19. doi: 10.1016/j.tsf.2012.04.058.

Liu, Quan, Yinsheng Xu, Qi Xia, Weiwei Li, Xianghua Zhang, Quan Liu, Yinsheng Xu, Qi Xia, Weiwei Li, and Xianghua Zhang. 2023. “Intense 2 . 7 Mu m Emission of Er3 + / Pr3 + Doped Ga5Ge20Sb10S65 Chalcogenide Glass.” *Journal of the American Ceramic Society* 106(10):5743–53. doi: 10.1111/jace.19181.

Liu, Yujia, Yiqing Lu, Xusan Yang, Xianlin Zheng, Shihui Wen, Fan Wang, Xavier Vidal, Jiangbo Zhao, Deming Liu, Zhiguang Zhou, Chenshuo Ma, Jiajia Zhou, James A. Piper, Peng Xi, and Dayong Jin. 2017. “Amplified Stimulated Emission in Upconversion Nanoparticles for Super-Resolution Nanoscopy.” *Nature* 543(7644):229–33. doi: 10.1038/nature21366.

Livage, J. 2004. *BASIC PRINCIPLES of SOL-GEL CHEMISTRY*. Technologi. edited by M. A. Aegerter and M. Mennig. Boston, MA: Springer.

Lluscà, M., J. López-Vidrier, A. Antony, S. Hernández, B. Garrido, and J. Bertomeu. 2014. “Up-Conversion Effect of Er- and Yb-Doped ZnO Thin Films.” *Thin Solid Films* 562:456–61. doi: 10.1016/j.tsf.2014.03.078.

Lojpur, Vesna M., Phillip S. Ahrenkiel, and Miroslav D. Dramićanin. 2013. “Color-Tunable up-Conversion Emission in Y2O3:Yb3+, Er3+ Nanoparticles Prepared by Polymer Complex Solution Method.” *Nanoscale Research Letters* 8(1):1–6. doi: 10.1186/1556-276X-8-131.

Loo, Jacky Fong-chuen, Yi-hsin Chien, Feng Yin, Siu-kai Kong, Ho-pui Ho, and Ken-tye Yong. 2019. “Upconversion and Downconversion Nanoparticles for Biophotonics and Nanomedicine.” *Coordination Chemistry Reviews* 400:213042. doi: 10.1016/j.ccr.2019.213042.

Lv, Zhijia, Longhai Jin, Yue Cao, Hao Zhang, Dongzhi Xue, Na Yin, Tianqi Zhang, Yinghui Wang, Jianhua Liu, Xiaogang Liu, and Hongjie Zhang. 2022. “A Nanotheranostic Agent Based on Nd 3 + -Doped YVO 4 with Blood-Brain-Barrier Permeability for NIR-II Fl Uorescence Imaging / Magnetic Resonance Imaging and Boosted Sonodynamic Therapy of Orthotopic Glioma.” *Light:*

*Science & Applications* 11(116):1–10. doi: 10.1038/s41377-022-00794-9.

Mahata, Manoj Kumar, Surya Prakash Tiwari, Shriparna Mukherjee, Kaushal Kumar, and Vineet Kumar Rai. 2014. "YVO4:Er3+ /Yb3+ Phosphor for Multifunctional Applications." *Journal of Optical Society America B* 31(8):1814–21.

Meijer, Janne Mieke, Linda Aarts, Bryan M. Van Der Ende, Thijs J. H. Vlugt, and Andries Meijerink. 2010. "Downconversion for Solar Cells in YF3: Nd3+, Yb 3+." *Physical Review B - Condensed Matter and Materials Physics* 81(3):1–9. doi: 10.1103/PhysRevB.81.035107.

Mhlongo. 2011. "Luminescence Investigation of Trivalent Rare Earth Ions in Sol-Gel Derived SiO2 and ZnO Co- Doped SiO2:Pr3+." University of Free State.

Minehan, W. T., G. L. Messing, and C. G. Pantano. 1989. "Titania-Silica Glasses Prepared by Sintering Alkoxide Derived Spherical Colloids." *Journal of Non-Crystalline Solids* 108(2):163–68. doi: 10.1016/0022-3093(89)90579-6.

Mir, Wasim J., Tariq Sheikh, Habibul Arfin, Zhiguo Xia, and Angshuman Nag. 2020. "Lanthanide Doping in Metal Halide Perovskite Nanocrystals: Spectral Shifting, Quantum Cutting and Optoelectronic Applications." *NPG Asia Materials* 12(1). doi: 10.1038/s41427-019-0192-0.

Mohamed, R. M., and I. A. Mkhalid. 2010. "The Effect of Rare Earth Dopants on the Structure , Surface Texture and Photocatalytic Properties of TiO 2 – SiO 2 Prepared by Sol – Gel Method." *Journal of Alloys and Compounds* 501:143–47. doi: 10.1016/j.jallcom.2010.04.061.

Mossad Ali, Atif, Adel A. Ismail, Rasha Najmy, and Ali Al-hajry. 2014. "Preparation and Characterization of ZnO – SiO 2 Thin Films as Highly Efficient Photocatalyst." *Journal of Photochemistry & Photobiology, A: Chemistry* 275:37–46. doi: 10.1016/j.jphotochem.2013.11.002.

Muniz, R. F., V. S. Zanuto, M. S. Gibin, J. V. Gunha, A. Novatski, J. H. Rohling, A. N. Medina, and M. L. Baesso. 2023. "Down- and up-Conversion Processes in Nd3+/Yb3+ Co-Doped Sodium Calcium Silicate Glasses with Concomitant Yb2+ Assessment." *Journal of Rare Earths* 41(3):342–48. doi: 10.1016/j.jre.2022.01.020.

Naresh, V., and S. Buddhudu. 2015. "Analysis of Visible-NIR Emission and

Photoluminescence Quenching in Er3+lasses: Bi2O3-AIF3-TeO2-B2O3." *Journal, Glasses European Science, Glass Part, Technology* 56(6):255–62. doi: 10.13036/17533562.56.5.255.

Nizamutdinov, A. S., S. V Kuznetsov, V. A. Konyushkin, A. N. Nakladov, E. I. Madirov, V. V Voronov, A. R. Khadiev, M. A. Marisov, and V. V Semashko. 2019. "LUMINESCENCE OF GdF 3 : Pr : Yb AND YF 3 : Pr : Yb SOLID SOLUTIONS SYNTHESIZED BY CRYSTALLIZATION FROM THE MELT." *Journal of Applied Spectroscopy* 86(5):795–801. doi: 10.1007/s10812-019-00895-1.

Ntwaeaborwa, O. M., and P. H. Holloway. 2005. "Enhanced Photoluminescence of Ce 3+ Induced by an Energy Transfer from ZnO Nanoparticles Encapsulated in SiO 2." *Nanotechnology* 16(6):865–68. doi: 10.1088/0957-4484/16/6/042.

Ofelt, G. S. 1962. "Intensities of Crystal Spectra of RareEarth Ions." *The Journal of Chemical Physics* 37(May 2012):511–20. doi: 10.1063/1.1701366.

Pellegrino, Anna L., Paolo Cortelletti, Marco Pedroni, Adolfo Speghini, and Graziella Malandrino. 2017. "Nanostructured CaF2:Ln3+ (Ln3+ = Yb3+/Er3+, Yb3+/Tm3+) Thin Films: MOCVD Fabrication and Their Upconversion Properties." *Advanced Materials Interfaces* 4(18):2–7. doi: 10.1002/admi.201700245.

Pisarski, Wojciech A., Joanna Pisarska, Marta Kuwik, Marcin Kochanowicz, Jacek Żmojda, Piotr Miluski, Agata Baranowska, Jan Dorosz, Magdalena Leśniak, and Dominik Dorosz. 2020. "Fluoroindate Glasses Co-doped with Pr3+/Er3+ for Near-infrared Luminescence Applications." *Scientific Reports* 10(0123456789):1–16. doi: 10.1038/s41598-020-77943-w.

Prathibha, K. N., R. Hari Krishna, B. V. Nagesh, D. Prakashbabu, B. S. Panigrahi, and R. Ananthanarayanan. 2021. "Investigation of Luminescence Spectroscopic Characteristics in Eu3+-Doped Zn2SiO4 by Judd–Ofelt Parameters." *Journal of Materials Science: Materials in Electronics* 32(15):20197–210. doi: 10.1007/s10854-021-06524-y.

Pudovkin, M. S., A. K. Ginkel, and E. V. Lukinova. 2021. "Temperature Sensitivity of Nd3+, Yb3+:YF3 Ratiometric Luminescent Thermometers at Different Yb3+ Concentration." *Optical Materials* 119(April):111328. doi:

10.1016/j.optmat.2021.111328.

Qiu, Jianrong, Kentarou Nouchi, Kiyotaka Miura, Tsuneo Mitsuyu, and Kazuyuki Hirao. 2000. “Room-Temperature Persistent Spectral Hole Burning of x-Ray-Irradiated Sm 3 + -Doped Glass.” *J. Phys.: Condens. Matter* 12:5061–5067.

Raevskaya, A. E., Ya V. Panasiuk, O. L. Stroyuk, S. Ya Kuchmiy, V. M. Dzhagan, A. G. Milekhin, N. A. Yeryukov, L. A. Sveshnikova, E. E. Rodyakina, V. F. Plyusnin, and D. R. T. Zahn. 2014. “Spectral and Luminescent Properties of ZnO-SiO2 Core-Shell Nanoparticles with Size-Selected ZnO Cores.” *RSC Advances* 4(108):63393–401. doi: 10.1039/c4ra07959k.

Rai, Suman, and Andrew L. Fanai. 2014. “Spectroscopic Studies of Ho 3+ Doped SiO 2-TiO 2 Nanoparticle for Photonic Applications.” *Science Vision* 14(3):112–17.

Reisfeld, R., and Y. Kalisky. 1981. “Nd3+ and Yb3+ Germanate and Tellurite Glasses for Fluorescent Solar Energy Collectors.” *Chemical Physics Letters* 80(1):178–83. doi: 10.1016/0009-2614(81)80084-X.

Richards, B. S. 2006. “Enhancing the Performance of Silicon Solar Cells via the Application of Passive Luminescence Conversion Layers.” *Solar Energy Materials and Solar Cells* 90(15):2329–37. doi: 10.1016/j.solmat.2006.03.035.

Rosales, Alicia, and Karen Esquivel. 2020. “SiO2@TiO2 Composite Synthesis and Its Hydrophobic Applications: A Review.” *Catalysts* 10(2):1–17. doi: 10.3390/catal10020171.

Saeed, N. A. M., E. Coetsee, and H. C. Swart. 2020. “Down-Conversion of YOF: Pr3+, Yb3+ Phosphor.” *Optical Materials* 110(February):110516. doi: 10.1016/j.optmat.2020.110516.

Sales, A. J. M., D. G. Sousa, H. O. Rodrigues, M. M. Costa, A. S. B. Sombra, and F. N. A. Freire. 2016. “Power Dependent Upconversion in Er 3+/ Yb 3+ Co-Doped BiNbO 4 Phosphors.” *Ceramics International* 42(6):6899–6905. doi: 10.1016/j.ceramint.2016.01.075.

Serrano, D., A. Braud, J. L. Doualan, P. Camy, A. Benayad, V. Ménard, and R. Moncorgé. 2011. “Ytterbium Sensitization in KY3F10: Pr3+, Yb3+ for Silicon Solar Cells Efficiency Enhancement.” *Optical Materials* 33(7):1028–31. doi: 10.1016/j.optmat.2010.07.023.

Shi, Gang, Jie Chen, Likui Wang, Dawei Wang, Jingguo Yang, Ying Li, Liping Zhang, Caihua Ni, and Lifeng Chi. 2016. “Titanium Oxide/Silicon Moth-Eye Structures with Antireflection, p–n Heterojunctions, and Superhydrophilicity.” *Langmuir* 32(41):10719–24. doi: 10.1021/acs.langmuir.6b03117.

Smentek, Lidia. 1988. “Theoritical Description of the Spectroscopic Properties of Rare Earth Ions in Crystal.” *Physics Reports* 297:155–237.

Smentek, Lidia, and Brian G. Wybourne. 2000. “Relativistic f ↔ f Transitions in Crystal Fields.” *Journal of Phsics B* 33:3647–51.

Song, Nan, Songbin Liu, Peng Zhang, Junshan He, Qinyuan Zhang, Feng Wang, and Bo Zhou. 2021. “Enhancing Upconversion of Nd3+ through Yb3+-Mediated Energy Cycling towards Temperature Sensing.” *Journal of Rare Earths* 39(12):1506–11. doi: 10.1016/j.jre.2021.06.013.

Soni, Abhishek Kumar, Riya Dey, and Vineet Kumar Rai. 2015. “Stark Sublevels in Tm3+–Yb3+ Codoped Na2Y2B2O7 Nanophosphor for Multifunctional Applications.” *RSC Advances* 5:34999–9. doi: 10.1039/C4RA15891A.

Srinivasa Rao, Ch, I. V Kityk, T. Srikumar, G. Naga Raju, V. Ravi Kumar, Y. Gandhi, and N. Veeraiah. 2011. “Spectroscopy Features of Pr 3 + and Er 3 + Ions in Li 2 O – ZrO 2 – SiO 2 Glass Matrices Mixed with Some Sesquioxides.” *Journal of Alloys and Compounds* 509:9230–39. doi: 10.1016/j.jallcom.2011.07.001.

Sta, I., M. Jlassi, M. Hajji, M. F. Boujmil, R. Jerbi, M. Kandyla, M. Kompitsas, and H. Ezzaouia. 2014. “Structural and Optical Properties of TiO2 Thin Films Prepared by Spin Coating.” *Journal of Sol-Gel Science and Technology* 72(2):421–27. doi: 10.1007/s10971-014-3452-z.

Strohhofer, C., J. Fick, H. C. Vasconcelos, and R. M. Almeida. 1998. “Active Optical Properties of Er-Containing Crystallites in Sol – Gel Derived Glass Films.” *Journal of Non-Crystalline Solids* 226:182–91.

Sukul, Prasenjit Prasad, and Kaushal Kumar. 2016. “Near-Infrared (808 and 980 Nm) Excited Photoluminescence Study in Nd-Doped Y2O3 Phosphor for Bio-Imaging.” *Methods and Applications in Fluorescence* 4(44005):1–9. doi: 10.1088/2050-6120/4/4/044005.

Sun, Ting, Ai Hua Li, Chao Xu, Yu Heng Xu, and Rui Wang. 2013. “Energy

Transfer Properties of Nd3+→Yb3+ in Nd:Yb:LiNbO3 Crystals." *Optics and Laser Technology* 56:322–25. doi: 10.1016/j.optlastec.2013.09.010.

Sun, Xiaoyu, Xiaozhuang Xu, Guanyu Song, Jielei Tu, Lei Li, Pinyuan Yan, Weinan Zhang, and Kai Hu. 2020. "Preparation of MgF2/SiO2 Coating with Broadband Antireflective Coating by Using Sol–Gel Combined with Electron Beam Evaporation." *Optical Materials* 101(November 2019):2–10. doi: 10.1016/j.optmat.2020.109739.

Tavernaro, Isabella, Christian Cavelius, Henrike Peuschel, and Annette Kraegeloh. 2017. "Bright Fluorescent Silica-Nanoparticle Probes for High-Resolution STED and Confocal Microscopy." *Beilstein Journal of Nanotechnology* 8:1283–96. doi: 10.3762/bjnano.8.130.

Tran, T. T. Va., T. M. Dun. Cao, Quang Vinh Lam, and Van Hieu Le. 2017. "Emission of Eu3 + in SiO2-ZnO Glass and SiO2-SnO2 Glass-Ceramic: Correlation between Structure and Optical Properties of Eu3 + Ions." *Journal of Non-Crystalline Solids* 459:57–62. doi: 10.1016/j.jnoncrysol.2016.12.040.

Tseng, Yung-kuan, Ming-hung Chuang, Yen-cheng Chen, and Chao-hsien Wu. 2012. "Synthesis of 1D, 2D, and 3D ZnO Polycrystalline Nanostructures Using the Sol-Gel Method." *Journal of Nanotechnology* 2012:1–9. doi: 10.1155/2012/712850.

Tung, Pham Son, Le Thi Thu Hien, Ngo Ngoc Ha, Tran Ngoc Khiem, and Nguyen Duc Chien. 2016. "Influence of Composition , Doping Concentration and Annealing Temperatures on Optical Properties of Eu3+-Doped ZnO–SiO2 Nanocomposites." *Journal of Nanoscience and Nanotechnology* 16(8):7955–58. doi: 10.1166/jnn.2016.12756.

Vasconcelos, Helena Cristina, and Afonso Silva Pinto. 2017. "Fluorescence Properties of Rare-Earth-Doped Sol-Gel Glasses." in *Recent Applications in Sol-Gel Synthesis*, edited by Usha chandra. IntechOpen.

Villanueva-Delgado, Pedro, Karl W. Krämer, and Rafael Valiente. 2015. "Simulating Energy Transfer and Upconversion in β-NaYF4: Yb3+, Tm3+." *Journal of Physical Chemistry C* 119(41):23648–57. doi: 10.1021/acs.jpcc.5b06770.

Walsh, Brian M. 2006. "Judd-Ofelt Theory: Principles and Practices." Pp. 403–33 in *Advances in Spectroscopy for Lasers and Sensing*, edited by B. Di Bartolo and

O. Forte. Netherland: Springer.

Wang, Fangke, Lei Cui, Zhengce An, Xiangting Zhang, Yanhua Song, Ye Sheng, and Haifeng Zou. 2019. “Interfacial Energy Transfer in Hollow Double-Shelled TiO2 : X % Eu3 + @ SiO2 : Y % Tb3 + Nanospheres for Tissue Imaging.” *ACS Applied Nano Materials* 1–28. doi: 10.1021/acsanm.9b01713.

Wang, Feng, and Xiaogang Liu. 2009. “Recent Advances in the Chemistry of Lanthanide-Doped Upconversion Nanocrystals.” *Chemical Society Reviews* 38:976–89. doi: 10.1039/b809132n.

Wang, Qun, Changyuan Xu, Fengjiao Zhao, and Hongming Yin. 2024. “Energy Transfer Er3+-Nd3+ Co-Doped in Tellurate via Energy Level Match.” *Current Applied Physics* 65:68–74.

Wang, Shuangyue, Hongwei Yan, Dengji Li, Liang Qiao, Shaobo Han, Xiaodong Yuan, and Wei Liu. 2018. “TEM and STEM Studies on the Cross- Sectional Morphologies of Dual- / Tri-Layer Broadband SiO 2 Antireflective Films.” *Nanoscale Research Letters* 13(49):0–8. doi: 10.1186/s11671-018-2442-4.

Wang, Xiaodong, Guangming Wu, Bin Zhou, and Jun Shen. 2013. “Thermal Annealing Effect on Optical Properties of Binary TiO 2 -SiO 2 Sol-Gel Coatings.” *Materials* 6:76–84. doi: 10.3390/ma6010076.

Wang, Ye-fu, Gao-yuan Liu, Ling-dong Sun, Jia-wen Xiao, Jia-cai Zhou, Chun-hua Yan, and Wang E. T. Al. 2013. “Nd 3+ -Sensitized Upconversion Nanophosphors : E Ffi Cient In Vivo Bioimaging Probes with Minimized Heating E Ff Ect.” *ACS Nano* 7(8):7200–7206.

Weisenbach, Lon, Brian J. J. Zeinski, John O. Kelly, Jeanne Morreale, Ronald L. Roncone, and James J. Burke. 1991. “The Influence of Processing Variables on the Optical Properties of SiO2-Ti02 Planar Waveguides.” *Submolecular Glass Chemistry and Physics* 1590:50–58.

Wen, Hongli, and Peter A. Tanner. 2011. “Energy Transfer and Luminescence Studies of Pr3+, Yb 3+ Co-Doped Lead Borate Glass.” *Optical Materials* 33(11):1602–6. doi: 10.1016/j.optmat.2011.04.024.

Wen, Shihui, Jiajia Zhou, Kezhi Zheng, Artur Bednarkiewicz, Xiaogang Liu, and Dayong Jin. 2018. “Advances in Highly Doped Upconversion Nanoparticles.” *Nature Communications* 9(1):1–12. doi: 10.1038/s41467-018-04813-5.

Xiao, F., R. Chen, Y. Q. Shen, Z. L. Dong, H. H. Wang, Q. Y. Zhang, and H. D. Sun. 2012. “Efficient Energy Transfer and Enhanced Infrared Emission in Er-Oped ZnO-SiO 2 Omposites.” *Journal of Physical Chemistry C* 116(24):13458–62. doi: 10.1021/jp304075g.

Xiao, F., R. Chen, Y. Q. Shen, B. Liu, G. G. Gurzadyan, Z. L. Dong, Q. Y. Zhang, and H. D. Sun. 2011. “Infrared Emission Properties and Energy Transfer in ZnO – SiO 2 : Yb 3 + Composites.” *Journal of Alloys and Compounds* 509(November 2018):7794–97. doi: 10.1016/j.jallcom.2011.05.011.

Xiaoqi, Meng, Li Lianqiang, Zou Kaishun, and Liu Juncheng. 2014. “The Effect of SiO2 on TiO2 Up-Conversion Photoluminescence Film.” *Optical Materials* 37(C):367–70. doi: 10.1016/j.optmat.2014.06.027.

Xu, Jian, S. O. Keefe, and Carole C. Perry. 2004. “The Preparation and Characterization of Sol – Gel Zinc Silicate Glass Particles with Pyramid Shape and Millimetre Size.” *Journal of Material Chemistry* 14:1744–48.

Yu, Lixin, and Masayuki Nogami. 2007. “Local Structure and Photoluminescent Characteristics of Eu 3 + in ZnO – SiO 2 Glasses.” *Journel of Sol-Gel Technology* 43:355–60. doi: 10.1007/s10971-007-1581-3.

Zareba-Grodz, Iwona, Robert Pazik, Włodzimierz Tylus, Witold Mielcarek, Krzysztof Hermanowicz, Wiesław Strek, and Krzysztof Maruszewski. 2007. “Europium-Doped Silica – Titania Thin Films Obtained by the Sol – Gel Method.” *Optical Materials* 29:1103–6. doi: 10.1016/j.optmat.2006.05.001.

Zhang, Q. Y., K. Pita, and C. H. Kam. 2003. “Sol – Gel Derived Zinc Silicate Phosphor Films for Full-Color Display Applications.” *Journal of Physics and Chemistry of Solids* 64:333–38.

Zhang, Q. Y., and G. F. Yang. 2007. “Cooperative Downconversion in GdAl3(BO3)4: RE3+, Yb3+ (RE=Pr, Tb, and Tm).” *Applied Physics Letters* 91(5):4–7. doi: 10.1063/1.2757595.

Zhao, Jiangbo, Dayong Jin, Erik P. Schartner, Yiqing Lu, Yujia Liu, Andrei V Zvyagin, Lixin Zhang, Judith M. Dawes, Peng Xi, James A. Piper, Ewa M. Goldys, and Tanya M. Monro. 2013. “Single-Nanocrystal Sensitivity Achieved by Enhanced Upconversion Luminescence.” *Nature Nanotechnology* (September):1–6. doi: 10.1038/nnano.2013.171.

Zhou, Bo, Bingyang Shi, Dayong Jin, and Xiaogang Liu. 2015. “Controlling Upconversion Nanocrystals for Emerging Applications.” *Nature Nanotechnology* 10(11):924–36. doi: 10.1038/nnano.2015.251.

Zhu, Wenjuan, Daqin Chen, Lei Lei, Ju Xua, and Yuansheng Wang. 2014. “An Active-Core/Active-Shell Structure with Enhanced Quantum-Cutting Luminescence in Pr – Yb Co-Doped Monodisperse Nanoparticles.” *Nanoscale Communication* 6(10500):10500–504. doi: 10.1039/C4NR02785J.

Zieliński, Michał, Bogdan Czajka, Mariusz Pietrowski, Iwona Tomska-Foralewska, Emilia Alwin, Monika Kot, and Maria Wojciechowska. 2017. “MgO-MgF2 System Obtained by Sol–Gel Method as an Immobilizing Agent of the Electrolyte Applied in the High Temperature Cells.” *Journal of Sol-Gel Science and Technology* 84(2):368–74. doi: 10.1007/s10971-017-4495-8.

Zou, Zehua, Lin Feng, Cheng Cao, Jiachi Zhang, and Yuhua Wang. 2016. “Near-Infrared Quantum Cutting Long Persistent Luminescence.” *Scientific Reports* 6(May):1–7. doi: 10.1038/srep24884.

*CHAPTER- 6*

# CONCLUSIONS AND SUMMARY

***This chapter is focused on summary and conclusions along with future prospect of the present thesis work.***

*Chapter -6*

---

## Conclusions and Summary

---

Photoluminescence (upconversion and downconversion luminescence) properties of different $RE^{3+}$ (e.g. $Pr^{3+}$-$Yb^{3+}$, $Nd^{3+}$-$Yb^{3+}$, $Nd^{3+}$-$Er^{3+}$, $Pr^{3+}$-$Er^{3+}$ etc) pairs have been interesting from the prospect of broader applicability in photonics. We have successfully synthesized novel $Pr^{3+}$-$Yb^{3+}$ and $Nd^{3+}$-$Yb^{3+}$ ion pair co-doped Silica-Titania and Zinc-Silicate dense glass ceramic and thin film materials via an ex-situ sol-gel method, with varying doping concentrations of $Yb^{3+}$ ion and fixed concentration of $Pr^{3+}$ and $Nd^{3+}$ ion, respectively.

For the first time, an ultra-broadband UCL of the SAMPLE I (STPYX-DGC) have been obtained optimized for the STPY15-DSC sample. PL confocal mapping of the STPYX-DGC material confirms UCL throughout the space material in powder form. The concentration of $Yb^{3+}$ ions has been observed as a color-tunable factor in UCL spectra, ranging from blue to red. Crystalline transformation of the as-synthesized material has been observed at annealing temperature higher than 700 ºC, resulting in the formation of anatase and rutile phases of $TiO_2$ composite. FTIR spectroscopy supports the formation of Ti-O-Si bonds to promote asymmetry in the host, with the absence of hydroxyl impurity ($OH^-$ group), benefiting the material from hydroxyl quenching.

In SAMPLE II, the crystallization of ZnO in amorphous silica has been confirmed at much low annealing temperatures, enhancing with the rise in annealing temperature. The formation of oxide phases (e.g. Zn-O-Zn, Si-O-Si, Zn-O-Si) was confirmed, with the absence of $OH^-$ molecules advantageous against hydroxyl quenching of $RE^{3+}$ ions. The formation of NBO contributes to the asymmetry of the host matrix. TEM monographs further confirm the growth of ZnO crystallites in the silica host. Elemental purity of the as-synthesized sample is resolved in EDS spectra. White UCL spectra have been observed for the entire sample under 980nm excitation,

with the UCL intensity of the SZNYX-DSC samples optimized for a 1.5 mol% $Yb^{3+}$ ion concentration. PL confocal mapping of the SZNY15-DGC sample at different locations confirms non-uniform luminescence throughout the space for the 980 nm excitation source.

Two other novel luminescent materials (SAMPLE III & IV) were developed by incorporating distinct RE ion pairs ($Nd^{3+}$-$Er^{3+}$ and $Pr^{3+}$-$Er^{3+}$) into *ex-situ* sol-gel derived Titania-Silicate or Zinc-Silicate dense glass ceramics hosts. The host synthesis via *ex-situ* sol-gel techniques remained unmodified, to demonstrate that low concentration co-doping of $Er^{3+}$/$Pr^{3+}$ and $Er^{3+}$/$Nd^{3+}$ ions in their respective hosts can enhance optical properties without altering the structural and morphological properties of the host material. These ion pairs were selected for their potential to adjust ionic interactions, enabling high concentrations of $RE^{3+}$ doping for photonics applications. Structural, morphological, and optical characterizations were conducted on both materials. Both pairs exhibited absorption and emission properties across UV-VIS and NIR regions. XRD analysis confirmed crystalline growth of $TiO_2$ or ZnO, while ATR-FTIR spectra showed NBO bonds without observable $RE^{3+}$ ions. UV-VIS-NIR absorption and DCL spectra exhibited distinct peaks of respective $RE^{3+}$ ions.

Thus, the as-obtained outcomes endorse that all four materials are optically active and capable of either UCL or DCL or both the luminescence which can be further used as in diverse photonic applications e.g., solar photovoltaic, thermal sensor, lightning and display device applications, soft robotics, soft electronics etc. Further optimization of various parameters is still required to enhance overall performance.

**Future prospects**

Based on the work carried out in the thesis and the results obtained, suggestions for further work are given as follows:

1. Analyze the DCL-QC luminescence of as-synthesized STPYX and SZNYX-DGC samples under different (e.g. 980/450/250 nm) laser excitation.
2. Investigate the temperature-dependent UCL properties of both the SAMPLE I/II (STPYX-DGC and SZNYX-DGC) for potential thermometric applications.

3. Scrutinize the power-dependent UCL properties of both the SAMPLE I/II for photonic applications.

4. Explore the UCL and DCL properties of SAMPLE III ($Er^{3+}/Pr^{3+}$:$TiO_2$-$SiO_2$) samples for potential photonic applications in greater detail.

5. Investigate the UCL and DCL properties of both the SAMPLE III ($Er^{3+}/Nd^{3+}$:ZnO-$SiO_2$) samples further for potential photonic applications.

6. Luminescence decay analysis of the entire four samples for respective excited state to understand quantum efficiency using radiative and non-radiative decay rate.

7. Analyze the potential biological application (*in-vitro* and *in-vivo*) possibility of the as-synthesized samples.

## List of publications

1. Mrigankadeep Bharadwaj, **S.** Rai, Ankita Gaur**;** *Structural and morphological characterizations of* **ex-situ** *sol-gel derived luminescent* $Nd^{3+}$-$Yb^{3+}$ *ion co-doped zinc-silicate dense glass-ceramic*; Journal of Non-Crystalline solids (2023) **619**: 122552. https://doi.org/10.1016/j.jnoncrysol.2023.122552

2. Mrigankadeep Bharadwaj, **S.** Rai, Ankita Gaur**;** *Color tunable upconversion luminescence from ex-situ sol-gel derived Titania-Silicate dense glass-ceramic co-doped with* $Pr^{3+}$-$Yb^{3+}$ *ion pair*; Optical Materials (2023) 146:**114492** **https://doi.org/10.1016/j.optmat.2023.114492**

**Papers presented in Conferences/Seminars/Workshop attended**

1. Oral presentation on ***Photonics 2023***, IISC Bangalore, on July 2023 (accepted). Title: *White Upconversion Luminescence of $Nd^{3+}$ -$Yb^{3+}$ Ions Pair Co-doped ex-situ Sol-Gel Synthesized Zinc-Silicate Dense Glass*; Mrigankadeep Bharadwaj, S. Rai, Ankita Gaur.
2. Poster presentation on ***7th International Conference on Luminescence and its application (ICLA-2023)*** organized by CSIR-IICT, Hyderabad & LSI, July 2023.
3. Oral presentation on ***International Conference on Recent Advances in Energy Materials and Its applications***, May 2023, PUC, Aizawl.
4. Participated in one-week FDP-STTP on ***Science and Technology of Advanced Material*** Organized by NIT, AP; Feb, 2021.
5. Completed two day program on ***NANOPHOTONICS: Material, Devices and Application*** organized by CIPET Bhubneswar on 1st week of Feb, 2021.
6. Participated in a one-week short term course on ***Emerging nano devices and their applications*** organized by the Department of ECE, NIT Mizoram, Feb, 2020.
7. Participated two days' workshop in the ***National Conference on Materials and Applications -2019 (NCFMA-2019)*** organized by Dept. of BS&HSS (physics), NIT MIZORAM during November, 2019.
8. Participated in a one day *national workshop on Ethics in Research And Preventing Plagiarism (ERPR 2019)* organized by Department of Physics, Mizoram University, Oct 2019

# BIODATA

1. **Name** : Mrigankadeep Bharadwaj
2. **Mother's Name** : Dipty Kotoky Boruah
3. **Father's Name** : Bipul Boruah
4. **Date of Birth** : 01/01/1988
5. **Address** : Namti, Sivasagar, Assam-785684
6. **Email Id** mrigankadeepbharadwaj@gmail.com
7. **Educational Qualifications**

| Degree | Year | Percentage | Board | Division |
|---|---|---|---|---|
| HSLC | 2003 | 61.0 | SEBA | 1st |
| HSSLC | 2006 | 52.7 | AHSEC | 2nd |
| B. Sc (Physics) | 2009 | 50.8 | Dibrugargh University | 2nd |
| M. Sc (Phyics) | 2016 | 63.7 | Sikkim University | 1st |
| GATE (Physics) | 2019 | -- | All India rank 2012 | -- |

## PARTICULARS OF THE CANDIDATE

| | | |
|---|---|---|
| **NAME OF CANDIDATE** | : | MRIGANKADEEP BHARADWAJ |
| **DEGREE** | : | DOCTOR OF PHILOSOPHY (Ph.D.) |
| **DEPARTMENT** | : | PHYSICS |
| ***TITLE OF THESIS*** | : | A STUDY OF DOWN-CONVERSION AND UP-CONVERSION IN LANTHANIDE DOPED IN SILICA GLASS CO-DOPED IN METAL NANO-PARTICLE TOWARDS PHOTONICS APPLICATIONS |
| ***DATE OF ADMISSION*** | : | 26th July 2019 |

**APPROVAL OF RESEARCH PROPOSAL :**

| | |
|---|---|
| **1. DRC** | : 27th May 2020 |
| **2. BOS** | : 05th June 2020 |
| **3. SCHOOL BOARD** | : 12th June 2020 |
| **MZU REGISTRATION NO.** | : 1906296 |
| **Ph.D. REGISTRATION NO. & DATE** | : MZU/Ph.D./1458 of 26.07.2019 |
| **EXTENSION IF ANY** | : No extension |

Head

Department of Physics

# ABSTRACT

# A STUDY OF DOWN-CONVERSION AND UP-CONVERSION IN LANTHANIDE DOPED IN SILICA GLASS CO-DOPED IN METAL NANO-PARTICLE TOWARDS PHOTONICS APPLICATIONS

**AN ABSTRACT SUBMITTED IN PARTIAL FULFILLMENT OF THE REQUIREMENTS FOR THE DEGREE OF DOCTOR OF PHILOSOPHY**

**MRIGANKADEEP BHARADWAJ**
**MZU REGISTRATION NO.: 1906296**
**Ph.D. REGISTRATION NO.: MZU/Ph.D./1458 of 26.07.2019**


**DEPARTMENT OF PHYSICS**
**SCHOOL OF PHYSICAL SCIENCE**
**MARCH, 2024**

**THESIS TITLE:** A STUDY OF DOWN-CONVERSION AND UP-CONVERSION IN LANTHANIDE DOPED IN SILICA GLASS CO-DOPED IN METAL NANO-PARTICLE TOWARDS PHOTONICS APPLICATIONS

## INTRODUCTION

In recent years, luminescent materials have gained widespread interest across disciplines for their light absorption and emission abilities spanning UV-visible and infrared regions. Quantum dots (QDs), organic dyes (ODs), and upconversion nanoparticles (UCNPs) have emerged as key luminescent materials, with UCNPs exhibiting anti-Stokes luminescence. Despite challenges like low quantum yields, UCL materials show promise for applications like anti-reflection coatings, spectral converters, bio-sensing, and optical memory. UCNPs and DCNPs, synthesized via sol-gel and hydrothermal routes, offer versatile shapes and sizes, making them ideal for photovoltaic and bio-photonics applications. Their use as spectral converters in solar cells enhances photon absorption, while $RE^{3+}$ ion pairs reduce tissue overheating in bio-applications. This study focuses on the synthesis and characterization of UCL and DCL materials, specifically exploring different Rare-Earth ($RE^{3+}$) ion pairs, outlining key applications and research objectives.

$RE^{3+}$ ions exhibit photoluminescence (PL) spectra, representing photon emission rather than fluorescence or phosphorescence, based on Strokes and anti-Strokes Laws. Downconversion luminescence (DCL) follows Strokes' law, splitting high-energy photons into multiple low-energy ones, categorized as quantum cutting (QC) or downshifting (DS). Upconversion luminescence (UCL), an anti-Stokes process, involves successive NIR excitation promoting nonlinear emission in the UV-VIS region, classified into excited-state absorption, energy transfer upconversion, cooperative sensitization upconversion, and photon avalanche.

The $RE^{3+}$ ion pairs (e.g. $Pr^{3+}$-$Yb^{3+}$/$Nd^{3+}$-$Yb^{3+}$/$Er^{3+}$-$Yb^{3+}$) are co-doped in various host materials through different synthesis routes, having unique structure, and luminescence properties. Additionally, the power and temperature dependencies of UCL or DCL spectra were also investigated by various researchers. Among UCL

processes, energy transfer upconversion (ETU) and cooperative sensitization upconversion (CSU) are highly efficient and necessitate sensitizer-activator ion pairs, highlighting the significance of the mentioned pairs.

The low-toxicity $Pr^{3+}$ ion boasts diverse emission bands, making it ideal for switchless scintillation, deep excitation penetration, and cell-free auto-fluorescence applications. Co-doped with $Yb^{3+}$ ions, the $Pr^{3+}$-$Yb^{3+}$ pair has been extensively studied in various host materials to obtain both upconversion luminescence (UCL) and downconversion luminescence (DCL) spectra. For instance, studies by Zhang and Yang demonstrated the synthesis of $Pr^{3+}$-$Yb^{3+}$ co-doped [$GdAl_3(BO_3)_4$] phosphor, revealing insights into DCL spectra variations with different $Yb^{3+}$ concentrations. Additionally, Dwivedi et al. reported white light emission from $Pr^{3+}$ - $Yb^{3+}$ co-doped tellurite glass, showcasing the potential of these materials in diverse applications. Similarly, Chen et al. and Braud et al. investigated DCL spectra in hexagonal $NaYF_4$ phosphor and $KY_3F_{10}$ glass, respectively, shedding light on the luminescence behavior of the $Pr^{3+}$-$Yb^{3+}$ pair under different conditions.

On the other hand, the $Nd^{3+}$ -$Yb^{3+}$ pair demonstrates promising characteristics for various applications, particularly in bio-photonics. With the highest absorption cross-section among $RE^{3+}$ ions at 808 nm and emission within biological windows I and II, $Nd^{3+}$ ions offer efficient energy transfer possibilities to sensitizer ions like $Pr^{3+}$, $Er^{3+}$, and $Ho^{3+}$ through $Yb^{3+}$ ions. The bio-applicability of the $Nd^{3+}$/$Yb^{3+}$ pair is highlighted by its ability to reduce overheating effects and enhance laser penetration depth in tissues. $Nd^{3+}$-$Yb^{3+}$ ion pairs co-doped in different host materials, reveals insights into their absorption, DCL, and UCL spectra characteristics. Studies by Reisfeld and Kalisky, Liegard et al., and Muniz et al. offer valuable insights into the luminescence behavior of $Nd^{3+}$-$Yb^{3+}$ co-doped glasses, crystals, and thin films, paving the way for diverse applications in photonic and biomedical fields.

## RESEARCH GAP

The luminescent properties of $Nd^{3+}$-$Yb^{3+}$ and $Pr^{3+}$-$Yb^{3+}$ ion pairs in Zinc-silicate and Titania-Silicate composites have not been explored in thin films, phosphors, or monolithic glass. Our investigation focuses on uncovering the upconversion luminescence (UCL) and downconversion luminescence (DCL) spectra of these ion pairs within $TiO_2$-$SiO_2$ and ZnO-$SiO_2$ binary composite hosts. Through a modified ex-situ sol-gel method, we aim to ensure uniform distribution of $RE^{3+}$ ions and potentially enhance luminescence properties by lowering phonon energy.

While previous studies have examined UCL and DCL spectra of $Pr^{3+}$-$Yb^{3+}$ ion pairs in various hosts, $TiO_2$-SiO composite hosts remain unexplored. Our approach involves synthesizing a host with lower phonon energy to advance understanding of the luminescence behavior under different excitation powers. Similarly, the $Nd^{3+}$-$Yb^{3+}$ ion pair's luminescence characteristics have been promising in diverse hosts but not in ZnO-$SiO_2$ composites. By adapting the ex-situ sol-gel synthesis method, we aim to uncover insights into luminescence efficiency and behavior under varying excitation powers, contributing to a deeper understanding of these luminescent systems.

## OBJECTIVES

- The synthesis of lanthanide ions (e.g. $Pr^{3+}$, $Er^{3+}$, and $Nd^{3+}$ with or without $Yb^{3+}$ ions) in silicate glass host along with Titanium Oxide and Zinc Oxide nano-particle.
- The samples will be examined for their structural and optical properties. Photonic applications of these materials are our key concern.

## EXPERIMENTAL METHODS

The structural, Morphological, thermal and optical characterization of the materials has been accomplished. The optical characterization of the samples has been carried out by recording Absorption spectra and Photoluminescence spectra.

### Synthesis

A novel ex-situ sol-gel method was utilized to prepare Titania-Silica and Zinc-Silicate host materials for $RE^{3+}$ ions. Separate solutions, "SOL-B" containing stabilized-ZnO/$TiO_2$ and "SOL-A" containing activated-$SiO_2$, were mixed in a 1:9 mol ratio. To prevent phase separation during hydrolysis-condensation of $SiO_2$, TEOS and water were pre-mixed in an alcoholic medium. The initial stage maintained an equimolar ratio (r=1) of TEOS and water to promote pre-hydrolysis. "SOL-A" was prepared by vigorously stirring a mixture of TEOS, EtOH, $H_2O$, and $HNO_3$ for 90 min at 60°C. Separate solutions of "AcAc-stabilized $TiO_2$" and "MEA-stabilized ZnO" were prepared before admixing them to the pre-hydrolyzed SiO2 solution to introduce asymmetry through NBO (Si-O-Ti and Si-O-Zn bonds). The composite $SiO_2$-ZnO/$TiO_2$ binary solution was stirred vigorously for an hour, and additional water was slowly added to maintain a 1:4 molar ratio of Si:DI water for hydrolysis and condensation. $RE^{3+}$ ion salts dissolved in MeOH were added to the $SiO_2$-$TiO_2$ and $SiO_2$-ZnO composite solution under uninterrupted stirring for 60 min to form the final solution (SOL-C).

The SOL-C solution was poured into a polypropylene container to form xerogel materials, which were aged at room temperature for three weeks. The annealing process involved gradually drying the materials in a hot air oven up to 235°C before heating at approximately 900°C for one hour in an electric muffle furnace, with a cooling rate of 1.0°C/min.

### Structural and morphological characterization

Structural analysis involved XRD and FTIR spectroscopy, with morphological analysis conducted via FESEM and FETEM. The ATR-FTIR Spectrometer (SHIMADZU, USA) provided IR absorption spectra without KBr pellets, with a

resolution of approximately 2 $cm^{-1}$. XRD was performed using a 9 kW Powder X-Ray Diffractometer (Rigaku Technologies, Japan) with CuKα radiation. FETEM analysis was conducted using a JOEL 2100F microscope (USA), while FESEM monographs were obtained using a Zeiss Sigma microscope (USA), with magnification up to 300,000x and 0.1 nm spatial resolution, and elemental analysis was performed using OXFORD EDS.

**Thermal Characterization**

The thermal studies were carried out by utilizing Thermo-gravimetry analysis and Derivative thermo-gravimetry analysis. TGA/DTG analysis had been done with the help of a thermal analyzer (Model: TGA-4000 from Perkin Elmer, UK) in the Analytical lab, School of Energy Science & Technology, IITG. The temperature range of the instrument is 15-900 °C.

**Optical characterization**

The optical studies were carried out by utilizing absorption spectra and photoluminescence spectra. The optical absorption spectra are acquired at room temperature by employing a spectrometer, specifically the iHR320 model from Horiba Scientific, in conjunction with the with the Syner JY$^{TM}$ software.

**RESULTS**

SAMPLE I (STPYX-DGC) materials have been successfully synthesized using an improved *ex-situ* sol-gel method and annealed at temperatures of 235, 700 & 900 ºC. The absence of OH- molecules with increasing annealing temperatures mitigates hydroxyl quenching of luminescence. Formation of a pure oxide phase and non-bridging oxygen (Ti-O-Si) bonds, promotes an asymmetric $TiO_2$-$SiO_2$ binary host, supporting luminescence of $Pr^{3+}$ and $Yb^{3+}$ ions in a crystalline environment. The existence of the $Pr^{3+}$ and $Yb^{3+}$ ion pair was confirmed by EDS spectra. Based on TG/DSC analyses, the material was found to be thermally stable, with thermal decomposition identified at 80 and 120 ºC. Therefore, the material can remain stable even in adverse environmental conditions. An ultra-broadband UCL of the STPYX-DGC materials was obtained for the first time, optimized for the STPY15-DSC

material, demonstrating color tunability from white to red. PL confocal mapping of the STPY15-DGC material confirms UCL throughout the space material in powder form. Thus STPYX-DGC material is optically active and capable of ultra-broadband red UCL for near-infrared excitation at 980nm, suitable for diverse photonic applications.

Similarly, the modified *ex-situ* sol-gel process facilitated the synthesis of the SAMPLE II (SZNYX-DGC) materials, observed to be crystalline in nature due to annealing temperature. The transparent dense glasses are free from OH molecule with higher phonon energy which promotes hydroxyl quenching of $RE^{3+}$ ion. The $Nd^{3+}$ and $Yb^{3+}$ ion are well distributed all over the thin film although voids are unavoidable from evaporation of adsorbed water and trapped solvents. Thus promotion of $Nd^{3+}$ and $Yb^{3+}$ ion codoped in Zinc-Silicate asymmetrical host with non-bridging oxygen (Zn-O-Si) is reported through this modified sol-gel synthesis route for future optoelectronic applications. FETEM are embedded in an amorphous silica matrix, with an interplanar spacing of 0.24 nm. TG and DSC analysis provide insights into the thermal behavior of the material. The synthesized materials exhibited white UCL spectra under 980nm excitation; with the optimum UCL intensity observed for the SZNY15-DSC samples. PL confocal mapping of the SZNYX-DGC sample revealed non-uniform luminescence due to the uneven topological surface in powder form. The optical activity of the SZNYX-DGC material, with both UCL and DCL properties, makes it promising candidates for various photonic applications.

Two other novel luminescent materials were developed by incorporating two distinct pair of $RE^{3+}$ ion ($Er^{3+}/Pr^{3+}$ and $Er^{3+}/Nd^{3+}$) into ex-situ sol-gel derived Titania-Silicate and Zinc-Silicate dense glass ceramic hosts respectively. The ex-situ sol-gel techniques for host synthesis remained unmodified, with only variations in $RE^{3+}$ ion pair. The primary aim was to demonstrate that co-doping $Er^{3+}/Pr^{3+}$ and $Er^{3+}/Nd^{3+}$ ions in their respective hosts could enhance optical properties without altering structural and morphological characteristics. These specific ion pairs were chosen due to their potential to tune ionic interactions, enabling high concentrations of $RE^{3+}$ doping for photonics applications.

Structural, morphological, and optical characterizations were conducted on both materials. Both pairs exhibited absorption and emission properties spanning UV-VIS and NIR regions. For the SAMPLE III ($Er^{3+}/Pr^{3+}$:$TiO_2$-$SiO_2$) material, XRD analysis confirmed the crystalline growth of $TiO_2$, while ATR-FTIR spectra revealed Si-O-Ti bonds without observable $RE^{3+}$ ions. TEM analysis unveiled $TiO_2$ nano-crystallites within an amorphous $SiO_2$ matrix. UV-VIS-NIR absorption and DCL spectra exhibited distinct peaks corresponding to $Er^{3+}$ and $Pr^{3+}$. Similarly, for SAMPLE IV ($Er^{3+}/Nd^{3+}$:ZnO-$SiO_2$, XRD confirmed the formation of α-$Zn_2SiO_4$, while ATR-FTIR indicated Si-O-Si bonds and Zn-O-Si vibrations. TEM analysis confirmed the presence of ZnO crystallites in the $SiO_2$ matrix, with UV-Vis-NIR absorption and DCL spectra showing different peaks for $Er^{3+}$ and $Nd^{3+}$.

**CONCLUSION:**

We have successfully synthesized four novel luminescent materials (SAMPLE I, II, III, IV) via an *ex-situ* sol-gel method with future potential photonic applications which can be further used in diverse photonic applications. Further optimization of the synthesis parameters and characterization of the optical properties are necessary to improve the luminescent efficiency and overall performance.